SEARCH FOR HEAVY RESONANCE DECAYS INTO TOP-QUARK PAIRS USING A LEPTON-PLUS-JETS FINAL STATE IN PROTON-PROTON COLLISIONS AT $\sqrt{s} = 13$ TeV WITH THE ATLAS DETECTOR

By

Kyle Krowpman

A DISSERTATION

Submitted to
Michigan State University
in partial fulfillment of the requirements
for the degree of

Physics — Doctor of Philosophy

2022

ABSTRACT

SEARCH FOR HEAVY RESONANCE DECAYS INTO TOP-QUARK PAIRS USING A LEPTON-PLUS-JETS FINAL STATE IN PROTON-PROTON COLLISIONS AT $\sqrt{s} = 13$ TeV WITH THE ATLAS DETECTOR

By

Kyle Krowpman

This thesis presents two studies in a search for new heavy resonances with 139 fb^{-1} of proton-proton collisions delivered by the Large Hadron Collider at $\sqrt{s} = 13$ TeV as measured by the ATLAS detector. In many Standard Model extensions, the top quark plays an important role in the dynamics of electroweak symmetry breaking, and so the studies presented here focus on heavy resonance searches in the top-antitop decay channel and their combination with searches for heavy resonances decaying into other final states. The first study detailed in this thesis is a search for new heavy resonances in a semileptonically decaying top-antitop final state where no significant excesses of data were observed with respect to the background prediction. That being so, exclusion limits at the 95% confidence level were placed on possible resonant masses for a Z' in a leptophobic topcolor-assisted technicolor model and for a bulk Randall-Sundrum graviton at 4.2 TeV and 1.0 TeV, respectively. This top-antitop search was combined with searches in orthogonal final states in an ATLAS-wide combination effort from which limit contours were placed at the 95% confidence level in the space of couplings to Standard Model particles for the Heavy Vector Triplet model.

ACKNOWLEDGMENTS

It is impossible to put into writing the gratitude I feel towards all the people who have played a part in making this thesis a reality. Although my name is on its title page, the effort put into its construction spans several decades and multiple continents. Recognition for what has been accomplished in this document is shared between myself, my collaborators, and the people thanked here.

Firstly to my fantastic advisor, Daniel Hayden, for whom every superlative would not be enough. Your mentorship made me a better and more inquisitive scientist, and I could not have asked for someone more supportive and intelligent to work with during my time at MSU.

A special expression of thanks and love for my mother, father, and sister, whose abiding confidence in my abilities allowed me to remain steadfast in my determination to finish this work. The seed of curiosity planted by you has bloomed and flourished.

Unbounded gratitude to Zachary Simon, my best friend of almost twenty years with his memorable humor and wit, and thanks to my kindred spirits to whom I escaped the world of particle physics after long days, Josh Vickery, Christopher Doss, Laken Adkins, Sam Munnis, and Austin Anderson. For those closest friends I have made in and out of physics during my time in Michigan, Isaac Yandow, Tamas Budner, Abigail Cathcart, Harrison Lawson, Daniel Paz, Caley Harris, and Joe Oehrli, thank you for keeping me on a stable footing during these times of shifting sands.

Thanks to Daniel Gilbert, a crusader for what is good and right in the world and whose career guidance has changed my life immeasurably. To Samantha Kendrick, my friend across the sea, I wish you were still here to see this.

TABLE OF CONTENTS

Chapter 1

Introduction

1.1 Particle Physics

The idea that the world of phenomena is constructed from simple parts dates back to the pre-Socratic philosophers Leucippus and Democritus. A consensus view on this question did not emerge until the early 19^{th} century, when John Dalton proposed the Law of Multiple Proportions, which related ratios of elements' masses to small whole numbers [1]. Nearly a century later, J.J. Thompson discovered that cathode rays, now known to be made of electrons, did not fall into this category [2]. Ernest Rutherford and James Chadwick then discovered the proton [3] and neutron [4], respectively, implying that the nucleus of the atom was also not simple. Scientists were also met with two apparent contradictions between the predictions of classical electrodynamics and observations: that known atomic structure allowed for negatively charged electrons to exist in a stable orbit around a positively charged nucleus and that light shone on a material could induce the ejection of electrons from its surface. Initial explanations for these phenomena were by their nature heuristic and often lacked the internal consistency that is expected from well-defined theory, but they were precursors to what is now considered modern quantum mechanics. Further experiments in the latter half of the 20^{th} century showed that the neutron and proton were also composed of constituent parts [5].

Particle physics today continues tradition of attempting to understand the observed world at its smallest and most fundamental scale. The most current and best understanding of these smallest-known parts and their interactions is summarized by the Standard Model (SM), which explains all the known matter content in the observable universe and its non-gravitational interactions. These interactions include the electromagnetic force, responsible for light and the attraction between electrically charged particles, the weak force, which describes radioactive decays, and the strong force, which describes the binding of nuclei. The observation of the Higgs boson by ATLAS and CMS experiments at the Large Hadron Collider (LHC) in 2012 represented the final experimental addition to the panoply of particles predicted by the Standard Model.

Although the Standard Model describes the results of almost all physical experiments with extreme precision and accuracy, there remain outstanding questions arising from observation. These include the apparent matter-antimatter asymmetry in the universe, the lack of viable Dark Matter candidates, the unexplained nature of gravity, and the failure to explain the orders of magnitude scale difference between gravity and the other known forces. Given these facts, it is commonly accepted that the Standard Model represents an incomplete understanding of the natural world; further explanations that build on or change the Standard Model are commonly referred to as Beyond the Standard Model (BSM) physics. This thesis will probe several BSM physics scenarios using the ATLAS experiment, which records data from proton-proton collisions at the LHC of energy in excess of 13 TeV at a rate of above 1 GHz.

1.2 Quantum Field Theory

Quantum Field Theory (QFT) is the mathematical formulation of our current understanding of the physics of particles at the smallest scale, where a particle is represented as a spatiotemporally localized excitation of a quantum field. The main model descriptor for a QFT is the Lagrangian density $\mathcal{L}$, which specifies the particle content of a model and its interactions. Lagrangians are typically broken into their kinetic terms ($\mathcal{L}_{\text{kin}}$), and their interaction terms ($\mathcal{L}_{\text{int}}$). The equations of motion for a given model can be derived from this Lagrangian from the principle of least action, which states that $\mathcal{S} = \int \mathcal{L} d^4x$ is stationary along a classical path. For a scalar field ϕ, this results in the Euler-Lagrange equations in dimension μ given by

$$\frac{\partial \mathcal{L}}{\partial \phi} = \partial_\mu \frac{\partial \mathcal{L}}{\partial(\partial_\mu \phi)}. \tag{1.1}$$

One fundamental calculation given by a QFT is the scattering of some initial state particles $|i\rangle$ into some final state particles $|f\rangle$. Fermi's Golden Rule gives the differential probability of this scattering as

$$dP = \frac{|\langle f|S|i\rangle|^2}{\langle f|f\rangle\langle i|i\rangle} d\Pi, \tag{1.2}$$

where S is the scattering matrix encoding the relevant physics and $d\Pi$ is the Lorentz invariant phase-space of the states given by

$$d\Pi = \prod_f \int \frac{d^3 p_f}{(2\pi)^3} \frac{1}{E_f} 2\pi^4 \delta\left(\sum p_i - \sum p_f\right). \tag{1.3}$$

Here, $\prod_f$ is the product over all final states, p_f and E_f represent the final state momenta

and energy, respectively, and $\sum p_i$ represents the momentum sum over all initial state particles. The S-matrix can be divided further into

$$\langle f|S|i\rangle = \langle f|I|i\rangle + (2\pi)^4 \delta\left(\sum p\right) \langle f|\mathcal{M}|i\rangle, \tag{1.4}$$

where I is the identity matrix representing the trivial case of no scattering and $\mathcal{M}$ represents the non-trivial scattering of states. Equations 1.2 and 1.4 can be combined to calculate the scattering probability, commonly referred to as the cross-section σ. For a given situation with two initial incoming particles X_1 and X_2 with corresponding energies E_1 and E_2 which scatter into a new state Y, the cross-section can be calculated as

$$\sigma(X_1 X_2 \to Y) = \int \frac{|\mathcal{M}_{X_1 X_2 \to Y}|^2}{2E_1 E_2 v} d\Pi, \tag{1.5}$$

where $\mathcal{M}_{X_1 X_2 \to Y}$ is the corresponding matrix element for the process and v is the relative velocity between the particles. The decay rate Γ of a particle X to some combination of particles Y can also be calculated as

$$\Gamma(X \to Y) = \frac{|\mathcal{M}_{X \to Y}|^2}{2m_X} d\Pi, \tag{1.6}$$

where m_X is the mass of particle X. The sum of these decay rates is known as the width, and the relative rate of a specific decay mode with respect to the width is referred to as the branching ratio/fraction.

1.3 The Standard Model

The Standard Model is a relativistic quantum field theory which is invariant under the non-abelian $\mathrm{SU}(3)_C \times \mathrm{SU}(2)_L \times \mathrm{U}(1)_Y$ gauge group, where the subscript C represents the color charge of the strong interaction, L denotes the left-chiral nature of the fermion coupling, and Y is the hypercharge. In this thesis, natural units ($h = c = 1$) are used.

1.3.1 The Fundamental Particles

Particles can be divided into the two categories of fermions and bosons depending on if they have half-integer or integer spin, respectively. Fermions, shown in table 1.1, can be subdivided further into two types: leptons and quarks, which are both classified in three generations. Each generation contains a charged lepton and its electrically neutral corresponding neutrino along with two opposite flavored quarks. Each of these fermions participates in the weak interaction and so has weak isospin charge; the quarks and charged leptons have associated anti-particles.

There are four spin-1 bosons and one spin-0 boson in the Standard Model, as shown in table 1.2; these mediate the electromagnetic, weak, and strong forces and provide the mechanism by which particles gain mass.

1.3.2 Quantum Chromodynamics

Quantum Chromodynamics (QCD) is the gauge field theory that describes strong interactions of colored quarks and gluons. It is represented by the SU(3) component of the SU(3)×SU(2)× U(1) Standard Model and its Lagrangian is given by

Generation	Particle Name	Symbol	EM Charge	Strong Charge	Mass [GeV]
			Quarks		
1^{st}	up	u	2/3	R/G/B	$2.16^{+0.49}_{-0.26}$
	down	d	-1/3	R/G/B	$4.67^{+0.48}_{-0.17}$
2^{nd}	charm	c	2/3	R/G/B	$(1.27 \pm 0.02) \times 10^3$
	strange	s	-1/3	R/G/B	93^{+11}_{-5}
3^{rd}	top	t	2/3	R/G/B	$(172.76 \pm 0.30) \times 10^3$
	bottom	b	-1/3	R/G/B	$(4.18^{+0.03}_{-0.02}) \times 10^3$
			Leptons		
1^{st}	electron	e	-1	0	$0.511 \pm 0.31 \times 10^{-8}$
	electron neutrino	ν_e	0	0	$< 1.1 \times 10^{-6}$
2^{nd}	muon	μ	-1	0	$105.66 \pm 0.24 \times 10^{-5}$
	muon neutrino	ν_μ	0	0	< 0.19
3^{rd}	tau	τ	-1	0	1776.86 ± 0.12
	tau neutrino	ν_τ	0	0	< 18.2

Table 1.1: Standard Model fermions from the Review of Particle Physics [6].

Particle Name	Symbol	EM Charge	Weak Charge (Isospin)	Strong Charge	Mass [GeV]
Photon	γ	0	no	no	$< 1 \times 10^{-24}$
Z-boson	Z	0	no	no	91.188 ± 0.002
W-boson	$W^{\pm}$	± 1	yes	no	80.379 ± 0.012
Gluon	g	0	no	yes	0
Higgs	h	0	yes	no	125.10 ± 0.14

Table 1.2: Standard Model bosons from the Review of Particle Physics [6].

$$\mathcal{L} = \sum_q \bar{\psi}_{q,a} \left(i\gamma^\mu \partial_\mu \delta_{ab} - g_s \gamma^\mu t^C_{ab} \mathcal{A}^C_\mu - m_q \delta_{ab} \right) \psi_{q,b} - \frac{1}{4} G^A_{\mu\nu} G^{A\mu\nu}, \tag{1.7}$$

where repeated indices are summed over. The γ^μ are the Dirac γ-matrices, the $\psi_{q,a}$ are quark-field spinors of flavor q and mass m_q and with a color index a running from $a = 1$ to $N_c = 3$, implying that quarks come in three "colors." Here one can see that quarks are the represented by the SU(3) group.

$\mathcal{A}^C_\mu$ represent the gluon fields, with C spanning the range from 1 to $N_c^2 - 1 = 8$, implying that there are eight different kinds of gluon. These gluons transform under the adjoint representation of the SU(3) color group, and t^C_{ab} correspond to the eight 3×3 matrices which are generators of the SU(3) group. These matrices encode the idea that a quark's color is rotated in SU(3) space when the quark interacts with a gluon. g_s is the QCD coupling constant, and the field tensor $G^A_{\mu\nu}$ is given by

$$G^A_{\mu\nu} = \partial_\mu \mathcal{A}^A_\nu - \partial_\nu \mathcal{A}^A_\mu - g_s f_{ABC} \mathcal{A}^B_\mu \mathcal{A}^C_\nu, \tag{1.8}$$

where f_{ABC} are structure constants of the SU(3) group.

Under this model neither quarks nor gluons can be observed "bare" as free particles. Hadrons are color neutral combinations of quarks, anti-quarks, and gluons, and they can be subdivided into mesons or baryons depending on if they do or do not contain an equal number of quarks and anti-quarks, respectively. The fundamental parameters of QCD are the coupling g_s ($\alpha_s = \frac{g_s^2}{4\pi}$) and the quark mass m_q.

1.3.3 The Electroweak Model

The Electroweak Model is based on the gauge group $\mathrm{SU}(2) \times \mathrm{U}(1)$ representing gauge bosons W_μ^i, $i = 1, 2, 3$, and B_μ for the SU(2) and U(1) factors, respectively. The model includes corresponding gauge coupling constants g and g', with the fermion fields of the i^{th} family transforming as the doublets $\Psi_i = \begin{pmatrix} \nu_i \\ l_i^- \end{pmatrix}$ and $\begin{pmatrix} u_i \\ d_i' \end{pmatrix}$ under SU(2), where $d \equiv \sum_j V_{ij} d_j$. V is the Cabibbo-Kobayashi-Maskawa (CKM) mixing matrix, and the right-handed fields are SU(2) singlets. From precision data it is known that there are three fermion families.

A complex scalar doublet $\phi = \begin{pmatrix} \phi^+ \\ \phi^0 \end{pmatrix}$ is added for mass generation through spontaneous symmetry breaking of the potential given by

$$V(\phi) = \mu^2 \phi^\dagger \phi + \frac{\lambda^2}{2} (\phi^\dagger \phi)^2. \tag{1.9}$$

For $\mu^2 < 0$, ϕ develops a non-zero vacuum expectation value given by $v/\sqrt{2} = \mu/\lambda$, where $v \approx 256$ GeV, which breaks part of the Electroweak gauge symmetry. After this only one neutral Higgs scalar, H, remains in the physical particle spectrum.

After symmetry breaking the Lagrangian for fermion fields, ψ_i, is given by

$$\begin{aligned} \mathcal{L}_F = & \sum_i \bar{\psi}_i \left(i\partial\!\!\!/ - m_i - \frac{m_i H}{v} \right) \psi_i \\ & - \frac{g}{2\sqrt{2}} \sum_i \bar{\Psi}_i \gamma^\mu \left(1 - \gamma^5 \right) \left(T^+ W_\mu^+ + T^- W_\mu^- \right) \Psi_i \\ & - e \sum_i Q_i \bar{\psi}_i \gamma^\mu \psi_i A_\mu \\ & - \frac{g}{2\cos\theta_W} \sum_i \bar{\psi}_i \gamma^\mu \left(g_V^i - g_A^i \gamma^5 \right) \psi_i Z_\mu. \end{aligned} \tag{1.10}$$

In this equation, $\theta_W = \arctan\left(g'/g\right)$ is the weak angle, $e = g\sin\theta_W$ is the positron electric charge, and $A \equiv B\cos\theta_W + W^3\cos\theta_W$ is the photon field (γ). $W^{\pm} \equiv \left(W^1 \mp iW^2\right)/\sqrt{2}$ and $Z \equiv -B\sin\theta_W + W^3\cos\theta_W$ are the charged and neutral weak boson fields, respectively. The Yukawa coupling of H to ψ_i in the first term in $\mathcal{L}$ is $gm_i/2M_W$. The boson masses in the Electroweak sector are given at tree level by

$$M_h = \lambda v, \tag{1.11a}$$

$$M_W = \frac{1}{2}gv = \frac{ev}{2\sin\theta_W}, \tag{1.11b}$$

$$M_Z = \frac{1}{2}v\sqrt{g^2 + g'^2} = \frac{ev}{2\sin\theta_W\cos\theta_W} = \frac{M_W}{\cos\theta_W}, \tag{1.11c}$$

$$M_\gamma = 0. \tag{1.11d}$$

The first term in $\mathcal{L}$ gives rise to fermion masses and Dirac neutrino masses (when in the presence of right-handed neutrinos). The second term in $\mathcal{L}$ represents the charged-current weak interaction, while T^+ and T^- are weak isospin raising and lowering operators. The third term in $\mathcal{L}$ represents electromagnetic interactions, while the last term represents the weak neutral-current interaction, where g_V^i and g_A^i are the vector and axial vector couplings.

1.3.4 Top Physics

The top quark is the heaviest of the known fundamental particles with a mass equal to approximately 172.5 GeV. Because it is so much heavier than the W-boson, the top is the only quark that can decay into an on-shell W. Also as a consequence of its large mass it has an extremely short lifetime of 5×10^{-25} s. This timescale is an order of magnitude smaller

than the characteristic time of hadronization in QCD of around 28×10^{-25} s, and therefore decays before forming hadronic bound states.

In hadron colliders like the LHC, top quarks are produced most often in pairs via quark anti-quark annihilation ($qq \to t\bar{t}$) and gluon fusion ($gg \to t\bar{t}$) at leading order (LO), with 80–90% of $t\bar{t}$ pairs being produced via gluon fusion [6]. Feynman diagrams of these processes can be seen in figure 1.1. $t\bar{t}$ pair production cross-sections are currently known to next-to-next-to-leading order (NNLO) precision [7]. In LHC physics a value of $m_t = 172.5$ GeV is used when calculating cross-sections.

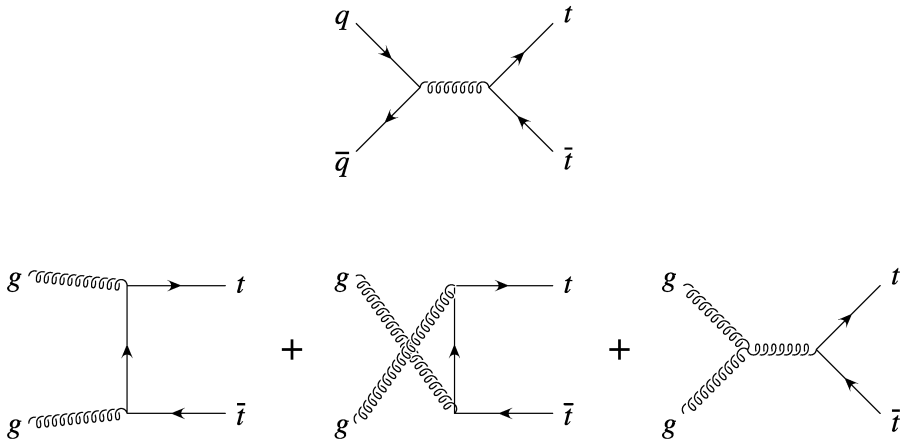

Figure 1.1: Leading order Feynman diagrams of top pair production.

The top quark decays almost universally (99.9%) into one b-quark and one W-boson as a consequence of the value of V_{tb} in the CKM matrix being close to unity. b-quarks quickly hadronize to form jets, while W-bosons decay hadronically into two quarks ($u\bar{d}$ or $c\bar{s}$) with 68% probability or a charged lepton and its corresponding neutrino ($l\nu_l$) with 32% probability [6]. In the literature, $t\bar{t}$ processes are typically classified into one of three categories, the proportions of which can be seen in figure 1.2:

- Hadronic – Both W-bosons decay hadronically via $t\bar{t} \to (bW^+)(\bar{b}W^-) \to (bq_1\bar{q}_2)(\bar{b}q_3\bar{q}_4)$. This final state occurs with probability of approximately 46%.

- Semi-leptonic (lepton + jets) – One W-boson decays hadronically and the other leptonically via $t\bar{t} \rightarrow (bW^+)(\bar{b}W^-) \rightarrow (bq_1\bar{q}_2)(\bar{b}l^-\bar{\nu}_\ell)$. Summing over the generations of leptons gives a probability of approximately 45% that this final state occurs. At LO, the final state of this process consists of an expected four jets, one charged lepton, and some missing transverse energy associated with the neutrino. Searches for this final state generally consider the electron and muon final states separate from the tau final states.

- Dilepton – Both W-bosons decay leptonically via $t\bar{t} \rightarrow (bW^+)(\bar{b}W^-) \rightarrow (bl_1^+\nu_{l,1})(\bar{b}l_2^-\bar{\nu}_{l,2})$. Again, summing over the lepton generations gives a probability of approximately 9%. At LO, two jets and two opposite charged leptons are expected, along with some missing energy associated with the neutrinos.

1.3.5 Limitations

The Standard Model is unparalleled in its success as a framework describing ordinary matter particles and their interactions. Its predictions have been tested in a wide array of different contexts over the last several decades, and the values of known SM parameters and reaction cross-sections have been measured at extreme precision. That said, there are several known deficiencies in the SM's explanatory power known through experiment. Of these problems, some of the best known are

1. The unexplained nature of Dark Matter (DM), for which there is now overwhelming evidence on astrophysical scales.

2. Baryon asymmetry, for which the magnitude of CP violation in the SM is too small to explain.

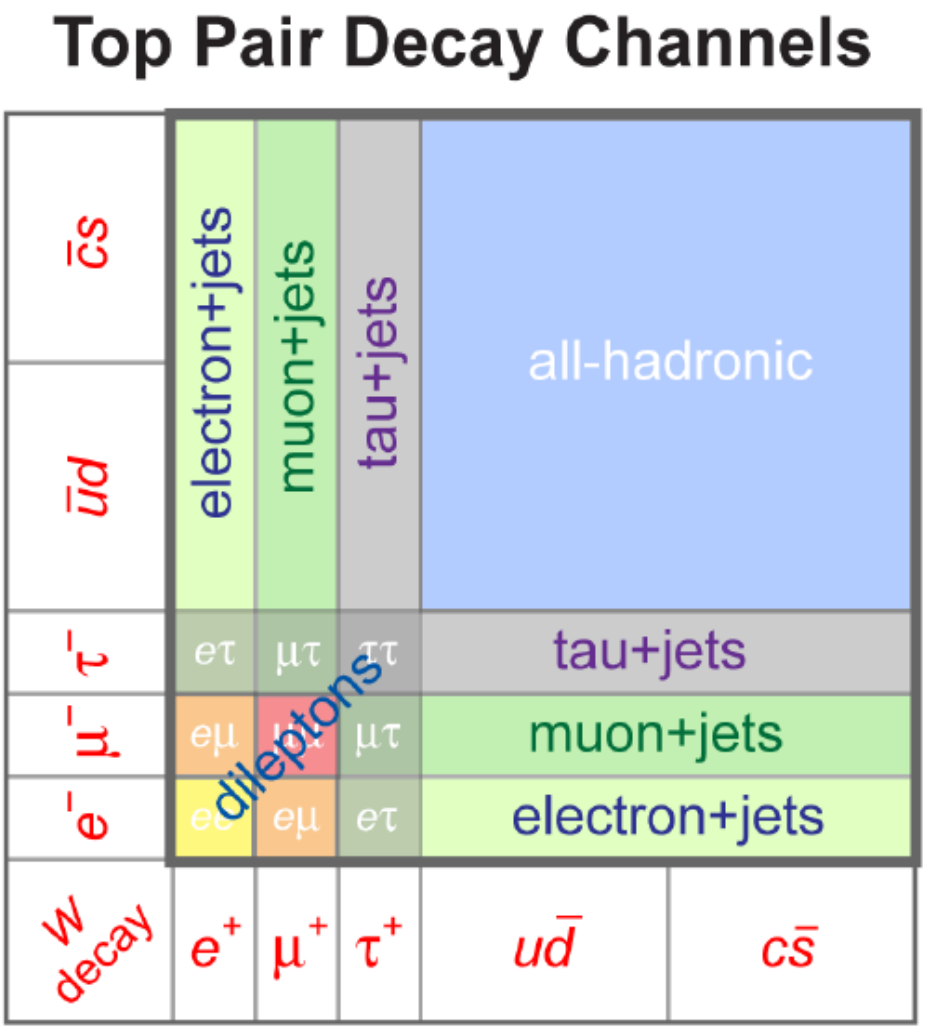

Figure 1.2: Branching ratios ($\mathcal{B}$) for different $t\bar{t}$ decay channels.

3. The origin of neutrino mass, for which the SM includes no description.

4. The electroweak hierarchy problem.

The electroweak hierarchy problem is most relevant to this thesis; it is associated with the existence of the Higgs boson at a mass of ~ 125 GeV. This introduces some conceptual issues, because the Higgs mass is associated with some quantum corrections by loops of other known particles. In the SM, the dominant contribution to this correction comes from the top quark loop to the Higgs propagator. If the momentum of these virtual particles associated

with the loops is cut off at a scale Λ, then the correction to the observed Higgs mass (relative to the bare boson mass with no loop correction) is proportional to Γ^2, where Γ refers to the relevant scale of the theory. In this case, the Higgs mass correction is not a issue up to the electroweak scale, but becomes a problem if we assume that the SM is part of a more complete theory valid up to a very high energy scale of a potential Grand Unified Theory uniting the three non-gravitational forces, with $\Gamma_{\text{GUT}} \sim 10^{16}$ GeV. In this case, the mass corrections become very large. Many SM extensions predict new particles to cancel out the large mass corrections.

1.3.6 Beyond the Standard Model

BSM theories very commonly predict new TeV-scale particles. Many of these models include extended gauge sectors, such as Grand Unified Theories (GUT) [8, 9] attempting to unify the electroweak and strong forces, as well as Kaluza-Klein (KK) modes of SM W/Z bosons from warped extra dimensions [10, 11]. This section will discuss several classes of possible observed particles originating from these types of models.

1.3.6.1 Spin-0: Radion

In the Randall-Sundrum (RS) framework [10], the gravitational fluctuations in a single extra spatial dimension (ED) correspond to scalar fields known as the radion [12] which are massless to zeroth order. In the original RS framework there was no mechanism to stabilize the radius of the compactified ED, r_c. One way this can be solved is via the introduction of an additional scalar radion which propagates in the bulk. Such a radion would be produced by gluon-gluon fusion (gg-F) with interactions localized at the two ends of the ED [13, 14]. This causes the radion field to acquire a mass term, and the coupling to SM fields scale inversely proportional

to the model parameter $\Lambda_R = ke^{-k\pi r_c}\sqrt{g(M_5/k)^3}$, where M_5 is the 5-dimensional Planck mass, k is the curvature factor for the extra dimension, and g is the trace of the 5-dimensional metric. The size of the extra dimension, $k\pi r_c$, is another parameter of the model; in this chapter the parameters are set to the commonly used values of $k\pi r_c = 35$ and $\Lambda_R = 3$ TeV.

The couplings of the radion to fermions are proportional to the masses of the fermions, while the couplings to bosons are proportional to the square of the boson masses. For radion masses above ~ 1 TeV, the dominant decay mode is into pairs of bosons. The decay width of the radion is approximately 10% of its pole mass, which results in observable mass peaks with a width comparable to the experimental resolution of the bosonic channels. The relevant Feynman diagrams for this process are shown in figure 1.3. A summary of the branching ratios for the radion are given in figure 1.4. The radion is not used in this thesis, which focuses on the $t\bar{t}$ channels for which the radion branching ratio rapidly decreases above $m_R^\star = 1$ TeV, but it is included here for completeness as it is used within the larger combination effort.

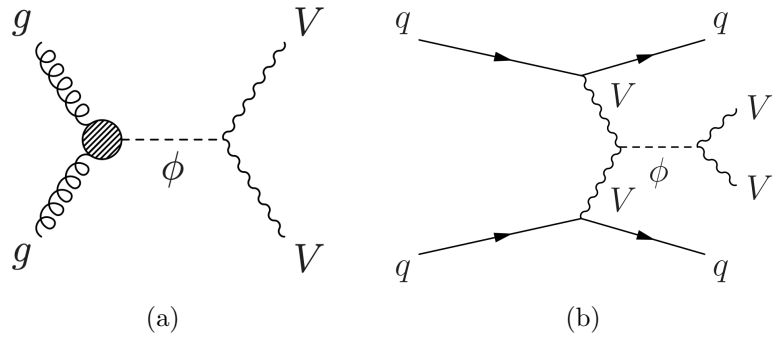

Figure 1.3: Feynman diagrams for heavy resonance (bulk RS radion) production and decay: (a) gluon–gluon fusion production of a radion and subsequent decay into VV (with $V = W$ or Z), (b) vector-boson fusion production of a radion and subsequent decay into VV.

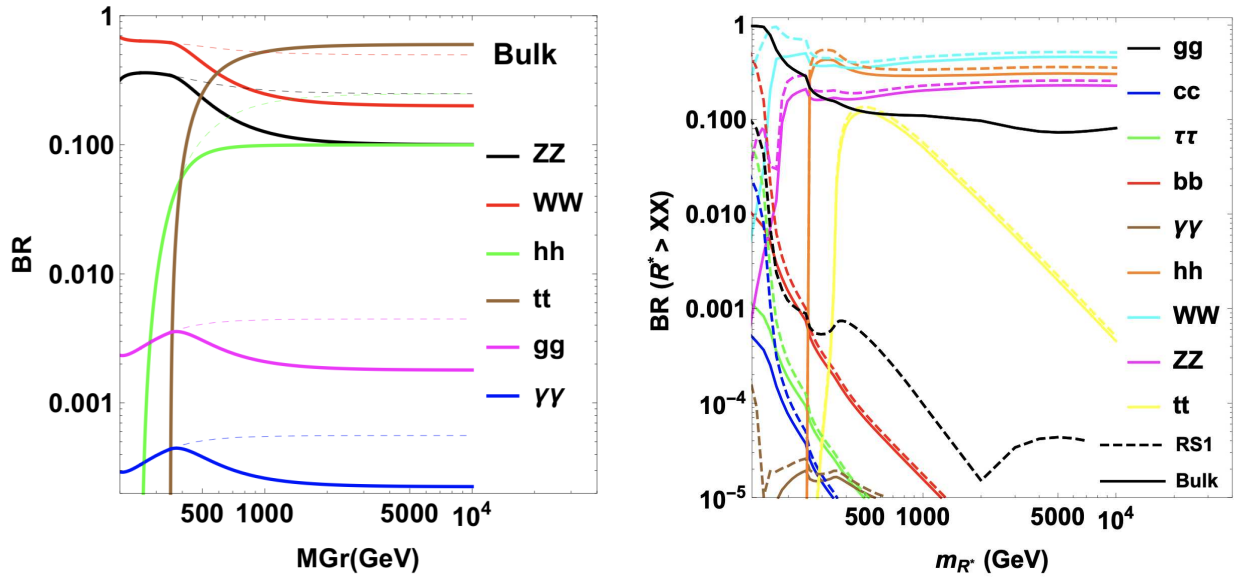

(a) (b)

Figure 1.4: From reference [12], branching ratios for the two body decay of the (a) G_{KK} and (b) radion in the bulk RS scenario. The solid and dashed lines show two hypotheses for fermion embedding, where the solid line is the relevant value for this chapter.

1.3.6.2 Spin-1: Topcolor Assisted Technicolor

The potential that the Higgs could be a bound state of fermions held together by a new strong interaction is one of the theories introduced to resolve the electroweak hierarchy problem. One of the models based on this concept includes a non-Abelian gauge group G_{TC} with associated "techniquarks" which are charged under both G_{TC} and the electroweak interaction. These types of theories are usually referred to as Technicolor theories [15, 16]. By including a new Technicolor gauge force that becomes strong around 100 GeV, Technicolor models can achieve electroweak symmetry breaking. However, they have some important-to-note problems, including that all the fermions are massless and that there is no clear path to the observation of a Higgs-like scalar. In an Extended Technicolor Model, where the SM gauge group G_{SM} and G_{TC} are embedded in a larger gauge group G_{ETC}, G_{SM} is connected with the Technicolor gauge group. Although it can yield non-zero fermion masses,

this method falls short of producing a mass on the scale of the top quark. Technicolor models were connected to so-called Topcolor models in order to resolve this problem.

In the Topcolor model, a dynamic $t\bar{t}$ condensate is formed in order to produce the top quark mass. Fermion condensates in this case are formed by a new strong gauge force which preferentially couples with third generation quarks. QCD gauge group $\mathrm{SU}(3)_C$ is embedded into a minimal $\mathrm{SU}(3)_1 \times \mathrm{SU}(3)_2$ group in this scheme. The first gauge interaction ($\mathrm{SU}(3)_1$) is strong and only acts on the third generation quarks, while the second gauge interaction ($\mathrm{SU}(3)_2$) is weaker and acts on the first and second generation quarks. A color octet of massive bosons referred to as "topgluons" is produced when the $\mathrm{SU}(3)_1 \times \mathrm{SU}(3)_2 \to \mathrm{SU}(3)_C$ symmetry is broken. These new bosons couple primarily to $t\bar{t}$ and $b\bar{b}$ condensates and produce degenerate top and bottom quarks around 600 GeV.

To get the masses of the two third generation quarks correct, $\mathrm{U}(1)'$ interactions which strongly couple to $t\bar{t}$ but weakly coupled to $b\bar{b}$ are introduced. This additional symmetry refers to a neutral gauge boson Z'_{TC2}, which in its most simple form is embedded in the weak hypercharge $\mathrm{U}(1) \to \mathrm{U}(1)_1\mathrm{U}(1)_2$. The different up and down type quarks are given different U(1) charges to achieve this tilting effect. All together, the gauge group structure of the Topcolor model with tilting takes the form

$$\mathrm{SU}(3)_1 \times \mathrm{SU}(3)_2 \times \mathrm{U}(1)_1 \times \mathrm{U}(1)_2 \times \mathrm{SU}(2)_L \to \mathrm{SU}(3)_C \times \mathrm{U}(1)_Q. \tag{1.12}$$

There are several versions of this model, but the one referred to in this thesis is a leptophobic, topophyllic Z'_{TC2} with a cross-section that is predicted to be large enough such that its observation is experimentally accessible at the LHC [17]. The model has several parameters, which include the Topcolor fitting parameter $\cos\theta_H$, which controls the width

and cross-section, and tilting parameters f_1 and f_2 controlling the coupling to up-type and down-type quarks, respectively. In this thesis, the model used for the $t\bar{t}$ resonance search has model parameters $f_1 = 1$ and $f_2 = 0$, which maximize the $t\bar{t}$ branching ratio. It is worth noting that although the in the post-Higgs discovery world a range of Technicolor models are considered to be eliminated as an alternative theory of electroweak symmetry breaking, a subset of these models with "walking technicolor" can still accommodate a Higgs-like scalar.

1.3.6.3 Spin-1: Heavy Vector Triplet

The Heavy Vector Triplet (HVT) model [18, 19] provides a broad phenomenological framework encompassing a range of scenarios involving new heavy gauge bosons and their couplings to SM fermions and bosons. In this model, a triplet $\mathcal{W}$ of colorless vector bosons is introduced with zero hypercharge. This leads to a set of nearly degenerate charged $W'^{\pm}$, and neutral, Z', states collectively denoted as V'. For the interpretation performed in this thesis the W' and Z' masses are taken to be degenerate. This framework allows one to explore different coupling strengths of those states to quarks, leptons, vector bosons, and Higgs bosons within the context of the interaction Lagrangian given by

$$\mathcal{L}_{\mathcal{W}}^{\text{int}} = -g_q \mathcal{W}_\mu^a \bar{q}_k \gamma^\mu \frac{\sigma_a}{2} q_k - g_\ell \mathcal{W}_\mu^a \bar{\ell}_k \gamma^\mu \frac{\sigma_a}{2} \ell_k - g_H \left(\mathcal{W}_\mu^a H^\dagger \frac{\sigma_a}{2} i D^\mu H + \text{h.c.} \right), \tag{1.13}$$

where q_k and l_k represent the left-handed quark and lepton doublets for fermion generation k ($k = 1, 2, 3$), H represents the Higgs doublet, σ_a ($a = 1, 2, 3$) are the Pauli matrices, and g_q, g_l, and g_H correspond to the coupling strengths between the triplet field $\mathcal{W}$ and the quark, lepton, and Higgs fields, respectively. Right-handed fermions do not participate in

these interactions, and the fermionic couplings can be further broken down into specific first, second, or third generation couplings. In this thesis, g_q denotes the generation universal quark coupling, $g_{q_{12}}$ denotes the coupling to the first and second generation quark specifically, and g_{q_3} denotes the coupling to third generation quarks. A similar scheme is used for the lepton generation-specific couplings. The triplet field interacts with the Higgs field and with the longitudinally polarized W and Z bosons by virtue of the equivalence theorem.

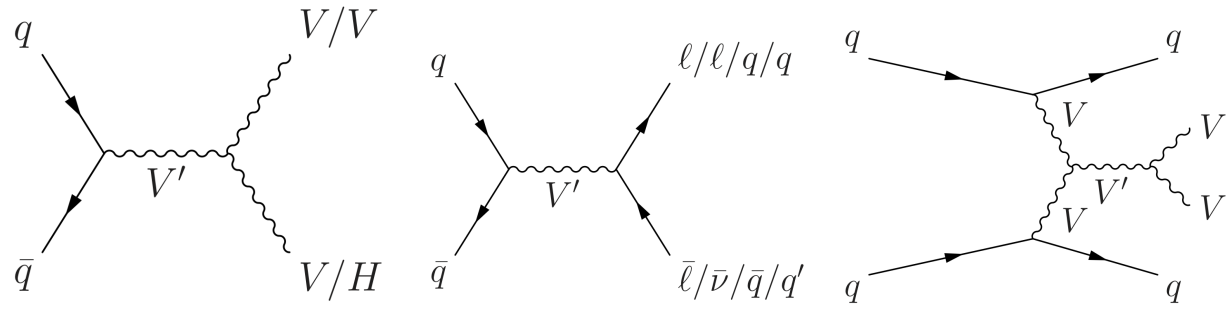

Figure 1.5: Feynman diagrams for heavy vector triplet resonance production and decay: (a) quark-antiquark annihilation (qq-A) production and decay into VV/VH, (b) qq-A production and decay into $\ell\ell/\ell\nu/q\bar{q}/qq'$, and (c) vector-boson fusion production and decay into VV (where $V = W$ or Z).

Three explicit HVT scenarios are used as benchmarks for the interpretation of results in this thesis. The first two processes are quark-antiquark annihilation (qq-A) production mechanisms (figure 1.5 (a) and (b)), while the third process is a vector-boson fusion (VBF) mechanism (figure 1.5(c)). Related to the first two processes, there are two points in the model parameter space used as benchmarks. The first qq-A benchmark, referred to as model A, reproduces the phenomenology of weakly-coupled models based on an extended gauge symmetry [20]. In this case, the couplings are $g_H = -0.56$ and $g_f = -0.55$, with the universal fermion coupling $g_f = g_q = g_l$. The second qq-A benchmark, referred to as model B, reproduces the phenomenology of a strongly-coupled scenario as in composite Higgs models [21]. In this case, the couplings are $g_H = -2.9$ and $g_f = 0.14$. In most of the

parameter space explored in this thesis, the relative width Γ/m is below 5%. A summary of branching fractions for models A and B are given in figure 1.6. A more detailed treatment of these points in the model space will be talked about in section 5.5.2.

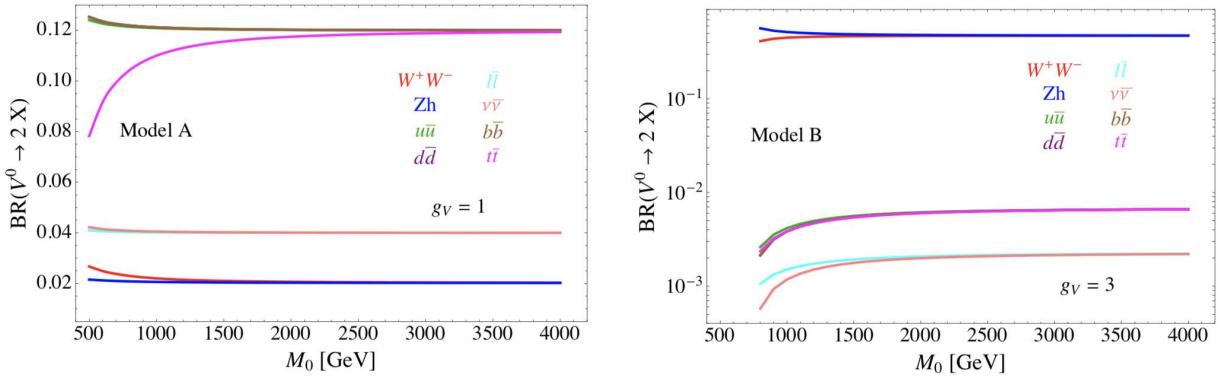

(a) (b)

Figure 1.6: From reference [18], branching ratios for the two body decay of the neutral vector boson V^0 for the (a) benchmark model A, (b) benchmark model B.

1.3.6.4 Spin-2: Graviton

Propagation of either only gravity or all SM fields in the extra dimension of the RS model leads to a tower of Kaluza-Klein (KK) excitations of gravitons (G_{KK}) and SM fields. In a scenario where all SM fields propagate in the extra dimension, KK gravitons are produced via qq-A and gg-F (with the latter dominating due to suppressed couplings to light fermions), and VBF, as seen in figure 1.7.

The coupling strength depends on k and M_5 as described in section 1.3.6.1. Both the production cross-section and decay width of the KK graviton scale as the square of k. For this thesis, a value of $k = 1$ is used for interpretation, and for this point in the parameter space, the relative width is approximately 6%. The G_{KK} branching fraction is largest into the $t\bar{t}$ final state, ranging from 42% for $m_{G_{KK}} = 0.5$ TeV to 65% for $m_{G_{KK}} > 1.0$ TeV. A

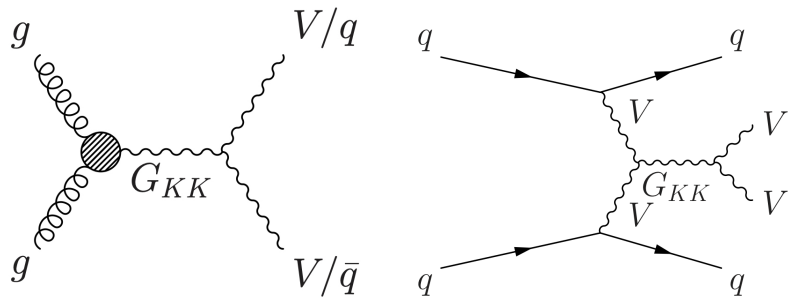

Figure 1.7: Feynman diagrams for heavy resonance (Bulk RS Graviton) production and decay: (a) gluon–gluon fusion production of a Graviton and subsequent decay into VV (with $V = W$ or Z) or $q\bar{q}$, (b) vector-boson fusion production of a Graviton and subsequent decay into VV.

summary of the branching fractions for G_{KK} is given in figure 1.4(a).

Chapter 2

The ATLAS Experiment at the LHC

The Large Hadron Collider [22, 23, 24, 25] (LHC) is a dual-ring particle accelerator intersecting the French-Swiss border near Geneva, Switzerland. It was constructed by the European Organization for Nuclear Research (CERN) between an initial project approval date in 1995 and inaugural tests in 2008. Its synchrotron design is capable of colliding two beams of protons or lead ions traversing its rings in opposite directions at the TeV energy scale. The bulk of the LHC is housed in a subterranean 27 km circular tunnel which previously housed the Large Electron-Positron Collider (LEP). After initial construction and during Run-1 (2010-2011) of data taking the center of mass energy (CME) started at 7 TeV and was gradually increased to 8 TeV during the latter period of data taking (2012). After a long shutdown for repairs and upgrades (2013-2014), the CME was increased to 13 TeV, which comes close to matching the design collision energy of 14 TeV. This 13 TeV CME was used through the entire Run-2 of data-taking during the period 2015–2018.

During operation, two beams traversing the beam pipes in opposing directions are guided by 1232 superconducting dipole magnets and focused by 392 quadrupole magnets. Stronger quadrupole magnets are placed near the four intersection points at the detector experiments to focus the beam and increase the probability of collisions. The magnets are made of a niobium-titanium alloy and are sustained in a superconducting phase at temperatures below 2 K by superfluid Helium to achieve magnetic flux densities greater than 8 T. The large

synchrotron ring is responsible for maintaining the final CME and final acceleration, however several smaller rings act as a chain of pre-accelerators that raise the beam energy in steps until they reach the minimum energy requirement of the large ring. First, proton beams from hydrogen atoms are created at 50 MeV and stripped of their electrons using the LINAC 2 linear accelerator. After this step they enter the Proton Synchrotron Booster (PSB) and are accelerated to a beam energy of 1.4 GeV. In the next steps, the Proton Synchrotron (PS) accelerates the protons first to an energy of 25 GeV before they are fed to the Super Proton Synchrotron (SPS) and accelerated to an energy of 450 GeV. Finally, the protons are injected into the main LHC accelerator ring where the proton beams are portioned into bunches of up to 10^{11} protons. As many as 2500 of these bunches per beam with a temporal spacing of 25 ns may be circulating in the accelerator at a given time.

There are four intersection points along the LHC rings, and at each of these intersection points detectors measure and record particle collisions. At opposite sides of the ring are two large, general purpose detectors: ATLAS [26] (A Toroidal LHC ApparatuS) and CMS [27] (Compact Muon Solenoid). There are also two specialized detectors: ALICE [28] (A Large Ion Collider Experiment) for recording proton-lead and lead-lead collisions to explore the properties of quark-gluon plasma and LHCb [29] (LHC-beauty) for studying b-hadron physics. This thesis will focus on experiments done using the ATLAS detector.

The ATLAS experiment at the LHC is a multipurpose particle detector with a cylindrically symmetric geometry and a near 4π solid angle coverage. It is approximately 46 meters in length, 25 meters in diameter, and weighs 700 tons. It consists of an inner detector for tracking surrounded by a thin superconducting solenoid which provides a 2 T axial magnetic field, electromagnetic and hadronic calorimeters, and a muon spectrometer. ATLAS uses a right-handed coordinate system with its origin at the nominal interaction point in the center

of the detector and its z-axis along the beam pipe. The x-axis points from the interaction point towards the center of the LHC ring, and the y-axis points upwards. Cylindrical coordinates (r, ϕ) are used in the transverse plane, with ϕ being the azimuthal angle around the z-axis. The pseudo-rapidity is defined in terms of the polar angle θ as $\eta = -\ln\tan(\theta/2)$. Angular distance is measured in units of $\Delta R \equiv \sqrt{(\Delta\eta)^2 + (\Delta\phi)^2}$.

Starting from the radially innermost portions of the detector:

1. The inner detector consists of silicon pixel, silicon microstrip, and transition-radiation tracking detectors. An innermost pixel layer, inserted at a radius of 3.3 cm, has been used since 2015.

2. Lead/liquid-argon (LAr) sampling calorimeters provide electromagnetic (EM) energy measurements with high granularity.

3. A hadronic (steel/scintillator tile) calorimeter covers the central pseudo-rapidity range of $|\eta| < 1.7$. The endcap and forward regions are instrumented with LAr calorimeters for both the EM and hadronic energy measurements up to $|\eta| = 4.9$.

4. The muon spectrometer surrounds the calorimeters and features three large air-core toroidal superconducting magnet systems with eight coils each. The field integral of the toroids ranges between 2.0 and 6.0 Tm across most of the detector. The muon spectrometer includes a system of precision tracking chambers up to $|\eta| = 2.7$ and fast detectors for triggering up to $|\eta| = 2.4$.

A two-level trigger system is used to select events. The first-level trigger is implemented in hardware and uses a subset of detector information to reduce the accepted rate to at most 100 kHz. This is followed by a software-based trigger level that reduces the accepted event rate to 1 kHz on average.

2.1 Inner Detector

The ATLAS Inner Detector (ID) is designed to provide robust pattern recognition and momentum resolution, along with both primary and secondary vertex measurements for charged tracks above a p_T threshold as low as 0.1 GeV within the pseudo-rapidity region $|\eta| < 2.5$. It is functionally necessary to distinguish between electrons and photons and also to reconstruct the sub-structure of jets and illuminate the flavor of initial decay quarks. The ID is fully contained within a cylindrical envelope of length $\pm$ 3512 mm and radius 1150 mm and is within a solenoidal magnetic field of strength 2 T. It consists of three independent sub-detectors shown in figure 2.1 which achieve μm precision in track reconstruction.

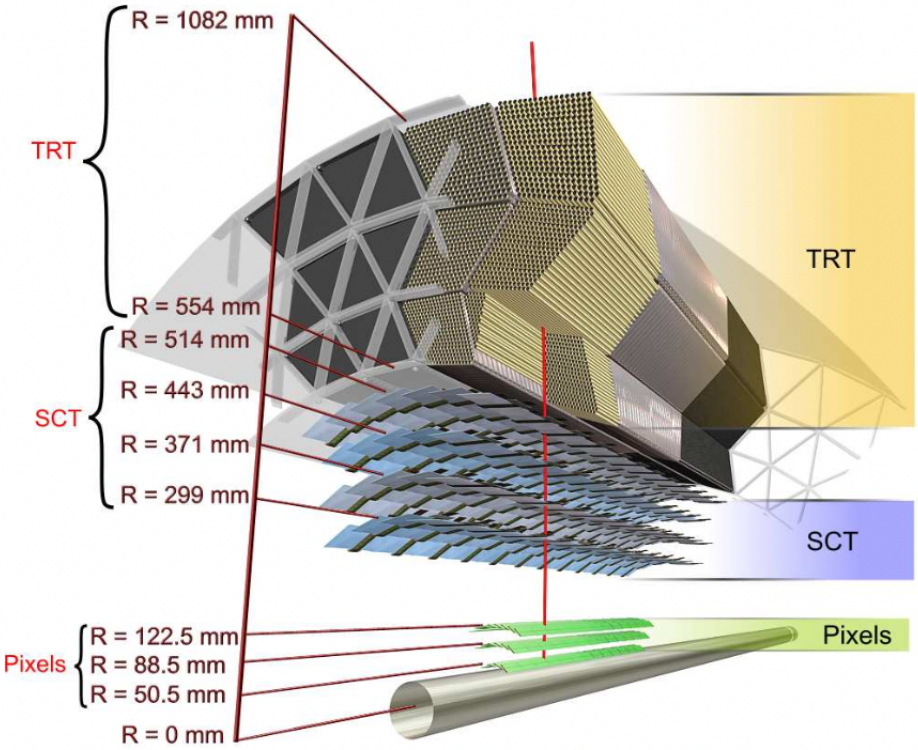

Figure 2.1: The inner sensors and structural elements traversed by a charged track of p_T = 10 GeV.

2.1.1 Pixels

The pixel detector is the innermost of the subdetectors in the ID; it is made up of three modular layers in the barrel region and three disks in each end-cap structure, and it consists of 1744 silicon pixel modules, each with 47232 pixels per sensor. These sensors are composed of silicon wafer readout pixels of size 50×400 μm^2. With use, the failure of modules in the pixel detector is inevitable and as such an additional fourth layer is necessary to guarantee robust tracking ability. This layer, called the invertible B-layer, is located between the beam-pipe and pixel detector at a radial distance of 33 mm from the beam-pipe center. Its proximity to the interaction point and small pixel size improves impact parameter resolution along the $R - \phi$ range for low p_T particles.

2.1.2 Semiconductor Tracker

The semiconductor tracker is a silicon strip detector located radially after the pixel detector. It is made of four cylindrical layers in the barrel region and nine disk layers in the end-cap region which together consist of 4088 modules of two strips each with mean pitch of 80 μm and respective tilt of 40 mrad. This allows each module to provide two-dimensional measurements in its respective plane and provide four space-points of measurement. Additionally, the semiconductor tracker provides measurements of the z-coordinate along the strip length.

2.1.3 Transition Radiation Tracker

The transition radiation tracker is the outermost region of the ID and is made of gas-filled drift tubes with a center gold-tungsten anode wire of 30 μm diameter. This configuration allows for particle tracking and identification using transition radiation, such that when a

charged particle passes through the drift tubes it ionizes the internal gas and the resulting electrons drift towards the wire and induce a large potential difference. This allows the inner detector to extract timing information from tube hits, resulting in a resolution of 130 μm along the direction of the wire. While this is a lower resolution than the more inner pixel detector and semiconductor tracker, the performance is compensated by the large number of points per track measured; on average a charged particle will deposit 36 hits throughout this sub-detector.

2.2 Calorimetry

The sampling calorimeter setup is given in figure 2.2. The calorimeters cover the range $|\eta| < 4.9$ and each is specialized to the requirements of the particular physical processes of interest and suited to its radiation environment. The $\eta < 2.5$ region of the electromagnetic (EM) calorimeter region corresponding to the inner detector has a fine granularity and is ideally suited for measurements of electrons and photons. The rest of the calorimeter system satisfies the physics requirements for jet reconstruction and measurements of the missing transverse energy E_T^{miss}, and has a coarser granularity. These calorimeters must provide good containment for electromagnetic and hadronic showers originating from the interaction point, thus the calorimeter depth is important in the detector's design.

2.2.1 LAr Electromagnetic Calorimeter

The EM calorimeter is a liquid argon (LAr) sampling calorimeter which is divided into two parts: the barrel ($|\eta| < 1.475$) and two end-cap components ($1.375 < |\eta| < 3.2$), with each housed in their own cryostat. Between alternating absorber plates made of lead is a

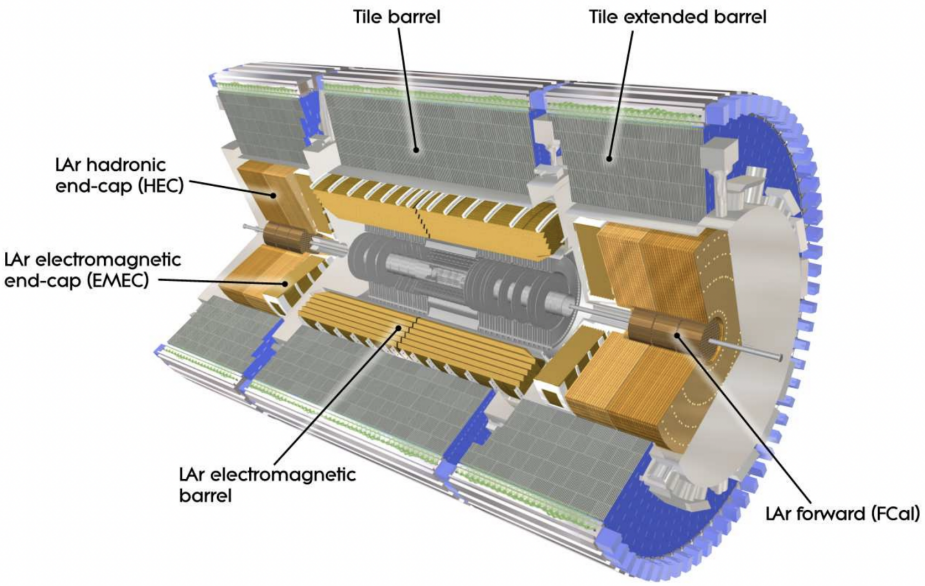

Figure 2.2: Cut-away view of the ATLAS calorimeter system.

LAr active medium which absorbs ions created by showers of electromagnetically interacting particles. These ions drift to three-layered copper read-out electrodes placed between two of these absorber plates; the outer electrodes are held at a potential difference of -2 kV, while the inner plate serves as a read-out channel. High energy, electromagnetically interacting particles which cross the EM calorimeter interact with the absorbing lead material and produce a chained shower of particles. Those particles which are fully absorbed can have their energies reconstructed by the signal measured in the LAr. The accordion geometry, as shown in figure 2.3, assists in achieving a homogeneous energy reconstruction efficiency. Electromagnetic interactions in the EM calorimeter are characterized by radiation lengths, X_0, where one radiation length is the average distance over which the energy of an electron is reduced by the factor $1/e$ by bremsstrahlung [30]. The total thickness of the EM calorimeter is more than $22X_0$ within the barrel region of the detector more than $24X_0$ in the end-cap region.

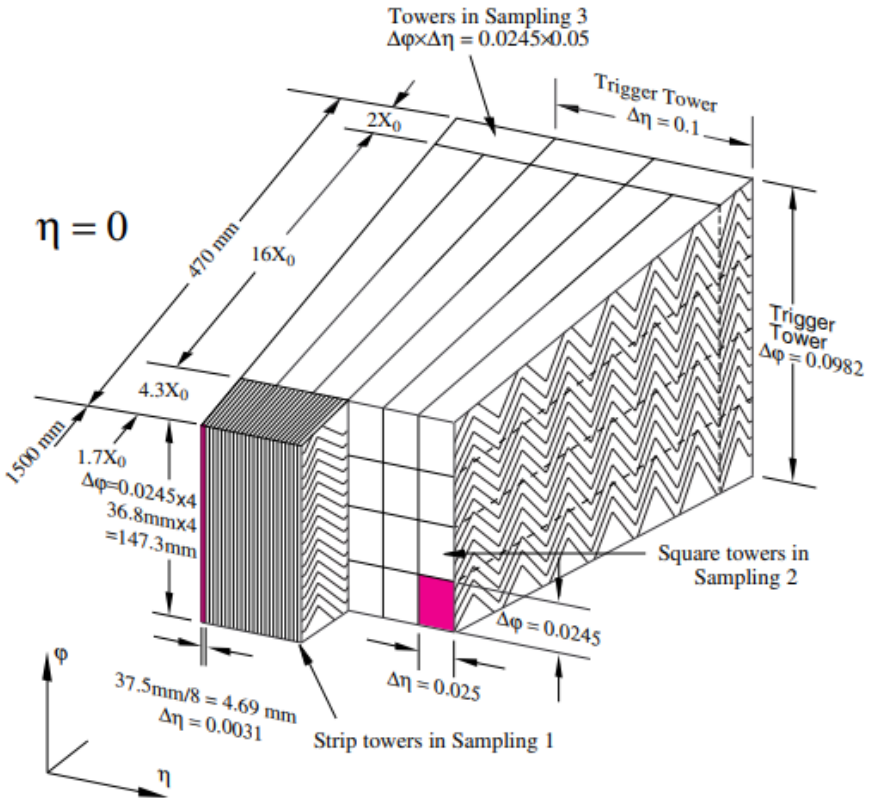

Figure 2.3: The LAr electromagnetic calorimeter accordian structure.

The barrel calorimeter is made of two identical half-barrels which are separated by a 4 mm gap at $z = 0$. Each end-cap calorimeter consists of two coaxial wheels: one outer wheel which covers the region $1.375 < |\eta| < 2.5$, and one inner wheel which covers the region $2.5 < |\eta| < 3.2$. The EM calorimeter is a lead-LAr detector with accordion-shaped kapton electrodes and lead absorber plates over its full coverage. This geometry provides complete ϕ symmetry with no azimuthal cracks, and the thickness of the lead plates is optimized as a function of η to maximize the EM calorimeter's performance in energy resolution. The end-cap calorimeters are structured as two wheels separated at $\eta = 2.5$, with the outer wheel covering the region $1.475 < \eta < 2.5$ and the inner wheel covering the region $2.5 < \eta < 3.2$. An anomalous inner layer of the EM calorimeter consists of one active LAr layer of thickness

1.1 cm in the barrel region and 0.5 cm in the end-cap regions. This layer is used to correct the energy of electrons and photons.

2.2.2 Hadronic Calorimeter

The hadronic calorimeter is divided into three sections: the tile calorimeter, the LAr hadronic end-caps, and the LAr forward calorimeter. The tile calorimeter is structurally similar to the EM calorimeter, but with steel absorber plates and a plastic scintillator sandwiched between them. The central barrel region of the calorimeter exists in the region $|\eta| < 1$, and the two forward extended barrels cover $0.8 < |\eta| < 1.7$. The barrel and extended barrels are divided azimuthally into 64 modules of $\Delta\phi \approx 0.1$. The tile calorimeter extends radially from 2.28 m to 4.25 m and is segmented into three layers in depth at approximately 1.5, 4.1, and 1.8 interaction lengths in the barrel and 1.5, 2.6, and 3.3 interaction lengths in the extended barrel, respectively. Two sides of the scintillating tiles are read out by wavelength shifting fibres into separate photomultiplier tubes.

The LAr hadronic end-caps are wheels places on each side of the EM calorimeter end-caps, cover a range $1.5 < |\eta| < 3.2$, and share the same cryostats as the EM calorimeters. To reduce any drop in material density at the transition ($|\eta| = 3.1$) between these end-cap calorimeters and the forward calorimeter, the end-cap calorimeter extends to $|\eta| = 3.2$, overlapping with the forward calorimeter. In a similar way, the end-cap calorimeter the end-cap calorimeter η overlaps that of the tile calorimeter ($|\eta| < 1.7$) by extending to $|\eta| = 1.5$. Each end-cap wheel is built from 32 identical wedge-shaped modules. Each wheel is constructed from two segments in depth for a total of four layers per end-cap.

The forward calorimeter is integrated into the end-cap cryostats to provide uniformity of the calorimetric coverage and to reduce radiation background levels in the muon spectrometer.

The front face of the forward calorimeter is recessed by about 1.2 m with respect to the EM calorimeter front face to reduce the amount of neutron albedo in the inner detector cavity. This fact implies that the depth of the calorimeter is limited and that the forward calorimeter has a high-density design. The forward calorimeter is approximately 10 interaction lengths deep and is made of three modules in each end-cap: the first is made of copper and is optimized for electromagnetic measurements while the are made of tungsten and measure the energy of hadronic interactions. Each module is constructed of a metal matrix of regularly spaced longitudinal channels filled with a structure of concentric rods and tubes parallel to the beam axis. There is LAr in the gap between the rods and tubes which acts as the detector medium.

In the hadronic calorimeter, shower development is determined by the nuclear interaction length λ_I, which represents the mean distance between relativistic hadronic interactions. For most materials the hadronic interaction length is significantly larger than the electromagnetic radiation length.

2.3 Muon Spectrometer

The ATLAS Muon Spectrometer (MS) is in the outermost region of the detector system and fully encloses the calorimeter system. Its purpose is to precisely measure the position and momenta of muons, a large fraction of which pass through the inner detector layers unabsorbed. Its operation is based on the premise that muon tracks will be deflected by magnetic fields generated by large, superconducting air-core toroid magnets. Over the range $|\eta| < 1.4$, this magnetic bending is provided by a large barrel toroid. In the region $1.6 < |\eta| < 2.7$ the muon tracks are bent by two smaller end-cap magnets which are inserted

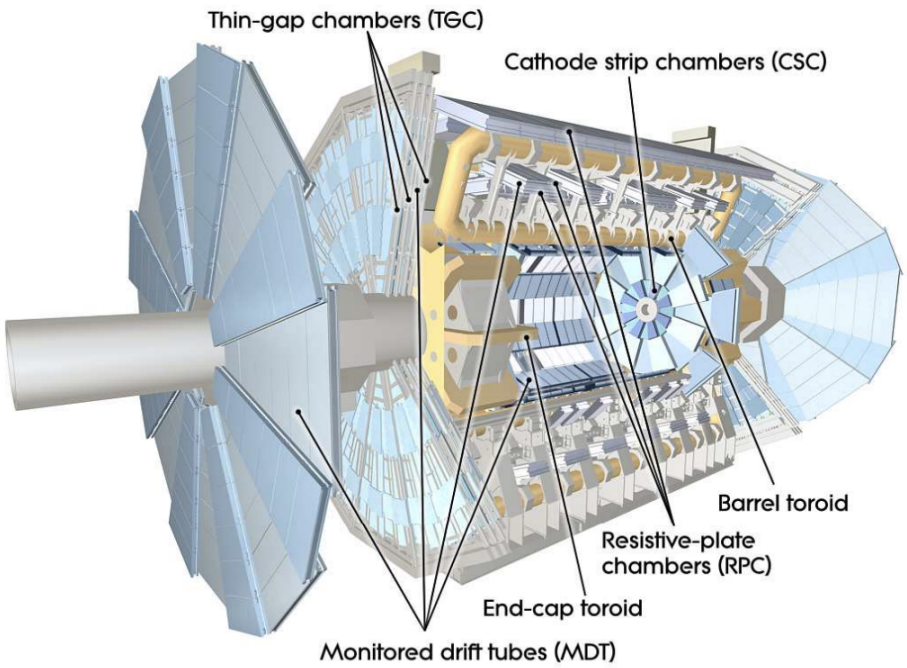

Figure 2.4: Cut-away view of the ATLAS muon system.

into the ends of the barrel toroid. In $1.4 < |\eta| < 1.6$, which is usually referred to as the transition region, magnetic deflection is provided by a combination of the barrel and end-cap fields. This configuration of magnets provides a field which is mostly orthogonal to muon trajectories from the interaction point and minimizes the worsening of the resolution due to multiple scattering. The conceptual layout, including the locations of the magnets, can be seen in figure 2.4.

In the detector's barrel region, muon tracks are measured in chambers arranged in three cylindrical layers around the beam axis. In the transition and end-cap regions, the chambers are installed in three layers perpendicular to the beam. Three large, air-core toroid magnets generate the field necessary for the muon spectrometer to measure the muons traversing curved paths; each of these toroids consist of eight coils which are fit radially around the beam axis. The barrel toroid coils are housed inside eight individual cryostats, while the

end-cap toroids are cold-linked and assembled as a single cold mass inside one large cryostat. These magnets together provide the bending power characterized by the field integral $\int Bdl$, where B is the field component normal to the muon direction and the integral is computed along an infinitesimal-momentum muon trajectory between the innermost and outermost muon-chamber planes.

Over most of the η range, the precision measurement of the track coordinates in the principal bending direction of the magnetic field is provided by Monitored Drift Tubes (MDTs). I carried out my ATLAS qualification task on an upgrade to this part of the detector, which is described in appendix A. These tubes are 30 mm in diameter and mechanically isolated, which guarantees a robust and reliable measurement from each of their respective sense wires. At large $|\eta|$, the Cathode Strip Chambers, which are multiwire proportional chambers with cathodes which are segmented into strips, are used with high granularity in the innermost plane of $2 < |\eta| < 2.7$ to withstand a more demanding rate and background conditions.

2.4 Trigger Systems

The ATLAS trigger system is used to quickly identify LHC collision events which are interesting by some preset criteria. This system is broken into three progressively stricter selections Level-1, Level-2, and event filter (L1, L2, and EF, respectively). The L1 trigger uses the muon trigger chambers and coarse-grained calorimeter information to select events with high-p_T muons, electrons, photons, jets, τ-leptons, and events with high E_T^{miss}. This reduces the event rate delivered by the LHC from approximately 40 MHz to 100 kHz. Regions of interest in $\eta - \phi$ space around objects passing certain criteria such as an energy threshold

are also designated by the L1 trigger system.

The L2 and EF triggers further filter events based on additional detector information from the regions of interest, including that from the tracking detector. Since these levels operate at with stricter criteria (such as higher energy thresholds), more refined definitions of object information is used. Together the L2 and EF triggers further reduce the event rate from approximately 100 kHz to 1 kHz [31].

2.5 Data Processing

The centralized "Tier-0" computing system is responsible for the prompt processing of the raw data coming from the detector to archive raw and derived data on tape, register data with the relevant catalogues, and distribute them to associated "Tier-1" clusters for further offline processing [32]. Tier-1 consists of 13 computer centers large enough to store LHC data, and they provide round-the-clock support for the CERN Computing GRID; each is responsible for storing a proportional share of the raw and reconstructed data, as well as large-scale reprocessing of that data and storing the associated output. Tier-2 systems (one of which is located at Michigan State University) are typically located at universities and other scientific institutions and can provide sufficient data storage and computing power to complete specific analysis tasks; there are roughly 155 Tier-2 sites around the world.

Chapter 3

Event Simulation and Reconstruction

To study the detector response for a general physics process it is important to have a detailed simulation infrastructure that consists of generated single proton-proton collisions at the LHC within the ATLAS detector (usually referred to as "events") run through a pipeline which has a final output in the format identical to the true detector. This simulation software is integrated into the ATLAS software framework Athena [33], and uses the GEANT4 simulation toolkit [34]. The simulation chain can be cleanly divided into three steps: the generation of the event and the simulation into its immediate decays, the simulation of the detector interactions, and digitization of the energy deposited in the relevant sensitive regions of the detector into voltages and currents that are comparable to actual readouts of the ATLAS detector. The ATLAS detector geometry used in this process is built from up-to-date databases which describe the physical construction and conditions of the detector.

3.1 Event Generation

3.1.1 Tree Level Generation

Event generation consists of the production of a set of particles which is passed to a detector simulation representing a collision and subsequent detector interactions. This generation process runs within the Athena framework, however most generators themselves are written

and maintained by teams external to ATLAS. Large-scale production is run in, for example, Pythia [35], Herwig [36], Sherpa [37], and MadGraph [38, 39]. MadGraph, for example, generates simulated events calculating the matrix elements for a set of Feynman diagrams that result in a final state chosen by the user. It is primarily used as a leading order (LO) generator, and calculates the contribution of diagrams to a physics process to some fixed order α_S.

To adequately calculate the cross-section of a given final state, it is necessary to use calculations that are produced from more than just tree-level diagrams, and as such next-to-leading order (NLO) generators work to address this issue by including loop diagram contributions for processes seen in the ATLAS detector to an order $n + 1$ for a process of order n with respect to α_S. Using these NLO generators helps to reduce analysis dependence on factorization and renormalization scales, but divergences can arise due to the momentum integration in loops. NLO generators compensate for this by cancelling with other divergences of the same order of α_S. MadGraph aMC@NLO is an example of such a NLO generator, and is used extensively in ATLAS for the generation of W, Z, single top, and $t\bar{t}$ events, particularly because the loop corrections to the LO scheme leads to a more accurate top quark p_T spectrum. LO generators are usually used for BSM signal generation to reduce model-specific dependence since these model types search for potentially new processes.

The non-abelian nature of QCD, which leads to color confinement at long distances, prevents the accurate prediction of many final states in hadron collider physics. The two main problems that arise from this fact are the description of hadron formation and the evolution of QCD final states from short to long distances. These problems can be approximately solved with Monte Carlo (MC) specifically for parton shower generation.

Parton distribution functions (PDFs) represent the probability to find partons in a hadron

as a function of the fraction of the proton's momentum carried by the parton [40]. They are determined from experimental results on short distance scattering of the partons, and their selection is an important consideration in generating simulated data.

3.1.2 Detector Simulation

The GEANT4 (GEometry ANd Tracking) [41, 42] software suite is used to simulate the interactions between particles produced by the event generators described in section 3.1.1 and the detector itself. The detector components are built into the GeoModel library [42], which is a library of primitives that can be used to accurately describe detector geometries. This detector description is made of over 300,000 physical primitives which are used by GEANT4 and is updated regularly to include information about misalignment and dead channel information.

After an event generator produces a set of particles they are processed stepwise through the detector using the GEANT4 library. Detector interactions and in-flight decays are simulated only for those particles for which $|\eta| < 6.0$ (the reach of the forward calorimeter), while particles outside this threshold are not simulated to save on both computing time and storage space. The information about energy deposits in the detector is stored in a file that contains the information needed for the digitization stage as well as truth information about the original particles.

"Fast simulation" is available for those scenarios where less precision is required. This scheme instead uses a parametrized detector response at a reduced computation cost for each of the slowest parts of the full simulation where available.

3.1.3 Digitization

The last step to successfully emulate the output of a true detector response is to convert the simulated energy deposits into digits representing the current or voltage readout of each respective detector piece. In the real detector, each detector piece has a specific schema and requirements for when a digit is created with minimum thresholds to avoid signal creation via electronic noise. In addition, there is information related to each run (such as information related to dead channels), that is included during the simulation to accurately reproduce detector response.

3.2 Event and Particle Reconstruction

Despite the fact that the events recorded by the ATLAS detector are run in a high pileup environment, it is still the case that the detector is able to reconstruct and accurately identify particles with the help of specifically constructed algorithms combining many pieces of extracted detector information. pileup in this context refers to the proton-proton collisions occurring in addition to the collision of interest. Since protons in the LHC move through the beam pipe in "bunches", pileup can refer to either collisions in the same bunch ("in time") or collisions from just before or after the collision of interest ("out of time"). These algorithms are developed and maintained by the Combined Performance (CP) groups, which provide recommendations to the entire collaboration on the use of standard physics objects, such as electrons and muons, across analyses. The CP group also provides calibrations and associated uncertainties for quantities related to these standard physics objects. This section will discuss object reconstruction algorithms relevant to the content of this thesis.

A schematic of various particle paths interacting with the ATLAS detector is given in

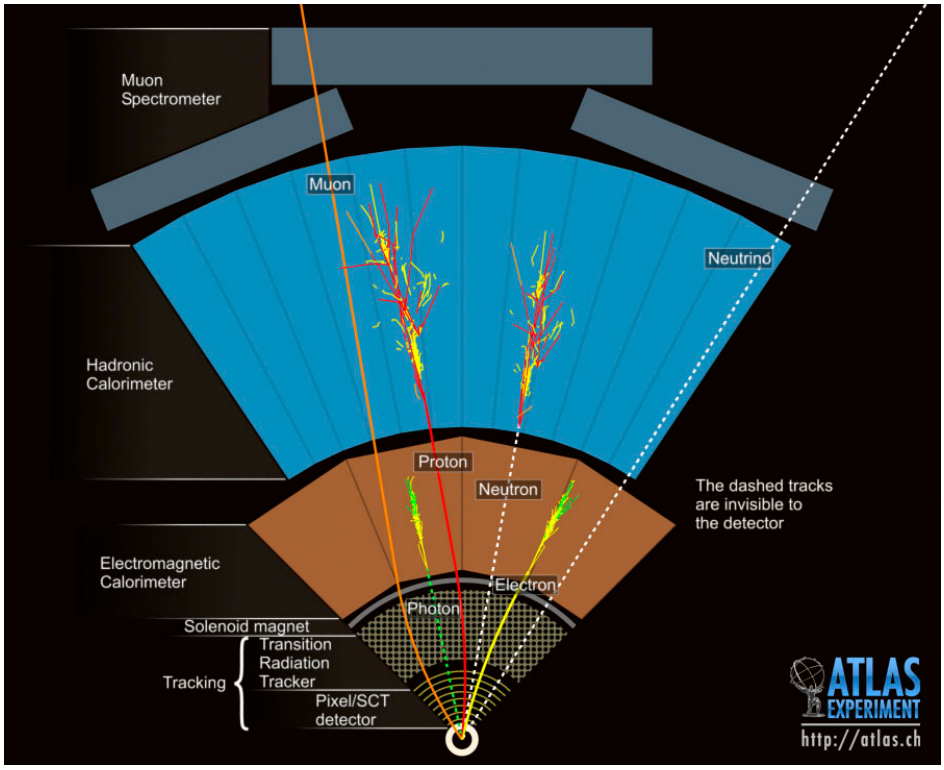

Figure 3.1: Cross-section of the ATLAS detector.

figure 3.1. Photons do not interact with the inner detector because they are electrically neutral, but do form a collimated shower of particles in the EM calorimeter. Electrons also form a similar shower type in the EM calorimeter, but do leave tracks in the inner detector since they carry an electric charge. Muons pass through the bulk of the detector, but interact only with the inner detector and muon spectrometer. Neutrons do not interact with the inner detector for the same reason as photons, but do deposit their energy in the hadronic calorimeter and create a collimated shower of particles. Protons act similarly in the hadronic calorimeter, but leave tracks in the inner detector because they are electrically charged.

3.2.1 Inner Detector Tracks

Track reconstruction begins using information from the pixel and SCT detectors. Once track candidates are reconstructed in the silicon detectors, they are extended outwardly using information from the transition radiation tracker. A more detailed description of this process can be found in reference [43]; it begins by clustering measurements from the SCT and pixel detectors. These clusters are used to create points in space that represent where a charged particle passed through the active material of the inner detector. After this clustering process, track candidates are reconstructed using a Kalman filter [44] to appropriate additional track points that are compatible with the initial cluster.

In the dense track environment in the inner detector created by the high-pileup environment in the ATLAS detector, particles pass so close to each other that it is common for track candidates to share interaction points in the inner detector. To disambiguate track candidates, each is given as score meant to represent the likelihood that a given candidate represents the trajectory of a charged particle by a solver using measurements such as cluster multiplicity and whether the interaction of a track candidate with a detector element contains a matching cluster where one is expected. Using this track score and additional information, ambiguous candidates are processed by a neural network meant to split merged clusters.

Once there are no clusters shared by multiple track candidates, the track finding algorithm is rerun to perform a final fit. The resulting output of this algorithm is given as a list of tracks given by the set of five parameters

$$(d_0, z_0, \phi, \theta, q/|p|)\,, \tag{3.1}$$

where d_0 and z_0 are the transverse and longitudinal impact parameters, ϕ and θ are the

azimuthal and polar angles with respect to the detector, and $q/|p|$ is the ratio of the particles charge to its momentum.

3.2.2 Primary Vertices

Primary vertices are those points in the space of the detector where a proton-proton interaction is said to have occurred. The process of reconstructing these can be found in reference [45] and can be split into two steps: vertex finding and vertex fitting.

In the finding step, reconstructed tracks are simply associated to candidate vertices, while the fitting step reconstructs the origin point of these tracks to define the vertex position. To do this, a selection process is applied to construct a list of input tracks along with an initial seed position. This information is used to create a best-fit position; the tracks are then increased or decreased in weight depending on their compatibility with this fit position. After the final vertex is determined, any tracks that are incompatible with it can be used to construct other vertices, and this procedure is repeated with all the remaining tracks until no new vertices can be formed.

This process is also responsible for the identification of the primary vertex associated with the hard-scatter event. This location is necessary to reconstruct the event's kinematics. The maximum sum of squared transverse momenta of the tracks with respect to the vertices ($\max_v \sum |p_T|^2$) is used to determine the hard-scatter vertex in contrast to pileup vertices. This criterion is based on the assumption that charged particles produced in a hard-scatter event have a higher average transverse momentum than those produced in pileup collisions.

3.2.3 Energy Clusters

Energy clusters consist of a set of calorimeter cells which contain deposits of energy and which share common edges. A single particle interacting with the ATLAS calorimetry system will most often deposit its energy into multiple cells, and as such the experiment uses several algorithms to collect that information into clusters of deposits. There are three types of clustering algorithms used in ATLAS: sliding-window, topological, and particle flow [46, 47] .

3.2.3.1 Sliding-Window Precluster (Seed) Finding

The sliding-window style clustering is used consists of three steps: tower building, precluster (seed) finding, and cluster filling. In the tower building step, the $\eta - \phi$ space of calorimeters in the region of interest is divided into a $N_\eta \times N_\phi = 200 \times 256$ grid of size $\Delta\eta \times \Delta\phi = 0.025 \times 0.025$. The energy of cells in all longitudinal layers is summer into a tower energy, and the tower edges do not correspond to calorimeter cell boundaries. The energy of a cell over more than one tower is split proportionally via the fraction of the cell's area over each tower.

In the seed-finding phase, a window of fixed size $N_\eta^{\text{window}} \times N_\phi^{\text{window}} = 5 \times 5$ is moved across each element of the tower grid defined in the tower building step. If the transverse energy sum inside the window is a local maximum above some energy threshold $E_T^{\text{thresh}} = 3$ GeV, a precluster is formed. The window size and threshold are optimized to obtain the best efficiency for finding these preclusters while limiting the rate of fake preclusters due to noise. Duplicate preclusters are removed such that only the precluster with the largest transverse energy is kept if their positions overlap.

In the cluster filling step, cells are assigned to electromagnetic clusters by taking all cells within a rectangle of size $N_\eta^{\text{cluster}} \times N_\phi^{\text{cluster}}$ centered on a layer-dependent seed position. The

final cluster energy is calculated based on the sum of the energy of the constituent towers along with the energy which is estimated to have not fallen within the final cluster window and the energy estimated to have fallen within the inner detector.

3.2.3.2 Topological Clustering

The basic idea of topological clustering is to group neighbors of cells into cluster that have significant energies compared to expected noise. The result of this process is clusters with a variable number of cells, in contrast to the fixed-sized clusters produced by the sliding-window algorithm. Cluster growth starts at seed cells with an energy significance (defined as signal-to-noise ratio) above a large threshold t_{seed}. Neighboring cells are iteratively added to the cluster if their significance is above a low threshold t_{cell}. A neighbor can serve as an additional seed to do cluster expansion if its significance is above a medium threshold t_{neighbor}. Having a low threshold at the perimeter ensures that the tails of showers are not discarded, whereas a higher threshold for seeds and neighbors suppresses both electronic and pileup noise.

In the standard ATLAS reconstruction, electromagnetic calorimeter clusters are formed with parameters $t_{\text{seed}} = 6$, $t_{\text{neighbor}} = 3$, and $E_T^{\text{thresh}} = 5$ GeV. In the hadronic calorimeter the clusters are formed with parameters $t_{\text{seed}} = 4$, $t_{\text{neighbor}} = 2$, and $E_T^{\text{thresh}} = 0$ GeV.

3.2.3.3 Particle Flow Clustering

The particle flow approach to clustering builds on the topological approach by incorporating measurements from both the tracker and calorimeter to form signals. The energy deposited in the calorimeter by all the charged particles is removed, and then jet reconstruction is performed on an ensemble of particle flow objects which consist of the remaining calorimeter

energy and tracks matched to the hard interaction.

Well measured tracks are selected which pass a stringent quality criteria: at least nine hits in the silicon detectors are required, and tracks must have no missing pixel hits when such hits would be expected. Tracks are required to be within $|\eta| < 2.5$ and pass a threshold $p_T > 0.5$ GeV. Tracks with $p_T > 40$ GeV are excluded from the algorithm because such energetic particles are often poorly isolated from nearby activity, which compromises the accurate removal of the calorimeter energy associated with the track. Any tracks matched to electrons or muons without any isolation requirements, identified with medium quality criteria, are not selected. The energy deposited in the calorimeter by electrons and muons is therefore taken into account in the particle flow algorithm and any resulting topological clusters are left unsubtracted.

The algorithm then attempts to match each track to a single topological cluster in the calorimeter. The expected energy in the calorimeter is computed based on the cluster position and track momentum. Given that, like the topological cluster algorithm, energy is commonly deposited into multiple clusters, each track/topological cluster system is evaluated for the probability that the particle energy was deposited in more than one cluster. On this basis the algorithm decides if it is necessary to add more topological clusters to the track/topological cluster system to recover the full shower energy. The discriminant used to distinguish between single and multiple topological cluster cases is the significance of the difference between the expected energy and the energy of the matched topological cluster, given by

$$S\left(E^{\text{clus}}\right) = \frac{E^{\text{clus}} - \langle E_{\text{dep}} \rangle}{\sigma\left(E_{\text{dep}}\right)}. \tag{3.2}$$

Lastly, if the remaining energy in the system is consistent with the expected shower fluctuation of a single particle's signal, the topological cluster remnants are removed.

3.2.4 Electrons

Electrons in ATLAS leave tracks in the inner detector and deposit the bulk of their energy in the electromagnetic calorimeter, and the experiment uses these to identify and reconstruct electrons. Most of their energy is lost due to bremsstrahlung when interacting with the detector material. The result of these interactions is a collimated shower of particles reconstructed in the electromagnetic calorimeter which can be reconstructed as a part of an energy cluster and matched to tracks in the inner detector. An electron object in the experiment is defined in terms of these components, and this reconstruction occurs in the detector region $|\eta| < 2.5$. A more detailed treatment of the methods described in this subsection can be found in references [48, 49].

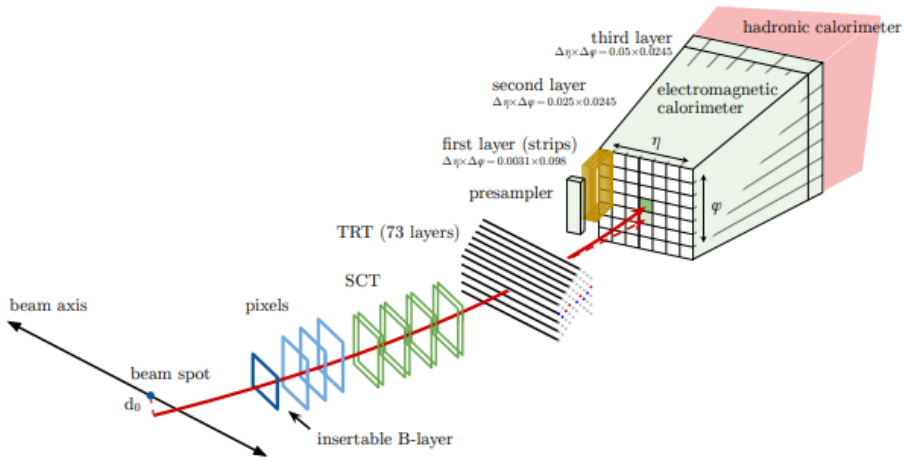

Figure 3.2: A schematic illustration of the path of an electron through the detector. Figure taken from reference [48].

The electron reconstruction process starts by finding energy clusters as detailed in section 3.2.3 for which $E_T > 2.5$ GeV. The reconstruction efficiency for electron spans 65% for $E_T =$

4.5 GeV, to 99% for $E_T = 7$ GeV, to greater than 99% for $E_T > 15$ GeV [49]. Inner detector tracks are found using the process described in section 3.2.1. Charged electrons lose energy when interacting with the detector material and therefore a procedure using a Gaussian-sum filter [50] takes into account non-linear effects in the tracks related to bremsstrahlung. These energy losses decrease the momentum of the electron, which causes them to bend more significantly in the toroidal magnetic field.

The identification of electrons is done with a likelihood-based method so that high-quality electrons are used for analysis and so non-prompt backgrounds are suppressed. This likelihood calculation combines information from the electron track in the inner detector, information about the shape of the electromagnetic shower, and information about the relative compatibility of the reconstructed energy cluster with the primary track associated with the electron. The probability distributions used for this estimation are derived from simulated data which has been corrected and scaled to more accurately represent real data, and a discriminator whose value increases with more electron-like objects for which associated tracks satisfy more stringent tracking requirements.

Using this discriminator, several identification working points are defined; we define them here in order of increasing electron purity. "Loose" electron criteria are primarily based on requirements on the fraction of the electromagnetic cluster E_T which leaks into the hadronic calorimeter, the shape of the shower, some track quality requirements, and the distance in $\Delta\eta$ between the track and the energy cluster. "Medium" electrons are a subset of "loose" electrons, where the more stringent requirements are on the number of hits in the silicon trackers and variables representing the shower shape. "Tight" electrons are a subset of "medium" electrons that have tighter criteria on the rejection of photon conversions, a maximum distance in $\Delta\phi$ between the track and energy cluster, and a requirement on the

ratio E/p. The "medium" and "tight" requirements are designed to reject 5,000 and 50,000 light-jets for every one accepted, respectively.

Electrons are often required to pass additional isolation criteria which are used after identification. Isolation variables are constructed to quantify the amount of activity around a candidate object, in this case an electron. There are two types of these isolation variables:

- E_T^{cone20} – This variable is constructed starting with the sum of transverse energy of topological clusters whose center of momentum falls within a cone $\Delta R = 0.2$ around the electron cluster center of momentum. E_T^{cone20} is constructed by subtracting from this energy the electron contribution, taking into account an additional correction due to pileup.

- $p_T^{\text{varcone20}}$ – A variable radius cone of size $\Delta R = \min\left(10 \text{ GeV}/p_T^e, 0.2\right)$ is constructed around the electron track. The p_T for all tracks with $p_T > 1$ GeV are summed.

These variables are used as discriminators on which points of varying efficiency requirements. The primary backgrounds to prompt electrons in ATLAS are hadronic jets, electrons from photon conversions, Dalitz decays, and semileptonic heavy flavor decays.

3.2.5 Muons

Muons are weakly interacting with the bulk of detector materials and so deposit little energy in the calorimeters, thus they are reconstructed using tracks in the muon spectrometer and inner detector. A detailed treatment of muon reconstruction and isolation can be found in reference [51]; this section will serve as a summary of its relevant contents. Tracks from the inner detector and muon spectrometer are constructed independently and then combined to form tracks extending the full radius of the detector. In the inner detector, muon tracks are

constructed as with any other particle described in section 3.2.1. In the muon spectrometer, this process begins by searching for hit patterns inside each chamber to form track segments. Potential tracks are formed by using a combinatorial fit of these segments, at least two of which are required to build a candidate muon track, so long as the candidate is not along the transition region between the barrel and end-cap, in which case a single high-quality segment can be used. After this the track candidates are fitted using a global χ^2 fit, and those passing a threshold are accepted.

The combined inner detector-muon spectrometer reconstruction is performed using multiple algorithms based on the information provided by the inner detector, muon spectrometer, and calorimeters. Using this information, four types of combined tracks are defined depending on which subdetectors were used in the reconstruction:

- Combined muon – Track reconstruction is performed independently in the inner detector and muon spectrometer, with which a combined track is formed using information from both. During the global fit procedure, muon spectrometer hits may be added or subtracted to improve fit quality.

- Segment-tagged muons – A track in the inner detector is classified as a muon if it is associated with at least a single track segment in the muon spectrometer once extrapolated. ST muons are used when muons cross only one layer of muon spectrometer chambers, either because of their low p_T or because the fall in regions with reduced muon spectrometer acceptance.

- Calorimeter-tagged muons – A track in the inner detector is identified as a muon if it can be matched to an energy deposit in the calorimeter compatible with a minimum-ionizing particle. While this category is of the lowest purity of all the listed types, it

recovers muons in the region where the muon spectrometer is only partially instrumented, thus this category is optimized for that region $|\eta| < 0.1$ and momentum range $15 < p_T < 10$ GeV.

- Extrapolated muons – This trajectory is reconstructed based only on the track in the muon spectrometer with a loose requirement on compatibility originating from the nominal interaction point. The parameters of the muon track are defined by taking into account an estimated calorimeter energy loss in relation to the interaction point. This category of muon is required to traverse a minimum of two layers of muon spectrometer chambers to provide a reliable track measurement or three layers in the forward region. The purpose of this category is primarily to extend muon reconstruction into the region $2.5 < |\eta| < 2.7$, which is not covered by the inner detector.

To identify muons from candidates quality requirements are applied that serve to suppress backgrounds, primarily from pion and kaon decays, while selecting prompt muons with high efficiency and/or guaranteeing robust measurement. Muon candidates originating from in-flight decays of charged hadrons in the inner detector are often seen with a "kink" track topology. A consequence of this is that the fit quality of the combined track is poor, and the momentum measured in the inner detector and muon spectrometer may be incompatible. To guarantee a robust measurement, there are specific requirements on the number of hits in the inner detector and muon spectrometer. We can use multiple variables to discriminate between prompt muons and background candidates:

- q/p significance – The absolute value of the difference between the ratio of charge and momentum as measured by the inner detector and muon spectrometer divided by the sum in quadrature of the respective uncertainties.

- ρ' – The absolute value of the difference between transverse momentum measurements in the inner detector and muon spectrometer divided by the p_T of the combined track.
- The normalized χ^2 of the combined track fit.

Isolation requirements are imposed on muon candidates for the purpose of rejecting non-prompt muons. While prompt muons are produced by by the decays of heavy bosons, non-prompt muons are typically produced busily surrounded by other track and calorimeter deposits. Similar to electron isolation, two isolation variables are constructed [52]:

- $E_T^{\text{topocone20}}$ – This variable is defined as the sum of the transverse energy of topological clusters within a cone $\Delta R = 0.2$ around the muon after subtracting the energy associated with the muon itself and applying corrections for pileup effects.
- $p_T^{\text{varcone30}}$ – Defined as the scalar sum of transverse momenta of tracks with $p_T > 0.1$ GeV within a cone of size $\Delta R = \min\left(10 \text{ GeV}/p_T^{\mu}, 0.3\right)$.

The isolation selection is determined using the *relative* isolation variables, defined as the ratio of track- or calorimeter-based isolation variables to the transverse momentum of the muon.

3.2.6 Jets

Color confinement precludes the possibility of stable bare quarks, which quickly hadronize to form color-neutral bound states. Therefore, in the ATLAS detector, final state partons produced in collisions quickly form showers of quarks and gluons, which collectively are referred to as a jet. These jets are primarily constituted of roughly 60% charged pions ($c\tau = 10$ mm) and photons, with the other 40% being made of kaons, light baryons, and

strange baryons. Jets leave tracks in the inner detector and subsequently deposit the bulk of their energy in the calorimeter system.

3.2.6.1 Anti-k_T Algorithm

The reconstruction process for jets uses a bottom-up approach by clustering constituent parts using the anti-k_T algorithm [53]. What counts as a jet constituent depends on which of the clustering algorithms from section 3.2.3 is used. The algorithm process is as follows:

1. Construct a set of all tracks and energy clusters.

2. Introduce two distinct sets of distances d_{ij} and d_{iB} defined as

$$d_{ij} = \min\left(k_{t,i}^{-2}, k_{t,j}^{-2}\right)\frac{\Delta_{ij}^2}{R^2} \tag{3.3a}$$

$$d_{iB} = k_{t,i}^{-2} \tag{3.3b}$$

   where $\Delta_{ij}^2 = (\eta_i - \eta_j)^2 + (\phi_i - \phi_j)^2$ and $k_{t,i}$, η_i, and ϕ_i are the transverse momentum, rapidity, and azimuth of particle i, respectively. B represents the beam and R is the radius parameter of the jet.

3. Find the smallest distance among the set of all d_{ij} and d_{iB}.

   - If d_{ij} is the minimum distance, objects i and j are removed and combined to form a new object k.
   - If d_{iB} is the minimum distance, object i is classified as a jet and removed from the list.

4. Repeat until the list is exhausted.

3.2.6.2 Small-R Jets

Small-R jets are defined as jets reconstructed with an $R = 0.4$ anti-k_T algorithm. Truth particles for this type of jet are matched with the requirement of $\Delta R < 0.3$ between the truth and reconstructed jet. Pileup effects are reduced by using the Jet Vertex Tagger (JVT) technique, which tags pileup jets using a 2D likelihood estimate [54]. These jets are built using one of two methods:

- EMTopo jets – These jets are built using only the topological clusters described in 3.2.3.2 as constituent parts. They are calibrated at the electromagnetic (EM) scale, which allows their energy associated with electromagnetic showers to be properly accounted for. After a jet is reconstructed it must be calibrated to correct the energy, mass, and direction so that those properties correspond to the underlying truth variables. These corrections include taking into account effects such as non-compensating calorimeter response and known differences between data and MC [55].

- Particle Flow (PFlow) jets – These jets used calorimeter information (in this case topological clusters) *and* inner detector information. A cell-based subtraction algorithm is used to remove any overlaps between momentum and energy measurements, and the topological clusters used are calibrated to the electromagnetic scale. Energy-subtracted topological clusters and tracks matched to the primary vertex are passed to the anti-k_T algorithm with $R = 0.4$. Tracks are required to satisfy the relation $|z_0 \sin\theta| < 2$, where z_0 is the track's distance of closest approach to the primary vertex.

3.2.6.3 Large-R Jets

Jets resulting from the hadronic decay of a high momentum H, W, Z, or t become so collimated in the detector that the decay results' signatures can become highly overlapped. These parts are thus reconstructed as a single jet from topological clusters using the anti-k_T algorithm with radius parameter $R = 1.0$. Unlike small-R jets, these jets are calibrated to the hadronic scale and are groomed with a trimming algorithm [56] to reduce pileup, soft emission effects on the measurement of the jet substructure.

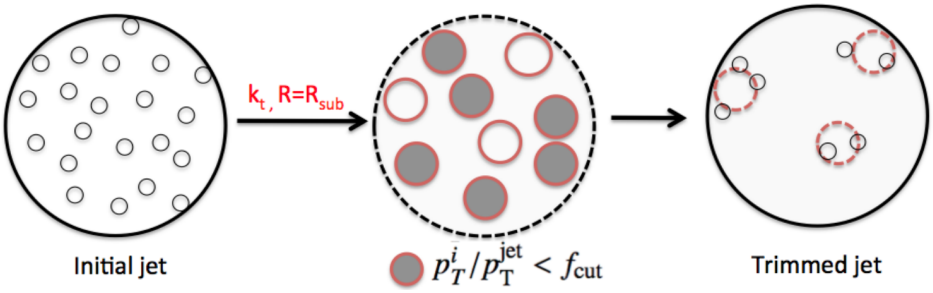

Figure 3.3: Diagram depicting the jet trimming procedure [57].

3.2.6.4 Variable-R Track Jets

Track jets are reconstructed using tracks from the inner detector in the region $|\eta| < 2.5$ with $p_T > 0.5$ GeV via the anti-k_T algorithm. To reduce pileup effects and raise the efficiency of constructing jets from tracks originating at the primary vertex, tracks used for variable-R jets are required to satisfy $z_0 \sin\theta < 3$ mm. Variable-R jets, as their name implies, use a non-fixed radius that it p_T dependent like [58]

$$R_{\text{eff}}(p_T) = \min\left(R_{\text{max}}, \max\left(R_{\text{min}}, \frac{\rho}{p_T}\right)\right) \tag{3.4}$$

where $\rho = 30$ GeV, $R_{\text{max}} = 0.4$, and $R_{\text{min}} = 0.2$. The effect of this algorithm is that reconstructed jets with high-p_T are allowed to be narrower, which allows jets close to these

high-p_T jets to be reconstructed more accurately.

3.2.6.5 Top Tagging

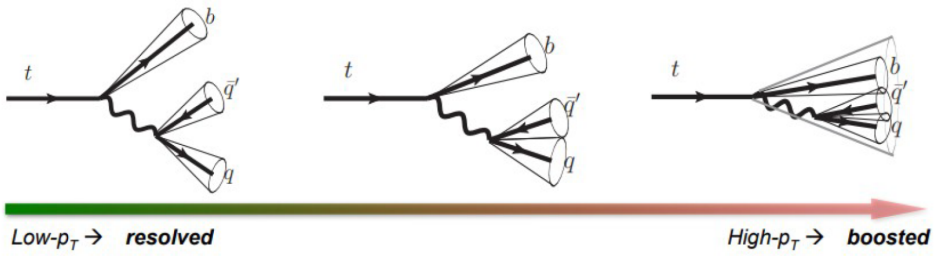

Figure 3.4: Jet topology categorization as a function of their collimation.

Decay products in the ATLAS detector can become highly collimated along the direction of travel of the parent particle as they become relatively more Lorentz boosted, as seen for top quarks in figure 3.5. The angular distance between the furthest daughter particles is proportionally given by the relationship $\Delta R \sim 2m/p_T$, where m and p_T are the mass and transverse momentum of the decaying parent particle, respectively. In the case of this analysis, in a high-momentum top quark decay, the outgoing W-boson's decay products and b-quark are angularly close to one another. In a boosted decay, the calorimeter clusters of the final state objects are reconstructed within a single large-R jet ($R = 1$) as described in section 3.2.6.3.

Top tagging is a technique for determining whether a large-R jet is the result of a boosted hadronic top decay. A top-originating jet is a combination of three distinct subjets, and this can be seen in the structures and patterns inside it. Substructure variables are constructed from these internal attributes to help distinguish top-jets from other non-top QCD jets, and top-tagging methods use these variables to identify top jets.

Many such substructure variables are used in top tagging, including variables like the jet mass, for which large-R jets originating from a top decay tend to have higher mass than other

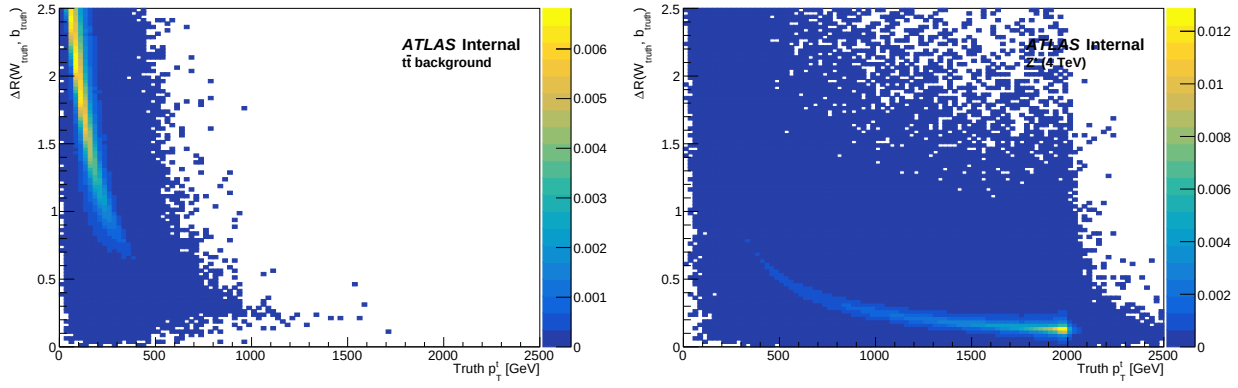

(a) SM $t\bar{t}$ (b) Z' (4 TeV)

Figure 3.5: Truth angular separation ΔR between the W-boson and b-quark in $t\bar{t}$ decays at parton level as a function of truth top quark p_T for a (a) SM $t\bar{t}$ background and (b) a 4 TeV $Z' \to t\bar{t}$ signal.

QCD jets. N-subjettiness (τ_N) is a measure of how well a jet can be described with N or fewer subjets, and ratios of these like $\tau_{32} = \tau_3/\tau_2$ and $\tau_{21} = \tau_2/\tau_1$ are used as discriminating variables to distinguish hadronic top-jets from other jets. The minimum pairwise invariant mass of the subjects $Q_w = \min_{i,j}\{m_{ij}\}$, where i and j are the subject indices, is another important substructure variable. A comprehensive list of the variables used can be found in reference [59].

Many combinations of jet substructure variables and jet mass have been used in algorithms to identify jets originating from a top quark decay. A Deep Neural Network (DNN) based method outperforms other methods and uses all the high-level substructure variables as input. It outputs a discriminant score used to differentiate top jets from other jets, and different working points are defined based on the efficiency and purity of the required threshold [59].

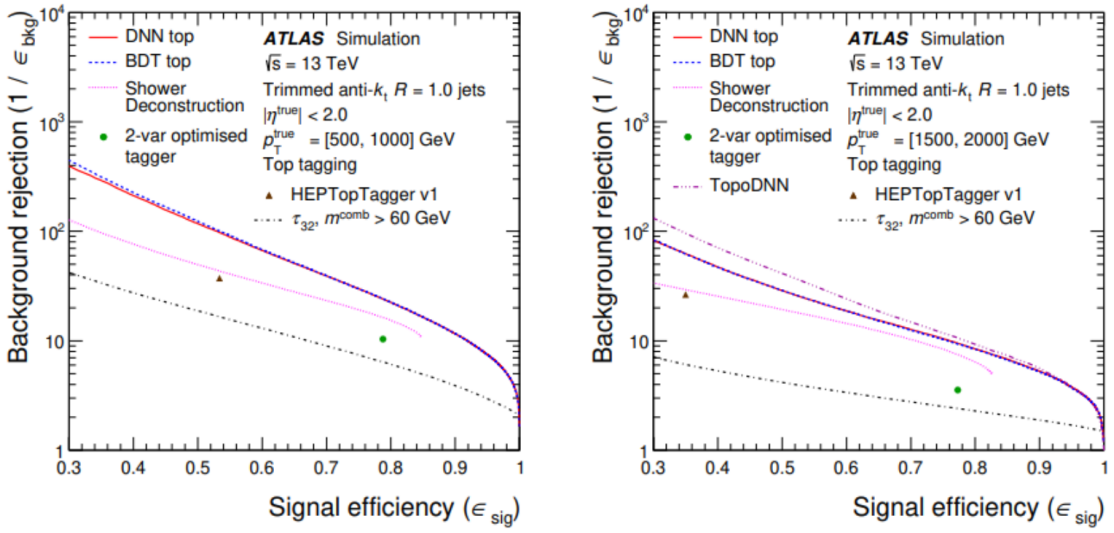

Figure 3.6: The performance comparison of the top quark taggers in a low-p_T^{true} (a) and high-p_T^{true} (b) bin. Performance is evaluated with the p_T^{true} distribution of the signal jets weighted to match that of QCD background samples [59].

3.2.6.6 *b*-Tagging

Jets coming from b-partons and containing b-hadrons are identified using b-tagging techniques and are referred to as b-jets; their identification is crucial for this thesis' reconstruction of top-quark decays. Since top quarks decay on the order of 10^{-25} s after formation, they do not hadronize and instead almost always decay into a W-boson and b-quark. To distinguish between b-jets and other jets, b-tagging uses b-hadron decay signatures and lifetimes. These additional jets include c-jets, which originate from c-quarks and include D-hadrons, and light-jets, which originate from gluons, first generation quarks, and s-quarks. b-hadrons are long-lived ($\tau \sim 1.5$ ps, $c\tau \sim 450$ μm) and thus create a vertex displaced from the primary collision point.

Because b-quarks are significantly more massive than any of their decay products, the decay products have a large p_T, which implies that the ensuing b-jet will have a high multiplicity, invariant mass, and contain low energy leptons with momentum perpendicular

to the jet. Hadrons containing b-quarks have sufficient lifetime that they travel some distance from the primary vertex before decaying inside the detector. This means that the secondary vertex displacement may be utilized to differentiate b-jets from other jets, and that the primary vertex reconstruction is crucial for b-tagging; the secondary vertex finding algorithm (SV1) is used to reconstruct a single displaced vertex in a jet. Tracks compatible with long-lived particles (e.g. K_s, Λ), photon conversion, or hadronic interaction with the detector material are rejected. The SV1 algorithm runs iteratively until it finds a reasonable track-to-vertex associated based on a χ^2 test and a vertex invariant mass under 6 GeV. If a single b-jet has many b- and c-vertices, the vertices are merged into a single vertex if they are near enough, or the vertex with the greatest jet multiplicity is reconstructed if they are not. The high-level taggers are fed eight discriminating variables related to the SV1 algorithm.

b-tagging is done on small-R jets ($R = 0.4$), as described in section 3.2.6.2, or variable-radius jets, as described in section 3.2.6.4. In the analysis described in this thesis a DL1 [60] algorithm is used, which is based on a DNN architecture with a multidimensional output corresponding to the probabilities for a jet to be a b-, c-, or light-flavor jet; its topology consists of a mixture of fully-connected hidden layers and maxout layers. This network is trained using a mixture of SM $t\bar{t}$ and $Z' \to b\bar{b}$ events, with b-jets as the classification signal and c-jets (7%) and light-jets (93%) as the background. The DL1 b-tagging discriminant is defined by combining the c-jet fraction in the background training sample (f_c) with the b-jet, c-jet, and light-jet probabilities (p_b, p_c, and p_{light}, respectively) as

$$D_{\text{DL1}} = \ln\left(\frac{p_b}{f_c \cdot p_c + (1 - f_c) \cdot p_{\text{light}}}\right). \tag{3.5}$$

3.2.6.7 Missing Transverse Energy

Momentum conservation implies that the vector sum of the momenta of final state particles created in proton-proton collisions should equal the vector sum of the momenta of the colliding protons. The colliding partons' transverse momenta may be considered to be zero because their motion is parallel to the beam axis; our expectation is that the final state system's transverse momentum will total to zero. Because neutrinos escape the ATLAS detector undetected, their existence must be inferred by an inequality in the final state energy. The Missing Transverse Energy (MET) is defined as the difference between zero and this imbalance and is parametrized by its magnitude and corresponding azimuthal angle in the transverse detector plane (E_T and ϕ, respectively). Particle and jet selections in a given analysis are reflected in E_T^{miss} to give a consistent interpretation of an event. All fully reconstructed particles in an event participate in the reconstruction of E_T^{miss}, including soft particles modeled via charged particle tracks from the primary vertex passing quality and kinematic selections, as

$$E_T^{\text{miss}} = -\sum p_T^e - \sum p_T^\gamma - \sum p_T^{\tau,\text{had}} - \sum p_T^\mu - \sum p_T^{\text{jet}} - \sum p_T^{\text{soft}}. \tag{3.6}$$

Chapter 4

Search for Heavy Resonance Decays to Top Quark Pairs Using a Lepton-Plus-Jets Final State

This chapter will detail a search for high mass top quark pair resonances in proton-proton collisions using 139 fb^{-1} of data collected at a center-of-mass energy of 13 TeV using the ATLAS detector at the LHC. Events are selected in the lepton+jets topology $t\bar{t} \to WbWb \to l\nu bqqb$. This leads to a signature with a high transverse momentum lepton, large missing transverse momentum, and hadronic jets. The analysis is optimized to cover different final state topologies:

- A boosted environment in which the $t\bar{t}$ system is highly energetic and the hadronic top decay products merge into a single large-R ($R = 1.0$) jet.
- A resolved environment in which the final state can be well separated into small-R ($R = 0.4$) jets.

A search is performed, and in the case where no statistically significant excess above the Standard Model expectation is observed, upper limits are set on the cross-section times branching ratio of a resonance decays to top-quark pairs as a function of the resonance mass.

Previous results with 36 fb^{-1} data were published in 2018 [61]. This analysis aims to improve the signal acceptance and signal-to-background ratio over the previous result with respect to the top-tagging (inclusive DNN top-tagger), b-tagging (DL1r tagger focused on the high p_T), dedicated overlap removal method for high p_T electrons and jets (electron-in-jets subtraction method), and a new $t\bar{t}$ NNLO (EWK + QCD) correction based on a recursive reweighting method. This analysis will be statistically combined, firstly with the $t\bar{t}$ fully-leptonic channel, and then with the $t\bar{t}$ fully-hadronic channel and will take part in the wider heavy resonance combination effort. This analysis focuses on the semi-leptonic $t\bar{t}$ final state in the electron and muon channel. The semi-leptonic top decay has the second largest $t\bar{t}$ branching ratio, constituting roughly 30% of $t\bar{t}$ decays. Single electron and muon triggers allow for an efficient way of selecting events with the presence of charged leptons, and as a result the sensitivity of this analysis is comparable to an all-hadronic $t\bar{t}$ search despite its lower branching ratio. Models described in section 1.3.6 predict a new, neutral gauge boson, the Z'. Specifically, although this analysis is performed in a generic way, benchmark signal models of a leptophobic, topphyllic Z'_{TC2} of width 1.2%.

4.1 Analysis Strategy

The search region spans between 300 GeV and 6 TeV of the invariant mass $m_{t\bar{t}}$ given in equation 4.12, and the selection cuts are re-optimized compared to the 2015+2016 analysis. Analysis events are split into categories based on the lepton (electron or muon) associated with the leptonic side of the decay, and the relative collimation of the jet(s) on the hadronic side of the decay. Events reconstructed as having one highly collimated large-R jet associated with a hadronic top decay and one small-R jet associated with the leptonic top decay (as

described in section 3.2.6) are categorized as "boosted", while events with a topology of four small-R jets are categorized as "resolved". All events are required to have exactly one lepton and a missing transverse energy associated with a leptonic W decay.

The main strategies of this analysis are:

1. The event selection is optimized for a narrow-width spin-1 signal of the form $Z'_{\mathrm{TC2}} \to t\bar{t}$.
2. The selection is split into four main categories: boosted and resolved regions for each of the electron and muon channels, along with a further categorization based on the number of b-tagged jets.
3. A high-level, optimized DNN with an inclusive top quark definition is used for top tagging.
4. b-tagging (DL1r) done on track-jets with variable radius.
5. An improved, dedicated overlap removal procedure (electron-in-jets subtraction).
6. All backgrounds other than QCD are estimated using MC simulation. QCD background is estimated using a matrix method which will be described in subsequent sections; QCD estimation is done using full Run-2 data in the QCD control region.
7. A binned $m_{t\bar{t}}$ distribution is used to perform a profile-likelihood fit; a frequentist confidence limit interpretation is used for limit setting.

4.2 Data and Simulation

This analysis uses the full Run-2 dataset collected at $\sqrt{s} = 13$ TeV during the 2015 (3.2 fb^{-1}), 2016 (33.0 fb^{-1}), 2017 (44.3 fb^{-1}), and 2018 (58.5 fb^{-1}), which combines to a total integrated

luminosity of 139 fb^{-1}. For use in this analysis, events in the datasets are required to pass the "`All_Good`" Good Run List (GRL), which is a list of data chunks satisfying quality restraints to ensure optimal, stable beam and detector conditions. To cover data-taking periods with different collision conditions and number of simultaneous interactions per bunch-crossing, multiple MC campaigns are necessary. The events in these MC campaigns are weighted to match the pileup conditions present in the data for the periods they correspond to.

The primary backgrounds for this analysis are irreducible SM $t\bar{t}$ production, W+jets, Z+jets, diboson, and single-top production, all of which are estimated with MC samples. There is an additional QCD multijet background which is estimated using a data-driven technique which will be described in a later section. Each of the MC samples used will be enumerated in detail below.

4.2.1 Simulated Backgrounds

This analysis attempts to select and reconstruct collisions resulting in the production of a heavy particle decaying semi-leptonically into a $t\bar{t}$ pair. However, the SM predicts a number of processes which may produce a significant number of events passing the selection criteria. These backgrounds are modeled via MC simulation, as described in chapter 3, and data driven methods.

Our largest background consists of SM $t\bar{t}$ events produced primarily through strong interactions. These are estimated via simulation using `POWHEG` [62, 63]+`PYTHIA 8` [64] using the NNPDF 3.0 NLO PDF [65] for showering and hadronization together with the A14 tune. This background consists only of events in which a minimum of one top quark decays leptonically, with fully hadronic events included in a separate, data-driven QCD background described later; it is considered to be "irreducible", as its final state is identical to the signal

process and therefore its contribution is difficult to reduce via improved kinematic cuts. However, SM $t\bar{t}$ exhibits a steeply falling distribution of the invariant mass $m_{t\bar{t}}$, which is the primary discriminating variable, and so a signal contribution can be distinguished as either a local excess of events or a differing distribution shape, depending on the signal width. For the SM $t\bar{t}$ background a normalization scheme is used to achieve a next-to-next-to-leading order (NNLO) cross-section ($\sigma \times \mathcal{B}_{t\bar{t}} = 451.59$ pb) computed with `top++ 2.0` that includes resummation of next-to-next-to-leading logarithmic (NNLL) soft gluon terms.

W+jets, Z+jets, and diboson production are generated using `SHERPA` 2.2.11 [66] using NNPDF 3.0 NNLO PDF. For the W+jets background, scale factors are derived from data and applied to correct the normalization of the W+jets background and fraction of events containing a jet originating from a heavy flavor quark. However, the Z+jets contribution is sufficiently small that no such normalization is needed. Diboson (WW, WZ, and ZZ) and $t\bar{t}$+boson ($t\bar{t}V$) backgrounds make modest contributions. Single top production is also generated by `POWHEG` + `PYTHIA 8` using the NNPDF 3.0 NLO PDF.

Each of these backgrounds contain leptons and/or jets associated with a vector boson decay. Additional backgrounds can result from the mis-reconstruction of non-prompt or fake leptons. These events primarily occur in "QCD", multijet production. Although the QCD background cross-section is orders of magnitude larger than the other background processes, its magnitude in this search is counterbalanced by the difficulty in faking a high quality lepton and as such contributes a modest number of events. Due to this large rejection rate, an enormous number of events would need to be simulated to accurately estimate the background quantity and shape, and so the QCD background contribution is estimated directly from data.

4.2.2 Data-driven Multijet Background

The multijet background is one of the most difficult to model because it is interwoven with detector-related quantities such as lepton identification and isolation criteria. These processes occur when a jet or photon is identified as isolated and gets mis-reconstructed as a prompt (originating from the main collision) lepton in the relevant final state topology. Estimation of these fake leptons is difficult as the probability of a singular jet or photon faking an electron is tiny, but the cross-section of the multijet background is very high and thus a very large number of simulated events would be required to model it. Additionally, electrons and muons originating from the semi-leptonic decay of hadrons (non-prompt leptons) can pass the charged lepton identification and isolation criteria for prompt leptons. To model the multijet background we instead use a matrix method which defines the prompt lepton identification efficiency (ϵ) and the non-prompt lepton misidentification probability (f) using "tight" and "loose" lepton definitions. Here, tight leptons are leptons passing the nominal analysis selection, while a loose lepton has lower identification criteria and no isolation requirement. Although summarized here for completeness, this is one of the few parts of the analysis I did perform directly. Further validation plots are provided in appendix C.

4.2.2.1 Matrix Method

The multijet background is estimated by modeling the kinematics of multijet events using real data. The normalization and shape of the background can be extracted from data through the reweighting of individual data events. Two separate selections on charged leptons are applied leading to two different datasets for both electrons and muons. This estimation is a two stage process, where a data sample is selected requiring the lepton to satisfy a loose isolation criteria; sub-sample is selected requiring the lepton to satisfy tight isolation criteria.

Lepton Isolation	Electron Channel	Muon Channel
Loose	MediumLH and No Isolation	Loose and No Isolation
Tight	TightLH and TightTrackOnly	Medium and TightTrackOnly_VarRad

Table 4.1: Definitions of the leptons used for the matrix method estimation.

These selections are summarized in table 4.1.

The tight criteria are chosen such that they match the final, analysis-optimized isolation criteria. Given these two samples, a system of equations can be constructed for the number of leptons in the loose and tight samples. The number of events with leptons satisfying the loose definition is defined as

$$N_L = N_{\text{prompt}} + N_{\text{QCD}} \tag{4.1}$$

where N_{prompt} and N_{QCD} are the number of signal-like leptons originating from the W-decay and the number of misidentified QCD leptons, respectively. The number of tight leptons N_T can be written as

$$N_T = \epsilon N_{\text{prompt}} + f N_{\text{QCD}}. \tag{4.2}$$

Thus we can define the efficiencies for real and fake leptons as

$$\epsilon = \frac{N_{\text{prompt}}^{\text{tight}}}{N_{\text{prompt}}^{\text{loose}}}, \qquad f = \frac{N_{\text{QCD}}^{\text{tight}}}{N_{\text{QCD}}^{\text{loose}}}. \tag{4.3}$$

Define the number of anti-tight leptons as $N_A = N_L - N_T$. Thus solving the above set of linear equations gives

$$N_{\text{QCD}}^{\text{tight}} = f N_{\text{QCD}} = \frac{\epsilon f - 1}{\epsilon - f} N_T + \frac{\epsilon f}{\epsilon - f} N_A \tag{4.4}$$

Electron Channel	Muon Channel
== 1 loose e	== 1 loose μ
== 0 tight μ	== 0 tight e
$E_T^{\text{miss}} < 20$ GeV, $E_T^{\text{miss}} + m_{T,W} < 60$ GeV	$E_T^{\text{miss}} < 20$ GeV, $E_T^{\text{miss}} + m_{T,W} < 60$ GeV
≥ 4 jets	≥ 4 jets
≥ 1 b-tagged jet	≥ 1 b-tagged jet

Table 4.2: Definitions of the QCD-enhanced control regions.

as the estimation of fake leptons in the signal region coming from the multijet processes, which is applied as a weight on a per-event basis where $N_T = 1$ if the event satisfies both the loose and tight selection criteria and $N_T = 0$ if the event satisfies only the loose criteria. This result cannot be used directly, as the parameters ϵ and f can depend on event kinematics and must be modeled accordingly. The fake rate, f, can be measured in collision data by selecting a control sample of events enriched in the background being estimated after a background subtraction is performed to remove the prompt lepton contamination in both the tight and loose lepton samples.

4.2.2.2 Estimation of Fake and Real Rates

The fake rate, f, can be interpreted as the probability for a misidentified, QCD-like lepton passing the loose selection to subsequently pass the tight selection criteria. This rate can be measured in collision data by selecting a control sample of events enriched in the background being estimated, defined as the region $\text{CR}_{\text{QCD}}^{4j,1b}$. The fake lepton efficiencies are estimated using the selection criteria given in table 4.2.

The real rate, ϵ, can be interpreted as the probability for a signal-like lepton passing the loose selection criteria to subsequently pass the tight selection criteria. This can be measured in simulated SM samples by applying both the loose and tight selection on a sample to be as signal-like as possible. Only events containing physically isolated leptons

should be included, where the best parameterizations of the signal efficiency ϵ are a function of the lepton isolation (topoetcone20) and lepton p_T. Additionally, f and ϵ depend strongly on the angular separation between the closest jet and muon, $\Delta R_{\text{min}}(\mu, \text{jet})$.

The parameterization is further improved for the muon channel by applying a correction factor to the real and fake rates, as

$$\epsilon_{\text{corr}}(\Delta R, p_T, \text{topoetcone20}) = \epsilon(p_T, \text{topoetcone20}) \frac{\epsilon(p_T, \Delta R)}{\epsilon(p_T)} \tag{4.5}$$

$$f_{\text{corr}}(\Delta R, p_T, \text{topoetcone20}) = f(p_T, \text{topoetcone20}) \frac{f(p_T, \Delta R)}{f(p_T)}. \tag{4.6}$$

This parameterization allows for a better description of the rates in the region $\Delta R_{\text{min}}(\mu, \text{jet}) < 0.4$, which is a particularly relevant region for boosted topologies.

4.2.3 W+jets Background Normalization

In pp colliders, the production cross-section of W^+ is slightly larger than that of W^- due to the asymmetry of u- and d-type quark content in the proton. The measured ratio of the cross-section σ_{W+}/σ_{W-} is ~ 1.46 and is well modelled. In this analysis the expected W+jets background is estimated using simulated events with the `Sherpa 2.2.11` event generator. The overall normalization is corrected in the signal regions using the following data driven method, which is computed independently for each of the four signal regions since the impact of heavy flavor may be impacted by the selection processes.

Let the overall normalization factor be f_W. It is obtained from the events in each signal region exploiting the fact that W charge-asymmetry in W+jets production is predicted with better precision than the overall normalization. For other flavor symmetric backgrounds

considered in this analysis, such as $t\bar{t}$, QCD multijet, and Z+jets, the charge asymmetry is zero. Here, the charge asymmetry is defined as the simple difference between the number of events with W^+ and W^- as

$$A^W = N^+ - N^-, \tag{4.7}$$

where $N^{\pm}$ is the number of events with a positively or negatively charged lepton. The charge asymmetry is calculated for data ($N^{\pm}_{\text{data}}$) by subtracting the MC contributions from all the charge-asymmetric processes ($N^{\pm}_{\text{MC, asym}}$) such as $t\bar{t}+V$, single top, and diboson. Thus, we define the corrected number of data events with positive and negative charged leptons as

$$N^{\pm}_{\text{data, corr}} = N^{\pm}_{\text{data}} - N^{\pm}_{\text{MC, asym}}. \tag{4.8}$$

The charge asymmetry in corrected data is compared with that of the MC W+jets process to calculate the charge asymmetry normalization. For each of the four signal regions, the charge asymmetry normalization is used as the overall W+jets normalization and can be written as

$$f^W = \frac{N^{W+\text{jets}}_{\text{data}}}{N^{W+\text{jets}}_{\text{MC}}} \approx \frac{A^W_{\text{data}}}{A^W_{\text{MC}}} = \frac{N^+_{\text{data, corr}} - N^-_{\text{data, corr}}}{N^+_{\text{MC, }W+\text{jets}} - N^-_{\text{MC, }W+\text{jets}}}. \tag{4.9}$$

Table 4.3 provides the results and statistical uncertainties for each signal region.

Resolved e	
cat 1	1.30 ± 0.05
cat 2	1.30 ± 0.05
cat 3	1.30 ± 0.05
Resolved μ	
cat 1	1.30 ± 0.05
cat 2	1.30 ± 0.05
cat 3	1.30 ± 0.05
Boosted e	
cat 1	1.38 ± 0.07
cat 2	1.38 ± 0.07
cat 3	1.38 ± 0.07
Boosted μ	
cat 1	1.38 ± 0.07
cat 2	1.38 ± 0.07
cat 3	1.38 ± 0.07

Table 4.3: Charge asymmetry normalization factors for the W+jets background.

4.2.4 $Z' \to t\bar{t}$ Signal Production

The signal process $pp \to Z' \to t\bar{t}$ was simulated using the `PYTHIA 8.186` event generator with default settings for generic Sequential Standard Model (SSM), which is a highly simplified model where the Z' has the same coupling to fermions as the SM Z, but a higher pole mass. Samples are generated for a variety of Z' masses using the NNPDF 2.3 LO PDF set, and signal interference with SM $t\bar{t}$ was not considered due to its large model dependence and negligible effect. The primary benchmark signal model employed in this analysis is a Topcolor Assisted Technicolor (TC2) model as discussed in section 1.3.6.2. The Heavy Vector Triplet (HVT) model is a secondary, generic model that is used to combine the analysis findings with other searches inside the ATLAS experiment.

In this analysis, the Z' signal cross-sections are scaled to their TC2 values, and samples are created for Z' masses range from 400 GeV to 5 TeV. The LO cross-sections for $\Gamma/M = 1.2\%$ and $\Gamma/M = 3\%$ are given in table 4.4 The widths of the signal samples are narrower than the reconstructed resolution. Following recommendations given in reference [17] and precedent from previous $t\bar{t}$ resonance searches, a multiplicative k-factor of 1.3 is used to scale the samples to NLO.

The HVT $Z'_{\mathrm{HVT}} \to t\bar{t}$ signal is simulated using `MadGraph5 aMC@NLO v2.6.0` and `PYTHIA 8.212` with the A14 set of tuned parameters for parton showering and hadronization.

Z'_{TC2} Mass [TeV]	LO Cross-Section ($\Gamma/M = 1.2\%$) [pb]
0.4	70.3
0.5	40.1
0.75	10.7
1	3.70
1.25	1.51
1.5	0.684
1.75	0.334
2	0.172
2.25	0.0924
2.5	0.0511
2.75	0.0289
3	0.0167
4	0.00213
5	0.000331

Table 4.4: Leading order theoretical cross-sections for the Z'_{TC2} signal, on top of which a k-factor of 1.3 is applied.

4.3 Object Definitions

4.3.1 Large-R Jets

To recover boosted top quarks, an $R = 1$ anti-k_T jet clustering algorithm is used as described in section 3.2.6.1; these jets are constructed using three-dimensional topological energy clusters described in sections 3.2.3 and 3.2.6.3. Reconstructed large-R jets are trimmed such that subjets clustered with radius parameter $R_{\mathrm{trim}} = 0.2$ are discarded from the $R = 1$ jet if their p_T constitutes less than 5% of the parent jet p_T ($f_{\mathrm{cut}} = 0.05$). Large-R jets are required to fulfill the requirements $p_T > 200$ GeV, $|\eta| < 2.0$, and $m_{\mathrm{jet}} > 40$ GeV, where m_{jet} is given by

$$m_{\mathrm{jet}} = \sqrt{\left(\sum_j E_j\right)^2 - \left(\sum_j p_j\right)^2} \tag{4.10}$$

where the energy and momentum are summed over all jet constitutes. Large-R jets are

Feature	Criteria
η Coverage	$\lvert\eta\rvert < 2.0$
Clustering algorithm	anti-k_T $R = 1$
Grooming algorithm	Trimming $R_{\text{trim}} = 0.2$ $f_{\text{cut}} = 0.05$
Mass	$m_{\text{jet}} > 40$ GeV
Momentum	$p_T > 200$ GeV
Top tagging	80% Working Point (DNN contained)
Input constituent	LCTopo

Table 4.5: Definitions of large-R jets used in this analysis.

also required to achieve a score above a certain threshold in the DNN-based top tagging algorithm described in section 3.2.6.5. These requirements are summarized in table 4.5.

4.3.2 Small-R Jets

$R = 0.4$ jets are clustered using the same anti-k_T algorithm as large-R jets, but have different selection criteria to match their expected origin; these jets are constructed using three-dimensional topological energy clusters described in sections 3.2.3 and 3.2.6.2. Small-R jets are required to fulfill the requirements $p_T > 25$ GeV and $|\eta| < 2.5$; they are subject to a "loose" working point to supply jet cleaning at a high efficiency [67]. A JVT > 0.50 cut is applied if the jet $p_T < 0.60$ GeV and $|\eta| < 2.4$ to reduce pileup effects. These requirements are summarized in table 4.6.

4.3.3 Electrons

Electron candidates are reconstructed from topological energy clusters in the electromagnetic calorimeter as described in section 3.2.4; they are associated with good quality particle tracks from the inner detector within $|\eta| < 1.37$ or $1.52 < |\eta| < 2.47$, excluding the transition region

Feature	Criteria
η Coverage	$\lvert\eta\rvert < 2.5$
Clustering algorithm	anti-k_T $R = 0.4$
Pileup mitigation	JVT > 0.50 for $p_T < 60$ GeV, $\lvert\eta\rvert < 2.4$
Overlap removal	Electron-In-Jet Subtraction $\Delta R(\mu, \text{jet}) > \min\left(0.4, 0.04 + 10\text{ GeV}/p_T^{\mu}\right)$
Momentum	$p_T > 25$ GeV
Jet cleaning	Loose
Input constituent	EM Particle Flow

Table 4.6: Definitions of small-R jets used in this analysis.

Feature	Criteria
η Coverage	$\lvert\eta\rvert < 1.37$ || $1.52 < \lvert\eta\rvert < 2.47$
Momentum	$p_T > 25$ GeV
Track-to-Vertex Association	$\lvert d_0^{\text{BL}}/\sigma_{d_0}\rvert < 5.0$ $\lvert z_0 \sin\theta\rvert < 0.5$ mm
Identification	(MediumLH) TightLH
Isolation	(No isolation) $p_T^{\text{varcone20}}/p_T^e < 0.06$

Table 4.7: (Loose) Tight Definitions of electrons used in this analysis.

between the barrel and endcap calorimeter. Several requirements are imposed on electron candidates to ensure that they are associated with a primary vertex, such as the impact parameter significance criteria $|d_0^{\text{BL}}/\sigma_{d_0}| < 5.0$ and the longitudinal impact parameter requirement $|z_0 \sin\theta| < 0.5$ mm. After that, electron candidates are required to pass a "tight" likelihood-based identification test with efficiency ranging from 67% at $E_T = 25$ GeV to 99% at $E_T = 100$ GeV, where $E_T = E_{\text{cluster}}/\cosh\eta_{\text{track}}$. A "TightTrackOnly" isolation requirement using the $p_T^{\text{varcone20}}$ variable as described in 3.2.4 such that $p_T^{\text{varcone20}}/p_T^e < 0.06$. These requirements are summarized in table 4.7; "loose" selection criteria are used here for QCD background estimation.

Feature	Criteria
η Coverage	$\lvert\eta\rvert < 2.5$
Momentum	$p_T > 25$ GeV
Track-to-Vertex Association	$\lvert d_0^{\mathrm{BL}}/\sigma_{d_0}\rvert < 3.0$ $\lvert z_0 \sin\theta\rvert < 0.5$ mm
Identification	(LooseLH) MediumLH
Isolation	(No isolation) $p_T^{\mathrm{varcone20}}/p_T^{\mu} < 0.06$

Table 4.8: (Loose) Tight Definitions of muons used in this analysis.

4.3.4 Muons

Muon candidates are reconstructed from muon tracks as described in section 3.2.5; they are reconstructed using both ID and MS tracks within $|\eta| < 2.5$. Several requirements are imposed on muon candidates to ensure that they are associated with a primary vertex, such as the impact parameter significance criteria $|d_0^{\mathrm{BL}}/\sigma_{d_0}| < 3.0$ and the longitudinal impact parameter requirement $|z_0 \sin\theta| < 0.5$ mm. Candidates must also meet the "medium" likelihood-based identification criteria, which supplies a $\sim 99\%$ efficiency for muons with $p_T = 100$ GeV. A "TightTrackOnly" isolation requirement using the $p_T^{\mathrm{varcone20}}$ variable as described in 3.2.5 such that $p_T^{\mathrm{varcone20}}/p_T^{\mu} < 0.06$. These requirements are summarized in table 4.8; "loose" selection criteria are used here for QCD background estimation.

4.3.5 Overlap Removal

Procedures for reducing overlaps between various physical objects in an event are known as Overlap Removal (OR). These strategies are used to avoid detector responses being counted twice after being used by multiple algorithms to reconstruct different physics objects. In this search OR is important for removing overlapping detector responses of leptons and jets in the boosted topology where jets and leptons are less likely to be angularly well separated. Because muons are reconstructed from the ID and MS tracks, whereas jets are rebuilt from

ID tracks and calorimeter clusters, overlap is primarily a concern when the lepton in an event is an electron. Thus, even if a muon and jet are separated such that $\Delta R(\mu, \text{jet}) < 0.4$, it is possible to reconstruct both reliably. In events with an electron close to a jet it is standard in ATLAS to require that $\Delta R(e, \text{jet}) > 0.4$; this scheme was used in the last search in this final state [61]. However, in this analysis signal events are expected to have a close electron and jet which are both products of a leptonic top decay, so reliably removing the electron and jet overlap for small $\Delta R(e, \text{jet})$ is important. We expect that events with a hypothetical, TeV-scale Z' will produce a significant number of high-p_T electrons for which $\Delta R(e, b) < 0.4$ compared to the main $t\bar{t}$ background, as seen in figure 4.1. For SM $t\bar{t}$, which is the largest background, $\Delta R(e, b) > 0.4$ for the vast majority of e+jets events. Additionally, figure 4.2 shows that we expect a significant number of these signal electrons in the region $\Delta R(e, b) < 0.4$ to have high p_T. To resolve this problem we test two methods:

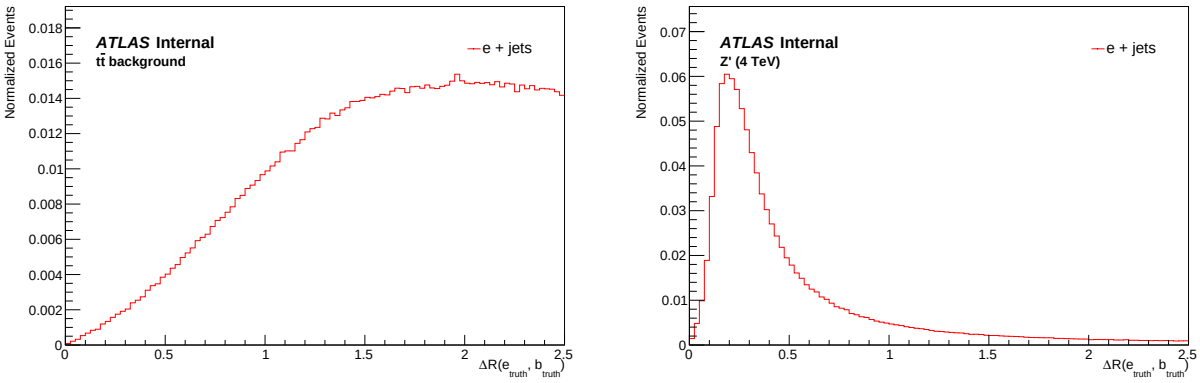

(a) SM $t\bar{t}$ (b) Z' (4 TeV)

Figure 4.1: Truth angular separation ΔR between the electron and b-quark in e+jets events at parton level for the (a) SM $t\bar{t}$ background and (b) a 4 TeV $Z' \to t\bar{t}$ signal.

- Sliding Window – The electron hit is removed if the condition $\Delta R(e, \text{jet}) < \min(0.4, 0.04 + 10 \text{ GeV}/p_T^e)$ is met.

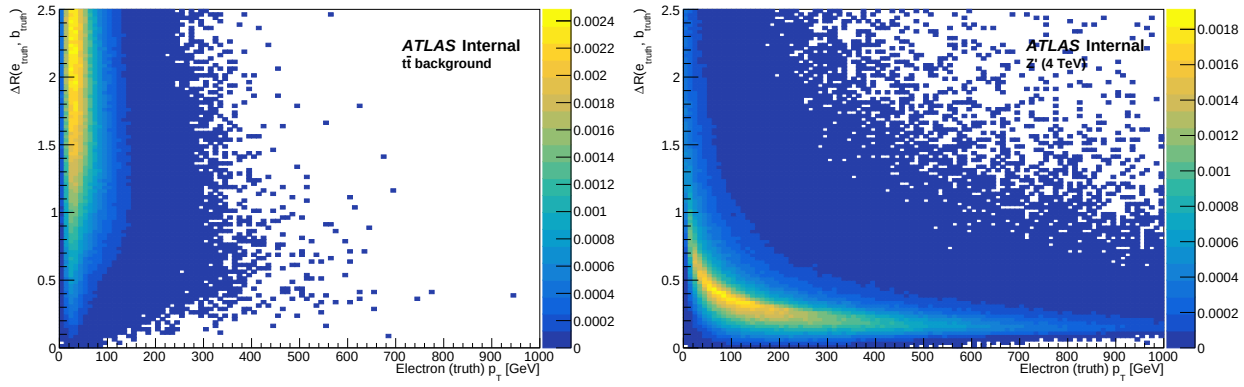

(a) SM $t\bar{t}$ (b) Z' (4 TeV)

Figure 4.2: Truth angular separation ΔR between the electron and b-quark in e+jets events at parton level as a function of truth electron p_T for the (a) SM $t\bar{t}$ background and (b) a 4 TeV $Z' \to t\bar{t}$ signal.

jet p_T range [GeV]	30-100	100-200	200-400	400-600	600-800	800-1200	1200-1600	1600-2000	> 2000
Δp_T cut [GeV]	30	70	90	120	130	230	700	1250	1350

Table 4.9: p_T dependent cuts for deciding whether to recalculate $\Delta R(e, e\text{-subtracted jet})$.

- Electron-In-Jet-Subtraction – A series of steps is taken to attempt to independently reconstruct the electron and the jet, described in section 4.3.6.

4.3.6 Electron-In-Jet-Subtraction

Electron-in-jet-subtraction (EiJS) is a two-step procedure for attempting to reliably reconstruct an electron and jet which have a high degree of calorimeter overlap. The procedure is as follows:

If there is a small-R jets satisfying $\Delta R(e, \text{jet}) < 0.4$, the electron 4-momentum is subtracted from the jet; the new jet is referred to as an "e-subtracted jet". A p_T-dependent threshold defined in table 4.9 is used to check if the e-subtracted jet has enough p_T to still be considered a well-defined jet.

- If $p_T < p_{T,\text{cut}}$, we assume the jet is constituted of electron clusters and is thus fake, in

which case it is removed from the events' jets and the momentum is considered fully part of the electron's.

- If $p_T > p_{T,\text{cut}}$, the $\Delta R(e, e\text{-subtracted jet})$ is calculated and one of the following steps is applied:
  - If $\Delta R(e, e\text{-subtracted jet}) > 0.2$ – Keep both the electron and e-subtracted jet. Use the e-subtracted jet as the actual jet.
  - If $\Delta R(e, e\text{-subtracted jet}) < 0.2$ – We assume the electron is from a B-hadron decay; the electron is removed from the event and its p_T is added to the e-subtracted jet p_T.

4.4 Event Selection

This analysis studies final states with both high and low momentum top quarks. For low momentum top quark decay ($p_T^t < 300$ GeV), three reconstructed small-R ($R = 0.4$) jets are expected from a hadronic top decay, and the lepton and jet associated with leptonic top quark decay are expected to be well-separated with little overlap; this topology is referred to as *resolved*. In high momentum top quark decay, jets produced in the hadronic top decay merge to form a single large-R ($R = 1.0$) jet, and significant overlap between the lepton and jet emerging from the leptonic top quark decay is expected; this topology is referred to as *boosted*.

A common selection is shared between these two categories and includes event quality cuts, trigger requirements, and cuts involving the leptonic W-decay products. All events are required to have exactly one reconstructed lepton with $p_T^\ell > 30$ GeV and associated

Year	Lepton	Trigger
2015	e	HLT_e24_lhmedium_L1EM20VH or HLT_e60_lhmedium or LT_e120_lhloose
	μ	HLT_mu20_iloose_L1MU15 or HLT_mu50
2016–2018	e	HLT_e26_lhtight_nod0_ivarloose or HLT_e60_lhmedium_nod0 or HLT_e140_lhloose_nod0
	μ	HLT_mu26_ivarmedium or HLT_mu50

Table 4.10: High-level lepton triggers.

$E_T^{\text{miss}} > 20$ GeV corresponding to a neutrino to suppress QCD and non-$t\bar{t}$ events. In addition, a combined criteria of E_T^{miss} and W-boson transverse mass $E_T^{\text{miss}} + m_{\text{T},W} > 60$ GeV is required to further improve background rejection, where the transverse W mass is given by

$$m_{\text{T},W} = \sqrt{2p_T^{\ell} E_T^{\text{miss}} \left(1 - \cos\Delta\phi(\ell, E_T^{\text{miss}})\right)}. \tag{4.11}$$

At least one selected jet must be b-tagged to further decrease QCD background events predominantly constituted of light-flavored jets. A DNN (DL1) algorithm with 77% efficiency is used for b-tagging as described in section 3.2.6.6.

All ATLAS detector subsystems must be operational during LHC collisions in order for data events to be used in this analysis. To accomplish this, a set of "Good Run List" (GRL) of luminosity blocks are kept that include periods suitable for analysis. Data used in this analysis comes only from periods included in the GRL. Additionally, events must fire one of several p_T dependent, offline "high level" triggers (HLT) with names given in table 4.10. Each name given represents the object the trigger applies to (e or μ), as well as a p_T threshold in GeV.

4.4.1 Boosted Selection

Top quarks with large momenta, and thus high collimation, are used in the boosted final state category. In the calorimeter, these events' hadronically decaying top quarks each form

a single large-R jet, hence the boosted region in this study requires the existence of at least one top tagged large-R jet using a DNN top tagger with a 80% efficient working point. The leptonically decaying top is expected to be angularly close to a high-p_T jet originating from a b-quark, and thus a requirement of $\Delta R(\ell, \text{small-}R \text{ jet}) < 2.0$ is imposed and the jet that satisfies the requirement is called "selected". If multiple jets satisfy this angular criteria, the highest p_T jet among them is categorized as selected. We also expect that the leptonically and hadronically decaying top quarks will be maximally angularly separated due to momentum conservation and the high invariant mass associated with boosted events, and so we require $\Delta R(\ell, \text{large-}R \text{ jet}) > 1.0$ and $\Delta R_{\text{min}}(\text{jet}, \text{large-}R \text{ jet}) > 1.0$.

4.4.2 Resolved Selection

Top quarks with small momenta are expected to have decay products which are angularly well separated and are used in the resolved final state category. In these events we expect at least four small-R jets, where one jet is associated with a b-quark from the hadronically decaying top, one jet is associated with a b-quark from the leptonically decaying top, and two jets are associated with light quarks from the hadronic W decay. At least one of these jets must be b-tagged. It is sometimes the case that initial and final state radiation can result in more than four jets.

4.4.3 Event Categories

Selected events in both boosted and resolved channels are split into two regions dependent on the selected lepton flavor (e or μ). In addition, each of these resulting four regions is further categorized based on the association of a b-tagged jet to the hadronic and leptonic

Feature	Criteria
	Common
GRL	Data events in the Good Run List (2015-2018)
Single lepton trigger	e and μ triggers (table 4.10)
Single lepton	$== 1$ e or μ ($p_T^\ell > 30$ GeV)
MET	$E_T^{\text{miss}} > 20$ GeV
MET + W transverse mass	$E_T^{\text{miss}} + m_{\text{T},W} > 60$ GeV
b-tagging	≥ 1 b-tagged jet
	Boosted
Large-R jet	≥ 1 large-R jet ($p_T > 300$ GeV)
Top tagging	≥ 1 top tagged large-R jet (DNN, 80% WP)
Selected jet	≥ 1 jet satisfying $\Delta R(\ell, \text{small-}R \text{ jet}) < 2.0$
Separated tops	$\Delta R(\ell, \text{large-}R \text{ jet}) > 1.0$ and $\Delta R_{\text{min}}(\text{jet}, \text{large-}R \text{ jet}) > 1.0$
	Resolved
Small-R jets	≥ 4 jets ($p_T > 30$ GeV)

Table 4.11: Summary of event selection criteria.

top candidates. The four b-tagging categories are:

- Category 0 – No b-tagged jet matching either top candidate.
- Category 1 – Only the leptonic top candidate has a matching b-tagged jet.
- Category 2 – Only the hadronic top candidate has a matching b-tagged jet.
- Category 3 – Each of the hadronic and leptonic top candidates has a b-tagged jet.

The relative background compositions in each of the 16 signal regions can be seen in figure 4.3.

4.5 Event Reconstruction

Our primary task in this analysis is to accurately reconstruct the invariant mass of the $t\bar{t}$ system, $m_{t\bar{t}}$. To accomplish this we must accurately reconstruct the 4-momentum of each top quark and combine them as

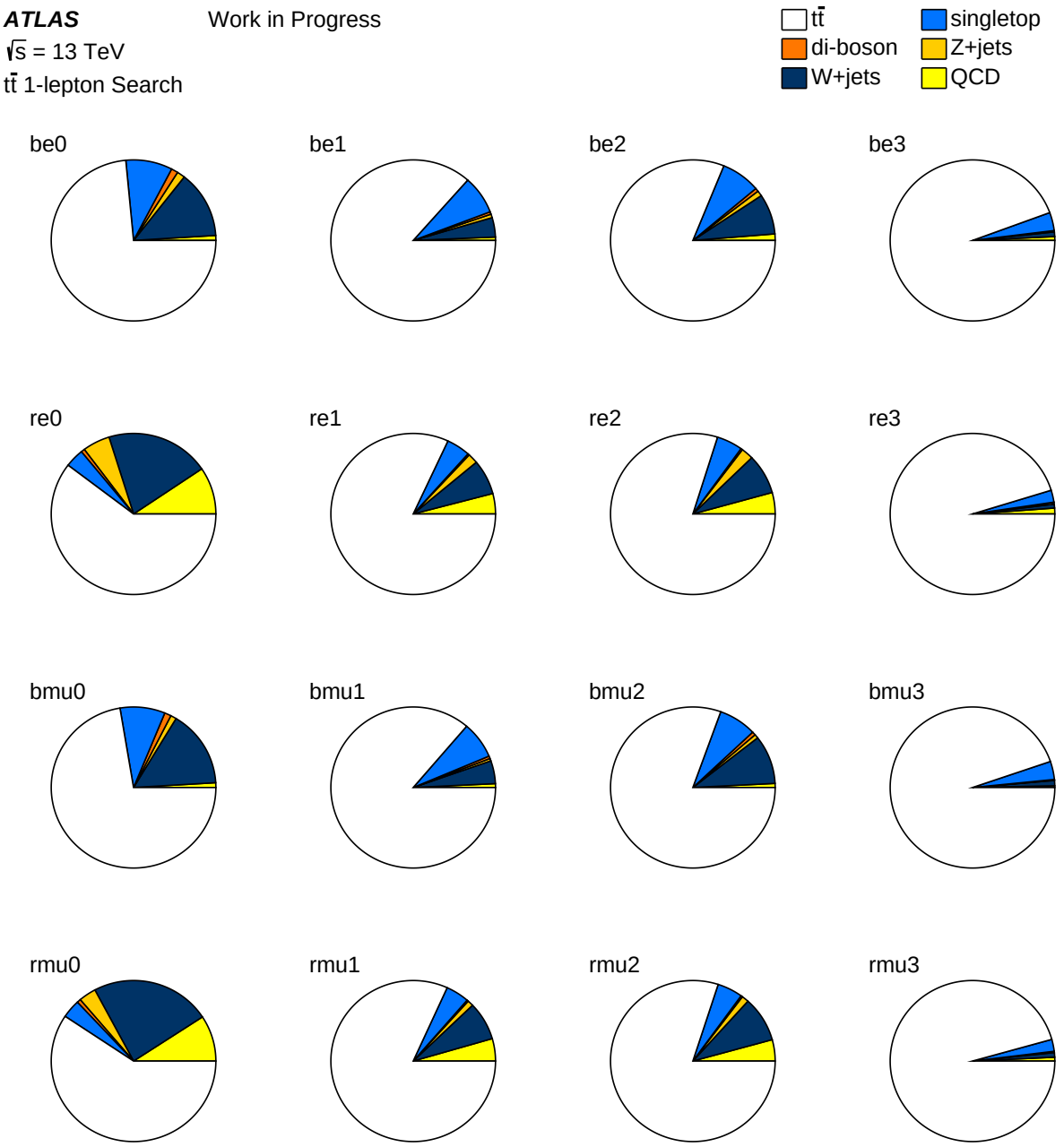

Figure 4.3: Background compositions in the 16 b-tagging categories. "b" and "r" refer to the boosted and resolved regions, respectively.

$$m_{t\bar{t}}^2 = \left(p^{t,\mathrm{lep}} + p^{t,\mathrm{had}}\right)^2. \tag{4.12}$$

4.5.1 Boosted Reconstruction

Because the top tagged large-R jet is chosen as the hadronically decaying top quark, reconstruction in the boosted region is extremely simple. The leptonically decaying top is reconstructing using its expected decay products, which are the lepton, highest p_T selected small-R jet, and neutrino calculated from E_T^{miss}.

4.5.2 Resolved Reconstruction

The resolved region involves a reconstruction process that is more complex. Since events passing the resolved selection have four or more jets it can be difficult to properly associate each jet with either the leptonically or hadronically decaying tops. To help find the best combination of jets forming the hadronic and leptonic top candidates, a χ^2 is defined using the 4-momentum of the selected physics objects as

$$\chi^2 = \left[\frac{m_{jj} - m_{W_h}}{\sigma_{W_h}}\right]^2 + \left[\frac{m_{jjb} - m_{jj} - m_{t_h - W_h}}{\sigma_{t_h - W_h}}\right]^2 + \left[\frac{m_{b\ell\nu} - m_{t_\ell}}{\sigma_{t_\ell}}\right]^2 + \left[\frac{\left(p_{T,jjb} - p_{T,b\ell\nu}\right) - \left(p_{T,t_h} - p_{T,t_\ell}\right)}{\sigma_{p_{T,t_h} - p_{T,t_\ell}}}\right]^2, \quad (4.13)$$

where the first term is a constraint on the dijet mass from the hadronically decaying W-boson, the second term is a constraint on the hadronic top quark mass (m_{jj} and m_{jjb} are highly correlated, so the contribution of the hadronically decaying W-boson is subtracted to decouple the first term from the second term), the third term is a constraint on the leptonically decaying top quark mass, and the last term enforces equality between the momentum of the hadronically and leptonically decaying top quarks. The expected values

Parameter	Value [GeV]
m_{W_h}	82.4
σ_{W_h}	9.6
$m_{t_h - W_h}$	89
$\sigma_{t_h - W_h}$	15.7
m_{t_ℓ}	166
σ_{t_ℓ}	17.5
$p_{T,t_h} - p_{T,t_\ell}$	0.43
$\sigma_{p_{T,t_h} - p_{T,t_\ell}}$	46.1

Table 4.12: Summary of parameters used in the resolved χ^2 reconstruction algorithm.

and their uncertainties are obtained from simulated Z' events by matching the reconstructed objects to truth partons subject to the constraint $\log_{10}\chi^2 < 0.9$ to remove badly reconstructed events. This χ^2 is evaluated for each possible permutation of selected jets and W-boson candidates satisfying a b-tagging requirement. In the absence of this criteria, the analysis accepts events with a reconstructed invariant mass much larger than its true value. This results in a significant increase in the number of events at high $m_{t\bar{t}}$, as the expected background is steeply falling in $m_{t\bar{t}}$.

4.5.3 Neutrino Reconstruction

Because neutrinos do not interact with the ATLAS detector, we must assume the missing transverse energy, E_T^{miss}, is the same as the transverse momentum of the neutrino p_T^ν. While we have information about the azimuthal component of the MET, we must reconstruct the z-component of the neutrino's momentum using the conservation relation

$$\mathbf{p}_W = \mathbf{p}_\ell + \mathbf{p}_\nu \tag{4.14}$$

where $\mathbf{p}_\ell$ is the lepton 4-momentum, $\mathbf{p}_W$ is the W-boson 4-momentum, and $\mathbf{p}_\nu$ is the neutrino 4-momentum. Assuming the mass of the neutrino is exactly zero ($\mathbf{p}_\nu^2 = 0$), and that the lepton and neutrino are from an on-shell W-boson decay, we can infer that

$$m_W^2 = (\mathbf{p}_\ell + \mathbf{p}_\nu)^2 = m_\ell^2 + 2\mathbf{p}_\ell \cdot \mathbf{p}_\nu. \tag{4.15}$$

Solving this equation for the neutrino momentum's z-component, $p_{z,\nu}$ gives

$$p_{z,\nu}^{\pm} = \frac{\mu p_{z,\ell}}{p_{T,\ell}} \pm \sqrt{\frac{\mu^2 p_{z,\ell}^2}{p_{T,\ell}^4} - \frac{E_\ell^2 p_{T,\nu}^2 - \mu^2}{p_{T,\ell}^2}}, \tag{4.16}$$

where $\mu = m_W^2 + p_{T,\ell} p_{T,\nu} \cos\Delta\phi(\ell, \nu)$. If no real solution is found, it is assumed that complex solutions arise because of a measurement error of E_T^{miss}. To solve this, E_T^{miss} is minimally rotated in the azimuthal plane to arrive at one real solution. If multiple real solutions exist, the smaller solution is used.

4.5.4 Reconstruction Effects

Signals in this analysis are heavy particles decaying semi-leptonically into $t\bar{t}$ pairs. The mass distributions of resonances can be approximated by the relativistic Breit-Wigner distribution, which can be modified via theoretical and experimental effects before being observed in data taken by the ATLAS detector. This analysis searches over a range of masses, from 400 GeV to 5 TeV. Collisions between partons of sufficient energy to create the types of high mass resonances this analysis searches for at 13 TeV are expected to be produced primarily on-shell. However, highly boosted top quarks tend to radiate, which results in an invariant mass of the observed $t\bar{t}$ pair which is below that of the parent particle, as seen in the Z'_{TC2} MC events shown in figure 4.4 and the $t\bar{t}$ events shown in figure 4.5.

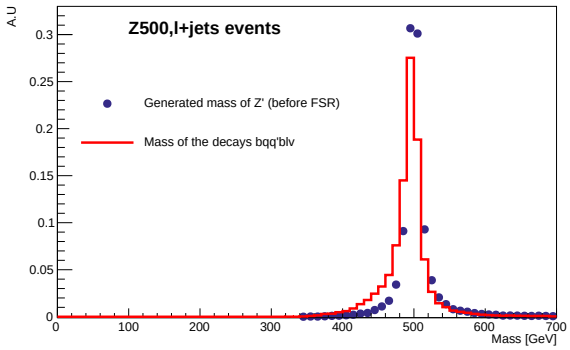

(a) 500 GeV

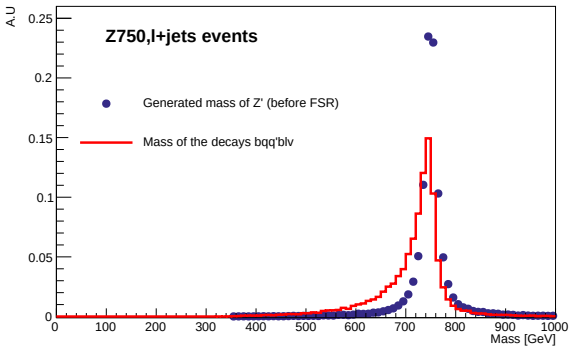

(b) 750 GeV

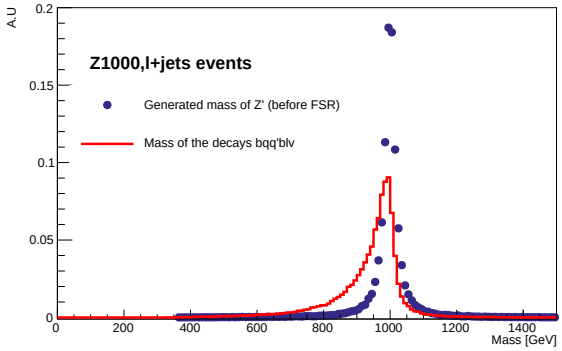

(c) 1000 GeV

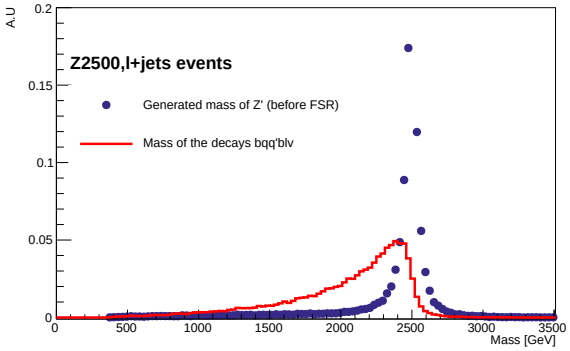

(d) 2500 GeV

Figure 4.4: Mass of the Z' signal (blue) and the reconstructed $t\bar{t}$ decays (red).

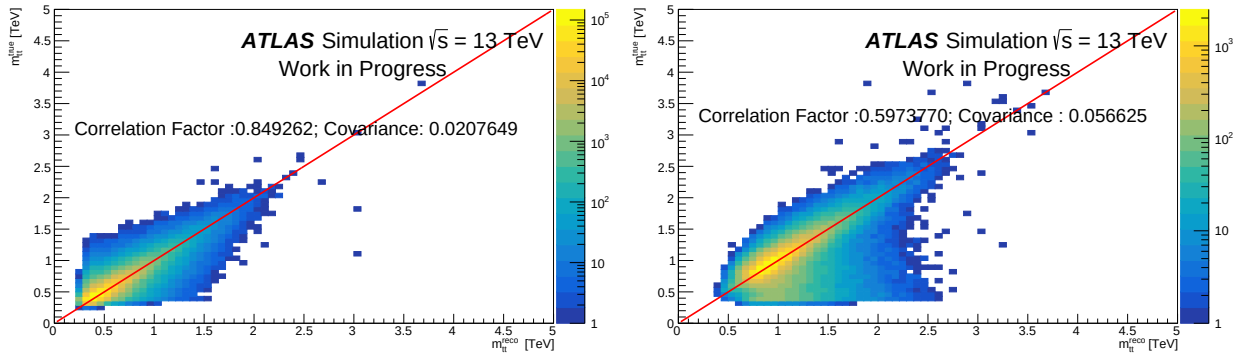

(a) Resolved e

(b) Boosted e

(c) Resolved μ

(d) Boosted μ

Figure 4.5: Reconstructed v. true $m_{t\bar{t}}$ for SM $t\bar{t}$ production using χ^2 methods for the resolved channels.

4.5.5 Signal Acceptance × Efficiency

Signal shapes for several representative mass points in the four signal regions are shown as a function of $m_{t\bar{t}}$ in figure 4.6, where the area under each curve is normalized to unity. Acceptance refers to the number of pre-selected events divided by the total number of generated events; efficiency refers to the number of events elected using the final criteria divided by the number of pre-selected events. Thus, acceptance × efficiency in this context refers to events passing the full analysis selection criteria. Here, pre-selection events are those events passing basic kinematic criteria (cuts on object p_T, η, etc.), but before tagging selection criteria. Figure 4.7 shows the acceptance × efficiency as a function of $m_{t\bar{t}}$ for the Z'_{TC2} signal across a number of pole masses for each of the signal selection regions; the total, combined boosted, and combined resolved acceptance × efficiency is shown in figure 4.8. All b-tagging categories are used here except category 0. The electron channel has a lower acceptance at high $m_{t\bar{t}}$ than the muon channel, which is the result of the looser requirement on $\Delta R(\mu, \mathrm{jet})$ as compared with the electron channel.

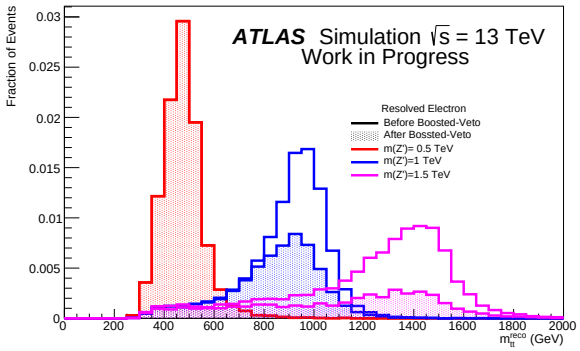

(a) Resolved e

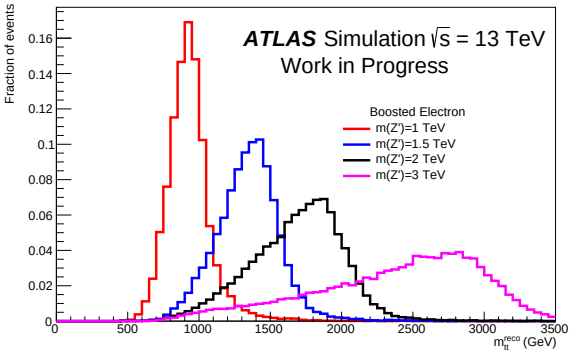

(b) Boosted e

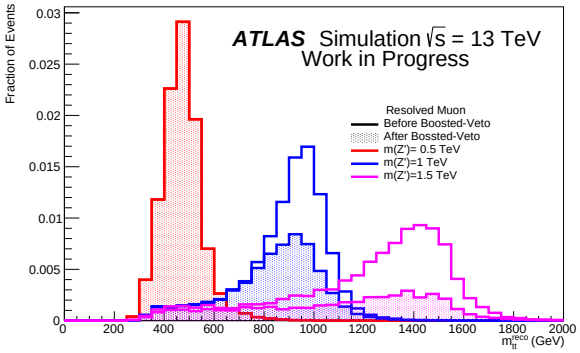

(c) Resolved μ

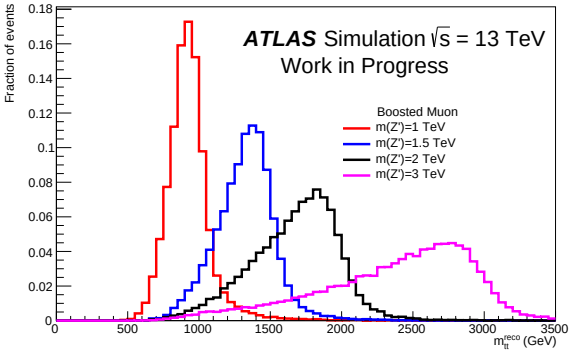

(d) Boosted μ

Figure 4.6: Reconstructed $m_{t\bar{t}}$ for selections on Z'_{TC2} signals.

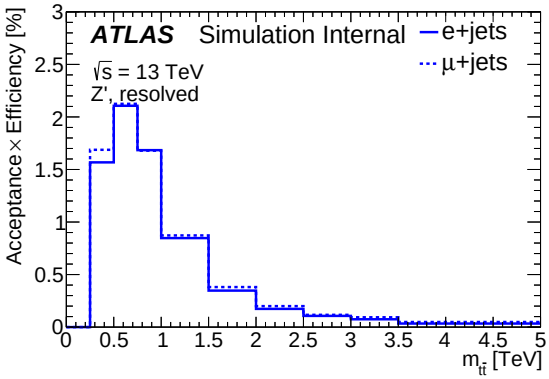

(a) Resolved

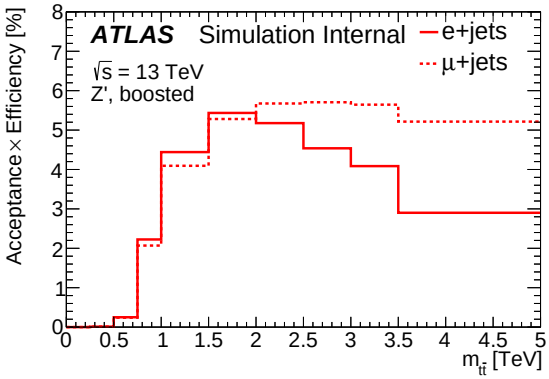

(b) Boosted

Figure 4.7: Acceptance times efficiency for Z'_{TC2} for the resolved and boosted topologies.

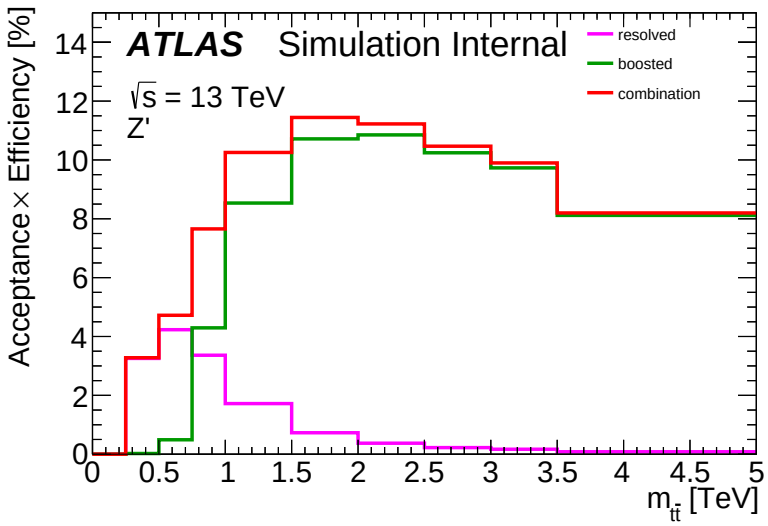

Figure 4.8: Acceptance times efficiency for Z'_{TC2} for the combined, resolved, and boosted topologies.

4.6 Studies

This chapter will describe the primary optimization studies I undertook in addition to the general work of the analysis.

4.6.1 Overlap Removal

This section will show the advantage of using an implementation of the Electron-in-Jet-Subtraction (EiJS) algorithm over the sliding window method in the electron channels of the analysis, each described in section 4.3.5. Figure 4.9 shows that EiJS allows the reconstruction of additional events for low $\Delta R_{\text{min}}(\ell, \text{jet})$. Figure 4.10 shows that, especially in the boosted channel, significance relative to the primary $t\bar{t}$ background increases with respect to increasing Z' signal mass. This increased significance in only the boosted electron channel is expected for EiJS over the sliding window algorithm, as EiJS only applies to events where the reconstructed lepton is identified as an electron and primarily applies to boosted events where for a larger fraction of events $\Delta R_{\text{min}}(\ell, \text{jet}) < 0.4$. These results also match our expectation that the significance will increase with increasing Z' pole mass, which implies a larger top p_T and thus a higher likelihood of small $\Delta R_{\text{min}}(\ell, \text{jet})$ (see figure 4.2). Given that the previous analysis placed upper limits at 95% confidence on the Z'_{TC2} production to a lepton-plus-jets decay topology above 3 TeV [61], we choose to optimize our sensitivity to the high mass region and so use the EiJS method for overlap removal.

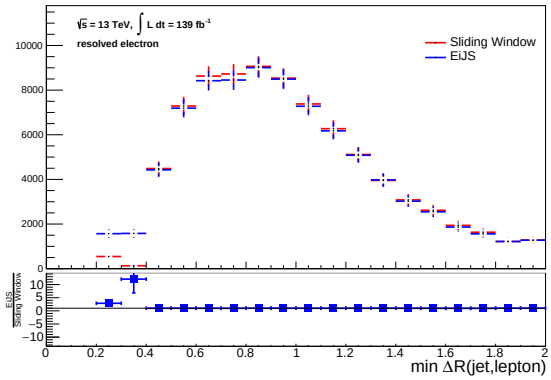

(a) 1 TeV Z'

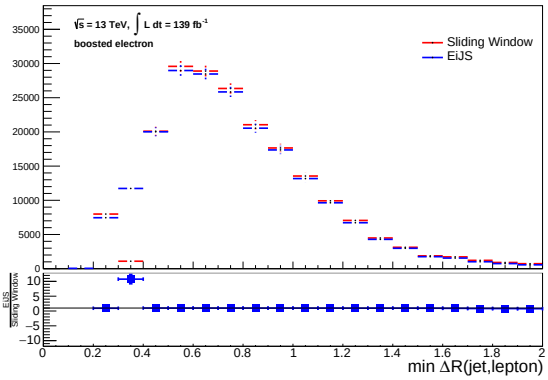

(b) 1 TeV Z'

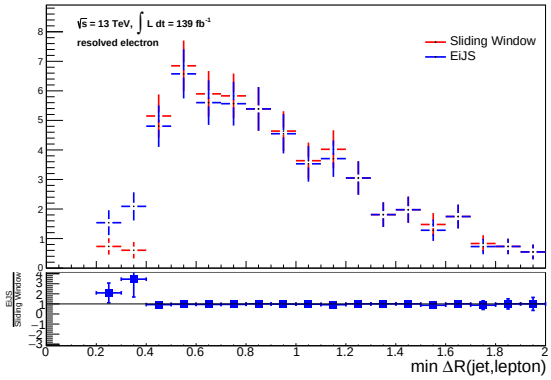

(c) 3 TeV Z'

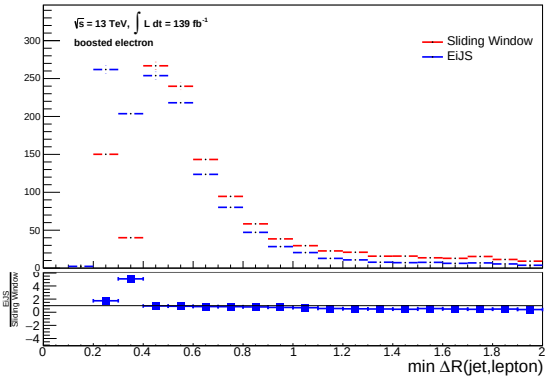

(d) 3 TeV Z'

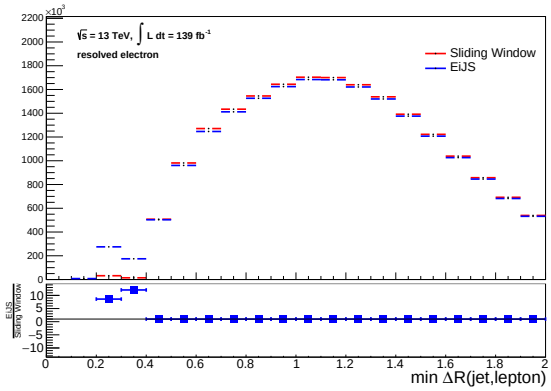

(e) $t\bar{t}$ background

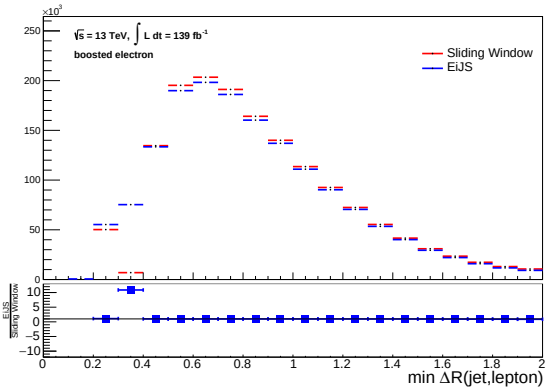

(f) $t\bar{t}$ background

Figure 4.9: $\Delta R_{\text{min}}(\ell, \text{jet})$ in the resolved electron (left) and boosted electron (right) channels for the 1 TeV Z' (top), 3 TeV Z' (middle), and $t\bar{t}$ background (bottom) samples.

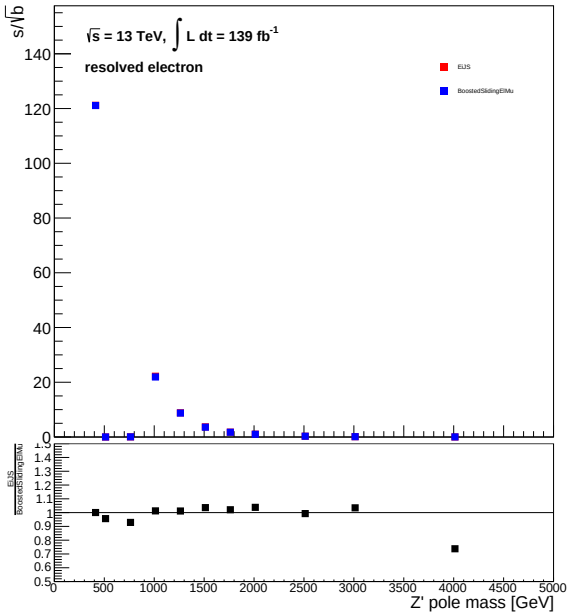

(a) Resolved electron

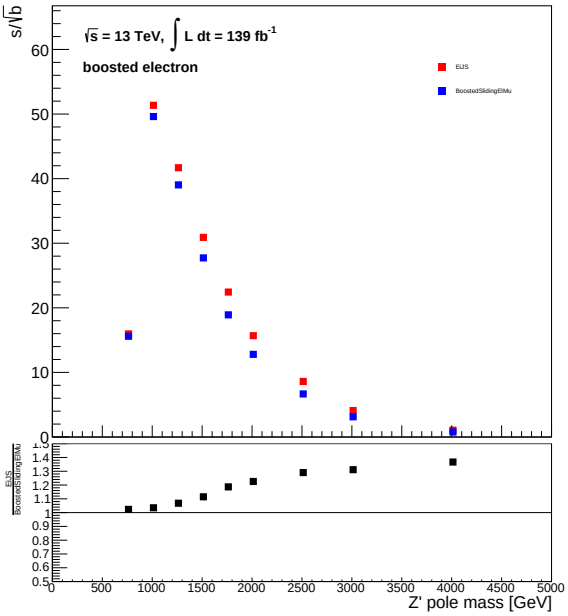

(b) Boosted electron

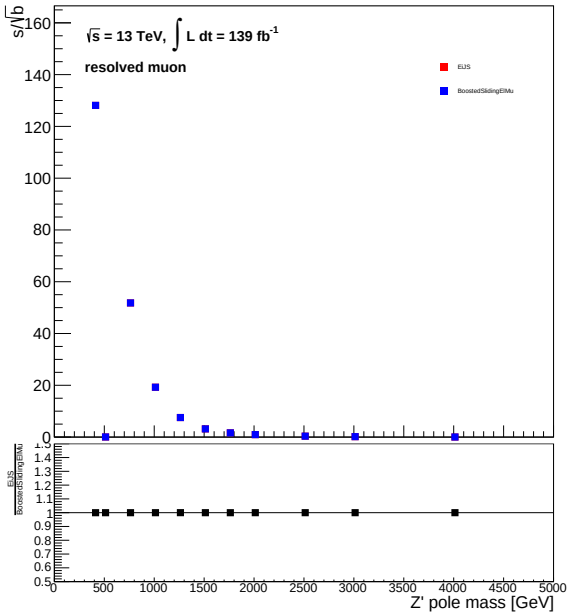

(c) Resolved muon

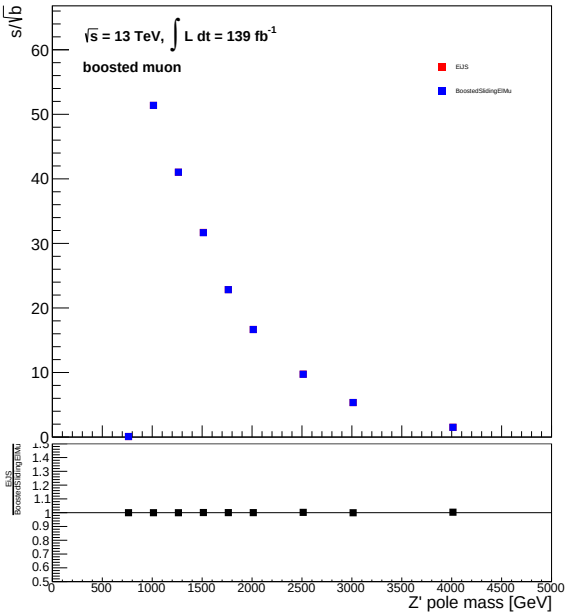

(d) Boosted muon

Figure 4.10: Significances in the analysis channels with respect to Z' pole mass for the study comparing the sliding window overlap removal in blue compared to the electron-in-jet subtraction method in red.

4.6.2 NNLO $t\bar{t}$ Reweighting

The top quark plays an important role in BSM searches as both a dominant background and signal signature. In both the ATLAS experiment and CMS Collaboration, the most notable feature in top physics analyses is the disagreement between MC and data of the top quark p_T spectrum shown in figure 4.11. Previous studies have seen improved agreement between data and prediction in $t\bar{t}$ events, particularly for the top quark p_T distribution, when comparing with NNLO calculations [68]. More recently, top quark pair differential calculations at NNLO QCD accuracy and including EW corrections have become available [69]. Hence, a small improvement to the modeling is incorporated by correcting all $t\bar{t}$ samples to match their top quark p_T distribution to that predicted at NNLO in QCD and NLO in EW accuracy. An uncertainty in the modeling of each distribution (top p_T, $m_{t\bar{t}}$, and $t\bar{t}$ p_T) is evaluated by taking the full difference between applying and not applying the correction. This idea can be extended to multiple variables via reweighting iteratively between variables to a terminating condition via the so-called "iterative recursive" method. This section shows several comparison tests for reweighting procedures which apply fixed-order corrections at NNLO to significantly improve the agreement between MC and data. The $t\bar{t}$ p_T theoretical distribution at NNLO QCD is produced using the MATRIX software [70]. The top p_T and $m_{t\bar{t}}$ are calculated at NNLO QCD + NLO EW from reference [69].

A recursive correction is applied to the $t\bar{t}$ background to approximately scale its cross-section to NNLO. Recursive options were explored for two-dimensional (using top p_T, $t\bar{t}$ mass) and three-dimensional (using top p_T, $t\bar{t}$ mass, and $t\bar{t}$ p_T) inputs. The recursive reweighting scheme iteratively scales kinematic distributions by diminishing factors, such that compared to reweighting only a single variable the process minimizes disagreement in

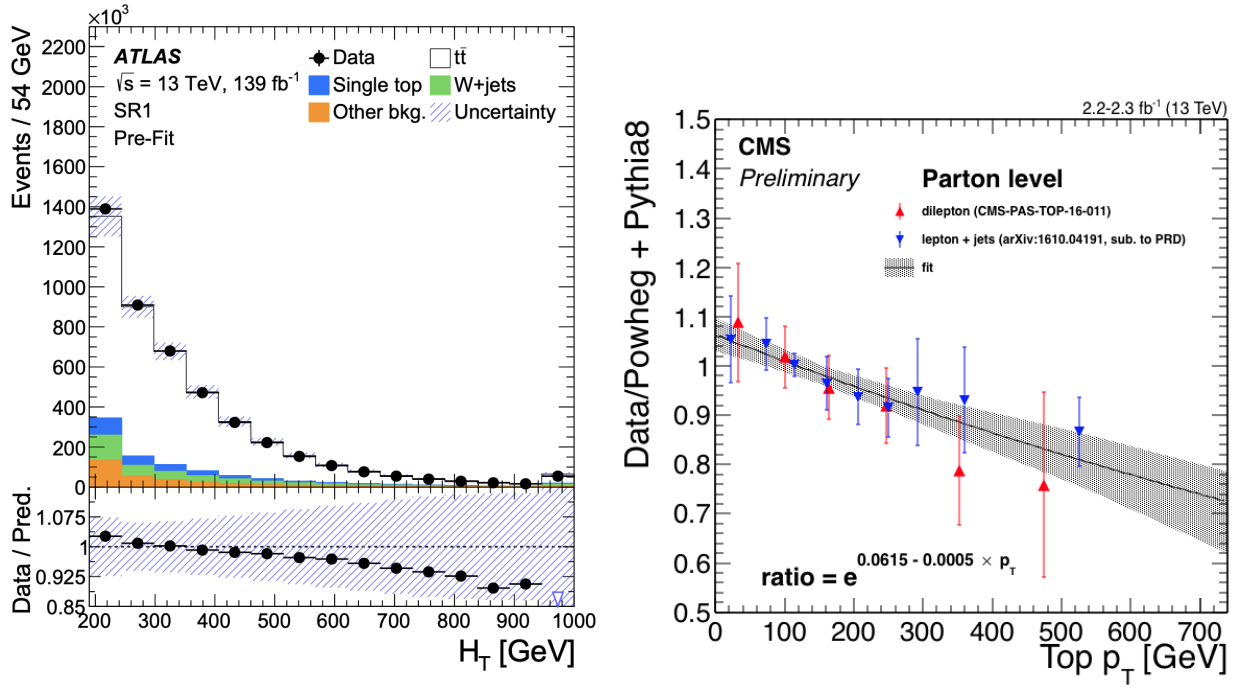

(a) (b)

Figure 4.11: (a) A clear slope due to top quark p_T mismodeling in the distribution of the scalar sum of jet p_T [71]. (b) Ratio between 13 TeV data and Powheg simulation for differential top quark pair cross-section as a function of top quark p_T [72].

other variables. Resolved kinematics for each reweighting scheme are shown in figure 4.12, and boosted kinematics are shown in figure 4.13.

These results indicate that the largest kinematic changes are in the large-R jet p_T distribution, with maximum changes of $\sim 20\%$. These changes are not seen in the discriminating variable, $m_{t\bar{t}}$, which is also reweighted according to the same scheme. Given the small magnitude of these changes, especially in $m_{t\bar{t}}$, the analysis uses the 2D scheme for $t\bar{t}$ NNLO reweighting.

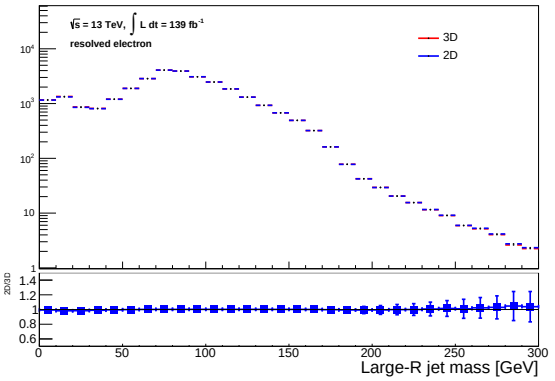

(a)

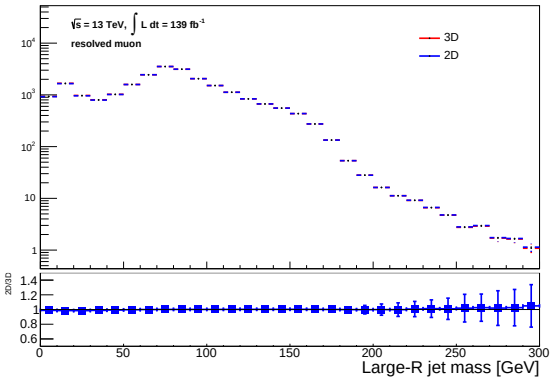

(b)

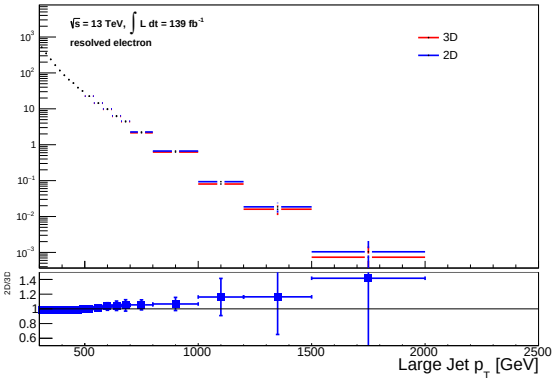

(c)

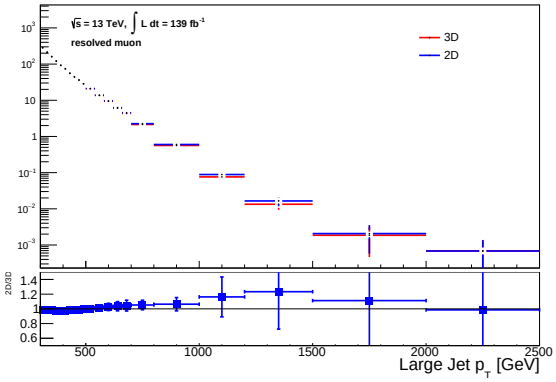

(d)

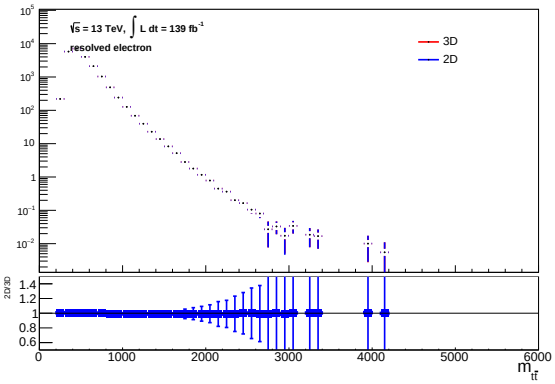

(e)

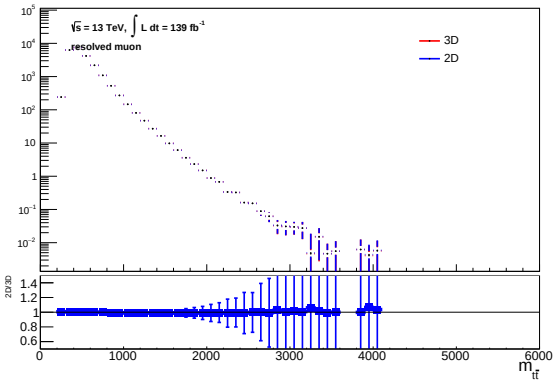

(f)

Figure 4.12: Kinematic distributions for the resolved electron (left) and resolved muon (right) channels in the $t\bar{t}$ background for 2D and 3D $t\bar{t}$ recursive NNLO reweighting.

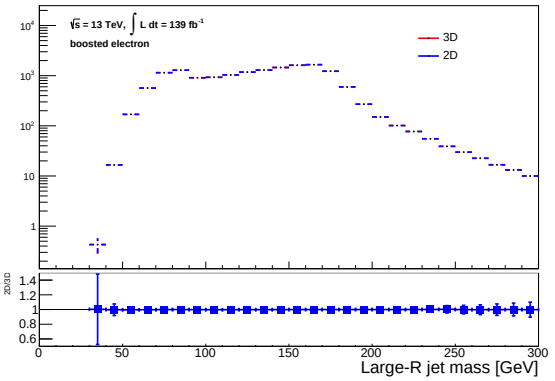

(a)

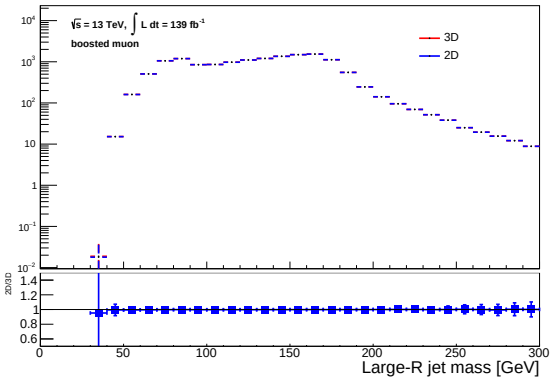

(b)

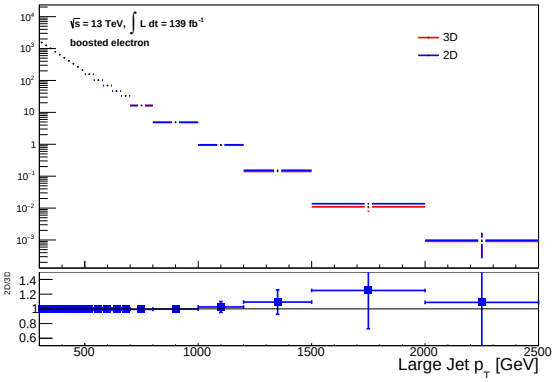

(c)

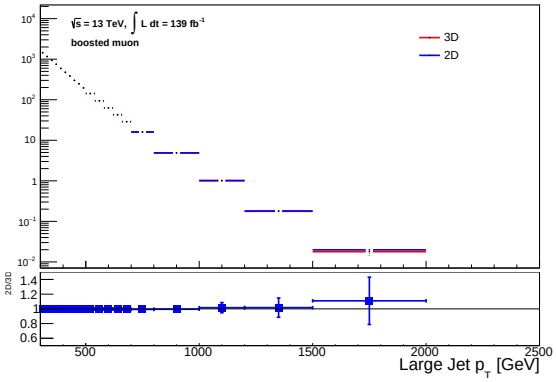

(d)

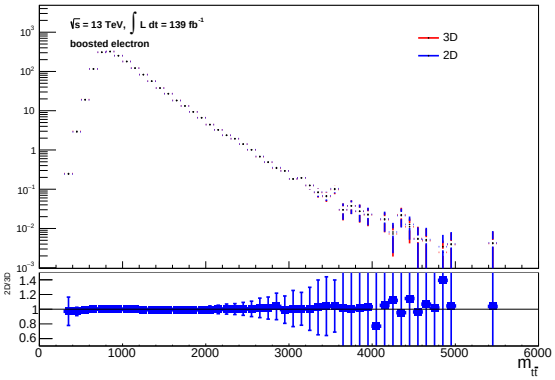

(e)

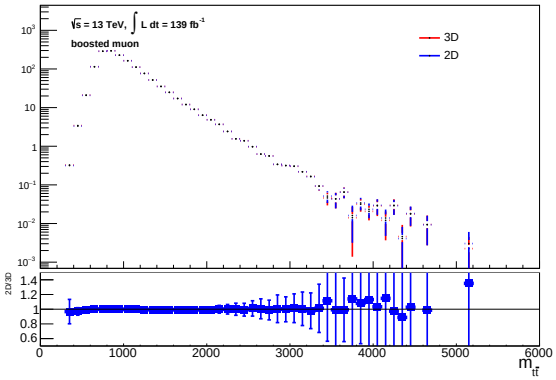

(f)

Figure 4.13: Kinematic distributions for the boosted electron (left) and boosted muon (right) channels in the $t\bar{t}$ background for 2D and 3D $t\bar{t}$ recursive NNLO reweighting.

4.6.3 Particle Flow Jets

The particle flow algorithm (described in section 3.2.3.3) defines anti-k_T small-R jets by matching each track from the inner detector to a topological cluster (described in section 3.2.3.2) in the calorimeter. The ATLAS collaboration as a whole has begun to move from using a topological cluster jet definition to a particle flow jet definition, and so it is necessary to assess whether this switch would have a detrimental effect on the sensitivity of the analysis. To evaluate any potential resolution differences, $(m_{t\bar{t}}^{\text{reco}} - m_{t\bar{t}}^{\text{truth}})/m_{t\bar{t}}^{\text{truth}}$ was calculated and the standard deviation of the results were binned into distributions with respect to $m_{t\bar{t}}^{\text{truth}}$. Figure 4.14 shows standard deviations of the relative difference between reconstructed and true $m_{t\bar{t}}$ for the particle flow and topological cluster jet definitions. There is no discernible difference between the resolutions of particle flow and topological cluster-only algorithms except for some possible resolution improvements for the particle flow jet definitions below 1 TeV. That being the case, this analysis uses the particle flow jet definition.

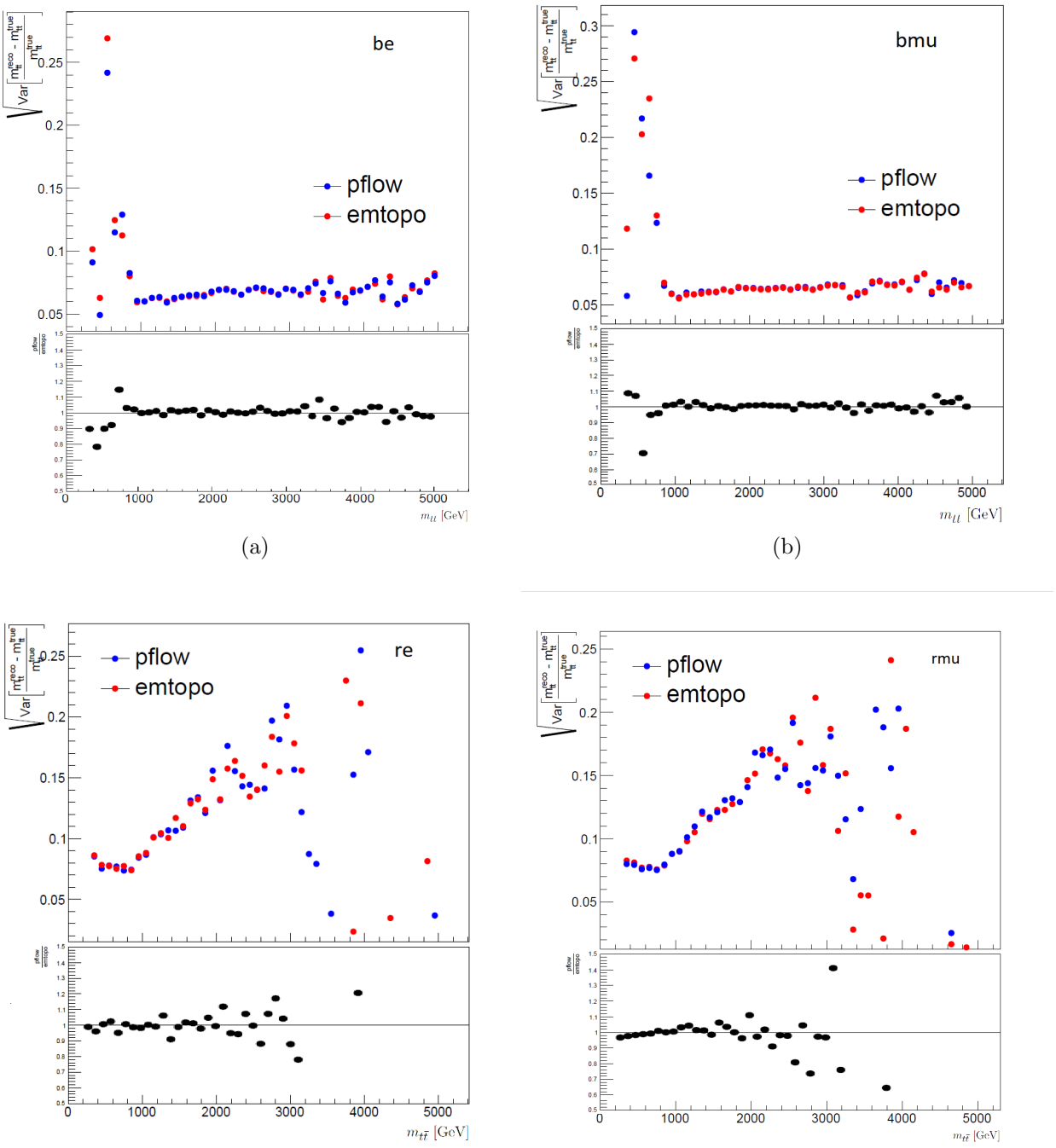

(a) (b) (c) (d)

Figure 4.14: Comparisons of resolutions for the particle flow and topological clustering algorithms.

4.7 Systematic Uncertainties

The sources of uncertainty in this analysis are broadly split into the categories of experimental and theoretical, with the experimental uncertainties being derived by the various ATLAS combined performance groups and provided in the form of recommendations, while the theoretical uncertainties are analysis dependent and are related to the dominant backgrounds and higher order calculations used. Important experimental contributions to the uncertainty arise from the jet energy scale and resolution for both the resolved and boosted signal regions, with the top tagging uncertainties having the largest overall experimental effect in the boosted channels. b-tagging uncertainties had a moderate impact and uncertainties associated with leptons generally have little impact and are taken as given by the recommendations of the ATLAS flavor tagging group [73]. For the theoretical contributions, the generator variations for $t\bar{t}$ background production are important, especially at high $m_{t\bar{t}}$. The dominant theory uncertainties arise from the h_{damp} parameter variation and renormalization scale variation. The data-driven multijet uncertainty contribution is assessed conservatively with a 50% uniform uncertainty but was found to have negligible effect on all signal regions except boosted electron at high $m_{t\bar{t}}$.

4.7.1 Integrated Luminosity and Pileup

The uncertainty in the integrated luminosity for the combined 2015-2018 data is 1.7%, as determined by the LUCID-2 detector [74]; this is applied as a constant shift to each simulated sub-background and signal. Each MC sample is reweighted to scale to the same pileup profile as the data for each period. The uncertainty associated with this reweighting is extracted from the official tool, and was found to have an effect of less than 1% on the total background

	Boosted e (%)		Boosted μ (%)		Resolved e (%)		Resolved μ (%)	
	bkg	4 TeV Z'	bkg	4 TeV Z'	bkg	4 TeV Z'	bkg	4 TeV Z'
Small-R jets	5.2	<1.0	4.9	<1.0	31	6.0	32	4.8
Large-R jets	4.4	<1.0	4.5	<1.0	-	-	-	-
E_T^{miss}	1.6	<1.0	1.0	<1.0	2.7	<1.0	2.1	<1.0
e	3.0	2.5	-	-	2.1	<1.0	-	-
μ	-	-	2.0	1.3	-	-	3.0	<1.0
Multijet	<1.0	-	<1.0	-	<1.0	-	<1.0	-
b-tagging	4.7	1.0	4.7	2.4	5.8	0.5	5.8	<1.0
top tagging	6.7	8.1	5.8	11	-	-	-	-
$t\bar{t}$ HS	2.9	-	2.6	-	<1.0	-	<1.0	-
$t\bar{t}$ had	1.9	-	2.5	-	2.6	-	2.2	-
$t\bar{t}$ h_{damp}	13	-	13	-	1.4	-	< 1.0	-
$t\bar{t}$ PDF	1.7	-	1.7	-	6.0	-	6.4	-
$t\bar{t}$ μ_{R} Scale	9.0	-	9.2	-	10	-	11	-
$t\bar{t}$ μ_{F} Scale	3.6	-	3.7	-	2.0	-	2.1	-
$t\bar{t}$ ISR (α_S)	<1.0	-	<1.0	-	<1.0	-	< 1.0	-
$t\bar{t}$ FSR (α_S)	3.5	-	3.2	-	2.1	-	2.0	-
$t\bar{t}$ NNLO	<1.0	-	<1.0	-	<1.0	-	<1.0	-

Table 4.13: Summary of the pre-fit impact of uncertainties on the expected number of total background events and 4 TeV Z'_{TC2} signal events in the four signal regions. The maximum of the $\pm 1\sigma$ variations are shown.

estimate in any signal region throughout the $m_{t\bar{t}}$ distribution, and up to 5% in the boosted channels at high $m_{t\bar{t}}$.

4.7.2 Electrons and Muons

Lepton efficiency scale factors[1], along with lepton energy scale and resolution, are associated with many sources of experimental uncertainty. The scale factor uncertainties for both electrons and muons consist of trigger, reconstruction, isolation, and identification sources. Given that the lepton has a relatively small impact on the $m_{t\bar{t}}$ in this search, these uncertainties have a small effect on the total background estimate. In the boosted channels these uncertainties are negligible, while in the resolved channels the most important are the reconstruction efficiency uncertainty and the electron identification efficiency uncertainty, each of which are at most 2%.

4.7.3 Small-R and Large-R Jets

The official ATLAS recommendations provide jet energy scale uncertainties for small-R jets which are broken down into more than 100 baseline nuisance parameters. To reduce the complexity of the inputs to the statistics tool, a set with only 30 components is used as uncorrelated nuisance parameters. Large-R jets are assigned systematic uncertainties using schemes that impact their energy scale (24 nuisance parameters), resolution (12 nuisance parameters), mass resolution (10 nuisance parameters), and scale (18 nuisance parameters). The systematic uncertainties affecting small-R and large-R jets are treated as uncorrelated.

[1] Efficiency scale factors are corrections to the MC based on the slight mismodelling of kinematic distributions. Well defined control regions (usually around the Z peak) are used to measure these scale factors in a p_T and η dependent manner so that they can be used in the signal regions of analyses. Uncertainties on these scale factors depend on both the MC samples being used and the methodology to extract the scale factors.

When added in quadrature, small-R jet uncertainties make up one of the analysis' largest sources of uncertainty, and large-R jet uncertainties have a modest effect of 4 - 10%.

4.7.4 b-Tagging of Particle Flow Jets

The prescription for implementing b-tagging uncertainty recommended by the ATLAS flavor tagging performance group has been followed. The eigenvector breakdown approach has been tested to avoid over-profiling. There are 9, 4, and 4 eigenvectors for the b-, c-, and light flavor quarks, respectively. There are also 2 eigenvectors specifically for the extrapolation of the scale factor into high-p_T regimes which are correlated across flavors. These uncertainties, when considered added in quadrature, have a modest effect of 4 - 10%.

4.7.5 Top Tagging

The prescription for implementing top tagging uncertainty recommended by the ATLAS flavor tagging performance group has been followed. This uncertainty has 18 components which are treated as independent nuisance parameters. Top tagging affects the boosted channels and has an effect of 5 - 15%, typically increasing with increasing $m_{t\bar{t}}$. This is the largest source of experimental uncertainty in the search.

4.7.6 E_T^{miss}

E_T^{miss} is altered consistently when one of its inputs (small-R jets or leptons) is modified by a systematic uncertainty. Additionally, 3 systematic uncertainties associated with the soft track term are used as recommended by the ATLAS JetEtMiss group. Each of these sources generally has an effect of less than 3% throughout the $m_{t\bar{t}}$ distribution of each signal region.

4.7.7 $t\bar{t}$ Cross-Section and Modeling

The uncertainty in the $t\bar{t}$ cross-section is one of the main sources of theoretical systematic uncertainty in the analysis, and is estimated at $^{+5.6\%}_{-6.1\%}$. The correction for electroweak loops has uncertainty of 10%. As the $t\bar{t}$ processes is the dominant background in the analysis, the following uncertainties related to its modeling are considered:

- Matrix Element – Shape comparison between `Powheg` + `Herwig` and `aMC@NLO`Herwig—. The impact on the shape is symmetrized to get a downward variation.
- Parton Showering – Shape comparison between `Powheg` + `Pythia 8` and `Powheg` + `Herwig 7` to determine which best tunes are used for showering (so-called "conservative approach"). The impact on the shape is symmetrized to get a downward variation.
- PDF – 30 eigensets of the `PDF4LHC_nlo_30` in an `aMC@NLO` sample are used and the relative effect in that sample is taken as a systematic uncertainty.
- ISR/FSR – Shape comparison between reweighted versions of the nominal sample and the nominal sample itself. The reweighting enables the analysis to reproduce a change of factorization and renormalization scales, or α_S in the ISR and FSR or of the amount of NLO radiation ($h_{\text{damp}} = 3$).
- NNLO Effects – The impact of the NNLO corrections are evaluated using the predicted differential cross-sections.

4.7.8 Single Top Modeling

The cross-section on the single top production modes are assigned an uncertainty of $\pm 5.3\%$. Additionally, the diagram removal method is compared with the diagram subtraction method

in the Wt channel and the difference is added as an uncertainty in the single top background. The effect of the uncertainty on the modeling of ISR/FSR has been found to be negligible and has not been used in the final fit.

4.8 Kinematic Distributions

This section will show kinematic distributions for data and all backgrounds. Additional kinematics can be found in appendix F.

4.8.1 Resolved Channels

Figure 4.15 shows the p_T distribution of the lepton and selected jet, and the E_T^{miss} distributions, each for the resolved electron and muon final states. Each distribution shows good agreement between data and MC within the uncertainties.

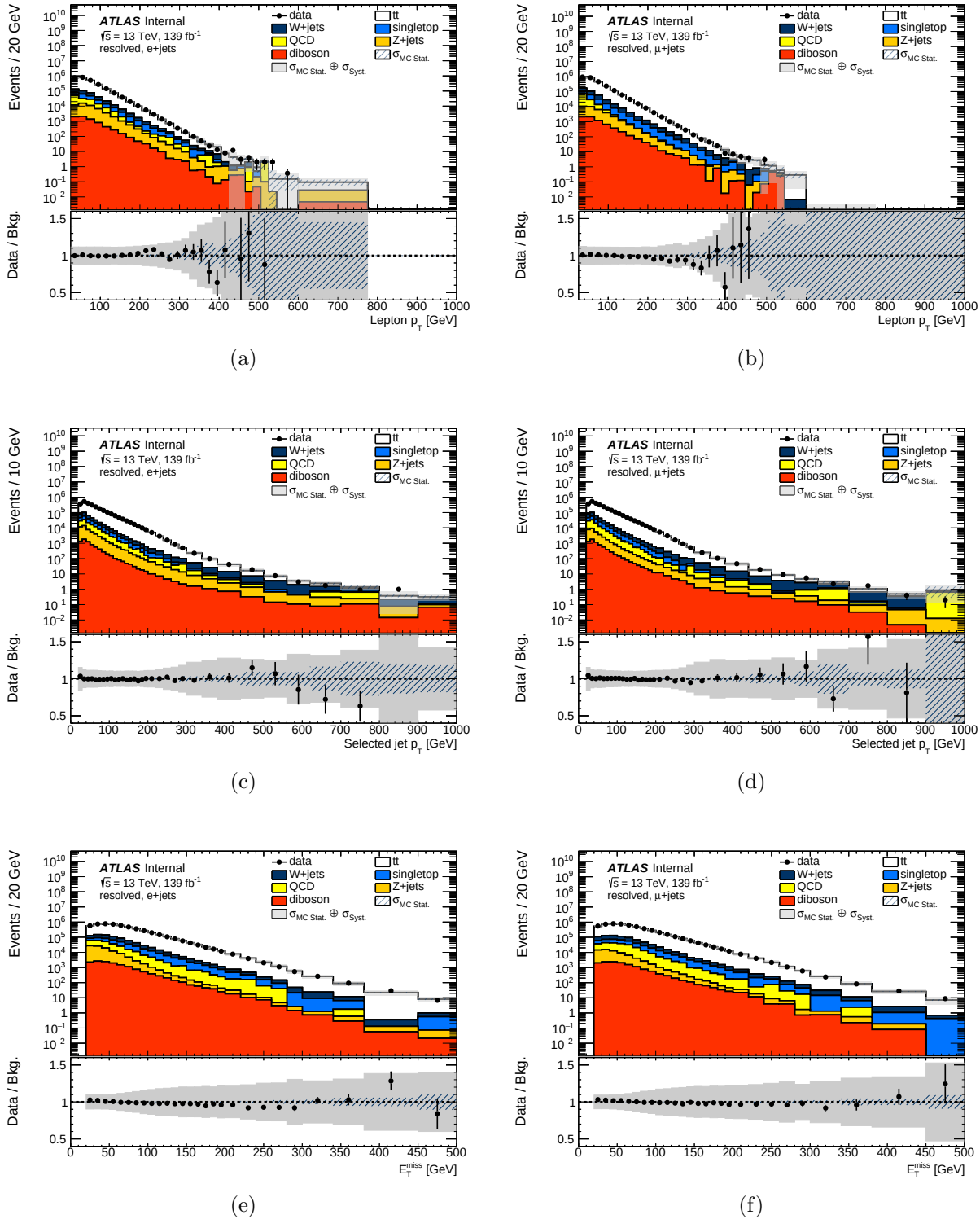

Figure 4.15: Kinematic distributions for the resolved e (left) and resolved μ (right) channels.

4.8.2 Boosted Channels

In figure 4.16, the large-R jet p_T, lepton p_T, and selected jet p_T are shown for the boosted electron and muon channels. Although agreement is within systematic uncertainties, there is a deficit of $\sim$10% of data with respect to MC. This is also seen in the differential $t\bar{t}$ cross-section measurements and is thought to come from the poor modeling of the top p_T spectrum in current generators, which becomes large in searches for high-momentum top quarks.

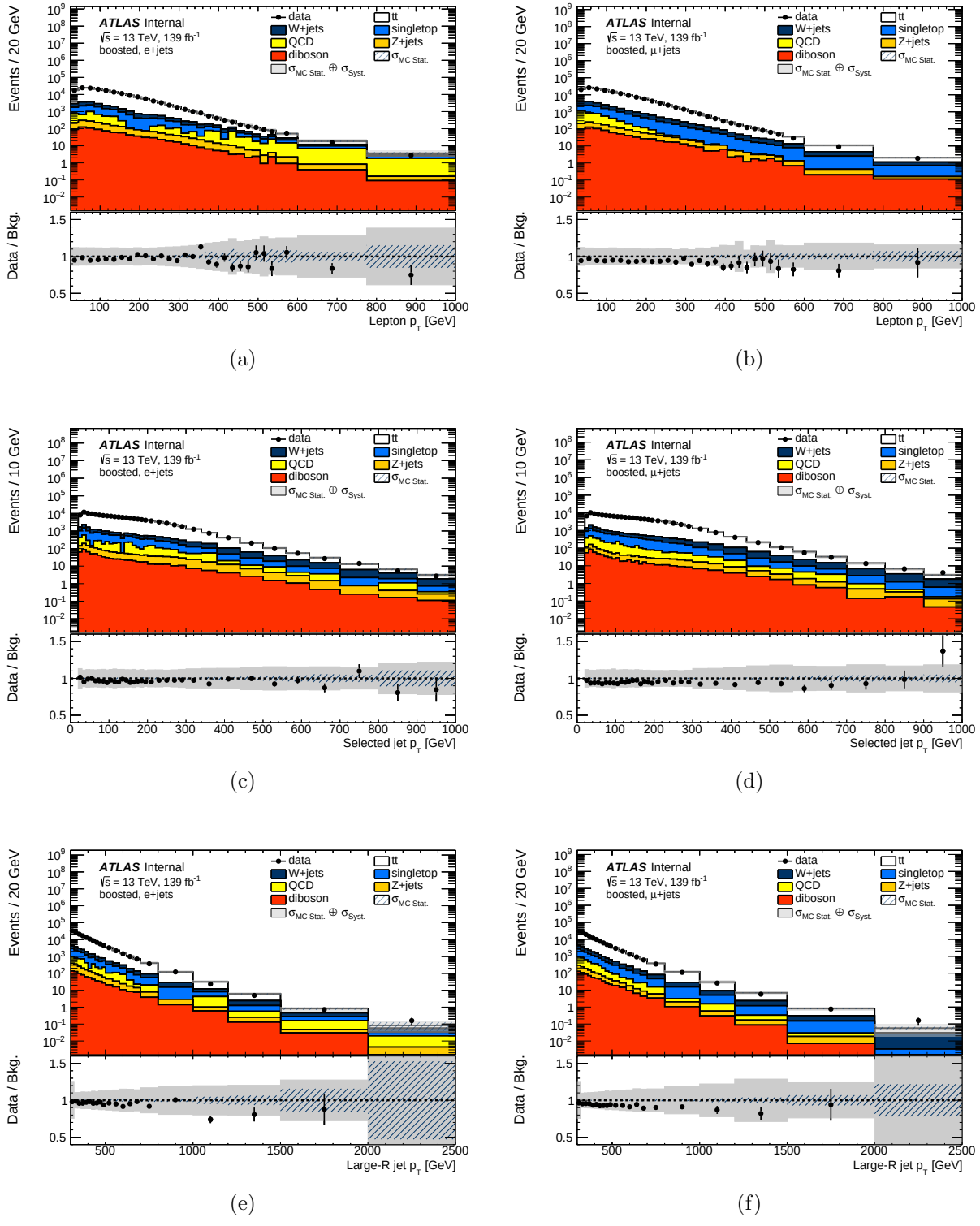

Figure 4.16: Kinematic distributions for the boosted e (left) and boosted μ (right) channels.

4.8.3 $t\bar{t}$ Invariant Mass

The invariant mass of the $t\bar{t}$ system ($m_{t\bar{t}}$) is the main discriminant in this analysis. A Z' signal is expected to appear as a resonance on the falling background spectrum. The observed $m_{t\bar{t}}$ spectra are shown for the four signal regions in figure 4.17.

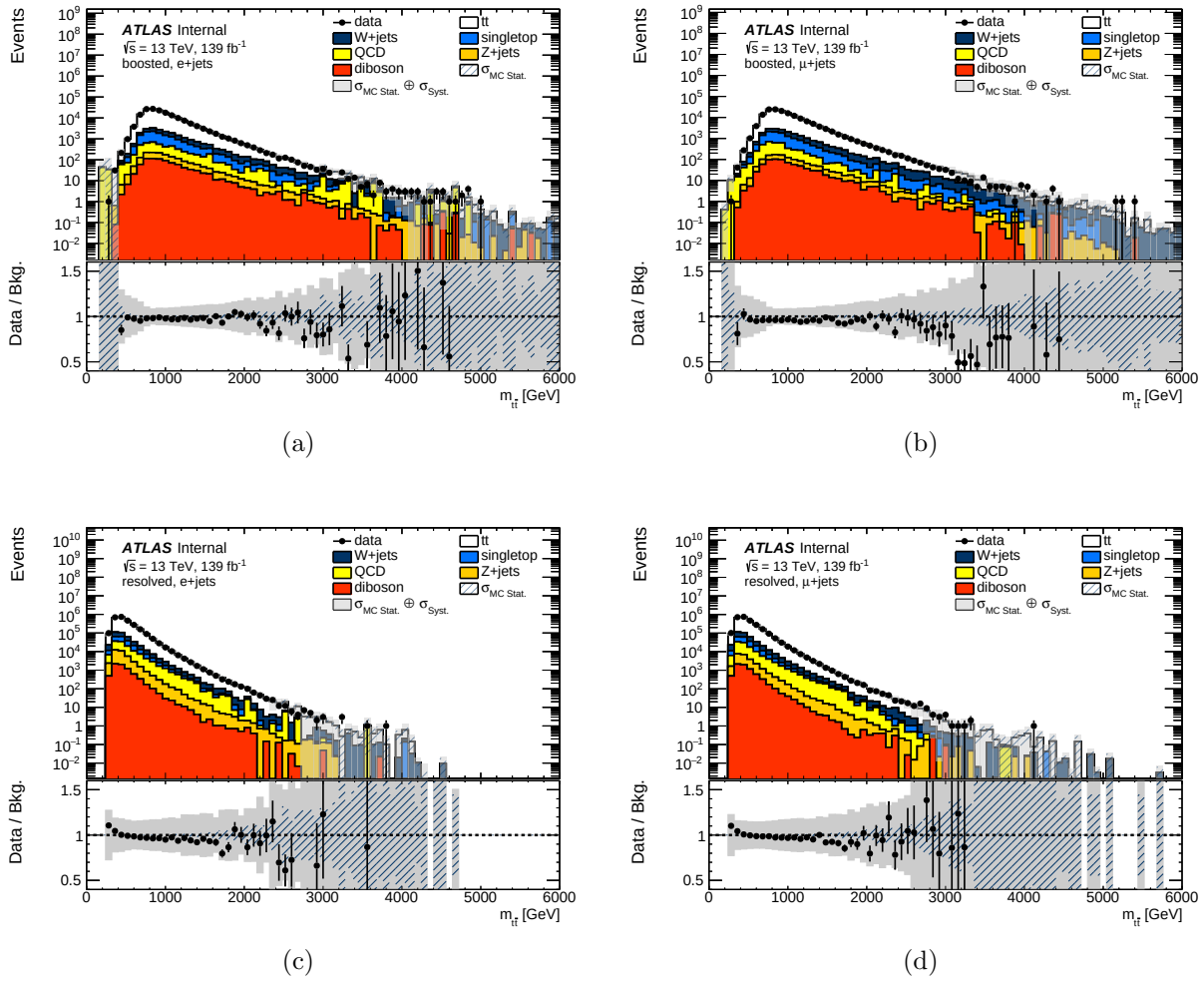

Figure 4.17: Observed $m_{t\bar{t}}$ distributions for the analysis signal regions.

4.9 Statistical Treatment

The statistical interpretation consists of two steps: first a search is performed for various signatures of new physics. Second, in the absence of any deviations from the SM-only hypothesis, upper exclusion limits are set on the cross-section times branching ratio at a 95% confidence level (CL), and theoretical cross-sections are overlayed for those models to extract lower limits on new physics resonance pole mass.

4.9.1 Search Phase

The search phase in this analysis is performed with `BumpHunter` [75], which is a hypothesis testing tool that searches for local data excesses or deficits in the data compared to the expected background in a model-agnostic way. The excess/deficit is allowed to span any invariant mass range from two bins to half of the number of bins in the distribution. This process is performed iteratively, comparing data and expected background in a series of sliding windows of variable size. For each window, a Poisson probability is calculated, and the smallest p-value from the scan is recorded. Systematic uncertainties are taken into account.

For each window i, data count (d_i) and background yield (b_i) defines a Poisson probability $P(d_i, b_i)$

$$P(d_i, b_i) = \begin{cases} \Gamma(d_i, b_i) = \sum_{n=d_i}^{\infty} \frac{b_i^n}{n!} e^{-b_i}, & d_i \geq b_i \\ 1 - \Gamma(d_i + 1, b_i), & d_i < b_i \end{cases}, \tag{4.17}$$

where Γ is the Gamma function. Equation 4.17 defines searching for an excess; inequality signs are reversed when searching for deficits. The smallest Poisson probability of all the

given windows is recorded as $P_i^{\min}$. To include the associated systematic uncertainties, the definition of $P(d_i, b_i)$ is extended to

$$P(d_i, b_i) \to P(d_i, b_i + \lambda_i \theta_i) e^{-\lambda_i^2/2}, \tag{4.18}$$

where θ_i is the total combined uncertainty for the considered window and a value $\lambda_i \in [-8, 8]$ is chosen such that

$$\lambda_i = \underset{\lambda_i}{\operatorname{argmax}} \frac{(b_i + \lambda_i \theta_i)^{d_i}}{d_i!} e^{-(b_i + \lambda_i \theta_i + \lambda_i^2/2)}. \tag{4.19}$$

The `BumpHunter` test statistic t is computed as

$$t = \begin{cases} 0 & d_i \leq b_i \\ -\log P_i^{\min} & d_i > b_i \end{cases}. \tag{4.20}$$

The p-value of the most discrepant bump is found by comparing the test statistic from data with the test statistics found in at least 10,000 pseudo-experiments, where pseudo-data is generated by Poisson fluctuations of the expected background. The p-value is defined as

$$p = \frac{\int_{t_{\text{obs}}}^{\infty} f(t)}{\int_0^{\infty} f(t)} \tag{4.21}$$

where $f(t)$ is the distribution of the test statistic values from the pseudo-data and t_{obs} is the test statistic obtained from data. The p-value represents the probability of observing a signal-like excess at least as significant as the one observed in data given that the background-only hypothesis is true. In the particle physics community, p-values are often converted into a number of standard deviations to denote significance (σ). 3σ is commonly referred to as "evidence" of new physics, while 5σ is the commonly taken standard to claim discovery.

4.9.2 Exclusion Limits

For this search, four distinct signal regions are studied, with resolved and boosted topologies considered separately for the e+jets and μ+jets channels. In the absence of a significant excess in the data compared to background expectations, exclusion limits are set on the cross-section times branching ratio ($\sigma \times \mathcal{B}$) at a 95% CL. The `TRexFitter` tool is used to perform the limit setting procedure, which follows a frequentist approach with a test statistic based on a profile-likelihood ratio [76]. This test statistic ($\mathcal{T}$) is defined as twice the negative logarithm of the ratio of the conditional (fixed-μ) maximum likelihood to the unconditional maximum likelihood, each obtained from a fit to the data as

$$\mathcal{T}(\mu) = -2\ln\frac{\mathcal{L}(\mu, \hat{\hat{\boldsymbol{\Theta}}}(\mu))}{\mathcal{L}(\hat{\mu}, \hat{\boldsymbol{\Theta}}(\hat{\mu}))}, \tag{4.22}$$

where $\boldsymbol{\Theta}(\mu)$ represent the nuisance parameters. The single circumflex indicates the unconditional maximum likelihood estimate of a parameter, while the double circumflex indicates the maximum likelihood estimate assuming a specific value of μ. The fitted signal strength, $\hat{\mu}$, is bounded from below at zero. The likelihood is given by

$$\mathcal{L} = \prod_i P\Big(d_i \Big| s_i(\mu, \boldsymbol{\Theta}) + b_i(\boldsymbol{\Theta})\Big) \prod_k f_k(\Theta_k), \tag{4.23}$$

where d_i, s_i, and b_i are the number of observed data events, total predicted background yields, and expected signal events in bin i, respectively. $\boldsymbol{\Theta}$ is the vector of nuisance parameters, and P is the Poisson distribution defined in equation 4.17.

The effect of a systematic uncertainty k on the binned likelihood is modeled with an associated nuisance parameter, Θ_k, constrained with a corresponding probability density

function $f_k(\Theta_k)$. This means that correlated effects across different channels are modeled by the use of a common nuisance parameter and its corresponding probability function. The $f_k(\Theta_k)$ terms are Poisson distributed for bin-by-bin MC statistical uncertainties and Gaussian distributed for all other terms. Assuming that the test statistic $\mathcal{T}$ follows a χ^2 distribution with one degree of freedom, the variation on the log-likelihood can be used to set a 95% CL on the upper limit of $\sigma \times \mathcal{B}$ and to estimate the impact of the systematic uncertainties on the discovery significance. Nuisance parameters (both systematic and statistical) which have less than a 0.1% effect on the signal or background normalization shape are pruned from the statistical interpretation to improve computing performance with a negligible effect on the result.

Due to some nuisance parameters suffering from statistical fluctuations which could destabilize the fit, the underlying histograms undergo the following smoothing procedure:

1. For each nuisance parameter bin, define $\delta M = \sqrt{\delta S^2 + \delta N^2}$.
2. For each pair of neighboring bins (i, j), define $X_{i,j} = \left| \frac{S_j - N_j}{N_j} - \frac{S_i - N_i}{N_i} \right|$ and $\delta X_{i,j} = \sqrt{\frac{\delta M_j^2}{N_j^2} + \frac{\delta M_i^2}{N_i^2}}$.
3. While there are neighboring bins with $X_{i,j} < \delta X_{i,j}$, merge the bins i and j with the largest $\delta X_{i,j}/X_{i,j}$.

4.10 Results

The post-fit plots derived from the process described in section 4.9.2 for the 1, 2, and 3 b-tagging categories are shown in figures 4.18, 4.19, and 4.20, respectively. Nuisance parameter pull plots, correlation matrices, and systematic ranking plots can be found in appendices D and E. The final search results using `BumpHunter` are shown in figure 4.21 for each of the four signal regions, with the highest local and the global significances given for each signal region in table 4.14. One notable feature in the results is a deficit on the 17^{th} bin of the boosted μ signal region. This deficit has a local significance of 3.9σ, but a global significance of only 2.8σ. Therefore, as no significant deviation from the SM is observed, we proceed to set exclusion limits on the signal models. The observed and expected limits on the Z'_{TC2} $\sigma \times \mathcal{B}$ which are derived from this process are shown in figure 4.22, while those for the G_{KK} are shown in figure 4.23. Table 4.15 shows the lower mass limits for each signal type. These mass limits improve upon previous results [61] based on 36 fb^{-1} of data by 1.2 TeV in the observed limit and 1.1 TeV in the expected limit for the Z'_{TC2} model. For the G_{KK} model, these limits improve upon the previous results by 0.35 TeV in the observed limits and 0.55 TeV in the expected limits.

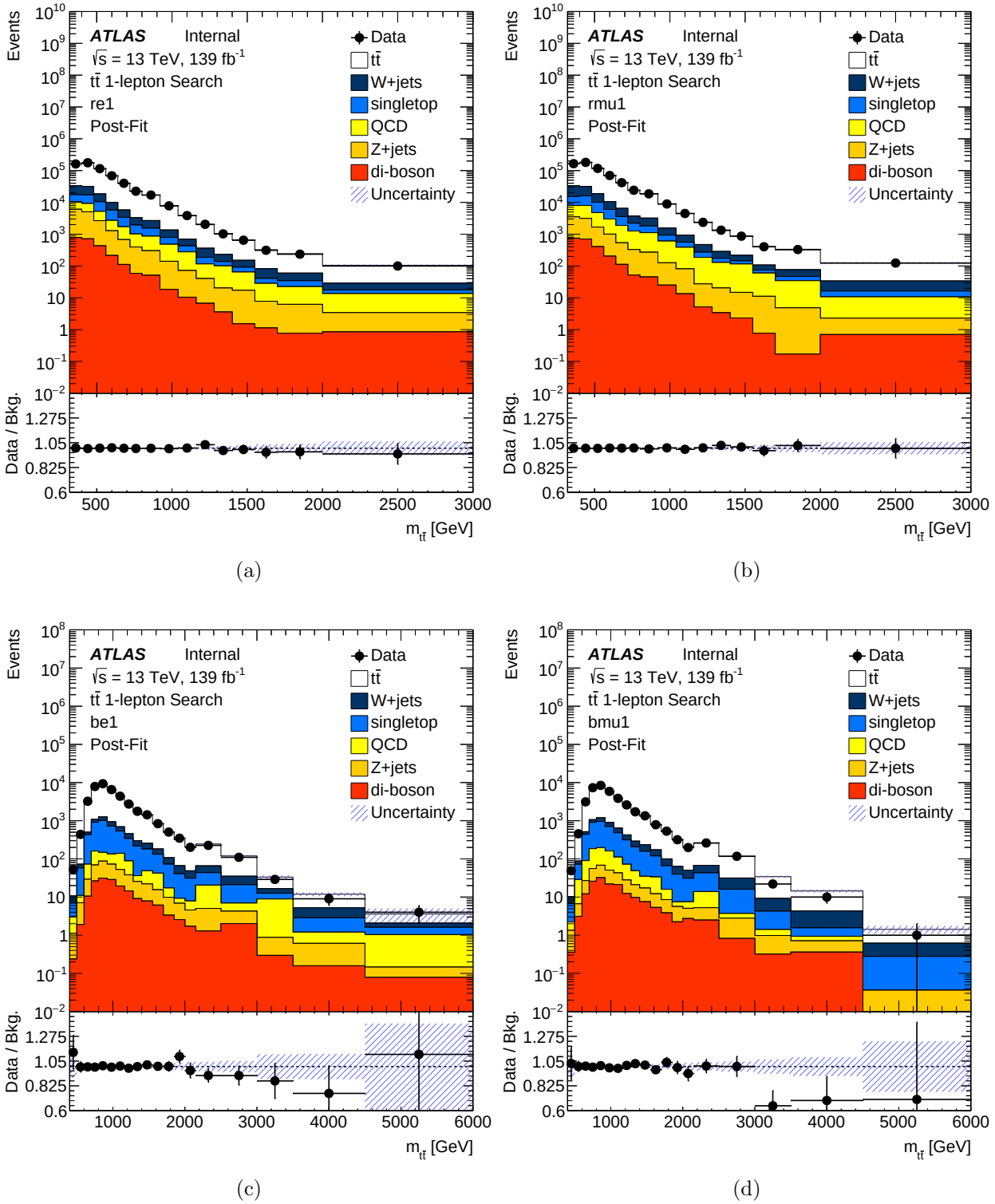

Figure 4.18: Post-fit plots for the 1 b-tag category for (a) resolved e, (b) resolved μ (c) boosted e, and (d) boosted μ.

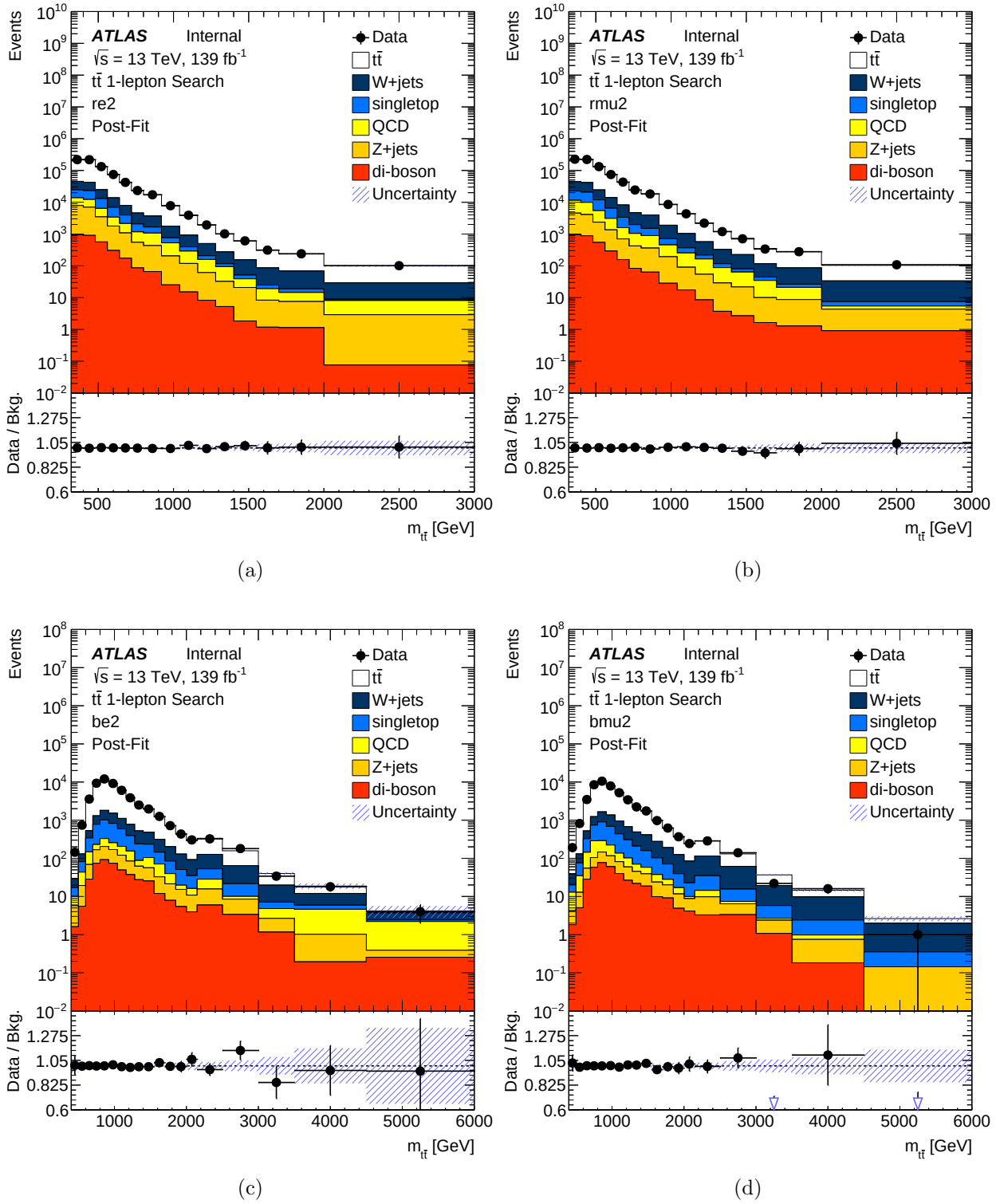

Figure 4.19: Post-fit plots for the 2 b-tag category for (a) resolved e, (b) resolved μ (c) boosted e, and (d) boosted μ.

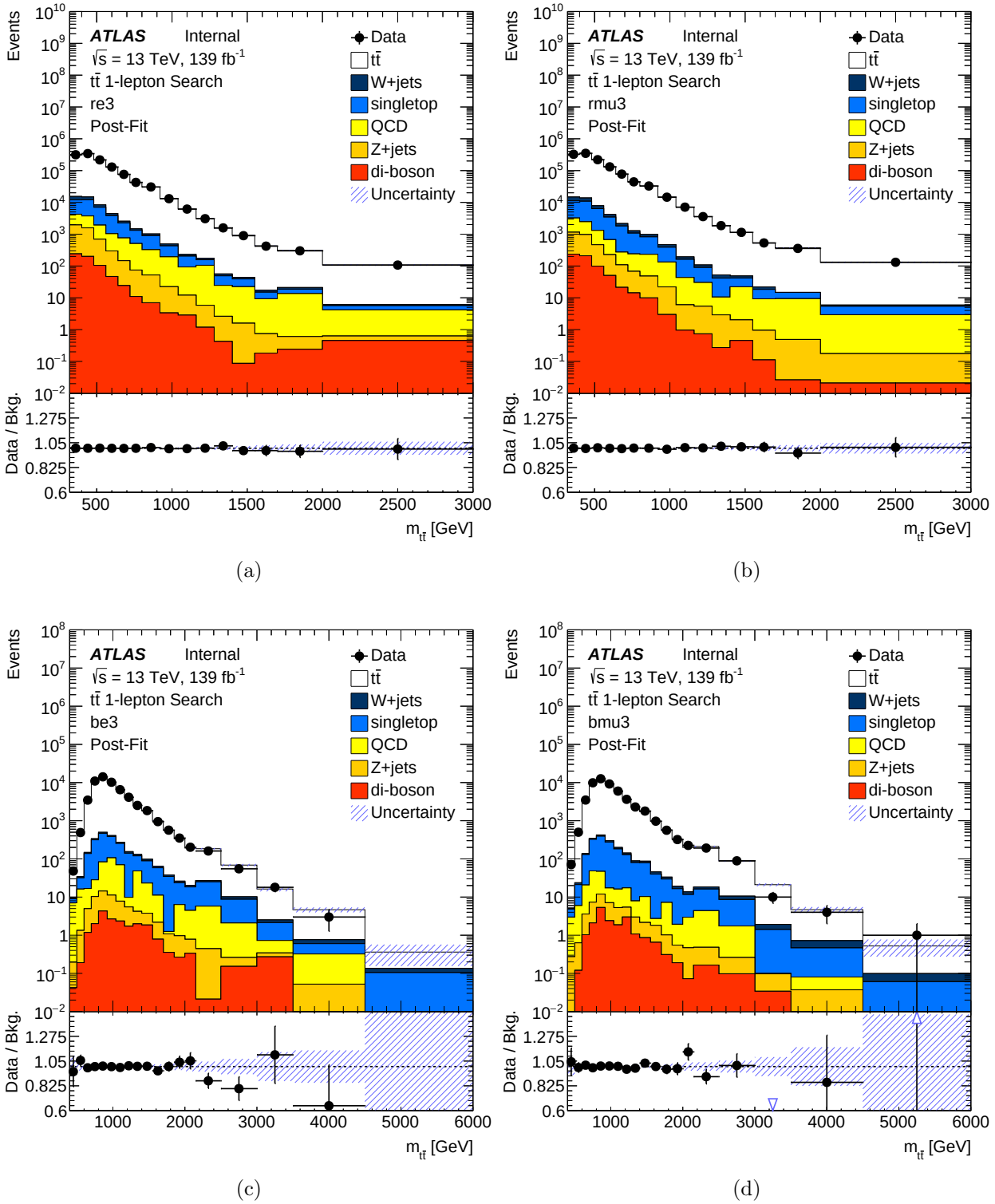

Figure 4.20: Post-fit plots for the 3 b-tag category for (a) resolved e, (b) resolved μ (c) boosted e, and (d) boosted μ.

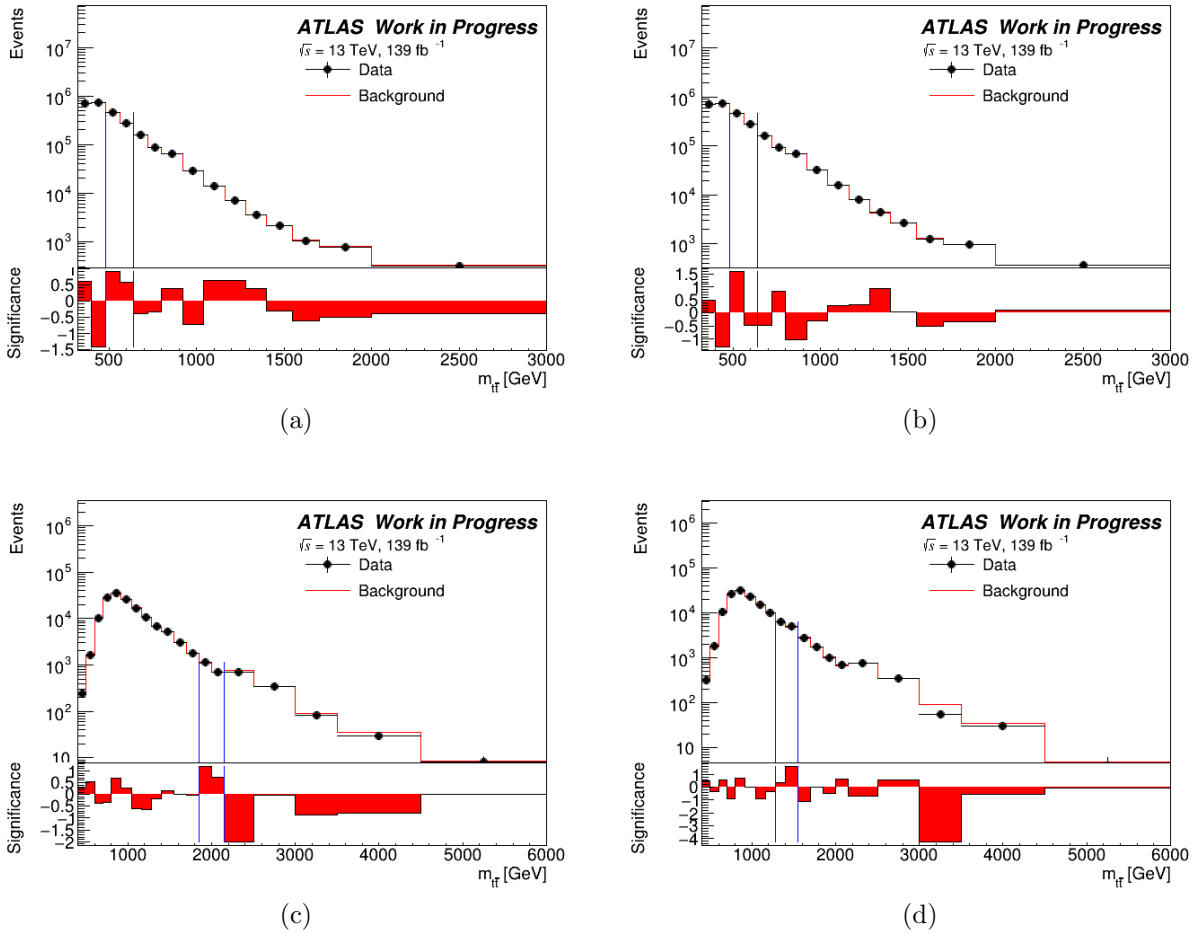

Figure 4.21: Model agnostic bump search for the (a) resolved e, (b) resolved μ, (c) boosted e, and (d) boosted μ. The post-fit distributions are used, with the vertical blue lines denoting the most significant excess interval for each region

Region	Local Excess (σ)	Global Excess (σ)
resolved e	1.1	-1.1
resolved μ	1.0	-1.2
boosted e	1.4	-0.7
boosted μ	1.3	-0.8

Table 4.14: Local and global excesses for the most significant deviations from background.

Signal	Expected Excluded Mass [TeV]	Observed Excluded Mass [TeV]
Z'_{TC2}	< 3.7	< 4.2
G_{KK}	[0.5, 1.2]	[0.5, 1.0]

Table 4.15: Expected and observed mass limits at a 95% confidence level for the Z'_{TC2} and G_{KK} benchmark models.

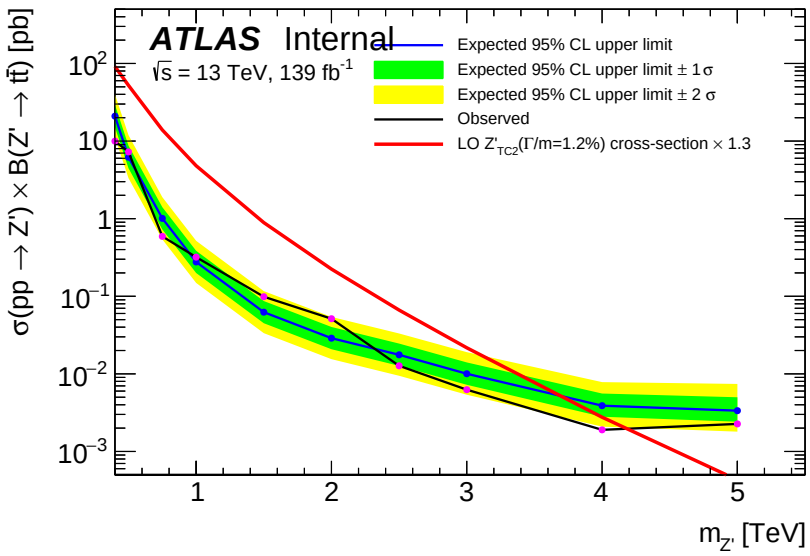

Figure 4.22: 95% confidence level exclusion limits on the Z'_{TC2} signal cross-section times branching ratio, as a function of $m_{Z'}$. All signal regions (e and μ channels, for both the resolved and boosted selection) are combined. The theoretical cross-section is overlaid as a red line, and used to extract the mass exclusion limit.

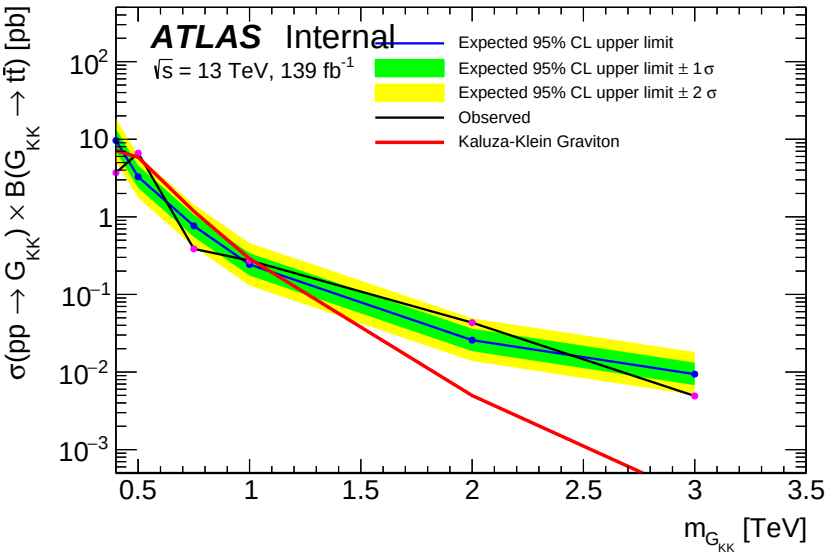

Figure 4.23: 95% confidence level exclusion limits on the G_{KK} signal cross-section times branching ratio, as a function of $m_{G_{KK}}$. All signal regions (e and μ channels, for both the resolved and boosted selection) are combined. The theoretical cross-section is overlaid as a red line, and used to extract the mass exclusion limit.

Chapter 5

Combination of Searches for Heavy Resonances

The search for new heavy resonances is a large part of the effort to uncover physics beyond the SM at the ATLAS detector and the LHC. Although there have been no significant excesses observed to date, strong constraints have been placed on the production of potential new heavy particles. A previous combination of searches for the production of heavy resonances was performed using proton-proton (pp) collisions at a center-of-mass energy of $\sqrt{s} = 13$ TeV corresponding to an integrated luminosity of 36 fb^{-1}, and has been published by the ATLAS [77] and CMS [78] collaborations, respectively. That combination included searches for a heavy resonance decaying into VV, VH (with $V = W, Z$ and H representing the SM Higgs boson) and their subsequent final states, as well as direct decays into $\ell\ell$ and $\ell\nu$. The combination described in this chapter includes the full Run-2 dataset from the LHC constituting a sample with an integrated luminosity of 139 fb^{-1}.

The specific searches used in this combination are those performed in the VV channels: $WZ \to qqqq$ [79], $\nu\nu qq$ [80], $\ell\nu qq$ [80], $\ell\ell qq$ [80], $\ell\nu\ell\ell$ [81], $WW \to qqqq$ [79], $\ell\nu qq$ [81], $\ell\nu\ell\nu$, $ZZ \to qqqq$ [79], $\nu\nu qq$ [81], $\ell\ell qq$ [81], $\ell\ell\nu\nu$, $\ell\ell\ell\ell$ the VH channels: $WH \to qqbb$ [82], $\ell\nu bb$ [83], $ZH \to \nu\nu bb$ [84], $\ell\ell bb$ [84], $qqbb$ [82]; and the lepton-antilepton channels: $\ell\ell$ [85], $\ell\nu$ [86], $\tau\nu$ [87], $\tau\tau$; and the di-quark channels: $q\bar{q}$ [88], $b\bar{b}$ [88], $tt \to qqqqbb$ [89], $tt \to qq\ell\nu bb$,

$tt \to \ell\nu\ell\nu bb$, $tb \to qqbb$, $tb \to \ell\nu bb$. The charged leptons, ℓ, are either electrons or muons, with the τ-lepton channels being a part of stand-alone searches. For the VV and VH decay channels involving leptonic vector boson decays, τ-leptons are included as part of the signal to include the small additional acceptance of τ-lepton decays into electrons and muons. The impact of the τ-leptons are included in the signal simulation, but the contamination of the reconstructed final states involving only electrons and muons is negligible. In this chapter, the VV and VH decay channels are collectively referred to as "bosonic", whereas the lepton-antilepton decay channels are collectively referred to as "leptonic", and the di-quark channels are collectively referred to as "quarkonic".

5.1 Combination Strategy

The combined approach takes into account orthogonal ATLAS analyses, each of which independently searches for a specific final state of novel physics, and combines them in a statistical interpretation that more tightly constrains the pertinent parameters of the models discussed in section 1.3.6.3. Various pairs of coupling parameters are expressed as exclusion contours in two-dimensional planes for a subset of resonance masses. These exclusion contours give theoretically interesting parts of phase space a more model-independent interpretation. The VBF production mode for the HVT signal lacks sensitivity compared to the qq-A production mode for masses above 1 TeV, and so in this chapter only qq-A channels are considered. In the larger combination effort, other modes such as gg-F and VBF are also considered for the relevant channels.

5.2 Data and Simulation

The 139 fb^{-1} of data for this combination was collected by the ATLAS detector during pp collisions running at the LHC at $\sqrt{s} = 13$ TeV during the period from 2015 to 2018. Events were chosen for the various channels using a variety of triggers, each of which is discussed in the relevant paper for that channel. Channels which feature charged or neutral leptons were selected with single or multiple electron and muon triggers with various p_T thresholds and isolation requirements, or with missing transverse momentum triggers with varying thresholds, and a high p_T jet trigger was used in the fully hadronic channels. All data must have been gathered under steady beam conditions and must meet the "All Good" quality standards, which are put into place using the Good Run List (GRL).

Interpreting the results of the combined channels relies on MC simulation to model the shape and normalization of the signals. Signal events for the HVT (Z', W') model A benchmark was generated for the qq-A production mechanism using `MadGraph5_aMC@NLO 2.6.5` at LO using the NNPDF23LO PDF set [65]. For all signal samples, the generated events were interfaced to `Pythia 8.240` [64] for parton showering and hadronization. Interference between signal events and SM processes was not taken into account, as this combination is being performed under the assumption of the narrow width approximation (NWA). Even without the NWA, the resonances considered are relatively narrow in width and so the interference effects are expected to be negligible. Examples of generator-level signal mass distributions are shown in 5.1.

Simulated background event samples are used to derive the main background estimates or to extrapolate backgrounds from control regions in the case of the channels $\ell\nu$, $\ell\nu\ell\ell$, $\ell\ell\ell\ell$, $tb0\ell$, $tb1\ell$, $tt1\ell$, and $tt2\ell$. In $\ell\ell$, $qqqq$, $qqbb$, $q\bar{q}$, $b\bar{b}$, and $tt0\ell$, the data are used to

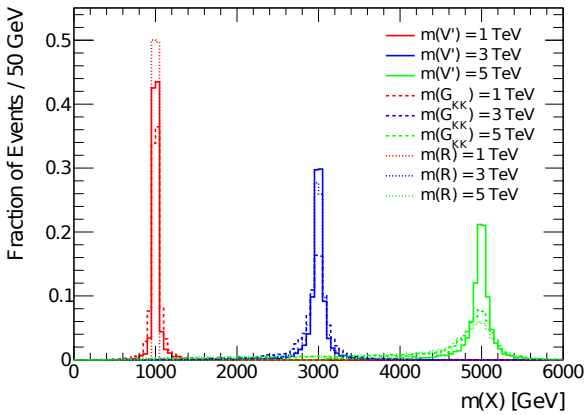

Figure 5.1: Truth level Monte Carlo distributions for the three types of signal considered in the combination.

extract the normalization and/or shape of the background distributions explicitly. Although the production of background MC samples differs somewhat depending on the particular analysis, most MC were produced as follows:

- Diboson (WW, WZ, ZZ) events were generated with `Sherpa` [37] or `Powheg-Box` [90, 91, 92].

- W+jets and Z+jets events were generated with `Sherpa` for up to two partons at NLO and up to four partons at LO using the OpenLoops [93] and Comix [94] programs, respectively.

- $t\bar{t}$ and single-top production was performed at NLO with `Powheg-Box`.

- For the $\ell\nu$ channel, the dominant DY background was modelled using `Powheg-Box` with mass-dependent corrections up to NNLO in QCD and NLO in electroweak.

More specific details can be found in the papers for each analysis listed in table 5.1.

Analysis	Leptons	E_T^{miss}	Jets	b-Tags	Top Tags	VBF	Discr.	Ref
$WW/WZ/ZZ \to qqqq$	0	Veto	$\geq 2J$	-	-	-	m_{VV}	[79]
$WZ/ZZ \to \nu\nu qq$	0	Yes	$\geq 1J$	0	-	Yes	m_{VV}	[80]
$WW/WZ \to \ell\nu qq$	$1e$, 1μ	Yes	$\geq 2j$, $\geq 1J$	0, 1, 2	-	Yes	m_{VV}	[80]
$WZ/ZZ \to \ell\ell qq$	$2e$, 2μ	-	$\geq 2j$, $\geq 1J$	0	-	Yes	m_{VV}	[80]
$ZZ \to \ell\ell\nu\nu$	$2e$, 2μ	Yes	-	0	-	Yes	m_{VV}	**TBC**
$WW \to \ell\nu\ell\nu$	$1e$+1μ	Yes	$0j$, $1j$, $2j$	0	-	Yes	m_{VV}	**TBC**
$WZ \to \ell\nu\ell\ell$	$3 \subset (e, \mu)$	Yes	-	0	-	Yes	m_{VV}	[81]
$ZZ \to \ell\ell\ell\ell$	$4e$, $2e$+2μ, 4μ	-	-	-	-	Yes	m_{VV}	**TBC**
$WH/ZH \to qqbb$	0	Veto	$\geq 2J$	1, 2	-	-	m_{VH}	[82]
$ZH \to \nu\nu bb$	0	Yes	$\geq 2j$, $\geq 1J$	1, 2	-	-	m_{VH}	[84]
$WH \to \ell\nu bb$	$1e$, 1μ	Yes	$\geq 2j$, $\geq 1J$	1, 2	-	-	m_{VH}	[83]
$ZH \to \ell\ell bb$	$2e$, 2μ	Veto	$\geq 2j$, $\geq 1J$	1, 2	-	-	m_{VH}	[84]
$\ell\nu$	$1e$, 1μ	Yes	-	-	-	-	m_T	[86]
$\tau\nu$	1τ	Yes	-	-	-	-	m_T	[87]
$\ell\ell$	$\geq 2e$, $\geq 2\mu$	-	-	-	-	Maybe	$m_{\ell\ell}$	[85]
$\tau\tau$	0, $1e$, 1μ	Yes	-	0, ≥ 1	-	-	$m_{\tau\tau}$	**TBC**
$tt0\ell$	0	-	$2J$	1, 2	2	-	m_{tt}	[89]
$tt1\ell$	$1e$, 1μ	Yes	$\geq$4j, $\geq(2j$+$1J)$	1, 2	0, 1	-	m_{tt}	**TBC**
$tt2\ell$	$2 \subset (e, \mu)$	Yes	$\geq 2j$	≥ 1	-	-	m_{tt}	**TBC**
$tb0\ell$	0	-	$\geq(1j$+$1J)$	≥ 1	1	-	m_{tb}	**TBC**
$tb1\ell$	$1e$, 1μ	Yes	$2j$, $3j$	1, 2	-	-	m_{tb}	**TBC**
qq	0	-	$2j$	0	-	-	m_{jj}	[88]
bb	0	-	$2j$	1, 2	-	-	m_{bb}	[88]

Table 5.1: Summary of object and event selection for the signal regions of the analyses in the combination. The entries which are comma separated denote an "OR" for different signal regions, while entries with a plus denote an "AND". For jets, "j" indicates a small-R radius jet, while "J" denotes a large-R radius jet. The symbol, $\subset$, denotes any combination of at least one of the objects inside the bracket up to the number shown. Entries denoted with a "-" indicate no requirement for that object. The VBF column denotes whether the analysis has an additional category for VBF events which requires additional selection.

5.3 Object Definitions

5.3.1 Leptons

Specific information on lepton definitions can be found in the respective analysis documents linked in this chapter. The selection criteria for electrons, muons, and taus use standard methods recommended by the EGamma [95], Muon [96], and Tau [97] CP groups, respectively. For light leptons, the identification and isolation working points are given in table 5.2.

Analysis	Electron ID	Muon ID	Electron Isolation	Muon Isolation
$WW/WZ \to \ell\nu qq$	Tight	Medium	FCTightHighPtCaloOnly	FCTightHighPtCaloOnly
$WZ/ZZ \to \ell\ell qq$	Loose	Loose	FCLoose	FCTightTrackOnly
$ZZ \to \ell\ell\nu\nu$	Loose	Loose	FCPFlowLoose	FCPFlowLoose
$WW \to \ell\nu\ell\nu$	Medium	Tight	FCTight	FCTight
$WZ \to \ell\nu\ell\ell$	Tight(W)/Medium(Z)	Tight	FCTight	FCTight
$ZZ \to \ell\ell\ell\ell$	Loose	Loose	FCPFlowLoose	FCPFlowLoose
$WH \to \ell\nu bb$	Tight	High-p_T	FCTight	FCTight
$ZH \to \ell\ell bb$	Loose	High-p_T	FCTight	FCTight
$\ell\ell$	Medium	High-p_T	Gradient	FCTightTrackOnly
$\ell\nu$	Tight	High-p_T	Gradient	FCTightTrackOnly
$tt1\ell$	Tight	Medium	FCTightTrackOnly	FCTightTrackOnly
$tt2\ell$	Tight	Medium	FCTightTrackOnly	FCTightTrackOnly
$tb1\ell$	Tight	Medium	FCTightTrackOnly	FCTightTrackOnly

Table 5.2: Light lepton identification and isolation working points for the constituent analyses of the combination that include at least one electron or muon in their selection criteria for the signal region(s).

5.3.2 Jets and Flavor Tagging

Specific information on jet collections and flavor tagging can be found in the respective analysis documents linked in this chapter. The anti-k_T algorithm, as described in section 3.2.6.1, is commonly used to reconstruct jets in the ATLAS detector, with different analyses using different combination of small-R and large-R jets. Table 5.3 shows the jet collections used by the constituent analyses of the combination, while Table 5.4 shows the flavor tagging working points.

5.4 Event Selection

Specific information on event selection can be found in the respective analysis documents linked in this chapter. A summary is provided in table 5.1.

Analysis	Small-R Jet	Large-R Jet
$WW/WZ/ZZ \to qqqq$	-	TCC
$WZ/ZZ \to \nu\nu qq$	EMTopo	TCC
$WW/WZ \to \ell\nu qq$	EMTopo	TCC
$WZ/ZZ \to \ell\ell qq$	EMTopo	TCC
$ZZ \to \ell\ell\nu\nu$	EMTopo	-
$WW \to \ell\nu\ell\nu$	PFlow	-
$WZ \to \ell\nu\ell\ell$	EMTopo	-
$WH/ZH \to qqbb$	-	TCC
$ZH \to \nu\nu bb$	EMTopo	TCC
$WH \to \ell\nu bb$	EMTopo	TCC
$ZH \to \ell\ell bb$	EMTopo	TCC
$\ell\nu$	EMTopo	-
$\tau\nu$	EMTopo	-
$\tau\tau$	EMTopo	-
$tt0\ell$	-	TCC
$tt1\ell$	PFlow	-
$tt2\ell$	PFlow	-
$tb0\ell$	PFlow	LCTopo
$tb1\ell$	PFlow	-
qq	EMTopo	-
bb	EMTopo	-

Table 5.3: Jet collections used for the constituent analyses of the combination that include at least one small-R or large-R jet in their selection criteria for the signal region(s).

Analysis	Resolved Jets	Boosted Jets	b-Tag Alg	b-Tag WP	Top-Tagging
$WH/ZH \to qqbb$	-	VR track-jets	MV2c10	77%	-
$ZH \to \nu\nu bb$	EMTopo	VR track-jets	MV2c10	70%	-
$WH \to \ell\nu bb$	EMTopo	VR track-jets	MV2c10	70%	-
$ZH \to \ell\ell bb$	EMTopo	VR track-jets	MV2c10	70%	-
$tt0\ell$	EMTopo	VR track-jets	DL1	77%	DNN
$tt1\ell$	PFlow	LCTopo	DL1r	77%	DNN
$tt2\ell$	PFlow	-	DL1r	77%	-
$tb0\ell$	PFlow	LCTopo	DL1r	85%	DNN
$tb1\ell$	PFlow	-	DL1r	85%	-
bb	EMTopo	-	DL1r	77%	-

Table 5.4: Flavor Tagging used for the constituent analyses of the combination that include at least b-quark or top-quark in their selection criteria for the signal region(s).

5.4.1 Analysis Orthogonality

There may be overlap in the data events accepted by different analyses due to the complexity of each individual selection criteria used in this combination. Without requiring that its events be orthogonal to the events of others', each analysis develops its own selection criteria to maximize the signal significance in its own final state. It is crucial to reduce, or perhaps remove entirely, double-counting of data events through well-studied orthogonality constraints. When analyses are combined with an orthogonality constraint, little to no sensitivity is lost since events excluded from one analysis are usually included in another (though requiring orthogonality may result in a slightly reduced sensitivity in any individual analysis). Before enforcing any specific orthogonality criteria, all analyses applied their event selection to a common set of HVT signal MC samples with pole masses ranging from 500 GeV to 3 TeV. The fraction of overlapping events selected by each pair of analyses is shown in a matrix in figure 5.2. The results of this study indicate that many analyses are orthogonal without adjustment, as empty cells indicate event overlap of less than 1%. Overlapping analyses where special orthogonality-enforcing criteria were studied and used include the VV/VH full-hadronic analyses, VV/VH semi-leptonic analyses, tt/tb analyses, tt/VH semi-leptonic analyses, VV fully-leptonic/($\ell\ell$ & $\ell\nu$) analyses, (qq & bb)/all. The VV/VH semi-leptonic overlap study will receive special consideration in the section 5.5.1, both because I conducted it and because it serves as a good example of the overlap removal process.

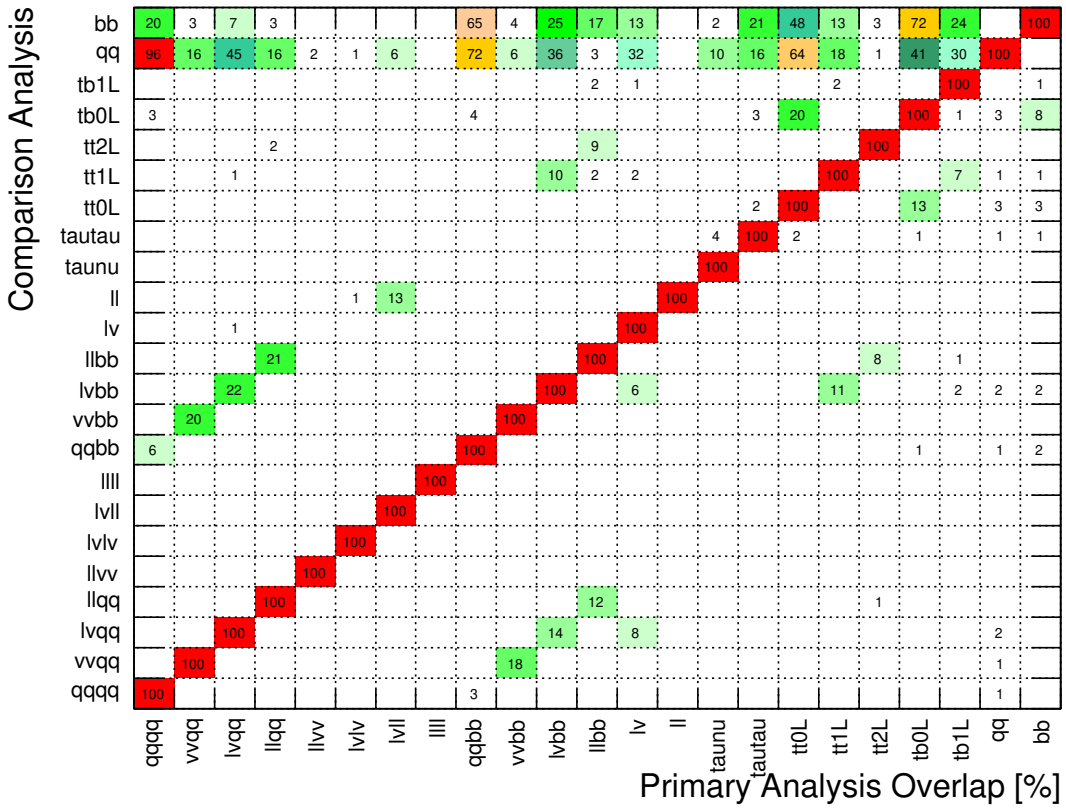

Figure 5.2: Orthogonality study using the full Run-2 dataset analysed by all analyses taking part in the combination. The contents of each cell indicate the percentage of data events common to the analysis selection of each corresponding row and column (y/x). Entries with "-1" have not been entered yet. The di-jet and di-b-jet entries remain as they are removed by-hand.

5.4.2 Data Overlap

A summary of all orthogonality requirements is given in table 5.5. After all orthogonality cuts are imposed a final check is done using the full Run-2 dataset, and the results are shown in figure 5.3. This check was done to ensure that the imposition of orthogonality criteria was successful and that no significant double-counting of data events is present in the combination.

Analysis	Original Selection	Additional Selection
$VH \to \nu\nu bb$	m_{jj} or m_J window	$m_{jj} > 100$ GeV
$VH \to \ell\nu bb$	m_{jj} or m_J window	$m_{jj} > 106$ GeV
$VH \to \ell\ell bb$	m_{jj} or m_J window	$m_{jj} > 100$ GeV
$VH \to qqbb$	p_T^J dependent	$m_J > 106$ GeV
$tb0\ell$	-	Second W and top tag veto
$tb1\ell$	-	Second W and top tag veto
qq	-	Remove overlapping events
bb	-	Remove overlapping events

Table 5.5: Original and additional selections to achieve orthogonality between all analyses taking part in the heavy resonance combination.

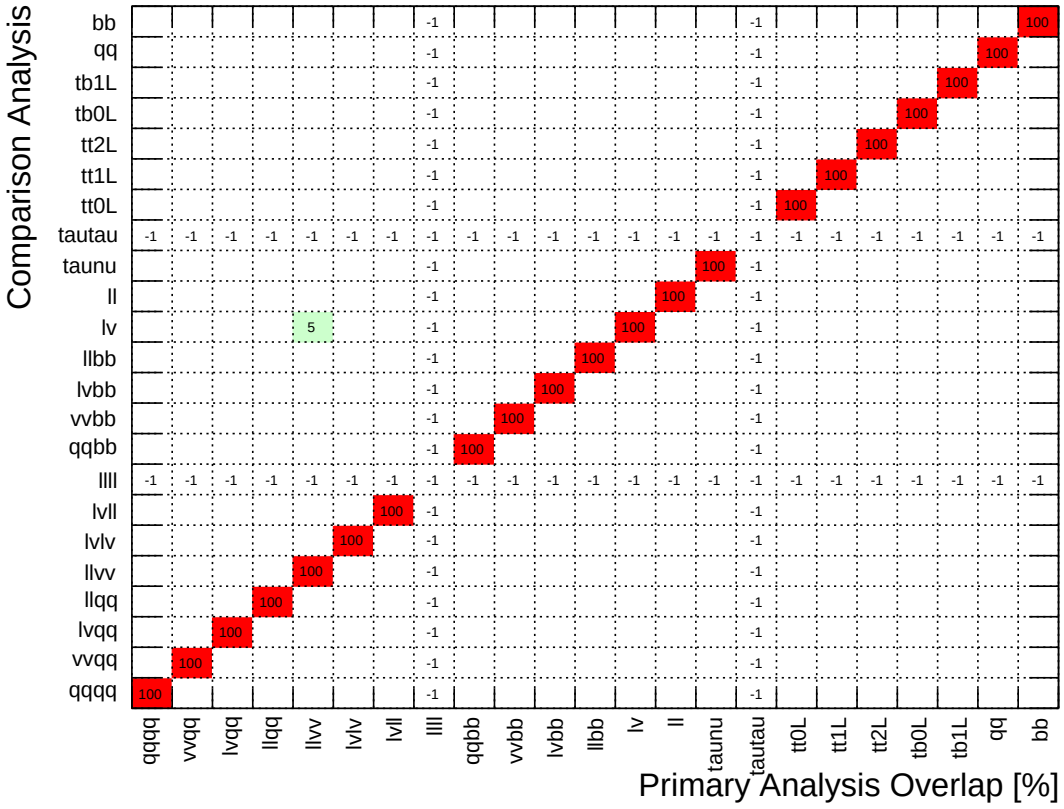

Figure 5.3: Orthogonality study using the full Run-2 dataset analysed by all analyses taking part in the combination. The contents of each cell indicate the percentage of data events common to the analysis selection of each corresponding row and column (y/x). Entries with "-1" have not been entered yet. The di-jet and di-b-jet entries remain as they are removed by-hand.

5.5 Studies

This chapter will describe several specific studies I undertook in addition to the general work of the combination.

5.5.1 VV/VH Semi-leptonic Overlap

There are resolved and boosted signal regions in the semi-leptonic VV and VH analyses, both of which must have orthogonality constraints applied. Three categories based on the number of charged leptons are defined in these final states: 0-lepton ($\nu\nu qq$ or $\nu\nu bb$), 1-lepton ($\ell\nu qq$ or $\ell\nu bb$), and 2-lepton ($\ell\ell qq$ or $\ell\ell bb$). Since the VV and VH analyses use a mass selection that is p_T dependent, and since the VV analysis does not select any events above a certain dijet mass m_{jj}, the VH analysis applied a complementary m_{jj} cut to enforce complete orthogonality between the two analyses in the resolved channels which is dependent on an event's number of charged leptons. Figures 5.4, 5.5, and 5.6 show the resolved cases for 0-, 1-, and 2-lepton categories, respectively. These show that orthogonality can be imposed by using an m_{jj} cut of 100 GeV, 106 GeV, and 100 GeV, respectively.

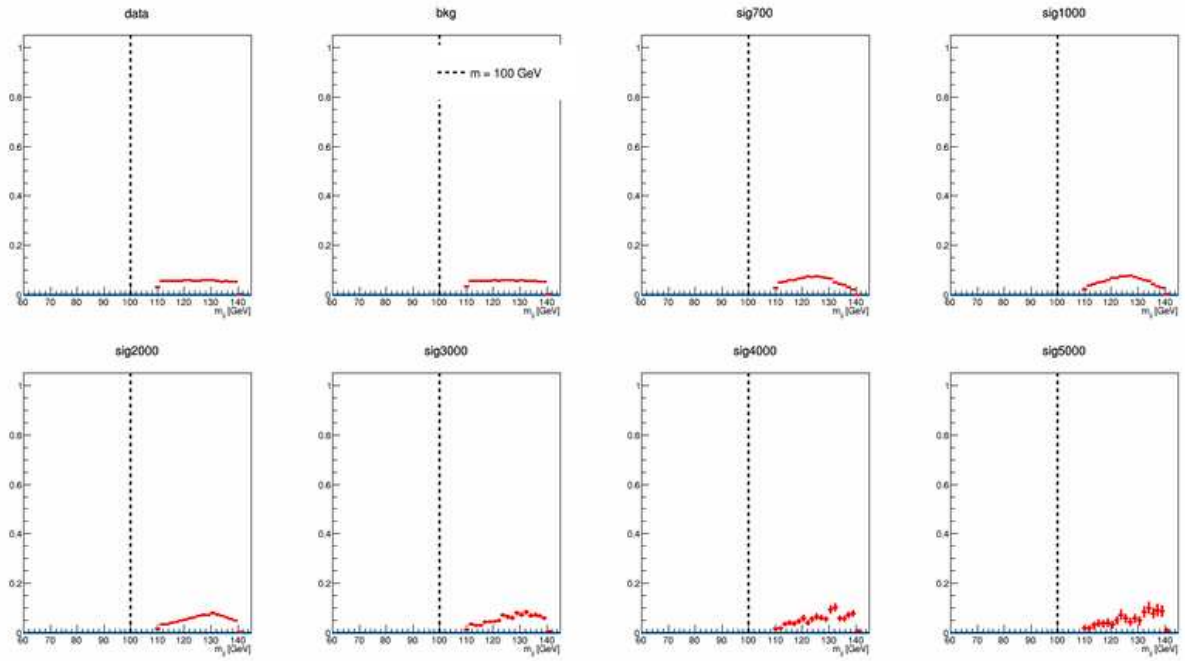

Figure 5.4: Comparisons between $VV \to \nu\nu qq$ (blue) and $VH \to \nu\nu bb$ (red) in the resolved channels using the di-jet invariant mass spectrum for 2015-2016 data, the background estimate, and various HVT signal masses, where available. The VV histograms are empty because the $\nu\nu qq$ analysis does not have a resolved region. A dashed vertical line is shown at 100 GeV for reference.

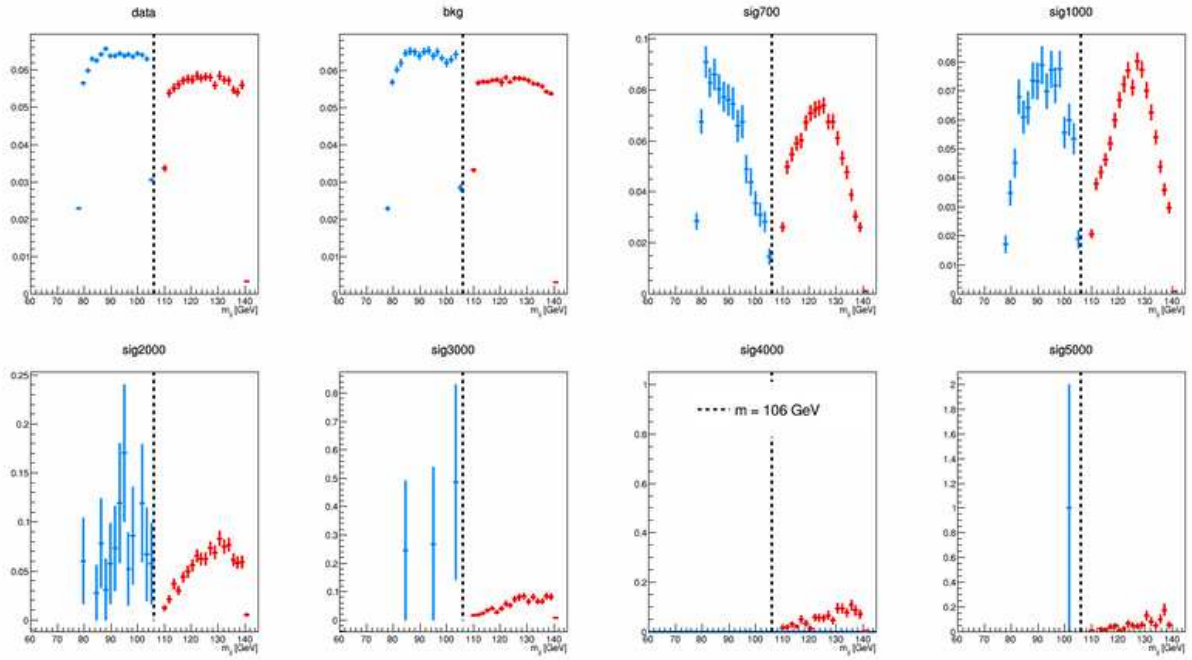

Figure 5.5: Comparisons between $VV \to \ell\nu qq$ (blue) and $VH \to \ell\nu bb$ (red) in resolved channels using the di-jet invariant mass spectrum for 2015-2016 data, the background estimate, and various HVT signal masses, where available. A dashed vertical line is shown at 106 GeV for reference.

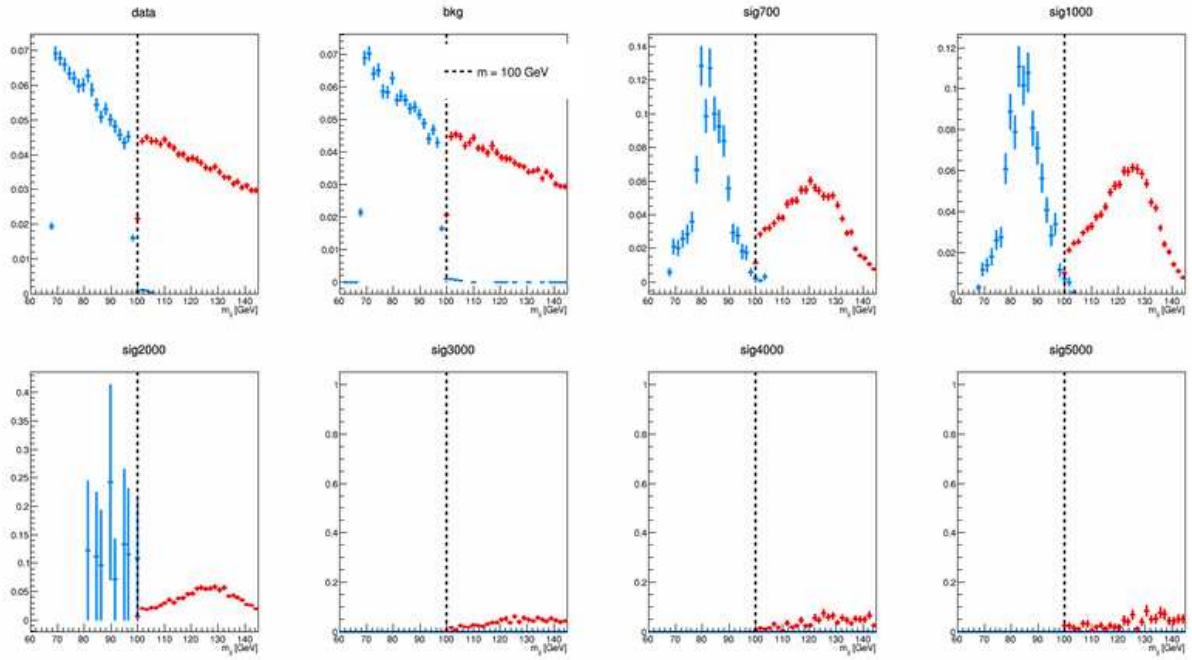

Figure 5.6: Comparisons between $VV \to \ell\ell qq$ (blue) and $VH \to \ell\ell bb$ (red) in resolved channels using the di-jet invariant mass spectrum for 2015-2016 data, the background estimate, and various HVT signal masses, where available. A dashed vertical line is shown at 100 GeV for reference.

The boosted analyses are more complicated to separate because the boosted jet mass (m_J) cut depends on the transverse momentum of the jet (p_T^J). In the boosted analyses, a cut on boosted jet mass (m_J) depends on the transverse momentum of a large-R jet p_T^J, which makes it more difficult to separate between the two analyses. Figures 5.7 shows events selected by the 1-lepton channel of the VV analysis, while figure 5.8 shows events selected by the 1-lepton channel of the VH analysis. These patterns hold for the 0-lepton and 2-lepton channels. The different orthogonality strategies studied were:

- selection-0 – No orthogonality cut.
- selection-1 – The VV mass window cuts were applied to VH.
- selection-2 – Mass cuts were made to both VV ($m_J < 100/106$ GeV) and VH ($m_j \geq 100/106$ GeV) with analysis dependent thresholds, trying to choose complementary values that least affect each individual analysis.
- selection-3 – The same as selection-2, except with no mass cuts applied to events with zero b-tags.

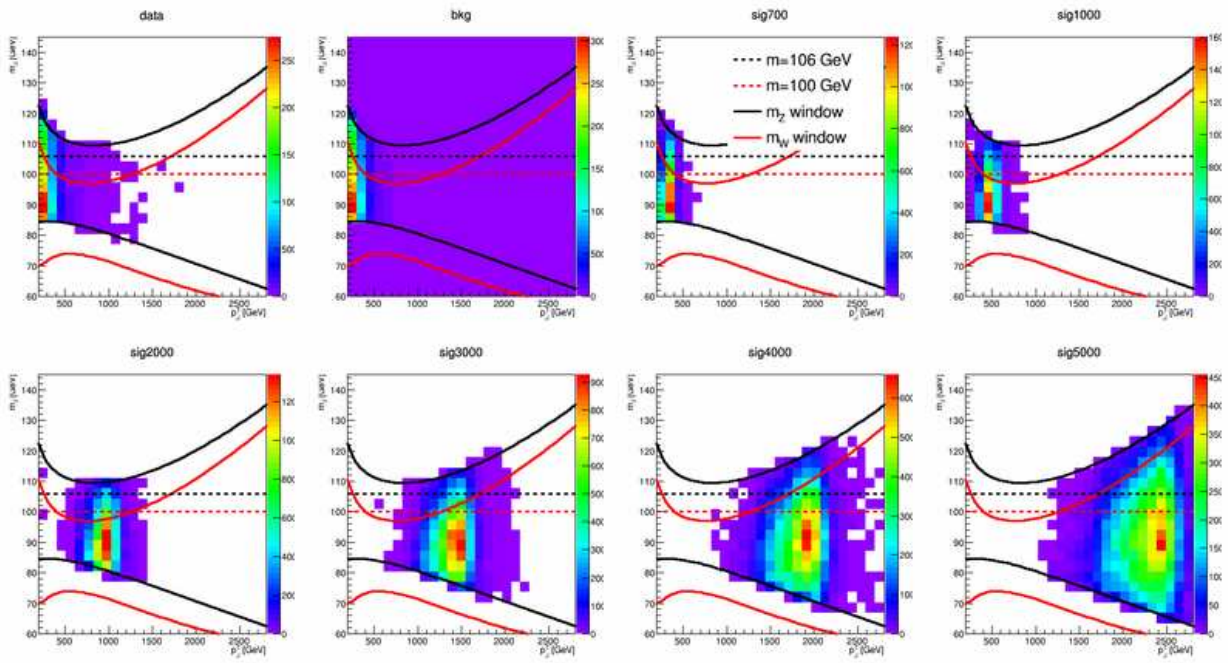

Figure 5.7: Distributions as a function of mass and p_T for the merged jet in the boosted $WZ \to \ell\nu qq$ analysis. Distributions are shown for 2015-2016 data, the background estimate, and various HVT signal masses, where available.

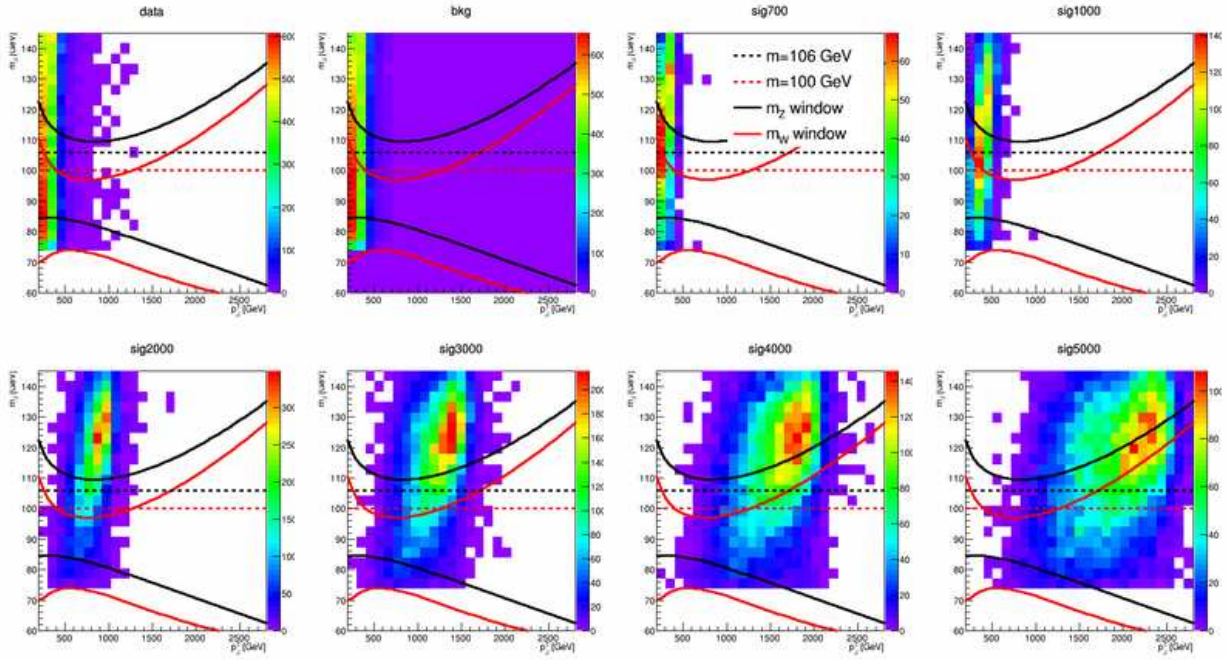

Figure 5.8: Distributions as a function of mass and p_T for the merged jet in the boosted $WH \to \ell\nu bb$ analysis. Distributions are shown for 2015-2016 data, the background estimate, and various HVT signal masses, where available.

To impose orthogonality, "selection-1" was used because of its simplicity and because using the different selection criteria give similar results. A complementary cut is applied to the sliding cut in the VV by the VH analyses in this strategy. While some of the VH-only analysis' channels experience a reduction in sensitivity as a result, the VV channels retain it, indicating that the combined analysis' overall sensitivity is still higher than either individual search, as shown in 5.9. The orthogonality criteria imposed on the semi-leptonic VV and VH analyses results in less than 1% remaining overlap between the channels.

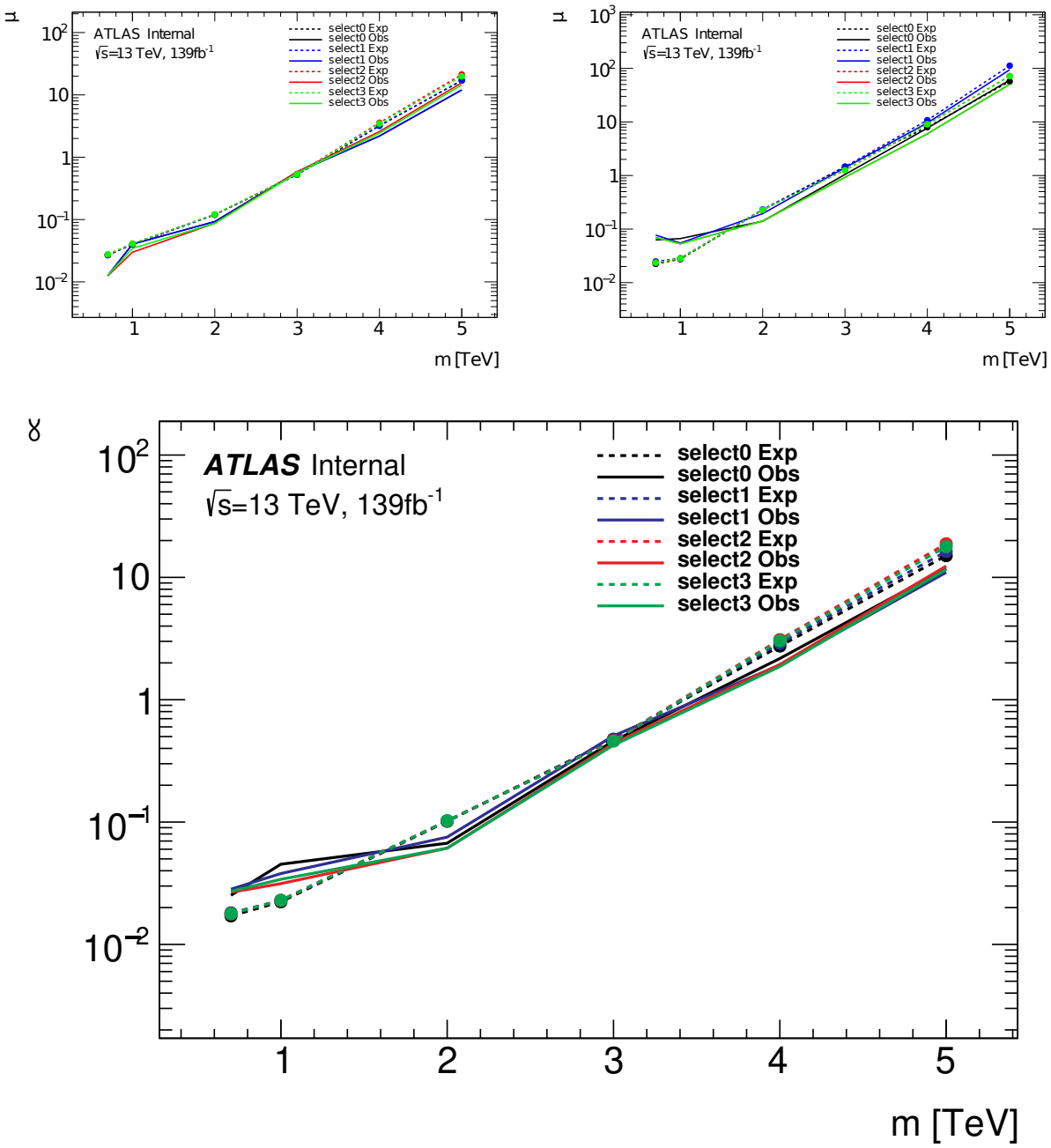

Figure 5.9: 95% CL Exclusion Limits divided by the HVT-A signal cross-section for different orthogonality solutions, shown for (upper-left) VV only, (upper-right) VH only, and (lower) VV/VH combined. Selection-0 is the nominal selection without orthogonality applied. Selection-1 applies matching VV mass cuts in the VH channels (chosen strategy for simplicity). Selection-2 applies balanced mass cuts in both VV and VH channels. Selection-3 is the same as selection-2, except that no mass cuts are applied on zero b-tag events in the VV channels. While the cuts cause more sensitivity loss in the individual VH channels, the expected sensitivity is mostly retained with orthogonality imposed for the VV/VH combination.

5.5.2 HVT Cross-Section Studies

A prerequisite to constructing the 2D limits with respect to the HVT coupling parameters referenced in section 5.1 is the production of planes of the relevant cross-sections. These planes of cross-sections were made using a Mathematica tool provided by the some of the combination's Analysis Consultants and Experts (ACEs) who are the authors of the HVT model [18]. Figures 5.10 and 5.11 show cross-sections for a 5 TeV V' in the (g_H, g_f) and (g_q, g_ℓ) planes with any parameters not shown on the axis set to their HVT-A values. Several iterations during the combination effort were made to verify new versions of the HVT calculator tool by confirming that its produced values were in agreement with previous versions of the tool and with MadGraph. A Clough-Tocher 2D interpolation scheme is used to give equally spaced points across the grid of interest [98].

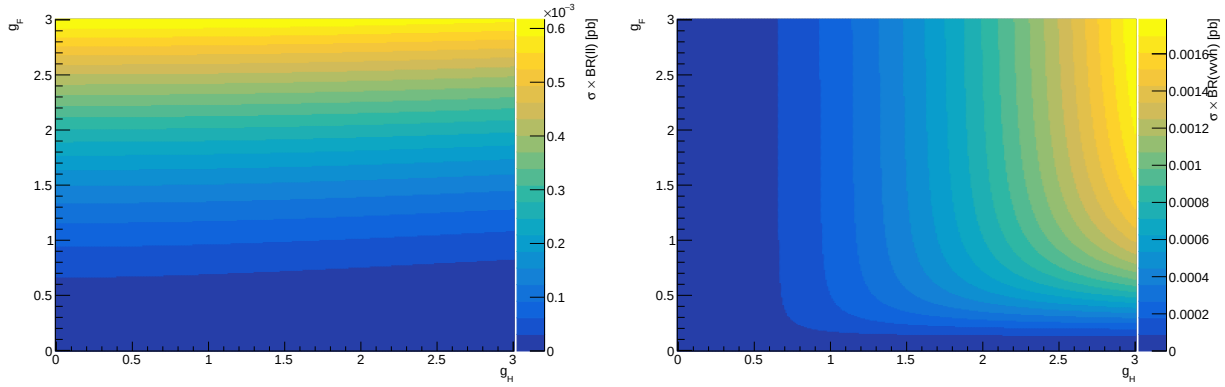

Figure 5.10: $\sigma \times \mathcal{B}$ in the (g_H, g_f) plane for 5 TeV V' in the (a) $\ell\ell$ and (b) the combined $VV + VH$ decay channels.

In any 2D plane with N unconstrained parameters, it will always be necessary to fix $N - 2$ of those parameters. Adding new benchmark points allows the investigation into regions which are interesting because of their strong 3$^{\text{rd}}$ generation coupling. These new 3$^{\text{rd}}$ generation points were chosen in two different ways, each by starting with the already benchmark point in the coupling space and increasing the 3$^{\text{rd}}$ generation couplings until

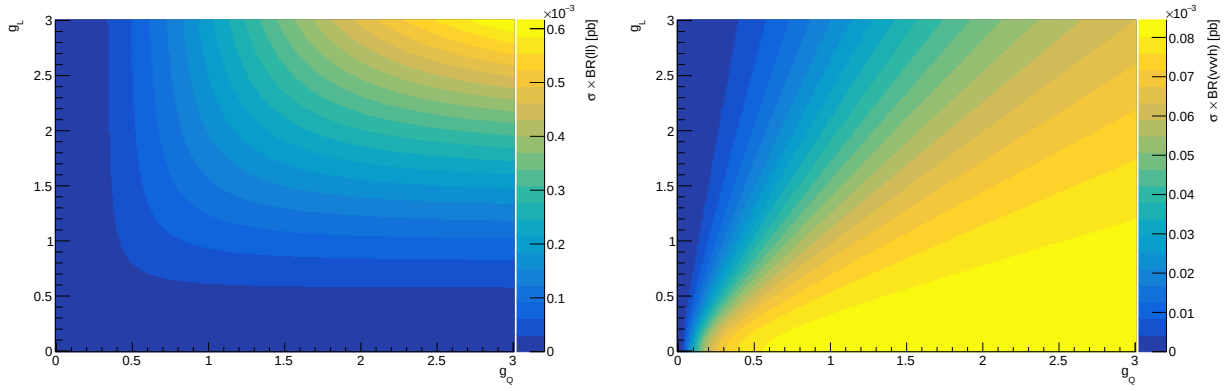

Figure 5.11: $\sigma \times \mathcal{B}$ in the (g_q, g_ℓ) plane for 5 TeV V' in the (a) $\ell\ell$ and (b) the combined $VV + VH$ decay channels.

the predicted cross-section to match some predefined criteria. Using this method we define two new benchmarks, one starting from HVT-A and increasing the 3$^{\text{rd}}$ generation couplings until the predicted-cross section reaches that of an already-defined model with strong 3$^{\text{rd}}$ generation coupling (in this case Topcolor), and one starting with HVT-B and increasing similarly until the cross-section times branching ratio is equal to that of the bosonic channels. Figure 5.12 shows the intersections defining each of these points, appropriately named HVT-A3 and HVT-B3, respectively.

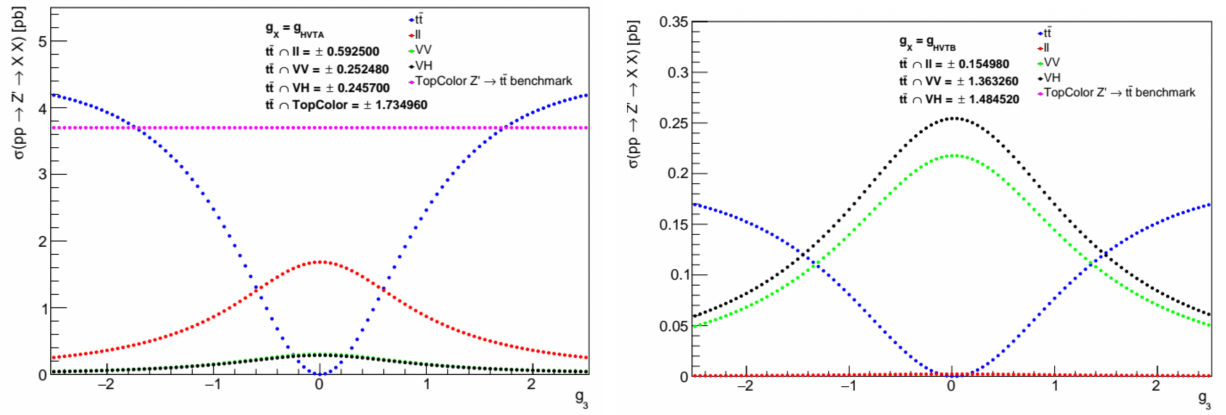

Figure 5.12: Cross-section times branching ratios showing the intersections defining (a) HVT-A3 and (b) HVT-B3.

Because this is the first time a combination has used final states including 3$^{\text{rd}}$ generation

particles, I worked with the combination ACEs to update the tool to include and validate separate 3_{rd} generation quark and lepton couplings, and undertook this study to investigate regions of the HVT parameter space which included stronger 3^{rd} generation couplings. Using these new tools and the studies resulting from them, the combination effort and ACEs decided that the most theoretically interesting planes in the HVT parameter space were:

1. (g_H, g_{q3}) with other parameters set to their HVT-A or HVT-B values.

2. (g_{q12}, g_{q3}) with other parameters set to zero.

3. (g_{q3}, $g_{\ell 3}$) with other parameters set to the HVT-A values.

5.6 Systematic Uncertainties

All of the analyses included in the combination take the respective systematic uncertainties into account. Further details for individual analyses can be found in their respective papers. Compared with only the statistical uncertainties, the the total weakening effect of the systematic uncertainties on the excluded cross-section limits is up to 20%.

5.6.1 Integrated Luminosity and Pileup

The uncertainty on the integrated luminosity is 1.7%, as determined by the LUCID-2 detector [74].

5.6.2 Leptons

Electron and muon identification, reconstruction, isolation, trigger efficiency uncertainties are included in this category, as well as uncertainties related to energy/momentum scale and resolution. Each of these uncertainties applies to both the signal and the simulated background distributions, and each are considered as correlated across the analysis channels where the same lepton selection criteria is used. Two systematics are viewed as entirely uncorrelated if they originate from the same source of uncertainty but are estimated differently (refer to table 5.2 for more details)

The $\tau\nu$ and $\tau\tau$ analyses have additional τ-specific related experimental uncertainties such as the τ energy scale, identification, reconstruction, and selection efficiencies. Depending on the number of τ particles the overlap removal procedure can also lead to non-negligible uncertainties, and the accurate simulation of material transport through the detector can lead to further uncertainties in the reconstruction efficiency loss.

Systematic Source	$WW \to \ell\nu\ell\nu$	$WW \to \ell\nu qq$	$WZ \to \ell\ell qq$	$WZ \to \ell\ell\ell\nu$	$WH \to \ell\nu bb$	$ZH \to \ell\ell bb$	$\ell\ell$	$\ell\nu$	$tt1\ell$	$tt2\ell$	$tb1\ell$
Electron energy resolution	S+B	S+B	S+B	S+B	S+B	S+B	S+B	S+B	S+B	S+B	
Electron energy scale	S+B	S+B	S+B	S+B	S+B	S+B	S+B	S+B	S+B	S+B	S+B
Electron identification	S+B	S+B	S+B	S+B	S+B	S+B	S+B	S+B	S+B	S+B	S+B
Electron reconstruction	S+B	S+B	S+B	S+B	S+B	S+B	S+B	S+B			
Electron isolation	S+B	S+B	S+B	S+B	S+B	S+B	S+B	S+B			
Electron trigger	S+B	S+B	S+B	S+B	S+B	S+B	S+B	S+B			
Muon momentum resolution	S+B	S+B	S+B	S+B	S+B	S+B	S+B	S+B	S+B	S+B	S+B
Muon momentum scale	S+B	S+B	S+B	S+B	S+B	S+B	S+B	S+B	S+B	S+B	S+B
Muon reconstruction	S+B	S+B	S+B	S+B	S+B	S+B	S+B	S+B	S+B	S+B	
Muon isolation	S+B	S+B	S+B	S+B	S+B	S+B	S+B	S+B			
Muon trigger	S+B	S+B	S+B	S+B	S+B	S+B	S+B	S+B	S+B	S+B	
Muon Sagitta	S+B	S+B	S+B	S+B	S+B	S+B	S+B	S+B	S+B	S+B	S+B

Table 5.6: Lepton systematic uncertainties. The abbreviations "S" and "B" stand for signal and background, respectively, while "negl." denotes uncertainties that are negligible. Each uncertainty is considered as correlated between the channels listed.

Systematic Source	$\tau\nu$	$\tau\tau$
Tau Energy Scale	S+B	S+B
Tau identification	S+B	S+B
Tau reconstruction	S+B	S+B
Tau selection	S+B	S+B
Tau overlap removal	S+B	S+B
Matter transport	S+B	

Table 5.7: Tau systematic uncertainties. The abbreviations "S" and "B" stand for signal and background respectively. Each uncertainty is considered as correlated between the channels listed.

5.6.3 $E_T^{\mathbf{miss}}$

Uncertainties associated with E_T^{miss} are from the soft term resolution and scale, as well as from the triggers used by some analyses. These uncertainties are always considered for both signal and background distributions, and are considered as correlated across the different analysis channels.

Systematic Source	$WW \to \ell\nu\ell\nu$	$WW \to \ell\nu qq$	$WZ \to \nu\nu qq$	$WZ \to \ell\ell\ell\nu$	$WH \to \ell\nu bb$	$ZH \to \nu\nu bb$	$\ell\nu$	$\tau\nu$	$tt1\ell$	$tt2\ell$	$tb1\ell$
E_T^{miss} Soft term resolution	S+B	S+B	S+B	S+B	S+B	S+B	S+B	S+B	S+B	S+B	S+B
E_T^{miss} Soft term scale	S+B	S+B	S+B	S+B	S+B	S+B	S+B	S+B	S+B	S+B	S+B
E_T^{miss} trigger					S+B	S+B		S+B			

Table 5.8: E_T^{miss} systematic uncertainties. The abbreviations "S" and "B" stand for signal and background respectively, while "–" denotes uncertainties that are not applicable, "negl." denotes uncertainties that are negligible. Each uncertainty is considered as correlated between the channels listed.

5.6.4 Small-R and Large-R Jets

For those analysis in the combination which include at least one small-R jet, experimental uncertainties are used for their associated sources. The scale and resolution of the jet energy are the most significant sources of uncertainty in this category. Following in magnitude are uncertainties related to jet flavor, pileup effects, punch-through, and uncertainties associated with the JVT. When using the same jet collection across study channels, these uncertainties are taken as correlated for both the signal and background distributions (refer to table 5.3). Large-R jets are also used in many analyses. For these, large-R jet energy and mass scale, along with resolution, are considered as experimental uncertainties on jet sub-structure variables such as the D_2 scale and resolution. These systematic sources are frequently divided into a number of orthogonal sub-components and treated as independent nuisance parameters in the different analyses. The uncertainties associated with large-R jets are also considered for both signal and background distributions.

Systematic Source	$WW \to \ell\nu\ell\nu$	$WW \to \ell\nu qq$	$WZ \to \ell\ell qq$	$WZ \to \nu\nu qq$	$WZ \to \ell\ell\ell\nu$	$WH \to \ell\nu bb$	$WH \to \nu\nu bb$	$\ell\nu$	$\tau\nu$	qq	$tt1\ell$	$tt2\ell$	$tb0\ell$	$tb1\ell$
Small-R jet energy resolution	S+B	S+B	S+B	S+B	S+B	S+B	S+B	S+B	S+B	S+B	S+B	S+B	S+B	S+B
Small-R jet energy scale	S+B	S+B	S+B	S+B	S+B	S+B	S+B	S+B	S+B	S+B	S+B	S+B	S+B	S+B
Small-R jet flavor	S+B	S+B	S+B	S+B	S+B	S+B	S+B	S+B	S+B		S+B	S+B	S+B	S+B
Small-R jet pileup	S+B	S+B	S+B	S+B	S+B	S+B	S+B	S+B	S+B		S+B	S+B	S+B	S+B
Small-R jet punch-through	S+B	S+B	S+B	S+B	S+B	S+B	S+B	S+B	S+B		S+B	S+B	S+B	S+B
Small-R jet JVT	S+B	S+B	S+B	S+B	S+B	S+B	S+B	S+B			S+B	S+B	S+B	S+B

Table 5.9: Small-R jet systematic uncertainties. The abbreviations "S" and "B" stand for signal and background respectively, while "negl." denotes uncertainties that are negligible. Each uncertainty is considered as correlated between the channels listed.

Systematic Source	$WW \to \ell\nu qq$	$WW \to qqqq$	$WZ \to \ell\ell qq$	$WZ \to qqqq$	$WZ \to \nu\nu qq$	$WH \to \ell\nu bb$	$WH \to \nu\nu bb$	$WH \to qqbb$	$ZH \to \ell\ell bb$	$ZH \to \nu\nu bb$	$ZH \to qqbb$	$tt0\ell$	$tt1\ell$	$tt2\ell$	$tb0\ell$
Large-R jet D_2 scale	S+B	S	S+B	S	S+B	S+B	S+B	S	S+B	S+B	S				
Large-R jet D_2 resolution	S+B	S	S+B	S	S+B	S+B	S+B	S	S+B	S+B	S				
Large-R jet scale	S+B	S	S+B	S	S+B	S+B	S+B	S	S+B	S+B	S		S+B	S+B	S+B
Large-R jet resolution	S+B	S	S+B	S	S+B	S+B	S+B	S	S+B	S+B	S		S+B	S+B	S+B
Large-R jet mass scale	S+B	S	S+B	S	S+B	S+B	S+B	S	S+B	S+B	S	S+B	S+B	S+B	S+B
Large-R jet mass resolution	S+B	S	S+B	S	S+B	S+B	S+B	S	S+B	S+B	S	S+B	S+B	S+B	S+B

Table 5.10: Large-R jet systematic uncertainties. The abbreviations "S" and "B" stand for signal and background respectively. Each uncertainty is considered as correlated between the channels listed.

5.6.5 Flavor Tagging

Many of the VV and VH analyses, as well as the tt and tb analyses, employ flavor-tagging to improve purity and help search separate signal regions. Flavor tagging uncertainties include those associated with b-tagging, c-tagging, light-jet tagging, and tagging extrapolation for high p_T regions.

Systematic Source	$WW \to \ell\nu\ell\nu$	$WW \to \ell\nu qq$	$WZ \to \ell\ell qq$	$WZ \to \ell\ell\ell\nu$	$WH \to \ell\nu bb$	$WH \to \nu\nu bb$	$WH \to qqbb$	$ZH \to \ell\ell bb$	$ZH \to \nu\nu bb$	$ZH \to qqbb$	bb	$tt0\ell$	$tt1\ell$	$tt2\ell$	$tb0\ell$	$tb1\ell$
b-tagging	S+B	S+B	S+B	S+B	S+B	S+B	S	S+B	S+B	S	S+B	S+B	S+B	S+B	S+B	S+B
c-tagging	S+B	S+B	S+B	S+B	S+B	S+B	S	S+B	S+B	S						
light-q tagging	S+B	S+B	S+B	S+B	S+B	S+B	S	S+B	S+B	S						
tagging extrapolation	S+B	S+B	S+B	S+B	S+B	S+B	S	S+B	S+B	S						

Table 5.11: Flavor-tagging systematic uncertainties. The abbreviations "S" and "B" stand for signal and background respectively. Each uncertainty is considered as correlated between the channels listed.

5.6.6 Background Theory Uncertainties

Only cross-section uncertainties are considered for top and diboson backgrounds in the leptonic searches since those background are relatively small, whereas VV and VH additionally consider uncertainties associated with these backgrounds' modelling. Multi-jet backgrounds frequently employ a data-driven approach, (such as that described in section 4.2.2), where uncertainties are considered in both the extrapolation method and modelling. The W+jets background and its uncertainties are included in this data-driven category for leptonic searches. These data-driven background uncertainties are considered as uncorrelated across analyses.

The $\tau\nu$ analysis, like the majority of the VV and VH analyses, takes modelling and cross-section uncertainty for the W+jets and Z+jets backgrounds into account. Those analyses which include W+jets as an important background (such as $WW \to \ell\nu qq$), the PDF eigenvector uncertainty, as well as the renormalization/factorization scale and α_S uncertainty, are included. The Drell-Yan background is dominant in the leptonic searches, and so their theoretical uncertainties are studied in great detail by their respective analyses, which take into account uncertainties related to PDF eigenvector variation, PDF choice, renormalization/factorization scales, α_S, electroweak corrections, and uncertainties associated with the photon-included background contribution. Drell-Yan uncertainties are specifically studied and arranged such that they are consistent and properly correlated across the leptonic analysis channels.

A summary table of all theoretical systematic uncertainties in their respective channels can be found in table 5.12.

Systematic Source	Corr	$WW \to \ell\nu\ell\nu$	$WW \to \ell\nu qq$	$WZ \to \ell\ell qq$	$WZ \to \nu\nu qq$	$WZ \to \ell\ell\ell\nu$	$WH \to \ell\nu bb$	$WH \to \nu\nu bb$	$ZH \to \ell\ell bb$	$ZH \to \nu\nu bb$	$\ell\ell$	$\ell\nu$	$\tau\nu$	$\tau\tau$	$tt0\ell$	$tt1\ell$	$tt2\ell$	$tb0\ell$	$tb1\ell$
Top cross section	No	B	B	B	B		B	B	B			B	B			B	B	B	B
Top modeling	No	B	B	B	B		B	B	B							B	B	B	B
Top extrapolation	No											B							
Diboson cross section	No	B	B	B	B		B	B	B				B						
Diboson extrapolation	No											B							
Multijet cross section	No		B			B	B						B			B	B	B	B
Multijet modeling	No					B	B				B	B							
Z+jets cross section	No		B	B	B		B	B	B				B						B
Z+jets modeling	No		B	B	B		B	B	B										B
W+jets cross section	No		B	B	B		B	B	B				B			B	B		B
W+jets modeling	No		B	B	B		B	B	B							B	B		B
W+jets PDF variation	No		B													B	B		B
W+jets scale	No		B													B	B		B
W+jets α_s	No		B													B	B		B
DY PDF variation	Yes										B	B	B						
DY PDF choice	Yes										B	B	B						
DY PDF scale	Yes										B	B	B						
DY α_s	Yes										B	B	B						
DY EW corrections	Yes										B	B	B						
DY Photon-Induced	Yes										B								

Table 5.12: Theoretical systematic uncertainties. The abbreviation "B" stands for background, while "–" denotes uncertainties that are not applicable, "negl." denotes uncertainties that are negligible, and "Corr" marks whether the uncertainty is correlated between the channels listed. The abbreviation "F" means that this parameter was left to float in the background control region for that channel. The systematic uncertainties in the background modeling for the fully hadronic analysis *qqqq* are embedded in the fit function used to model the background.

5.7 Statistical Treatment

The statistical interpretation of combining individual channels is done with a simultaneous analysis of the signal discriminants across all channels. For each signal model tested, only the channels sensitive to that hypothesis are considered in the combination. The statistical treatment of data is done using the RooFit [99], RooStats [100], and HistFactory [101] data modeling and handling toolkits. The signal parameterization used is to construct two-dimensional upper limits on the HVT model coupling strengths to SM particles.

5.7.1 Two-Dimensional Limits

To evaluate two-dimensional constraints on coupling strengths, signal yields are parameterized with a set of coupling parameters ($\mathbf{g}$), which allow the relative proportions of each signal to vary independently. Thus in the two-dimensional limit calculation, equation 4.22 is modified to allow the set of coupling parameters to be considered independently as

$$\mathcal{T}'(\mu) = -2\ln\frac{\mathcal{L}(\mathbf{g},\hat{\hat{\boldsymbol{\Theta}}}(\mathbf{g}))}{\mathcal{L}(\hat{\mathbf{g}},\hat{\boldsymbol{\Theta}}(\hat{\mathbf{g}}))}. \tag{5.1}$$

This coupling parameterization assumes all signal production proceeds via the qq-A process, which is proportional to g_q^2, and the signal decays are proportional to the square of their relevant couplings, which can be seen in table 5.13.

Multiple 2D coupling spaces are considered. The first coupling scenario makes the assumption of common fermionic couplings ($g_f = g_\ell = g_q$), and probes the (g_H, g_f) plane. The second coupling scenario allows independent fermionic coupling and probes the (g_q, g_ℓ) plane with either $g_H = 0$ or $g_H = -0.56$, where the latter takes the value predicted in the HVT-A benchmark scenario.

Coupling		Constraining Decays
g_f		$\ell\ell$, $\tau\tau$, $\ell\nu$, $\tau\nu$, $q\bar{q}$, $b\bar{b}$, $t\bar{t}$, tb
g_H		VV, VH
g_q	g_{q12}	$q\bar{q}$
	g_{q3}	$b\bar{b}$, $t\bar{t}$, tb
g_ℓ	$g_{\ell 12}$	$\ell\ell$, $\ell\nu$
	$g_{\ell 3}$	$\tau\tau$, $\tau\nu$

Table 5.13: HVT coupling parameters and the decay modes which constrain them.

The third coupling plane explored is (g_H, g_{q3}), where the values of g_ℓ and g_{q12}, or $g_{\ell 12}$ and g_{q12}, are set to their HVT-A or HVT-B values. An interesting region of the theoretical phase space is where the bosonic coupling is high as well as either the third generation quark coupling or both the third generation quark coupling and lepton coupling, which is represented by model point HVT-B. The top quark is expected to be particularly sensitive to novel physics related to the electroweak symmetry breaking and/or fermion mass hierarchy because of its strong Yukawa coupling. This idea overlaps with popular, explicit models of new physics such as the composite Higgs model [21]. To cause electroweak symmetry breaking in a composite Higgs model, the top is mostly composite. This explains the top quark's strong coupling to the Higgs and implies a strong coupling of the resonances of the composite sector, one of which is the heavy vector iso-triplet under study in this combination. Being composite, the HVT couples strongly to the Higgs (g_H can be large) and to the left-handed top and bottom quarks (g_{q3} can be large). Given that light-quarks and leptons are mostly elementary (g_{q12} and g_ℓ are small), this scenario couplings weakly to them. It is necessary to scan over g_{q3} and g_H couplings because their precise value is undetermined. The derived constraints are important in assessing the viability of these models.

Due to the hierarchical structure of the CKM matrix, research into these third generation couplings to new particles is also motivated from an experimental standpoint to help avoid

flavor limits. Even if there are typically strong electroweak precision limits on the couplings of the left-handed b-quark to new particles, these limits are much weaker for any scenario of the HVT model, as it preserves custodial symmetry. As a result, the direct searches at the LHC may be more sensitive to g_{q3} than electroweak precision data across wide portions of the parameter space.

The 95% CL upper limit contours in each coupling space are determined using $\mathcal{T}'$ by normalizing signal rates to the $\sigma \times \mathcal{B}$ predictions of the HVT model for the specified values of $\mathbf{g}$ at a given point in the space and calculating the value of $\mathrm{CL_s}$ at that point. Upper limits on coupling parameters are thus defined by contours of constant $\mathrm{CL_s} = 0.05$ in each coupling plane considered.

5.8 Results

Exclusion limits are presented for signal pole masses, of 2, 3, and 4 TeV in various coupling planes for the different sub-combinations of channels. As described in section 1.3.6.3, the coupling of the HVT W' and Z' to SM particles is determined independently from parameters in the HVT Lagrangian (equation 1.13). In this section there are limits set on three of the coupling planes which were explored: (g_H, g_f), (g_q, g_{q3}), and (g_H, g_{q3}) for reasons described in section 5.7.1. Here, the (g_H, g_f) planes are shown in figure 5.13 for the $t\bar{t}$ analyses and their combination and in figure 5.14 for the full combination and various sub-combinations. The (g_q, g_{q3}) planes are shown in figure 5.15 for the $t\bar{t}$ analyses and their combination and in figure 5.16 for the full combination and various sub-combinations. The (g_H, g_{q3}) planes are shown in figure 5.17 for the $t\bar{t}$ analyses and their combination and in figure 5.18 for the full combination and various sub-combinations; in this plane, the Z'_{TC2} benchmark model

for which limits were set in chapter 4 exists at the point (g_H, g_{q3}) = (-0.55, 1.73).

In each $t\bar{t}$ plane the combination of the $t\bar{t}$ channels produces stronger constraints than any individual channel alone, with constraints on the various model parameters becoming weaker with increasing resonance mass. For the $t\bar{t}$ combination plots, it is clear the $tt0\ell$ analysis is generally the strongest due to its high cross-section. $tt1\ell$ is also sensitive with a reasonable and better $m_{t\bar{t}}$ resolution than the $tt0\ell$ channel. $tt2\ell$ was found to be less sensitive, though still interesting and worth including, with the relatively low sensitivity coming from having the lowest cross-section, despite it having the best $m_{t\bar{t}}$ resolution. Figure 5.14 shows sub-combination contours in the (g_H, g_f) plane; when looking at all of the fermion couplings together the leptonic channels naturally dominate, with the third generation channels adding some slight further sensitivity. In figures 5.15 and 5.16, as $g_H = g_\ell = 0$, the limits are centered on a region of phase space that is quark dominated.

In the planes of various combinations, it is easy to see how the full combination constraints are constructed from constraints from the various sub-combinations. In figure 5.16, for example, the full combination limits are constrained to a cross centered at the origin by the $tt + tb + bb$ sub-combination and further constrained vertically by the qq results. 5% and 10% width contours are overlaid on each plane to show the regions where the narrow width approximation holds. These width contours are especially relevant in figure 5.18, where the $tt + tb + bb$ contour is out of view for the 3 TeV and 4 TeV cases, but which we consider to be less relevant to our results as the contour is outside of the narrow width approximation regime. Here, the $qq + \ell\ell + \ell\nu + \tau\nu$ limits do not have a direct dependence on g_H or g_{q3}, though their cross-sections are not necessarily negligible in this region of phase-space. Their strength indirectly relies on the parameters being scanned over as more or less branching fraction is available to their decay channels. This means that the interpretation

of this contour is slightly different than the others shown, as the $qq + \ell\ell + \ell\nu + \tau\nu$ on its own excludes almost the entire plane. For 3 TeV and 4 TeV the dominance of the $qq+\ell\ell+\ell\nu+\tau\nu$ sub-combination subsides. Note here that for the full combination, the allowed regions are those areas at the top and bottom of the shown planes. In this region, the $tt+tb+bb$ channels would enter from the top and bottom of the shown region, but are too weak in sensitivity to enter the planes as shown. However, they are still included in the full combination.

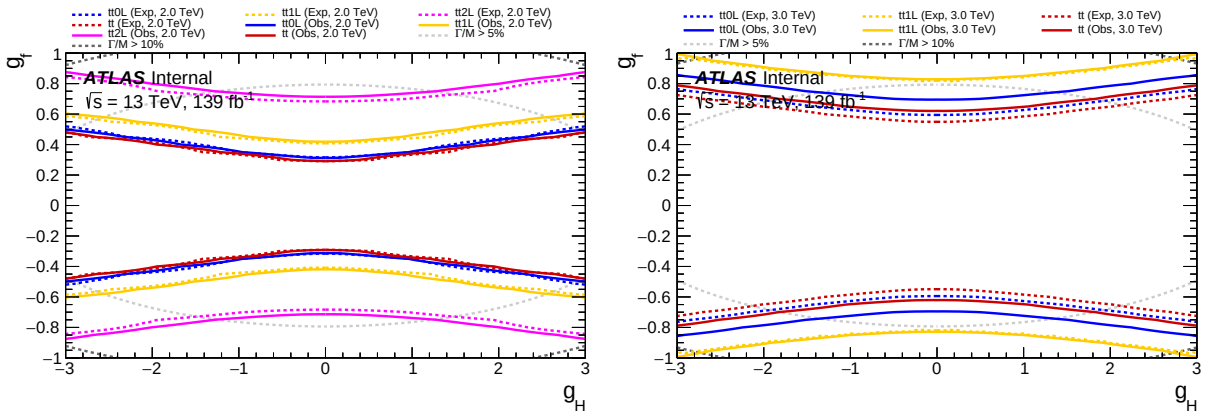

(a) (b)

Figure 5.13: Excluded limits at 95% confidence for the $t\bar{t}$ analyses on the HVT model in the slice of parameter space (g_H, g_f) with other parameters set to their HVT-A values for (a) 2 TeV and (b) 3 TeV resonances. 4 TeV contours were calculated but exist off the plane shown here. Solid lines denote the observed limits, while dashed lines denote expected limits. Dashed grey and black lines denote resonance width (Γ/M) regions for 5% and 10%, respectively.

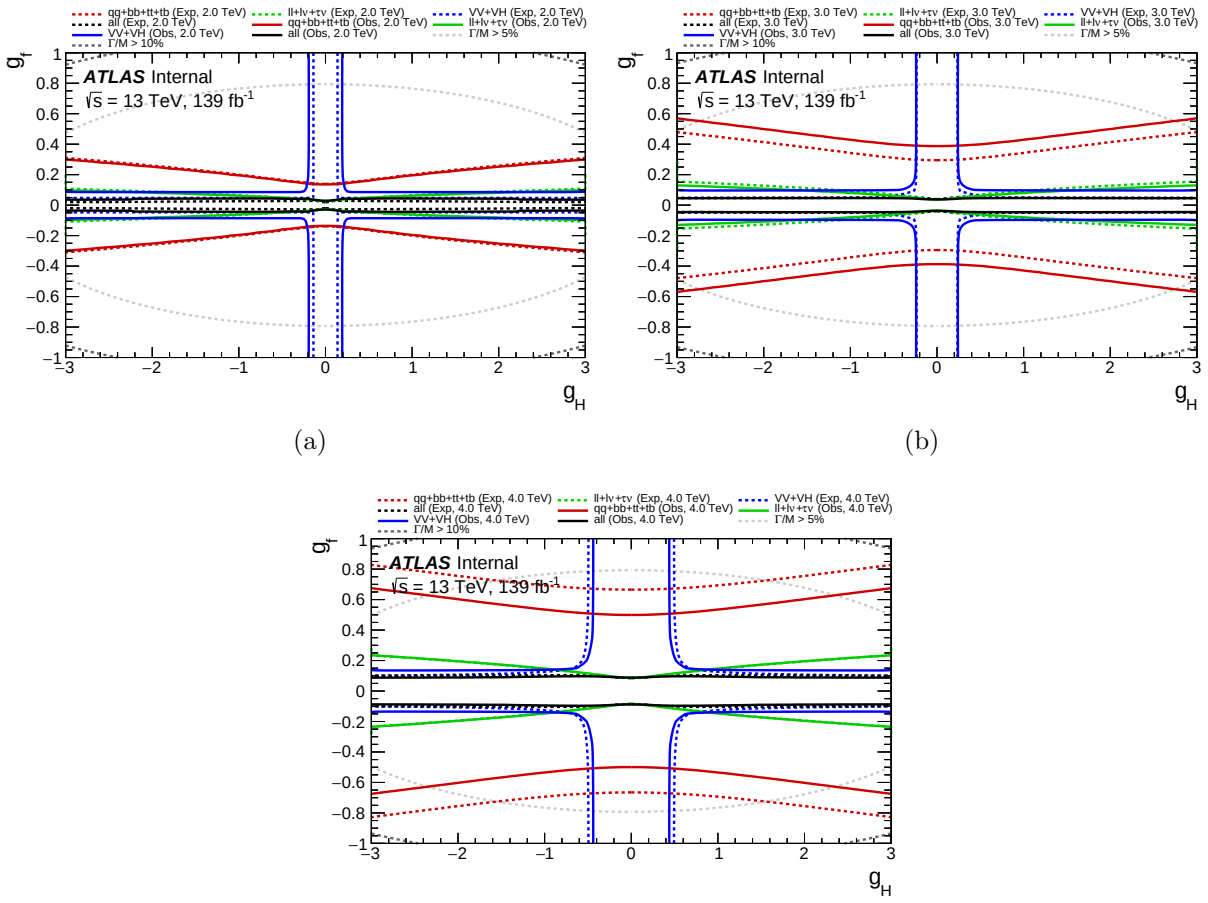

(a) (b)

(c)

Figure 5.14: Excluded limits at 95% confidence for different combinations on the HVT model in the slice of parameter space (g_H, g_f) with other parameters set to their HVT-A values for (a) 2 TeV, (b) 3 TeV, and (c) 4 TeV resonances. Solid lines denote the observed limits, while dashed lines denote expected limits. Dashed grey and black lines denote resonance width (Γ/M) regions for 5% and 10%, respectively. "All" denotes the full combination.

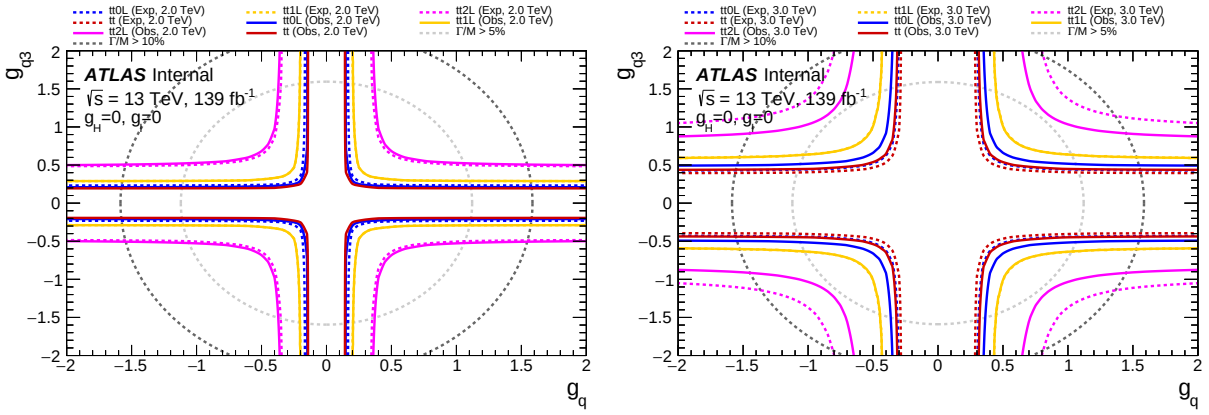

(a) (b)

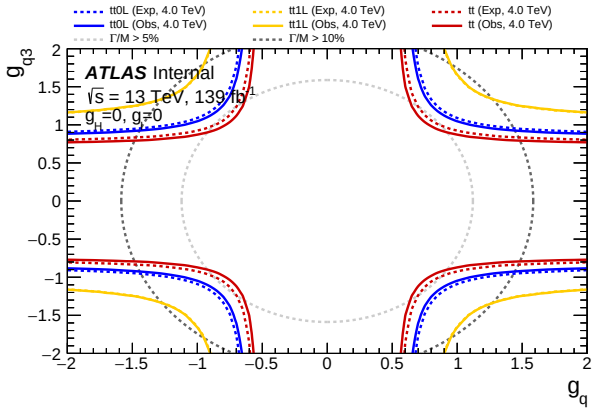

(c)

Figure 5.15: Excluded limits at 95% confidence for the $t\bar{t}$ analyses on the HVT model in the slice of parameter space (g_q, g_{q3}) with other parameters set to zero for (a) 2 TeV, (b) 3 TeV, and (c) 4 TeV resonances. Solid lines denote the observed limits, while dashed lines denote expected limits. Dashed grey and black lines denote resonance width (Γ/M) regions for 5% and 10%, respectively.

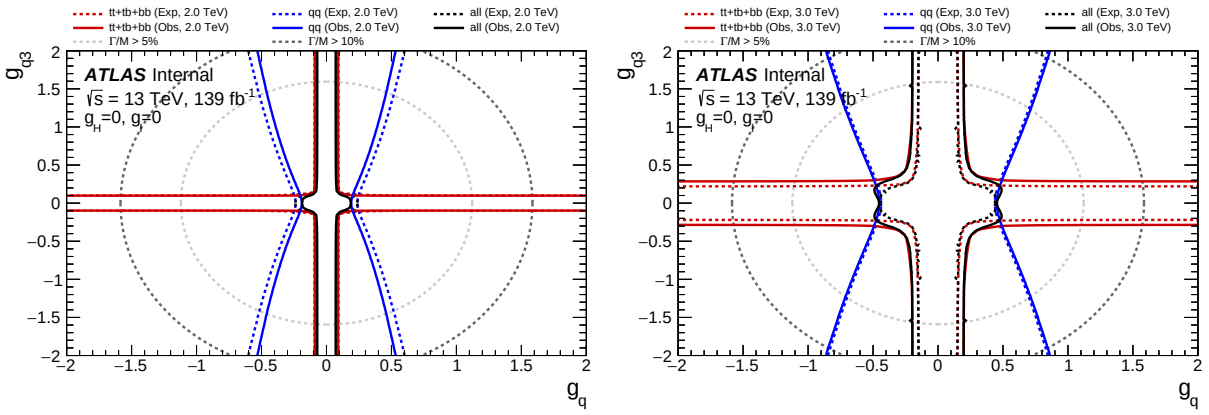

(a) (b)

(c)

Figure 5.16: Excluded limits at 95% confidence for different combinations on the HVT model in the slice of parameter space (g_q, g_{q3}) with other parameters set to zero for (a) 2 TeV, (b) 3 TeV, and (c) 4 TeV resonances. Solid lines denote the observed limits, while dashed lines denote expected limits. Dashed grey and black lines denote resonance width (Γ/M) regions for 5% and 10%, respectively. "All" denotes the full combination.

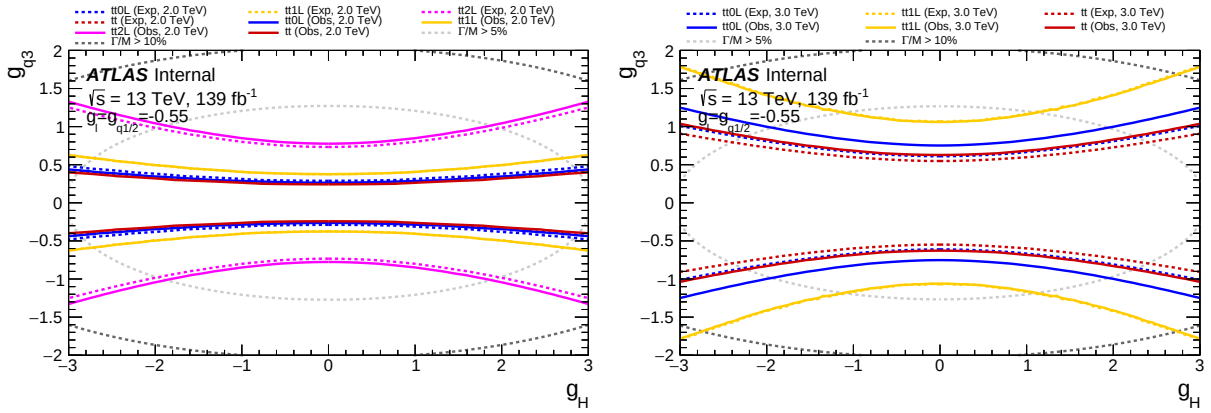

(a) (b)

Figure 5.17: Excluded limits at 95% confidence for the $t\bar{t}$ analyses on the HVT model in the slice of parameter space (g_H, g_{q3}) with other parameters set to their HVT-A values for (a) 2 TeV and (b) 3 TeV resonances. 4 TeV contours were calculated but exist off the plane shown here. Solid lines denote the observed limits, while dashed lines denote expected limits. Dashed grey and black lines denote resonance width (Γ/M) regions for 5% and 10%, respectively.

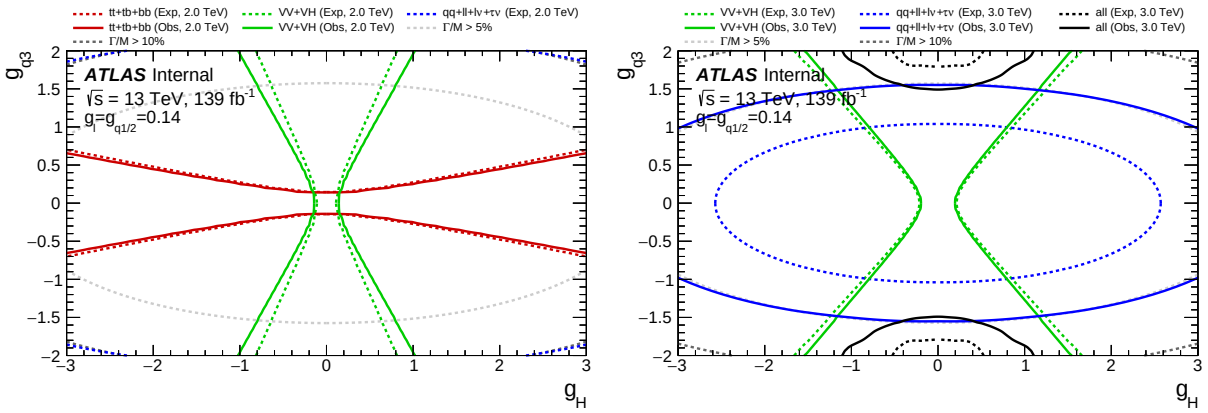

(a) (b)

(c)

Figure 5.18: Excluded limits at 95% confidence for different combinations on the HVT model in the slice of parameter space (g_H, g_{q3}) with other parameters set to their HVT-B values for (a) 2 TeV, (b) 3 TeV, and (c) 4 TeV resonances. Solid lines denote the observed limits, while dashed lines denote expected limits. Dashed grey and black lines denote resonance width (Γ/M) regions for 5% and 10%, respectively. "All" denotes the full combination.

Chapter 6

Conclusions

This thesis represents my work on searches for heavy resonances in (a) a $t\bar{t}$ semi-leptonic final state and (b) the combination of that $t\bar{t}$ search with many other analyses searching for heavy resonances in other final states. The studies presented here pay special attention to possible resonant production of BSM bosons coming from new U(1) symmetries. Each search uses data corresponding to an integrated luminosity of 139 fb^{-1} from 13 TeV pp collisions gathered using the ATLAS detector from 2015-2018. Additionally, I performed my ATLAS authorship qualification task on a hardware upgrades to the ATLAS Muon Spectrometer, which is detailed in appendix A.

6.1 Search for Heavy Resonance Decays to Top Quark Pairs Using a Lepton-Plus-Jets Final State

A search for new resonant states decaying $t\bar{t}$ in the $l\nu bqqb$ final state was performed. This analysis used 139 fb^{-1} of data and advances in top-tagging, b-tagging, overlap removal, and $t\bar{t}$ NNLO reweighting to improve upon previous results from a search in the same final state using 36 fb^{-1} of data. The main discriminant in the search was the invariant mass of the $t\bar{t}$ system, where any potential signal was expected to be observed as a bump in the falling background spectrum. All major SM backgrounds were modelled using Monte Carlo

simulation except for the QCD multijet processes, which were estimated using a data-driven method. The primary search strategy was to perform a model-independent statistical search on $m_{t\bar{t}}$; in the absence of any significant derivations, an upper limit at 95% confidence was set on the cross-section times branching ratio of the Z'_{TC2} and G_{KK} signal models. The observed 95% confidence lower limit on the mass of Z'_{TC2} is found to be 4.2 TeV, while the limit on the mass of G_{KK} is found to be 1.0 TeV. This represents an improvement over previous results using 36 fb^{-1} of data of 1.2 TeV and 0.35 TeV for the Z'_{TC2} and G_{KK}, respectively.

6.2 Combination of Searches for Heavy Resonances

The above $t\bar{t}$ heavy resonance search was combined with other heavy resonance searches in different final states. The combined results were interpreted in the context of models with a heavy vector boson triplet. This combination made improvements on previous combination efforts by using an 139 fb^{-1} of data, exploring new and theoretically interesting planes in the HVT coupling space, and including analyses searching for heavy resonances decaying into light and third generation quarks and leptons for the first time in the ATLAS collaboration. Compared to individual analyses, the results of the combination strengthened the constraints on BSM physics and allowed those constraints to be expressed in terms of the couplings of potential new physics to known SM particles. The combined results were used to place constraints on the couplings of heavy vector bosons to quarks, leptons, and bosons.

APPENDICES

Appendix A

sMDT Construction

A new style of small-diameter Monitored Drift Tube (sMDT) [102] has been designed for the Muon Spectrometer (described in section 2.3) of the ATLAS detector for the purpose of handling higher collision rates expected after the High Luminosity LHC (HL-LHC). The MDTs currently installed in the ATLAS detector are 30 mm in diameter, while the sMDT diameter is 15 mm. sMDTs are made of aluminum and have a sensing wire of diameter 50 μm through their center. They are operated at a potential of 2700 V and are filled with a gas mixture of Ar:CO_2 at a ratio of 93:7 and a pressure of 3 bar. This decreased diameter allows for a significantly shorter drift time of ionized particles in the gas contained in the drift tubes, which can be seen in figure A.1. Due to the nonlinear space-to-drift time relationship, the maximum drift time is reduced from 700 ns for the MDT tube to 200 ns for the sMDT tube. With the smaller cross-section of the sMDT and smaller maximum drift time, this improves the drift tube occupancy by a factor of eight. As such, sMDTs are well suited for high detection rates in a harsh radiation environment. My responsibilities on this project were to help design the quality control tests and set up their associated apparatuses, train undergraduates in the construction of sMDTs, and design initial version of software for data collection.

The Michigan State University ATLAS group is responsible for the construction and quality assurance of 260,000 of these tubes, after which they are sent to the University of

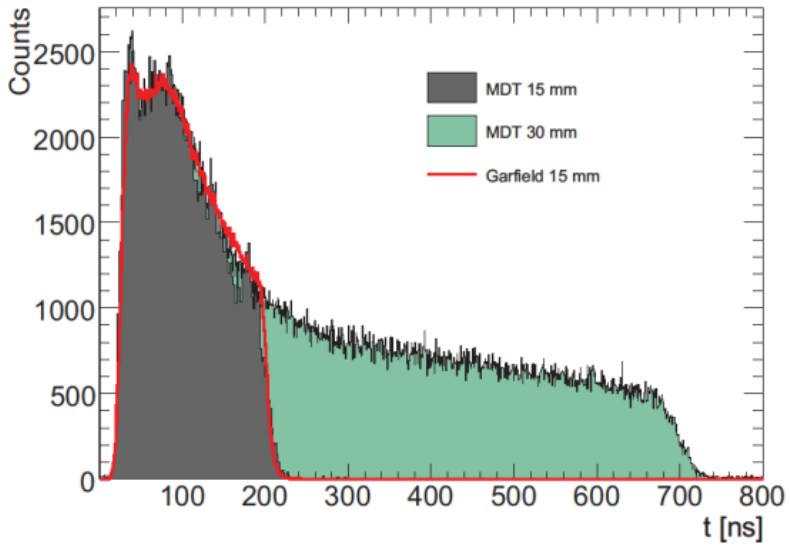

Figure A.1: Drift time spectrum for the MDT (green) and sMDT (grey) tubes. Prediction from the GARFIELD simulation [103] for the sMDT tube is shown by the red line [104]. Figure from reference [105]

Michigan for installation into sMDT chambers which will replace the current MDT chambers of the barrel inner station of the Muon Spectrometer. This process includes wiring the tube and pre-made end-cap combos, swaging the tube and end-cap to create a robust seal and proceeding with quality control tests.

The first these quality control tests is for the tension of the wire which extends down the length of the tube. For a wire of length L and tension T, let the mid-point displacement be given by

$$\Delta = \kappa \frac{L^2}{T}, \tag{A.1}$$

where κ is characteristic of the wire material and geometry. For the sMDT tubes described here, the sag tolerance is 17 ± 1 μm, which corresponds to a wire tension of $T = (350 \pm 15)g$ grams, where g is the acceleration due to gravity [102]. The wire inside

a tube is fixed on both ends and so vibrations cause a standing wave given by the one dimensional wave equation

$$\frac{\partial^2 u}{\partial t^2} = \frac{T}{\mu}\frac{\partial^2 u}{\partial x^2}. \tag{A.2}$$

Solving the wave equation give the wire tension as a function of its fundamental frequency f, the linear density, and the length of the wire

$$T = 4L^2 f^2 \mu. \tag{A.3}$$

Because the length and linear density of the wire are known quantities, the tension can be measured by measuring the wire's fundamental frequency. To accomplish this, we take advantage of the fact that the sMDT forms a cylindrical capacitor with a capacitance determined by the position of the wire. By placing the sMDT in a strong magnetic field and changing the wire with a current, we can cause the capacitance to change as

$$U(t) = U_0 \left[1 - \exp\left(-\frac{t}{RC(t)}\right)\right]. \tag{A.4}$$

Thus, by measuring the voltage of the wire with respect to a ground, the capacitance can be measured as a function of time. Once the capacitance measurements are known, the fundamental frequency can be arrived at via a Fast Fourier Transform (FFT). The hardware for running this test can be seen in figure A.2.

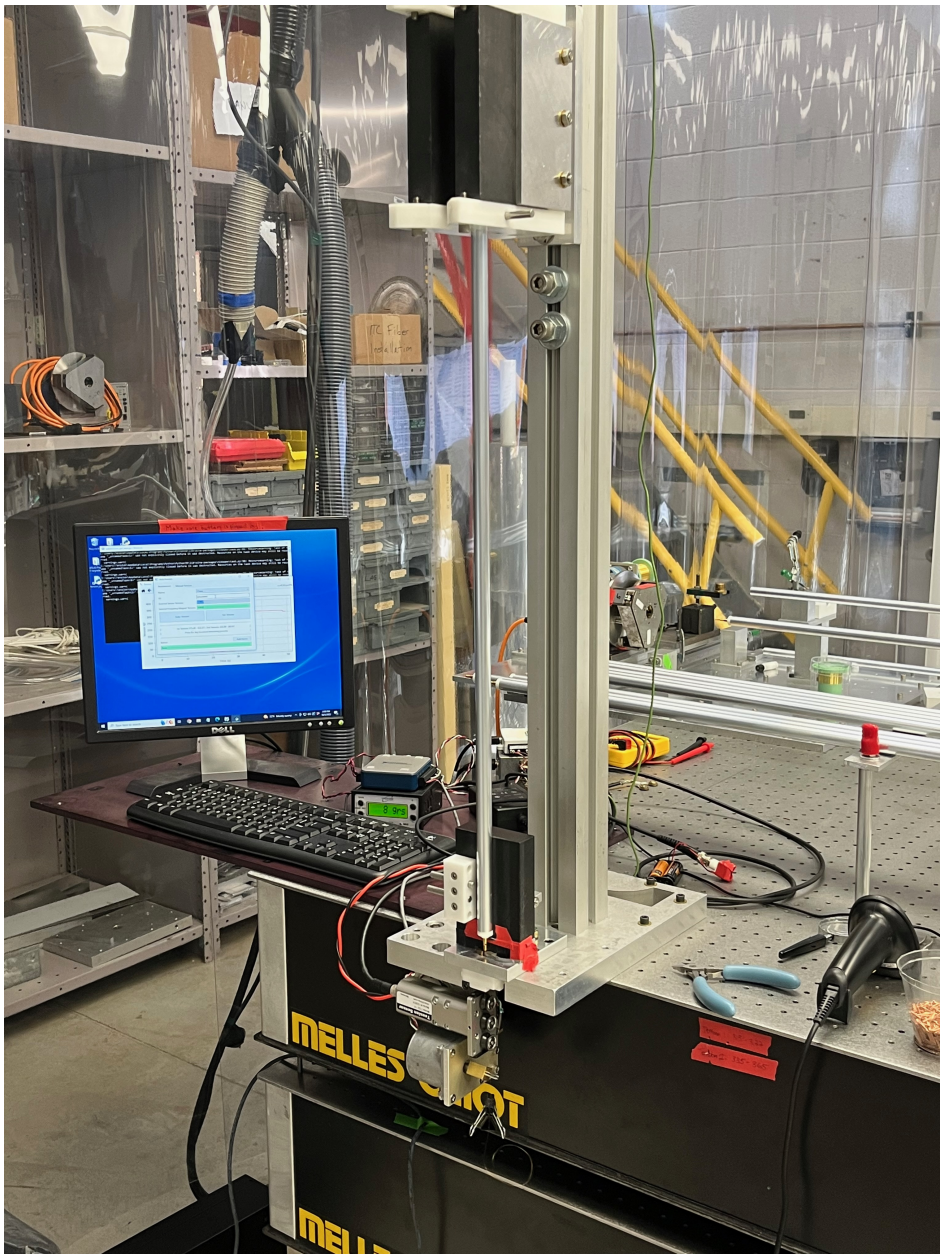

Figure A.2: Tension testing station for the sMDT internal wire.

To test the rate of gas leakage for the $ArCO_2$ mixture, each tube is placed in a vacuum chamber created by an Agilent leak detector. After a vacuum is created outside the tube, the tube itself is filled with helium gas and the leak detector checks the vacuum for helium. The acceptable failure rate for the $ArCO_2$ gas mixture is 1×10^{-8} $\frac{\text{mbar} \times \text{cm}^3}{\text{s}}$. The Agilent leak detector and vacuum pipe for inserting the tube into can be seen in figure A.3.

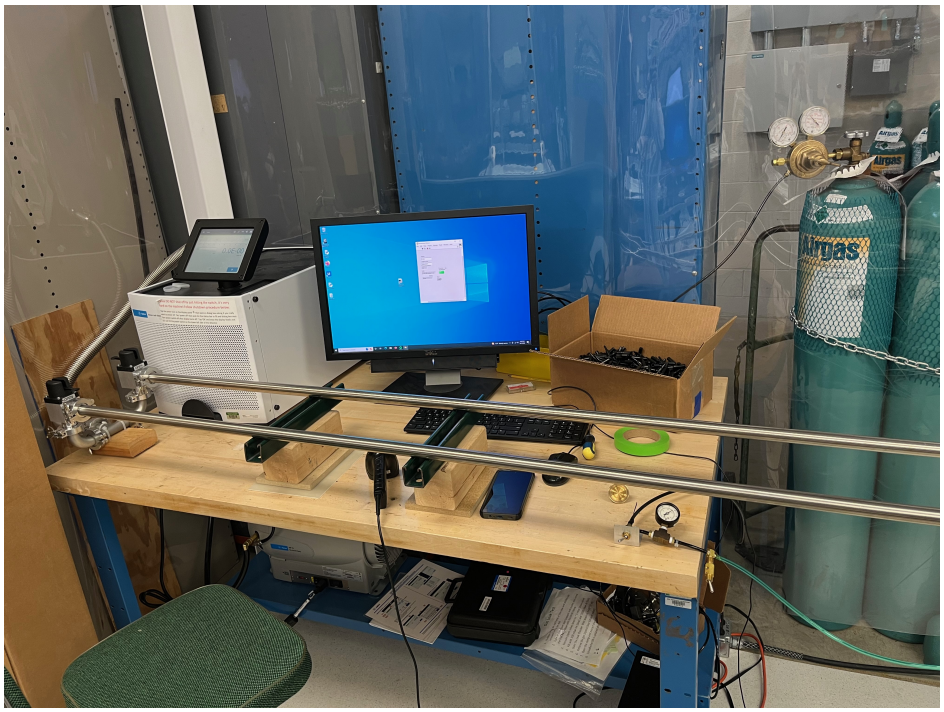

Figure A.3: Leak testing station for the sMDT tube.

Lastly the current leakage between the central wire and outer surface of the tube is tested. The wire and tube surface are held at a potential difference of 3 kV overnight. The maximum acceptable tube dark current is 2 nA. The dark current testing setup is shown in figure A.4. Each tube is individually tested for leakage current in a test that takes approximately one hour to test 32 tubes.

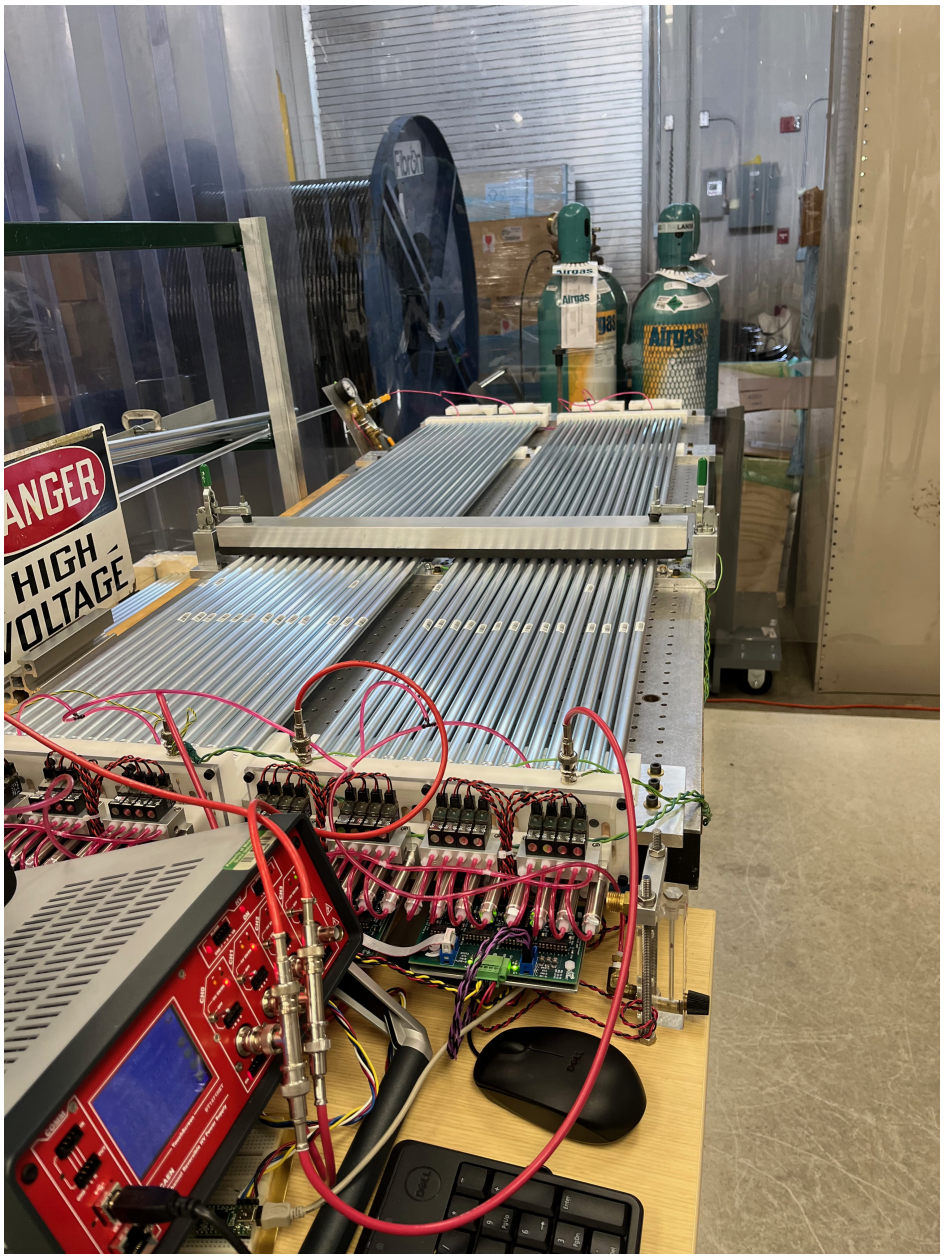

Figure A.4: Leak testing station for the sMDT tube.

Appendix B

Pre-fit $m_{t\bar{t}}$ Spectra for the $t\bar{t}1\ell$ Analysis

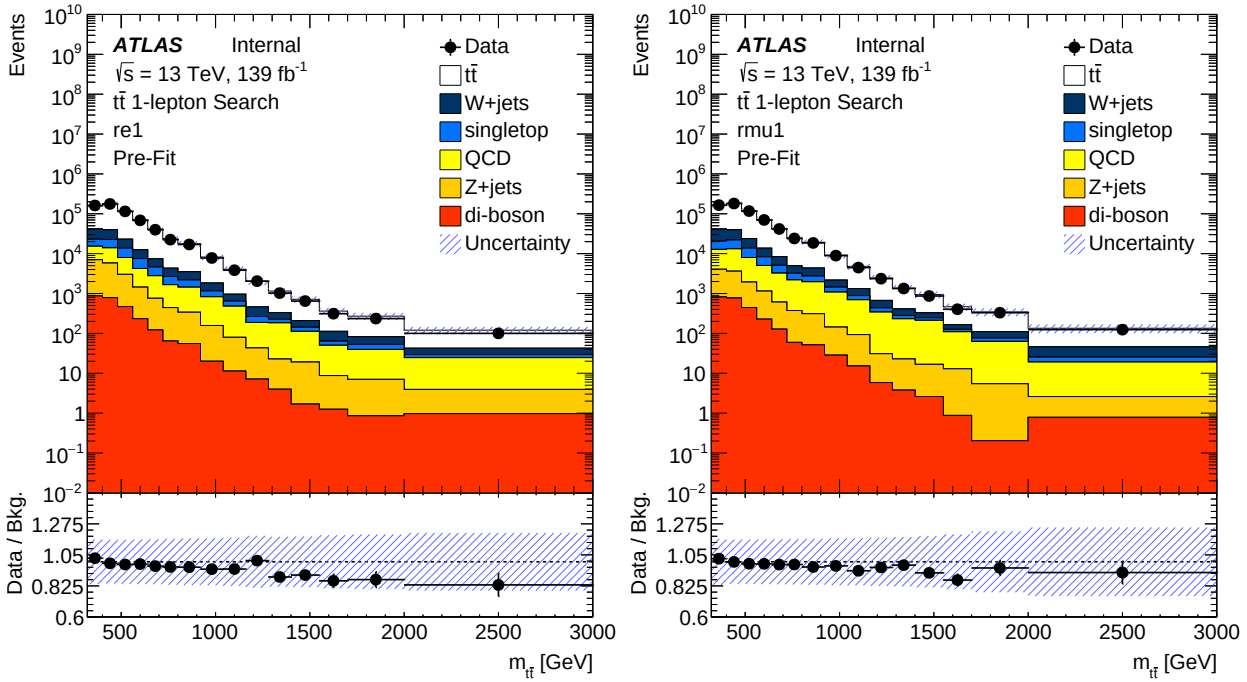

(a)

(b)

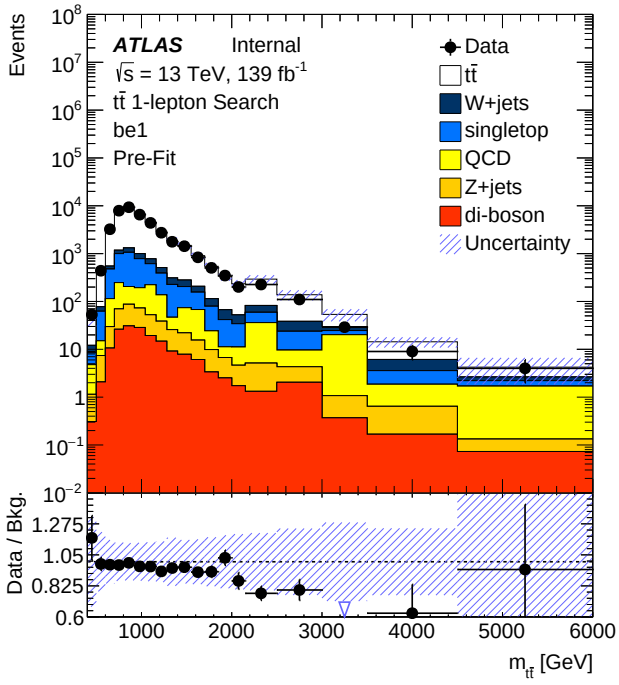

(c)

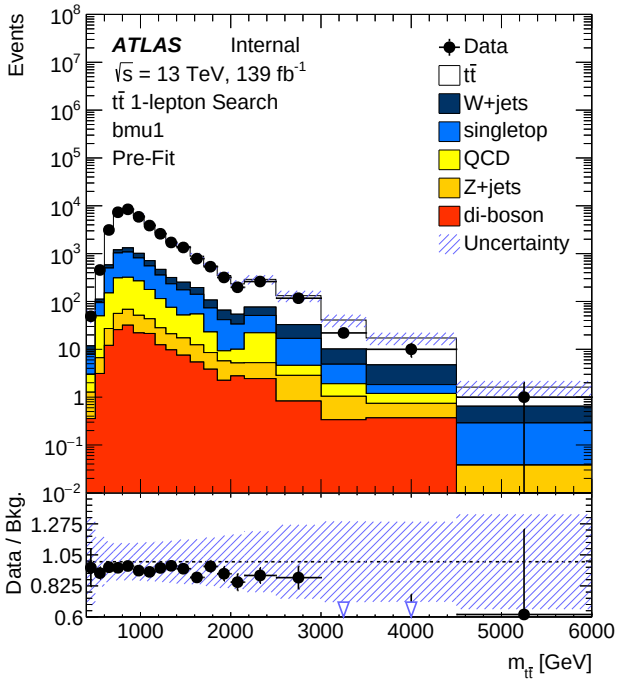

(d)

Figure B.1: Pre-fit plots for the 1 b-tag category for (a) resolved e, (b) resolved μ (c) boosted e, and (d) boosted μ.

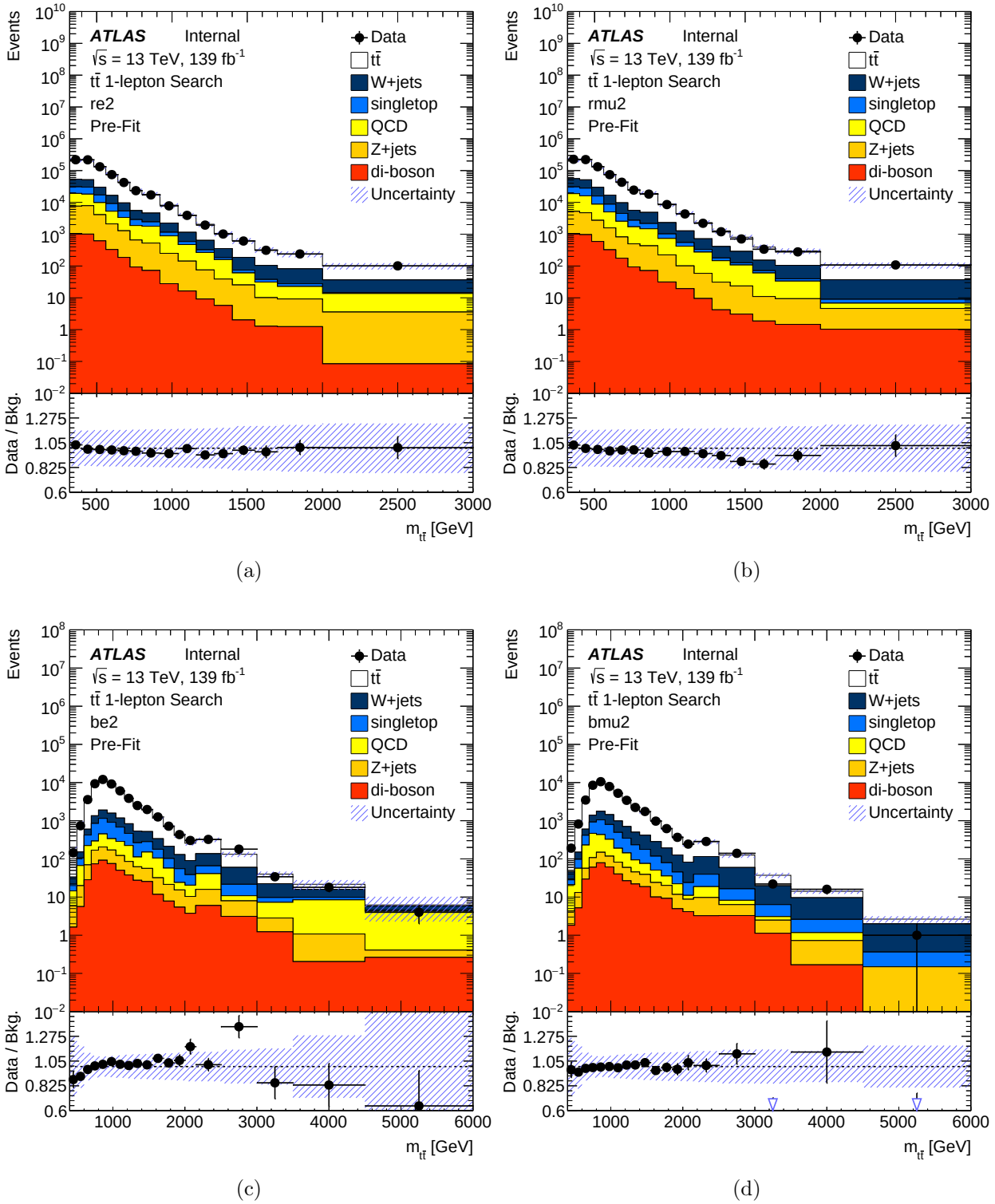

Figure B.2: Pre-fit plots for the 2 b-tag category for (a) resolved e, (b) resolved μ (c) boosted e, and (d) boosted μ.

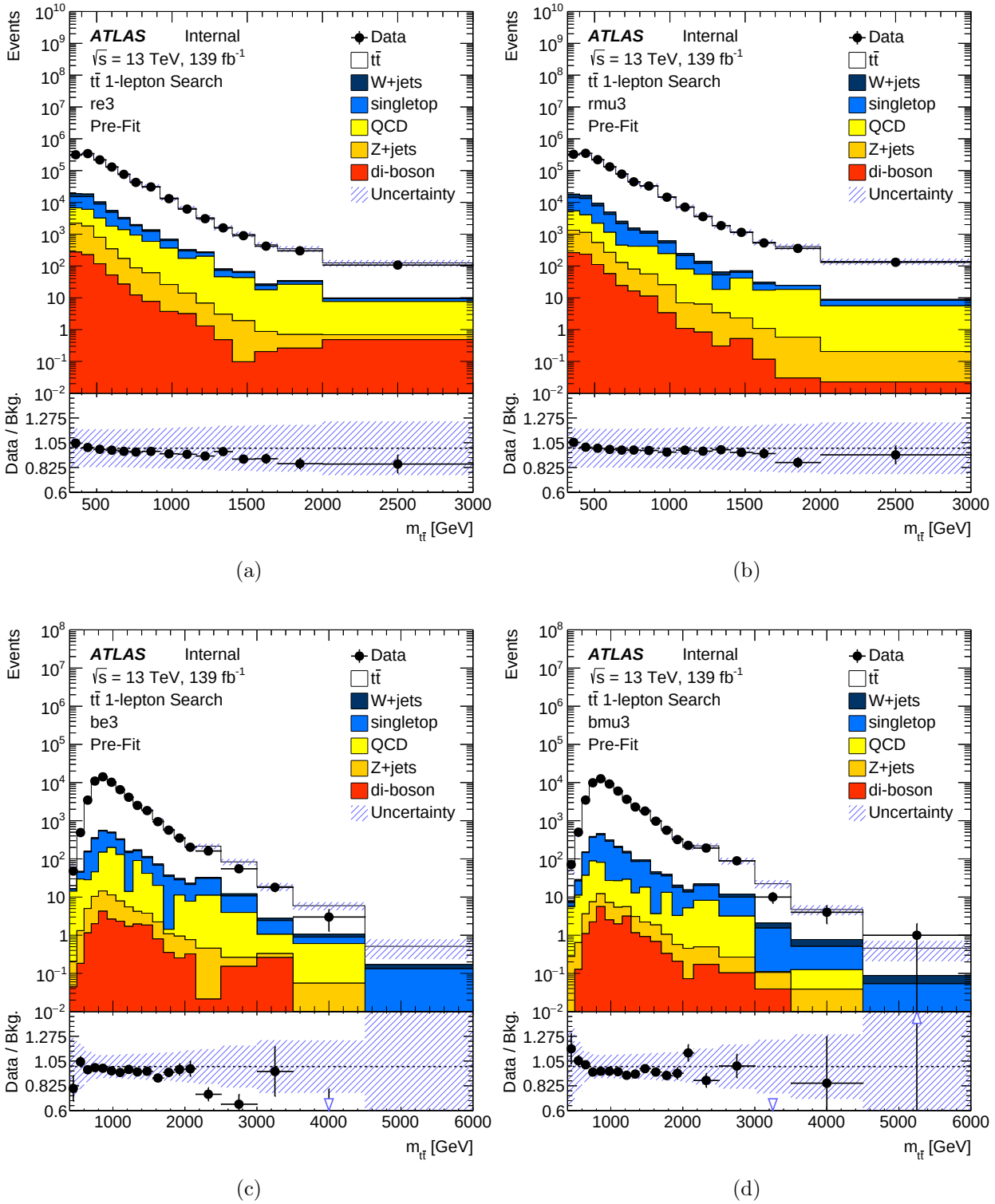

Figure B.3: Pre-fit plots for the 3 b-tag category for (a) resolved e, (b) resolved μ (c) boosted e, and (d) boosted μ.

Appendix C

Performance of the QCD multi-jet background estimation

To study the performance the multijet prediction the distributions of several observables have been validated in the $CR^{4j,1b}_{\text{QCD}}$ control region. Figures C.11 and C.12 show a good agreement between the data and the prediction. This closure test demonstrates the chosen parametrisation is able to reproduce the main kinematic dependence of the fake rates. Then two validation regions $VR1^{4j,1b}_{\text{QCD}}$ and $VR2^{4j,1b}_{\text{QCD}}$ have been defined in order to validate the multijet predictions using the same selection considered in $CR^{4j,1b}_{\text{QCD}}$, expect the selection cuts listed in C.1. Figures C.13, C.14, C.15 and C.16 show the good agreement between the prediction and the data for both validation regions and both muon and electron channels respectively in the resolved regime. The impact of the ΔR correction for the muon channel is shown on Figures C.17.

Validation region definition	
First validation region,$VR1^{4j,1b}_{\text{QCD}}$	Second Validation region, $VR2^{4j,1b}_{\text{QCD}}$
$E_T^{\text{miss}} < 20$ GeV, $E_T^{\text{miss}} + m_T^W > 60$ GeV	$E_T^{\text{miss}} > 20$ GeV, $E_T^{\text{miss}} + m_T^W < 60$ GeV

Table C.1: Definitions of validation regions.

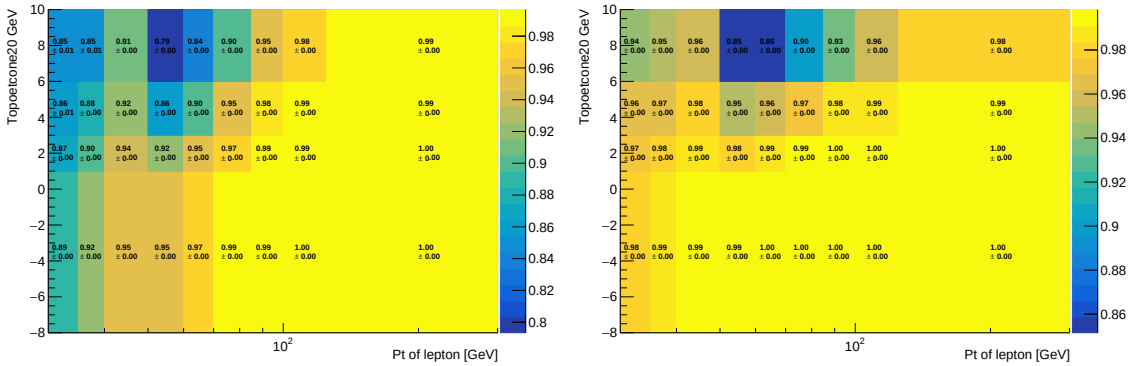

Figure C.1: Signal efficiency in the muon channel for $\Delta R_{\text{min}}(\ell, j) > 0.4$ (a) and for $\Delta R_{\text{min}}(\ell, j) < 0.4$ (b).

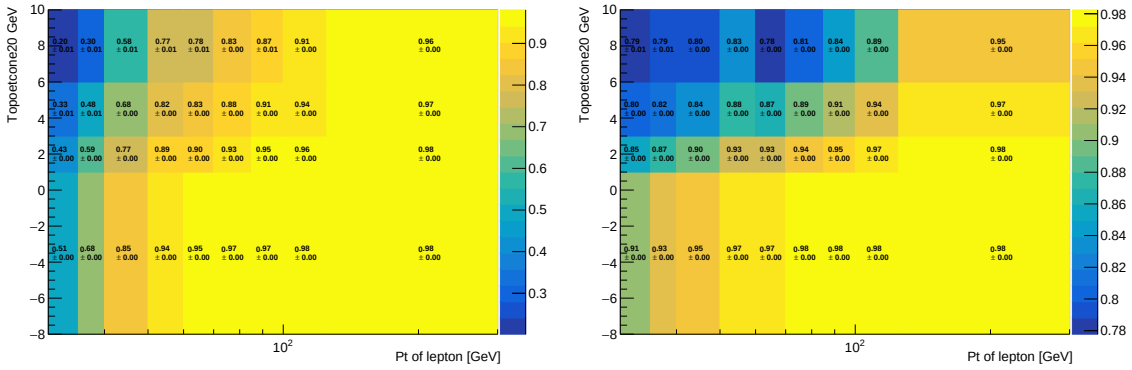

Figure C.2: Signal efficiency in the electron channel for $\Delta R_{\text{min}}(\ell, j) > 0.4$ (a) and for $\Delta R_{\text{min}}(\ell, j) < 0.4$ (b).

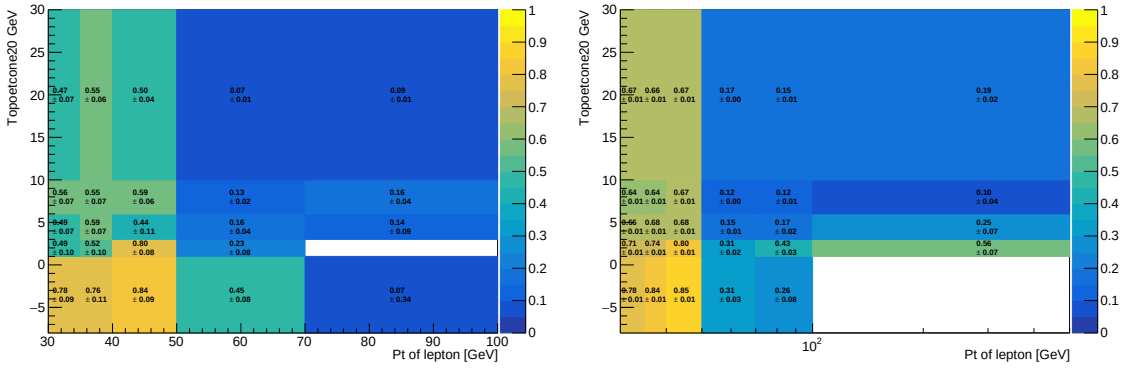

Figure C.3: Fake rate in the muon channel for $\Delta R_{\text{min}}(\ell, j) > 0.4$ (a) and for $\Delta R_{\text{min}}(\ell, j) < 0.4$ (b).

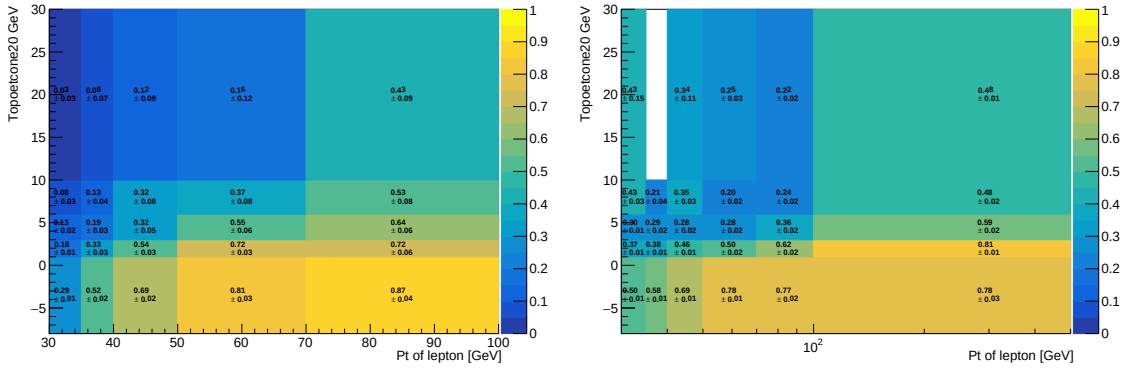

Figure C.4: Fake rate in the electron channel for $\Delta R_{\text{min}}(\ell, j) > 0.4$ (a) and for $\Delta R_{\text{min}}(\ell, j) < 0.4$ (b).

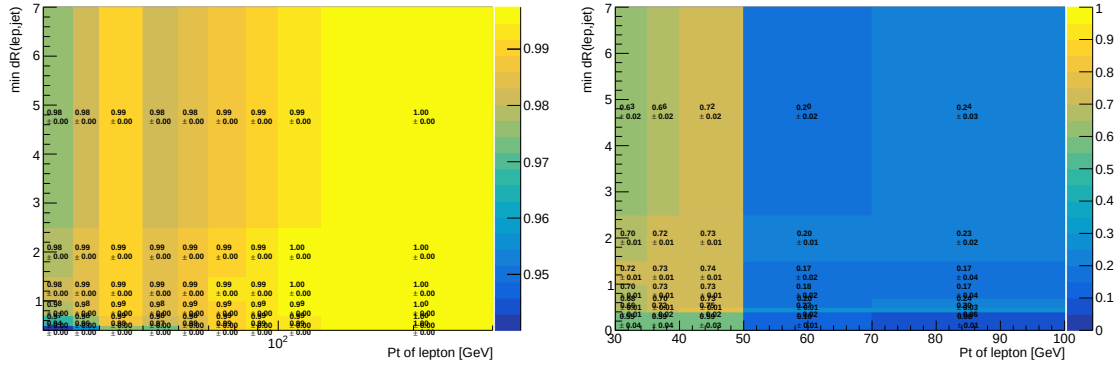

Figure C.5: Signal efficiency (a) and fake rate (b) in the muon channel. The fractions are split into muon p_T and $\Delta R_{\text{min}}(\ell, j)$ bins.

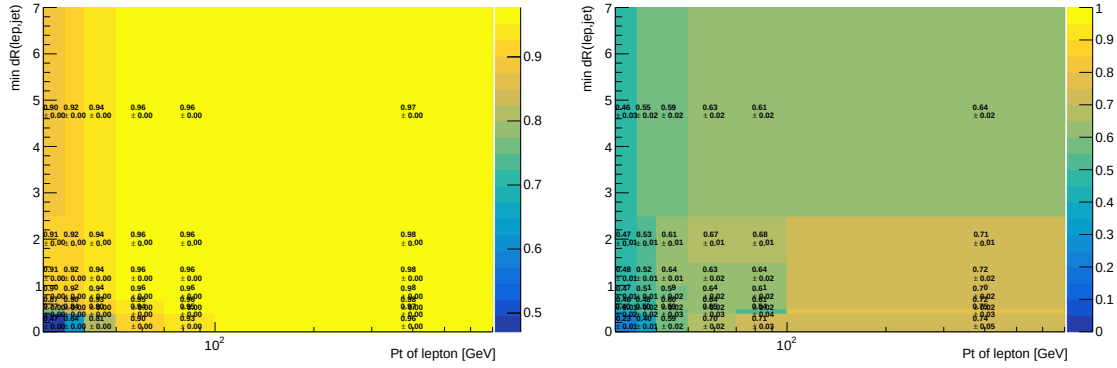

Figure C.6: Signal efficiency (a) and fake rate (b) in the electron channel. The fractions are split into muon p_T and $\Delta R_{\text{min}}(\ell, j)$ bins.

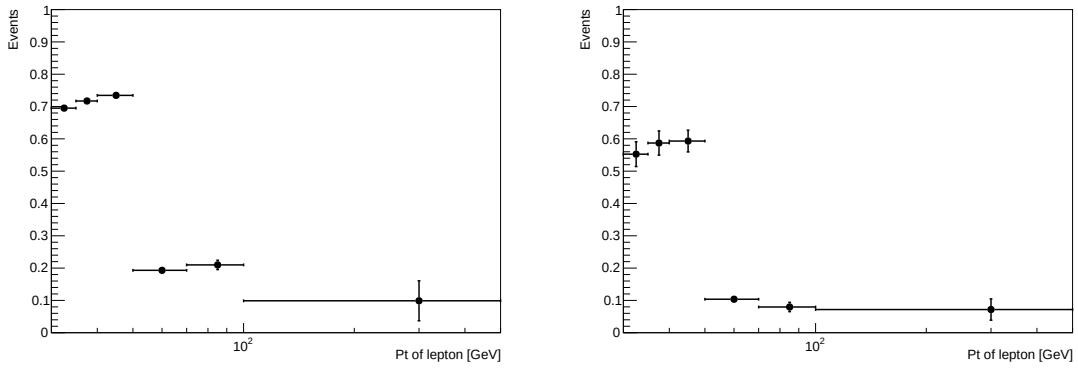

Figure C.7: Fake rate in the muon channel for $\Delta R_{\min}(\ell, j) < 0.4$ (a) and for $\Delta R_{\min}(\ell, j) > 0.4$ (b).

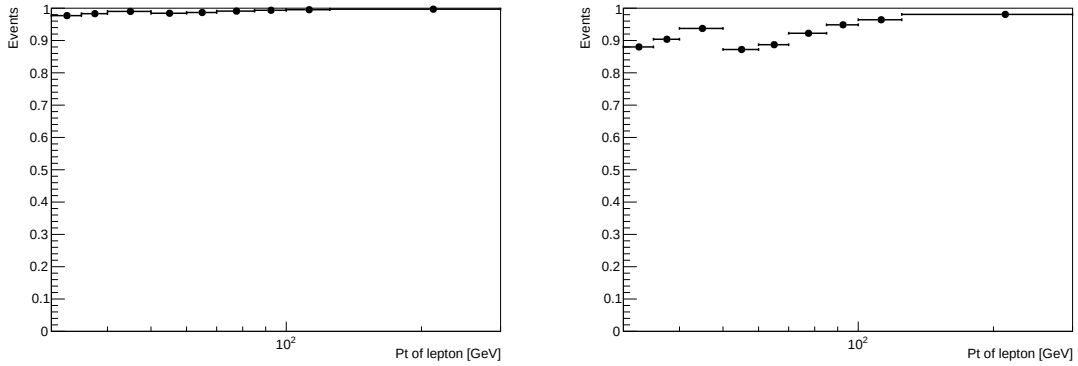

Figure C.8: Signal efficiency in the muon channel for $\Delta R_{\min}(\ell, j) > 0.4$ (a) and for $\Delta R_{\min}(\ell, j) < 0.4$ (b).

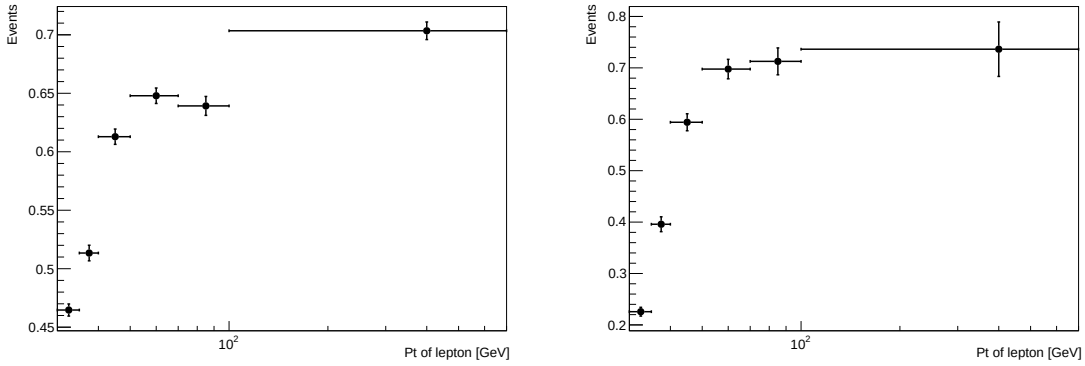

Figure C.9: Fake rate in the electron channel for $\Delta R_{\min}(\ell, j) > 0.4$ (a) and for $\Delta R_{\min}(\ell, j) < 0.4$ (b).

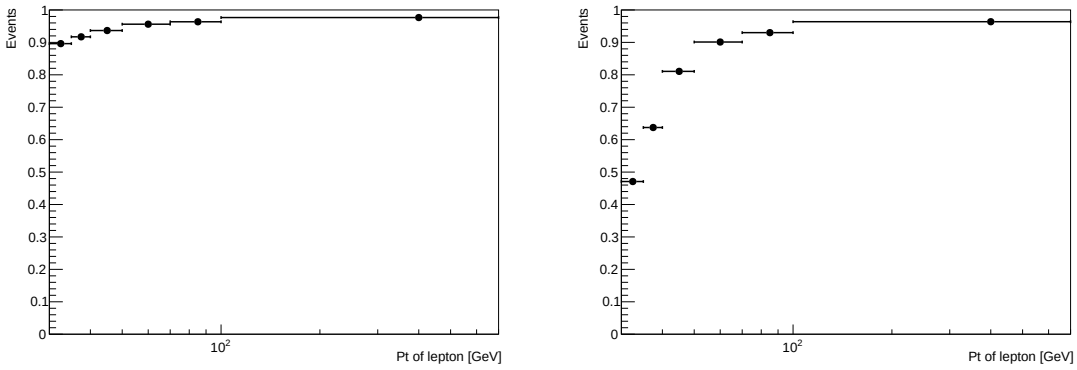

Figure C.10: Signal efficiency in the electron channel for $\Delta R_{\min}(\ell, j) > 0.4$ (a) and for $\Delta R_{\min}(\ell, j) < 0.4$ (b).

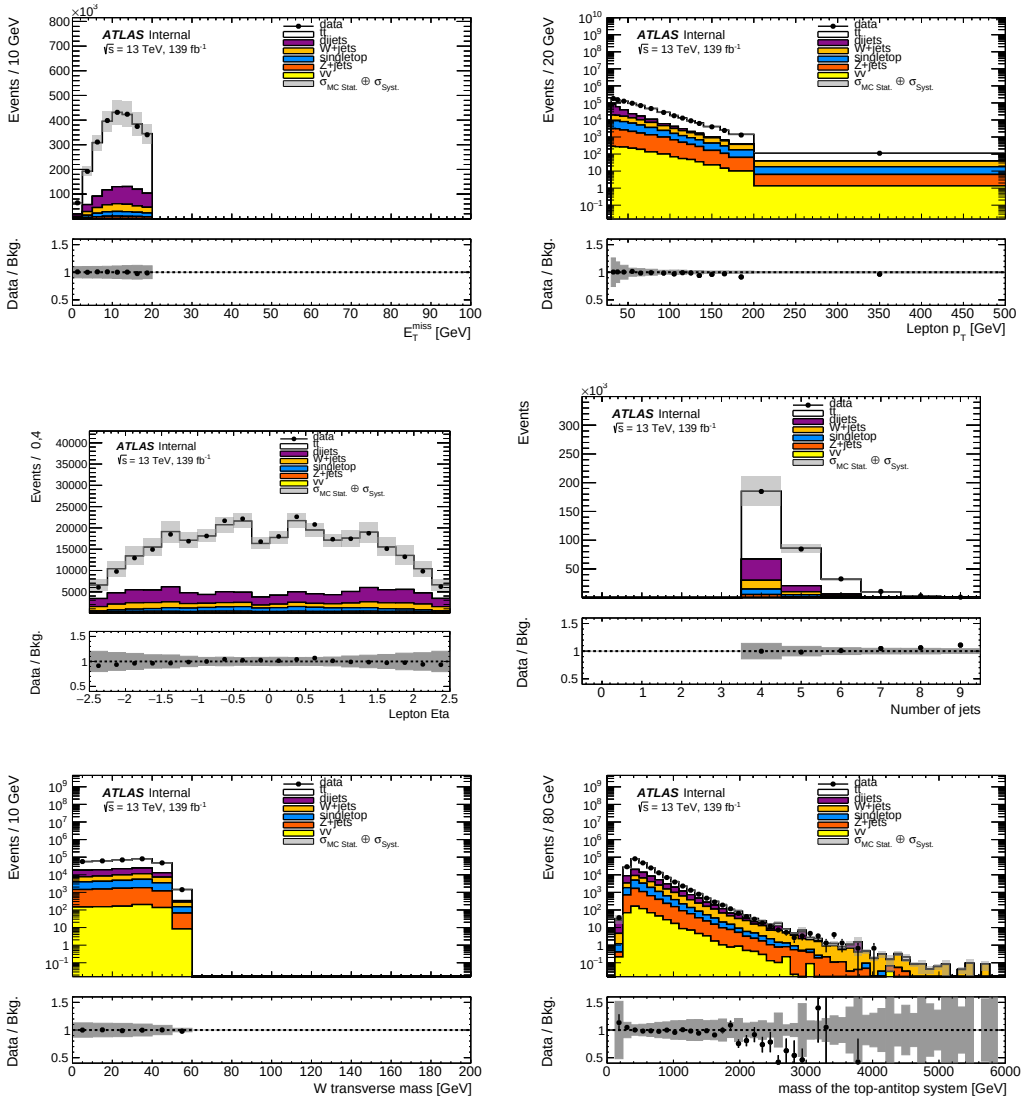

Figure C.11: Distribution of E_{miss} (top-left), p_T (top-right), muon eta (middle-left), number of jets (middle-right), m_W (bottom-left) and $m_{t\bar{t}}$ (bottom-right) in the $cR^{4j,1b}_{\text{QCD}}$ control region for the muon channel. The gray band represents both the systematic and the statistical uncertainties associated to the multijet background.

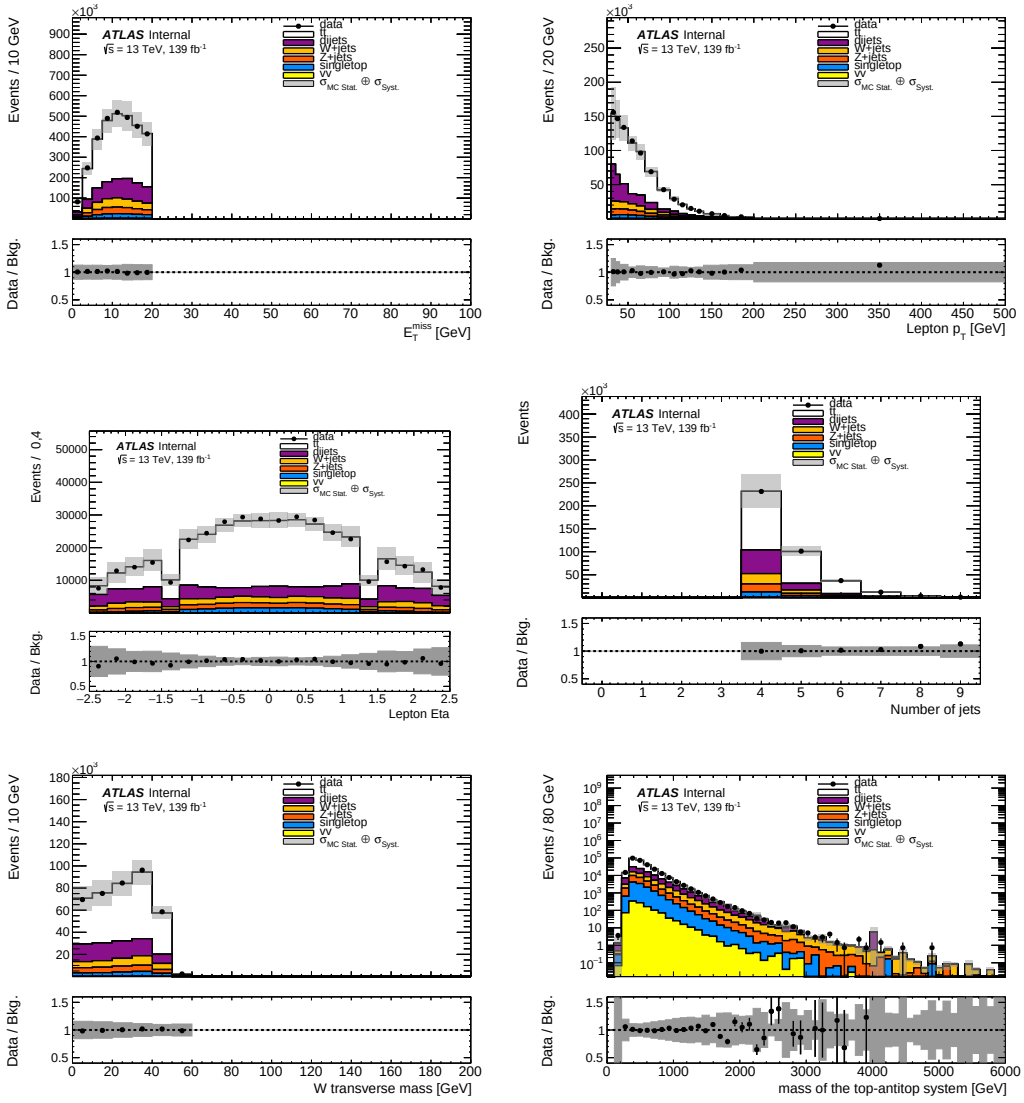

Figure C.12: Distribution of E_T^{miss} (top-left), p_T (top-right), electron η (middle-left), number of jets (middle-right), m_W (bottom-left) and $m_{t\bar{t}}$ (bottom-right) in the $CR_{\text{QCD}}^{4j,1b}$ control region for the electron channel. The gray band represents both the systematic and the statistical uncertainties associated to the multijet background.

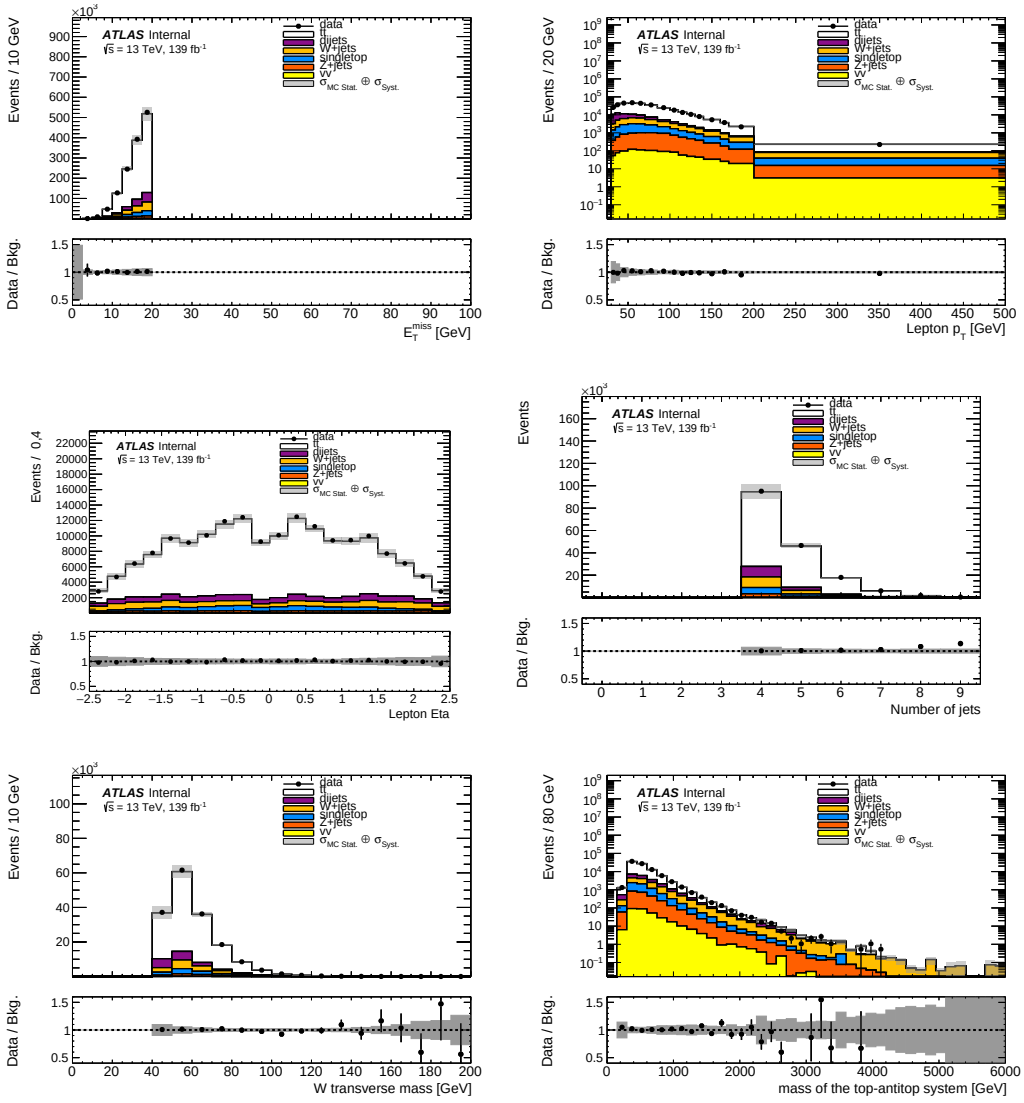

Figure C.13: Distribution of E_T^{miss} (top-left), p_T (top-right), muon η (middle-left), number of jets (middle-right), m_W (bottom-left) and $m_{t\bar{t}}$ (bottom-right) in the $VR1^{4j,1b}_{\text{QCD}}$ validation region for the muon channel. The gray band represents both the systematic and the statistical uncertainties associated to the multijet background.

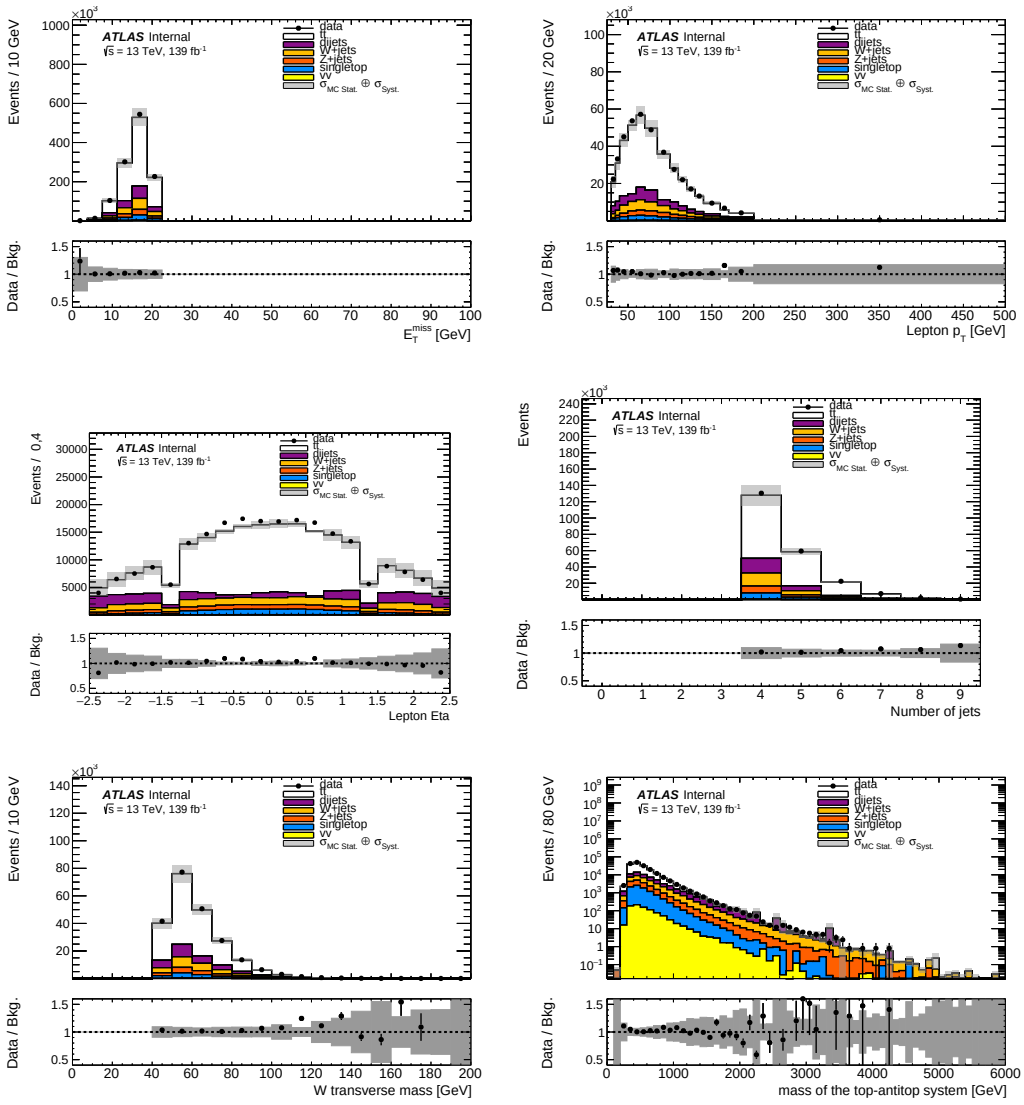

Figure C.14: Distribution of E_T^{miss} (top-left), p_T (top-right), muon η (middle-left), number of jets (middle-right), m_W (bottom-left) and $m_{t\bar{t}}$ (bottom-right) in the $VR1^{4j,1b}_{\text{QCD}}$ validation region for the electron channel. The gray band represents both the systematic and the statistical uncertainties associated to the multijet background.

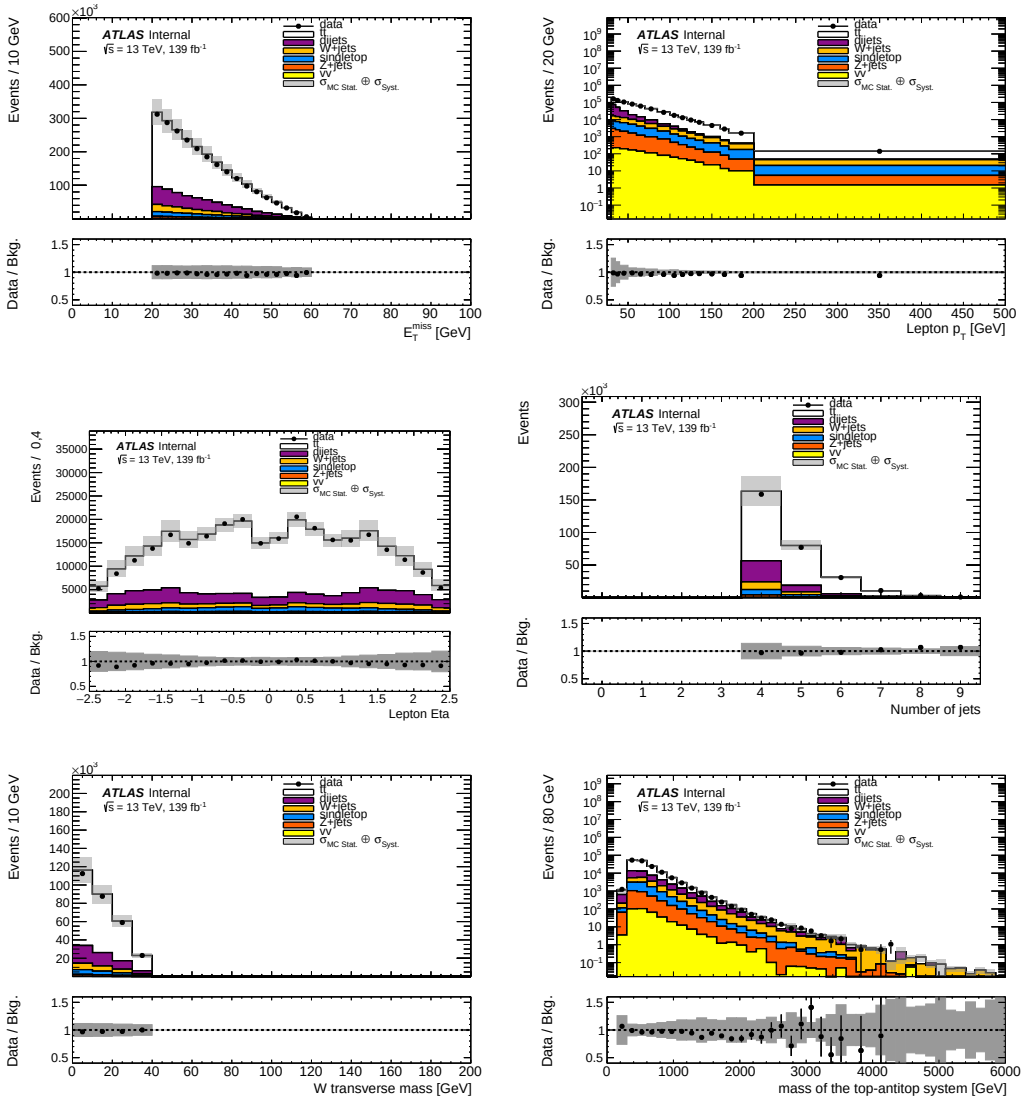

Figure C.15: Distribution of E_T^{miss} (top-left), p_T (top-right), muon η (middle-left), number of jets (middle-right), m_W (bottom-left) and $m_{t\bar{t}}$ (bottom-right) in the $VR2_{\text{QCD}}^{4j,1b}$ validation region for the muon channel. The gray band represents both the systematic and the statistical uncertainties associated to the multijet background.

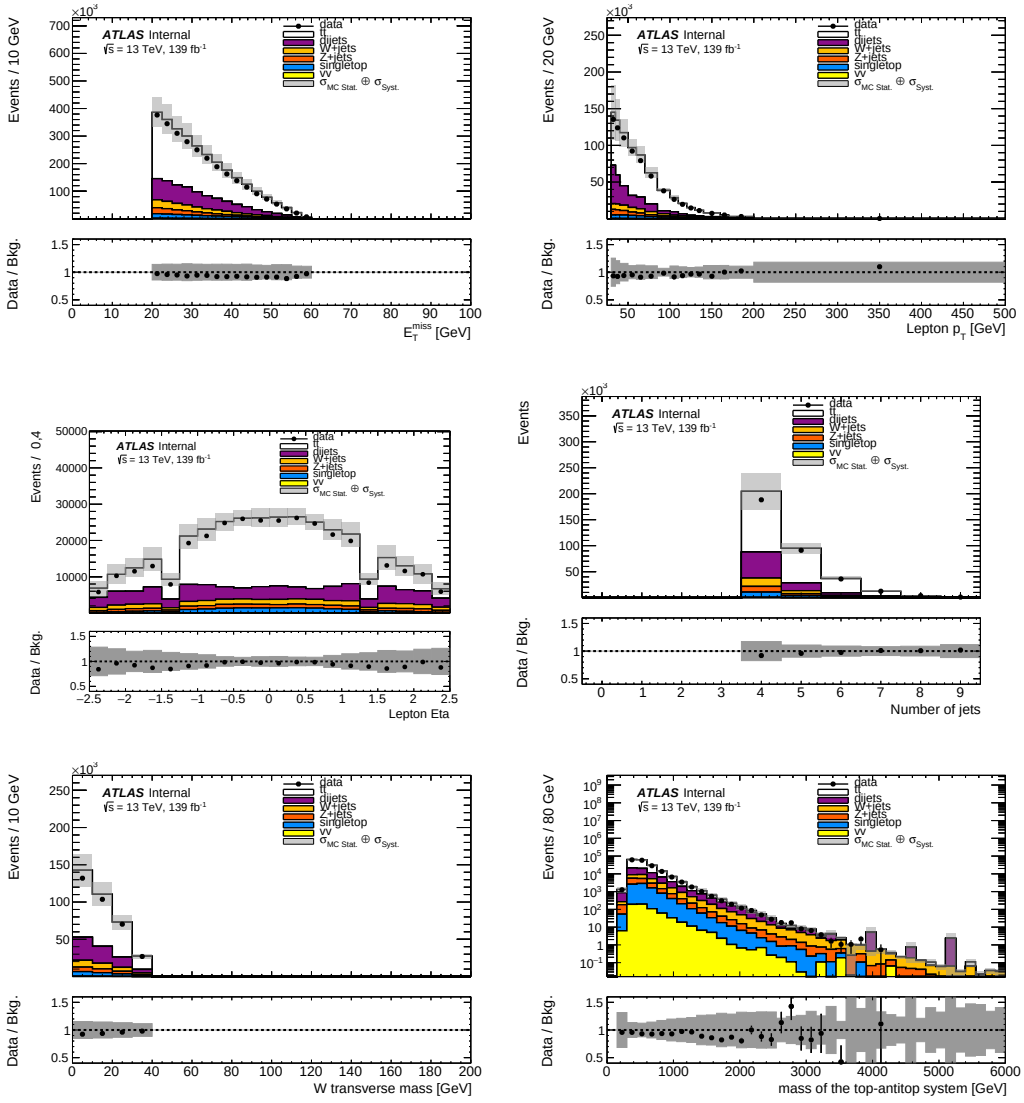

Figure C.16: Distribution of E_T^{miss} (top-left), p_T (top-right), muon η (middle-left), number of jets (middle-right), m_W (bottom-left) and $m_{t\bar{t}}$ (bottom-right) in the $VR2^{4j,1b}_{\text{QCD}}$ validation region for the electron channel. The gray band represents both the systematic and the statistical uncertainties associated to the multijet background.

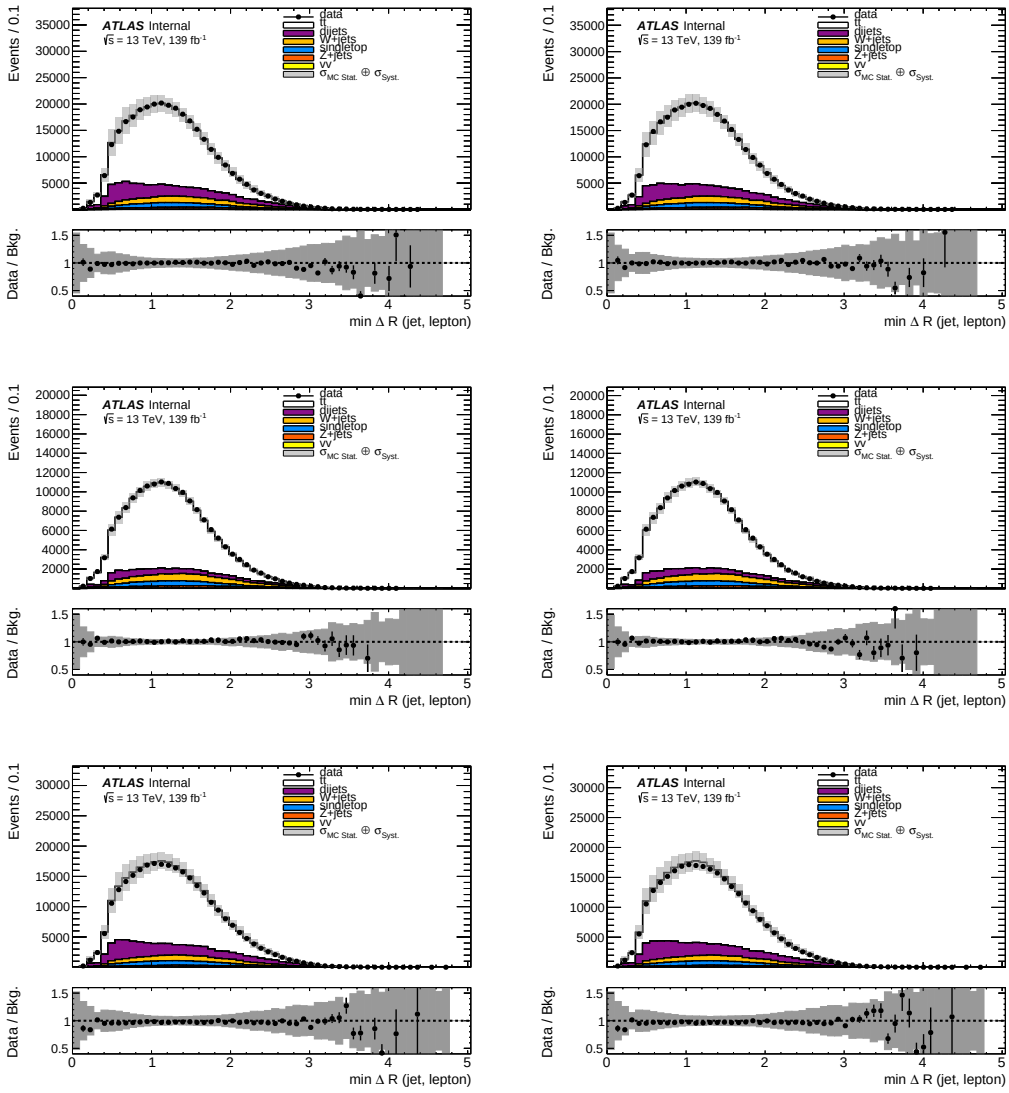

Figure C.17: Distribution of ΔR (left), ΔR_{corr} (right) in the $CR^{4j,1b}_{\text{QCD}}$, (top) $VR1^{4j,1b}_{\text{QCD}}$ (middle) and $VR2^{4j,1b}_{\text{QCD}}$ (bottom) for the muon channel. The gray band represents both the systematic and the statistical uncertainties associated to the multijet background.

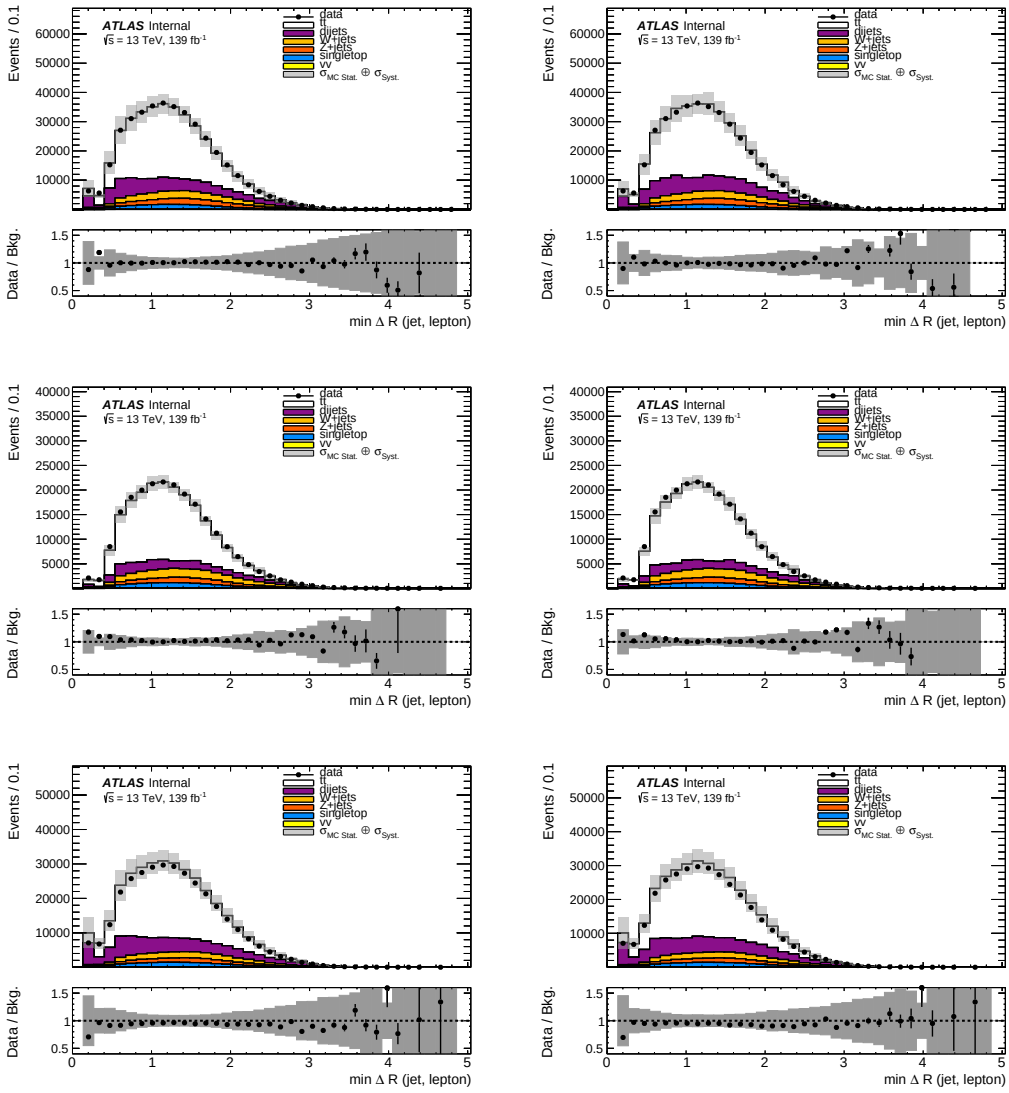

Figure C.18: Distribution of ΔR (left), ΔR_{corr} (right) in the $CR^{4j,1b}_{\text{QCD}}$, (top) $VR1^{4j,1b}_{\text{QCD}}$ (middle) and $VR2^{4j,1b}_{\text{QCD}}$ (bottom) for the electron channel. The gray band represents both the systematic and the statistical uncertainties associated to the multijet background.

Appendix D

$t\bar{t}1\ell$ Analysis Nuisance Parameter Pulls

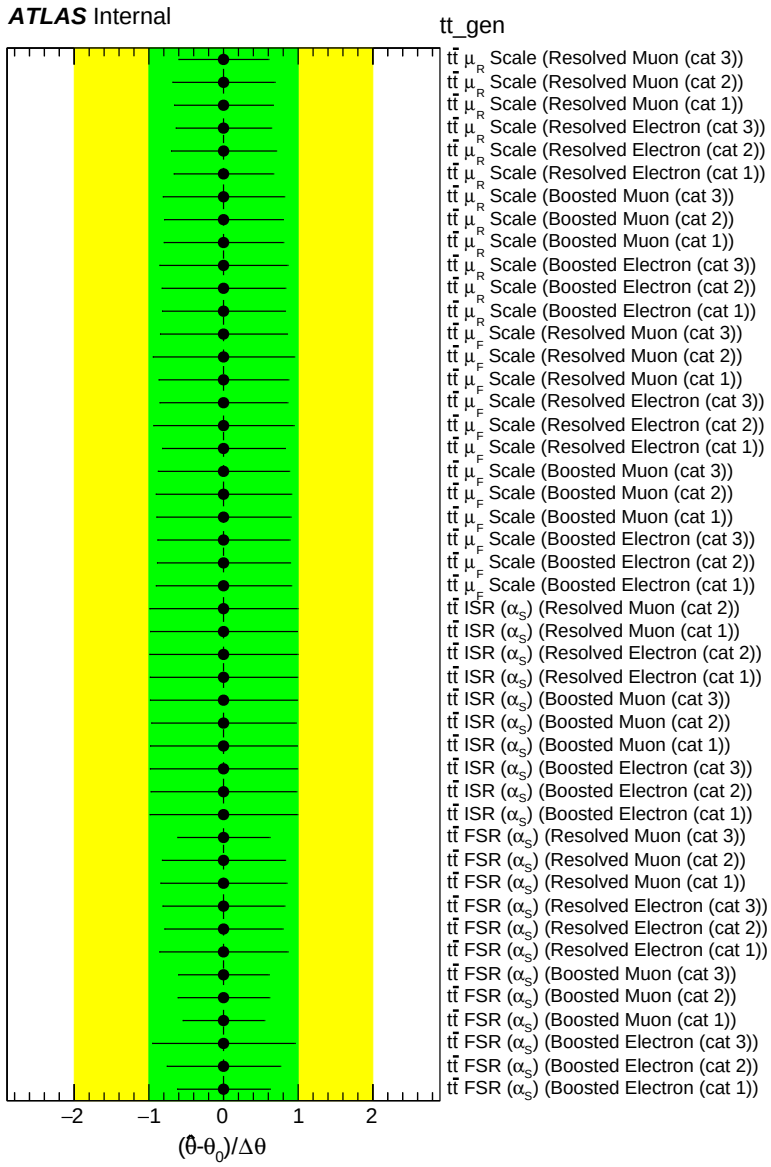

Figure D.1: $t\bar{t}$ generator (μ_R, μ_F, ISR, FSR) nuisance parameter pulls.

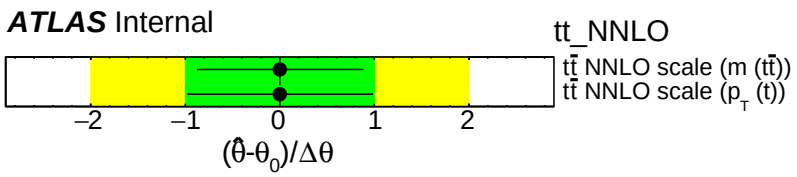

Figure D.2: $t\bar{t}$ NNLO reweighting nuisance parameter pulls.

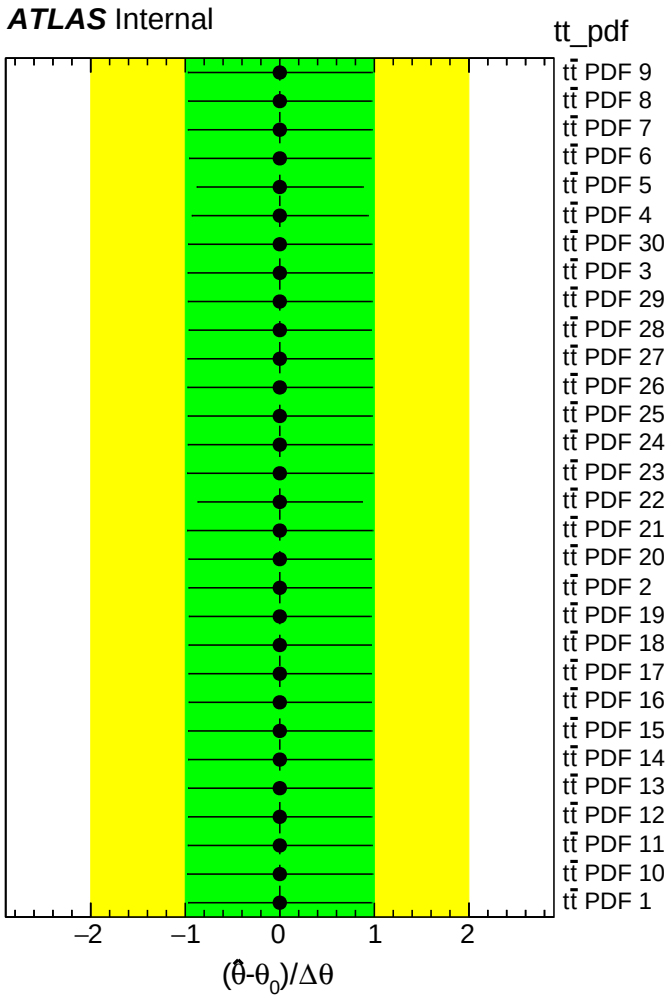

Figure D.3: Nuisance parameter pulls for the 30 PDF variations on the $t\bar{t}$ background.

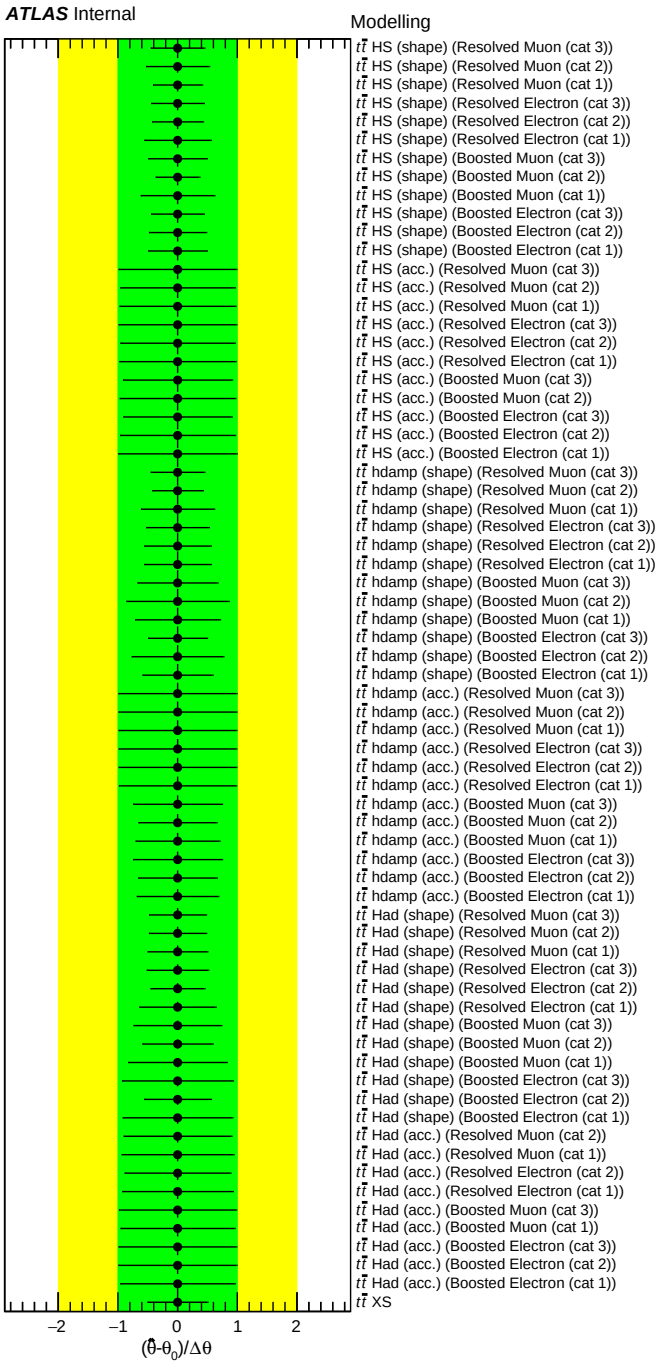

Figure D.4: $t\bar{t}$ modeling (parton shower, hadronization, h_{damp}) nuisance parameters. These are 2-point systematic uncertainties and are estimated using alternative $t\bar{t}$ samples.

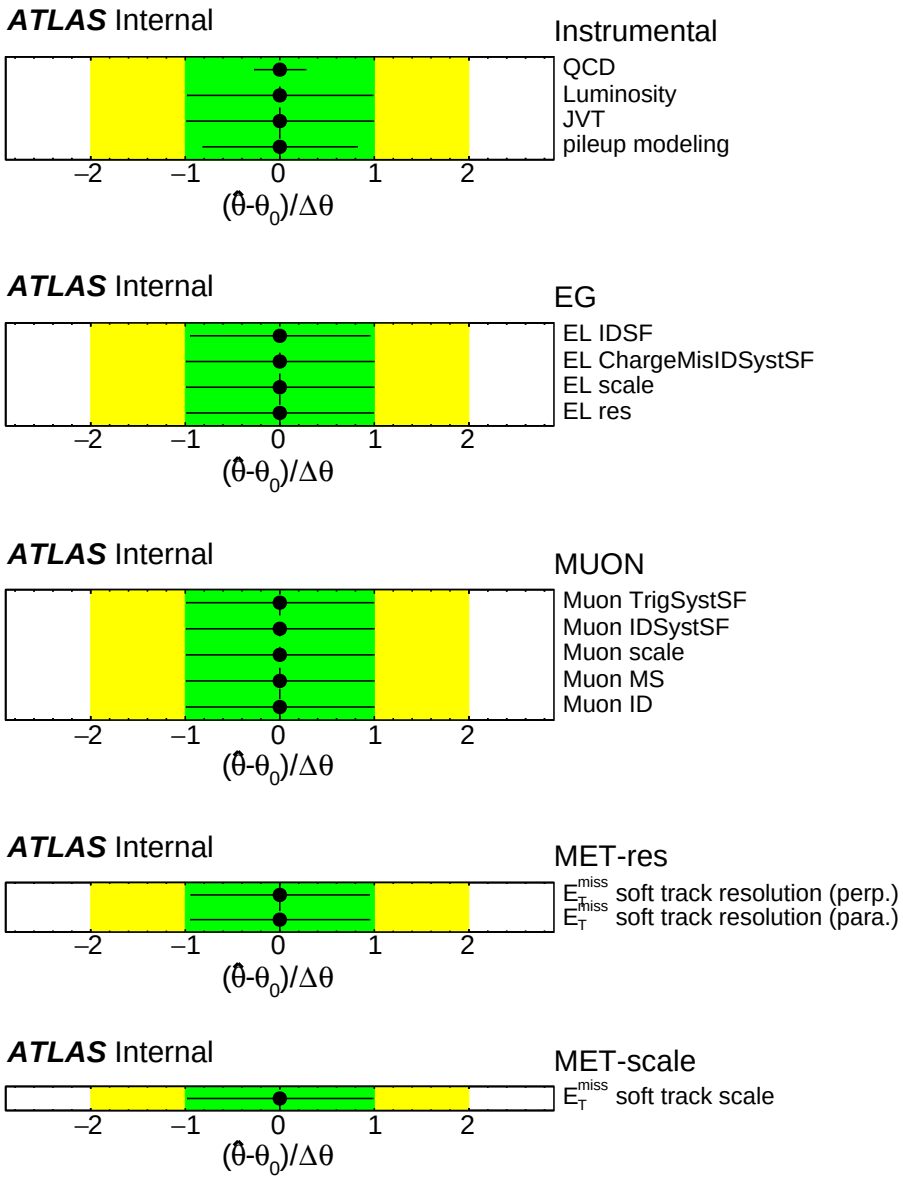

Figure D.5: Nuisance parameter pulls for the luminosity, JVT, pileup modelling, electron, muon, and MET systematic uncertainties.

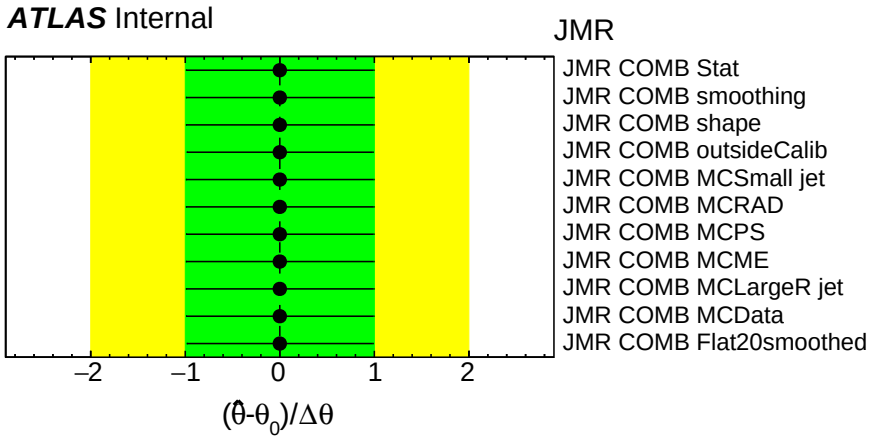

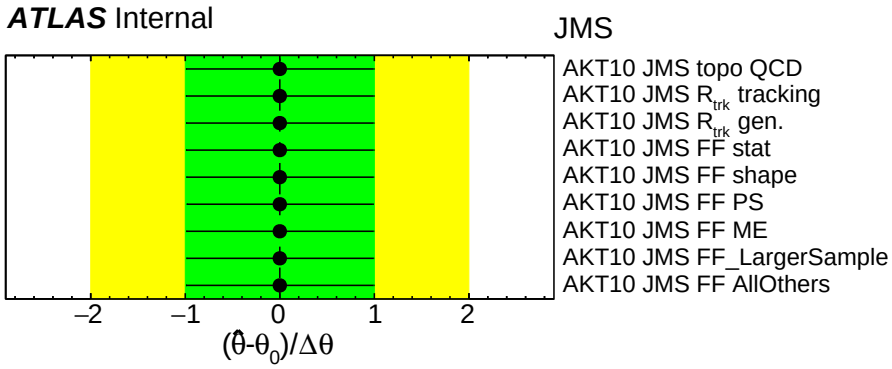

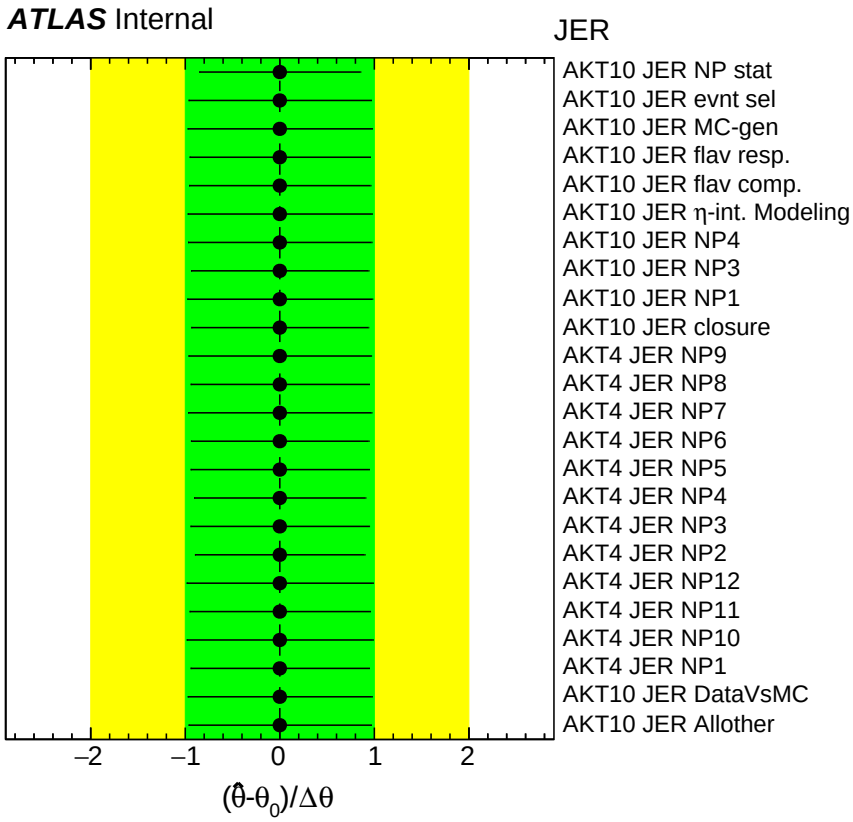

Figure D.6: JMR, JMS and JER nuisance parameter pulls.

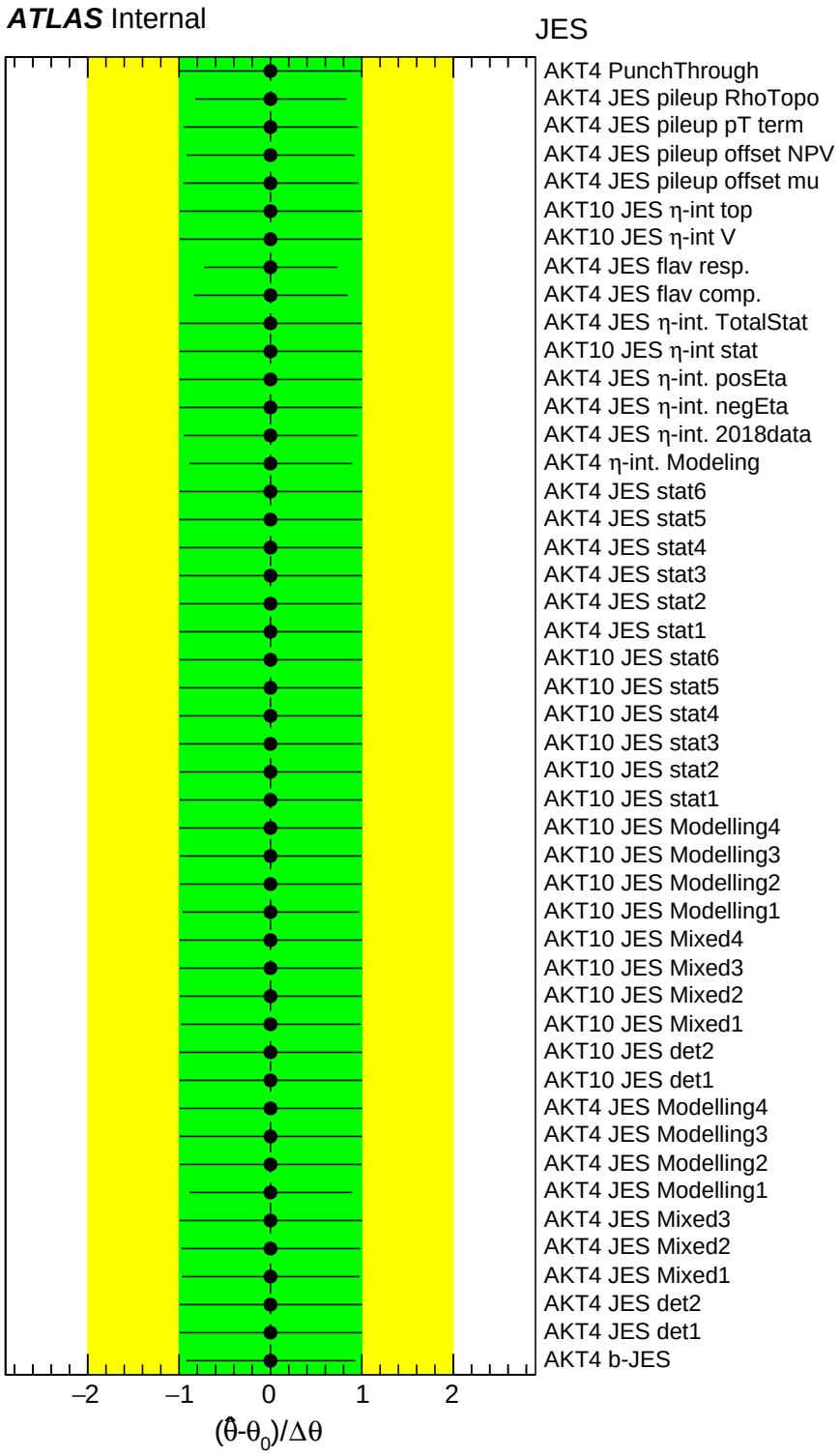

Figure D.7: JES nuisance parameter pulls.

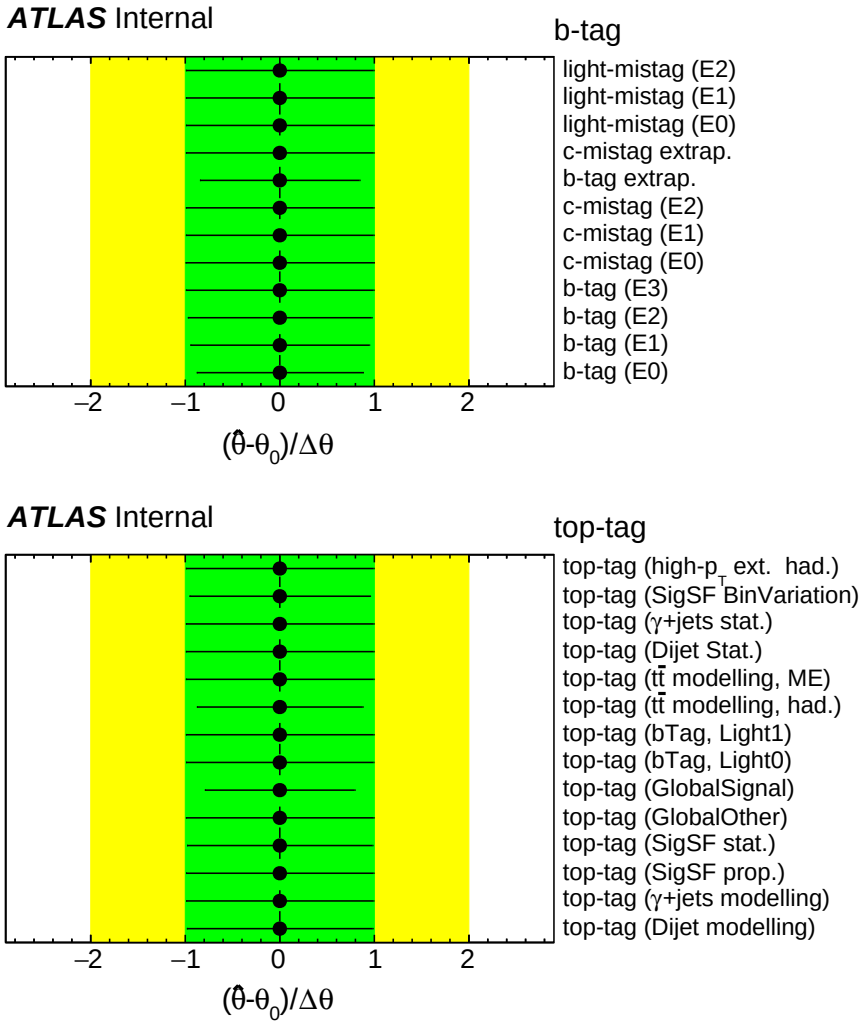

Figure D.8: Nuisance parameter pulls for the b-tagging and top-tagging SF uncertainties.

Appendix E

$t\bar{t}1\ell$ Correlation Matrix and Normalization Factors

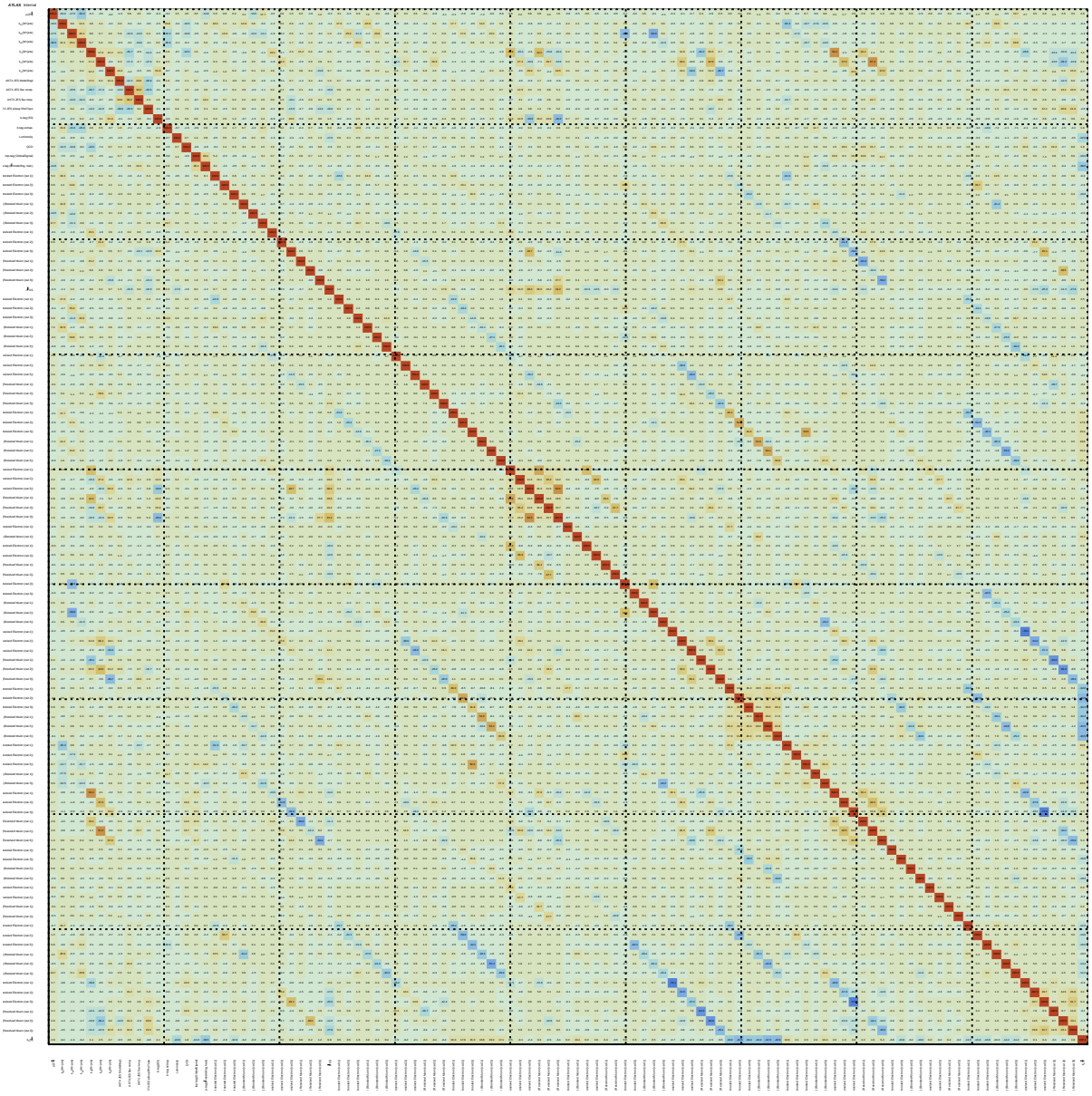

Figure E.1: The correlation matrix.

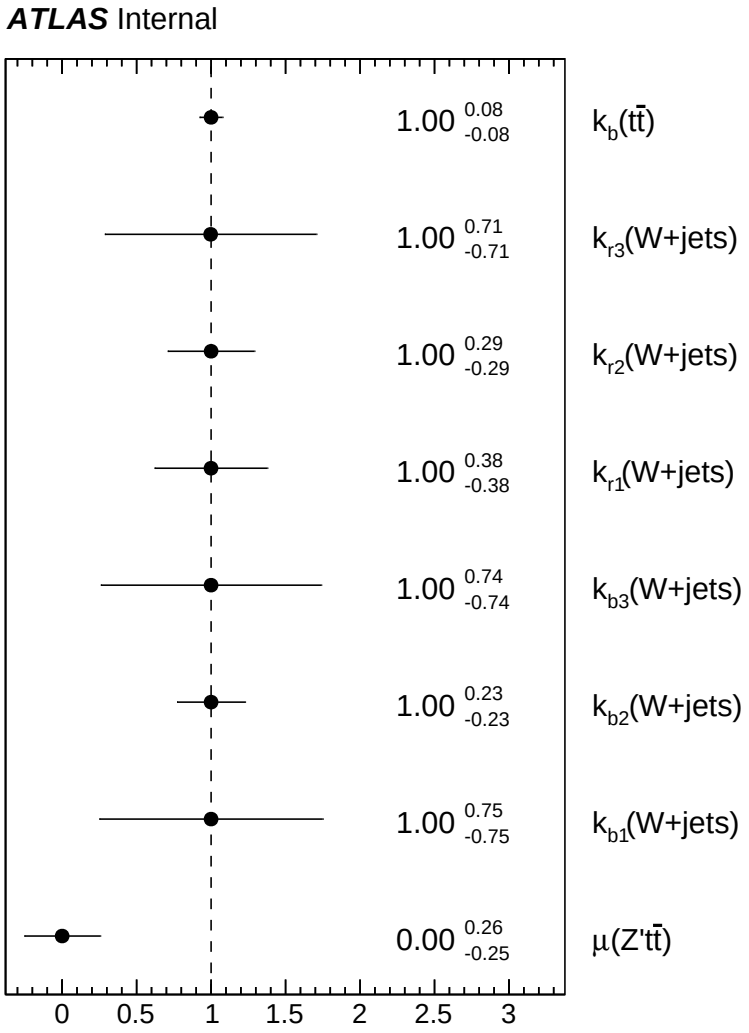

Figure E.2: Normalization factors for various background components and the signal strength (Parameter Of Interest).

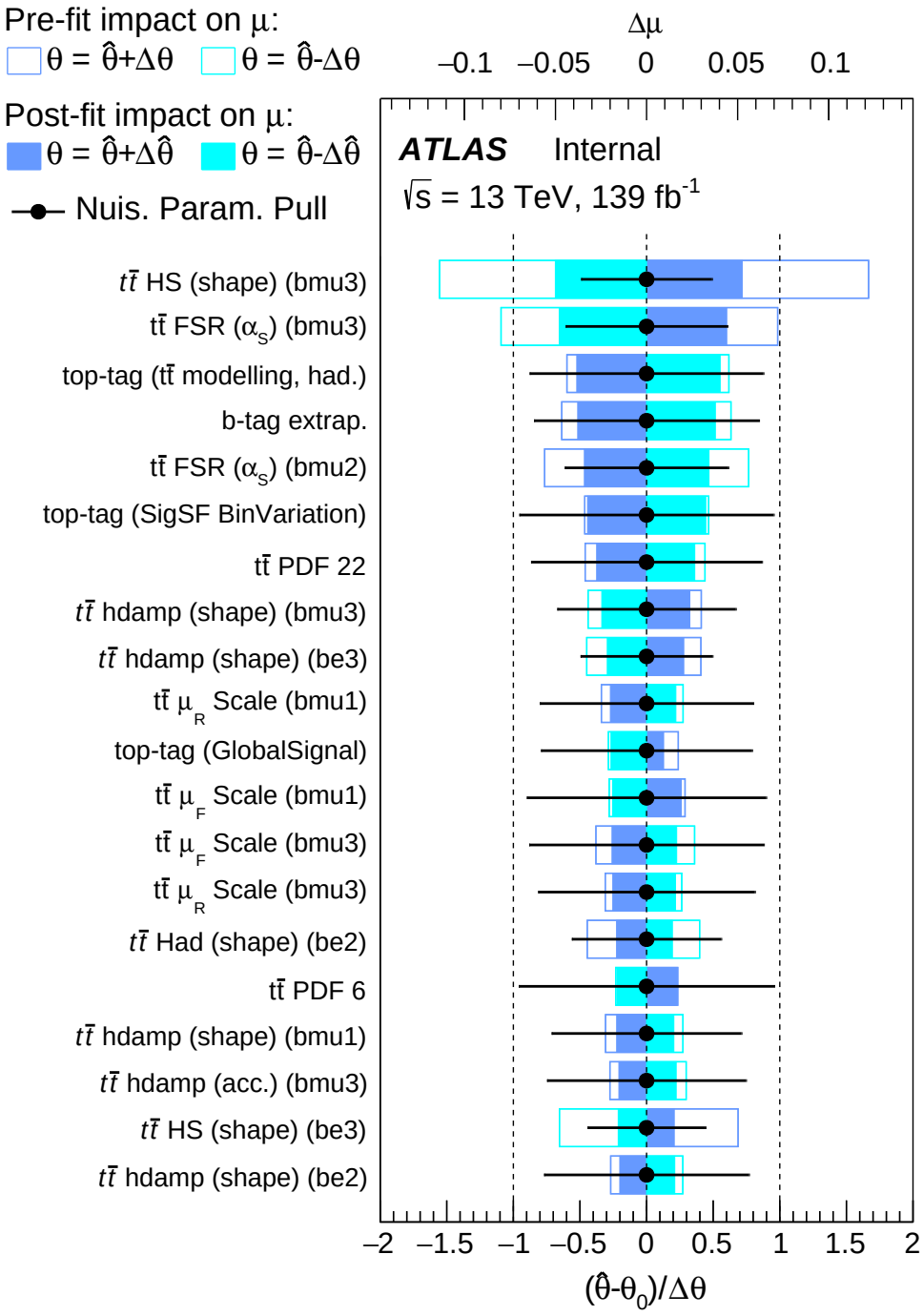

Figure E.3: Ranking plot showing the top 20 nuisance parameters based on impact.

Appendix F

Additional $t\bar{t}1\ell$ Kinematic Distributions

F.1 Resolved Channels

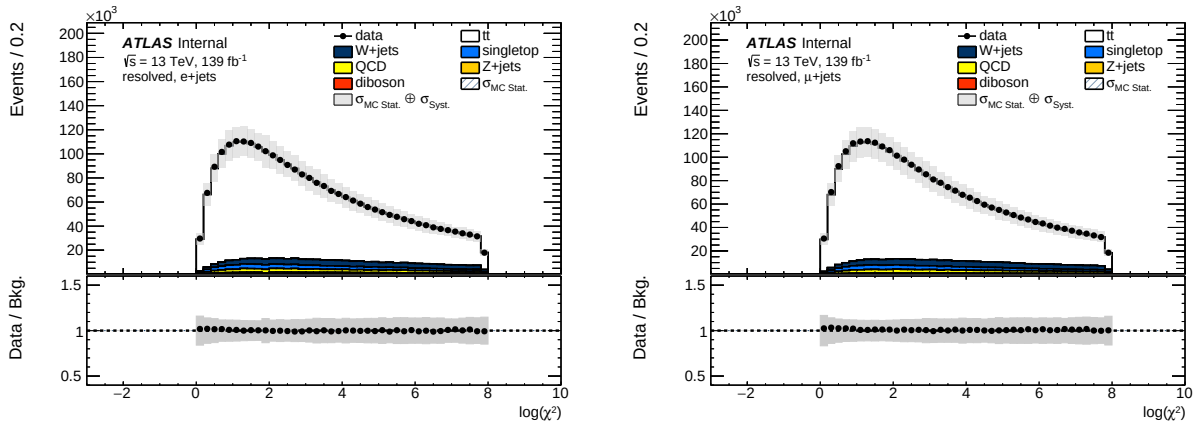

(a) (b)

Figure F.1: Reconstruction χ^2 distributions for the resolved e (left) and resolved μ (right) channels.

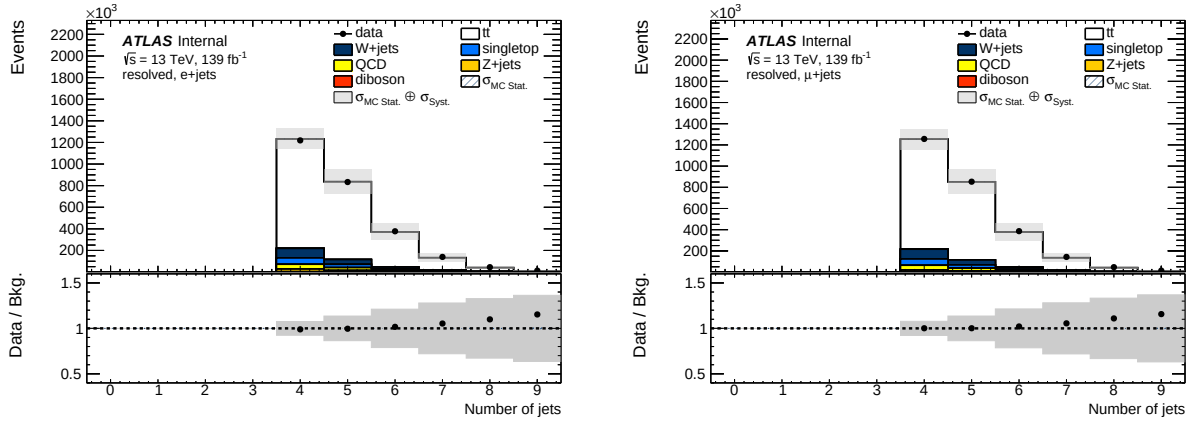

(a) (b)

Figure F.2: Number of jets distributions for the resolved e (left) and resolved μ (right) channels.

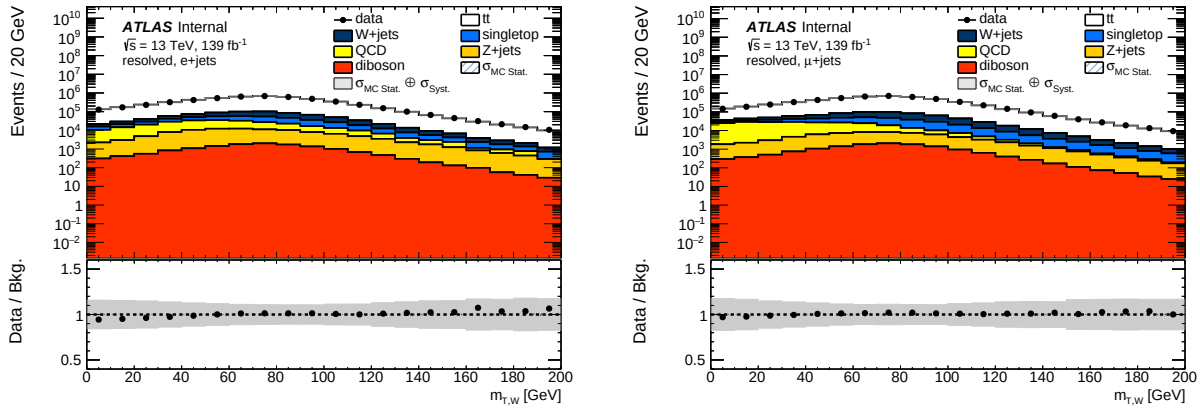

(a) (b)

Figure F.3: $m_{T,W}$ distributions for the resolved e (left) and resolved μ (right) channels.

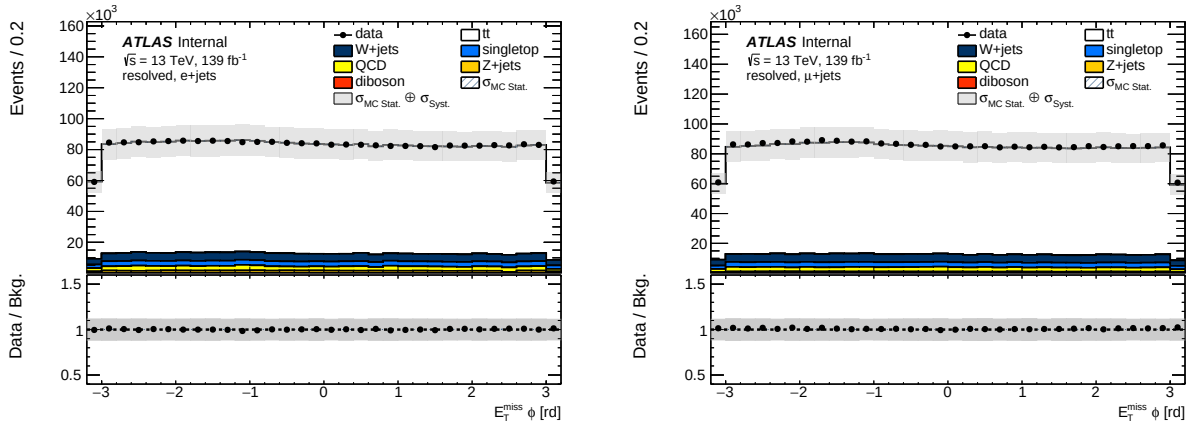

(a) (b)

Figure F.4: E_T^{miss} ϕ distributions for the resolved e (left) and resolved μ (right) channels.

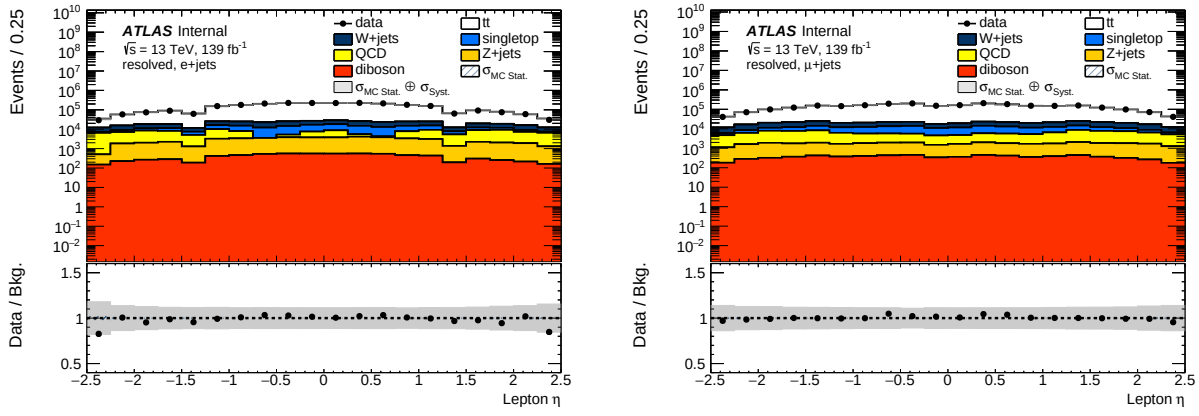

(a) (b)

Figure F.5: Lepton η distributions for the resolved e (left) and resolved μ (right) channels.

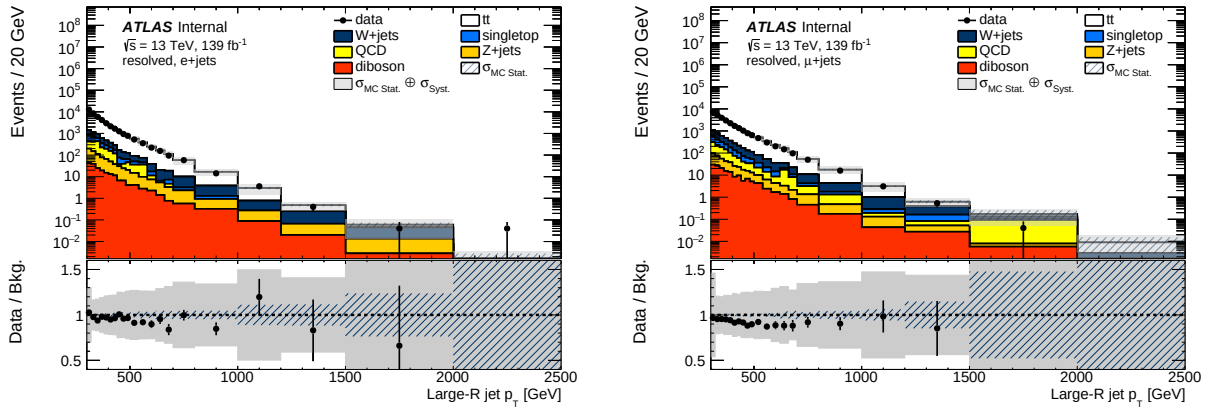

(a) (b)

Figure F.6: Large-R jet p_T distributions for the resolved e (left) and resolved μ (right) channels.

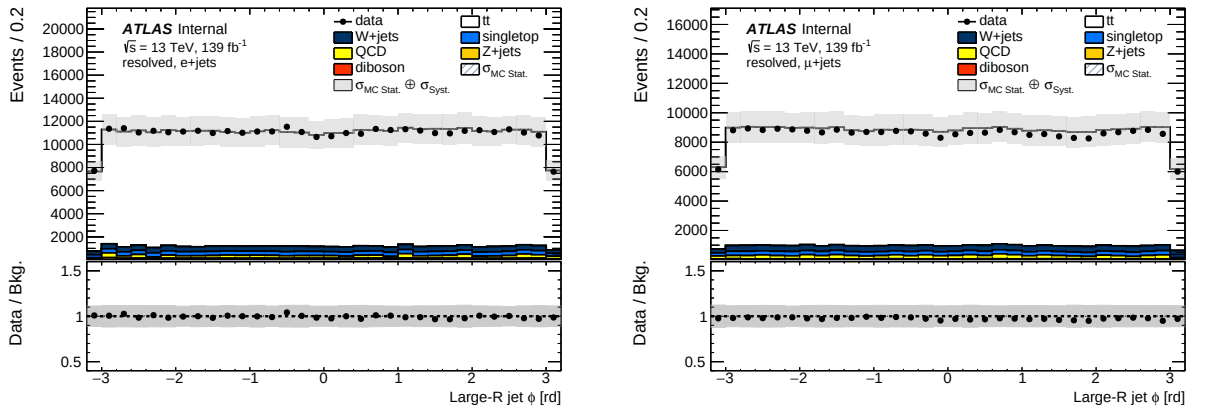

(a) (b)

Figure F.7: Large-R jet ϕ distributions for the resolved e (left) and resolved μ (right) channels.

F.2 Boosted Channels

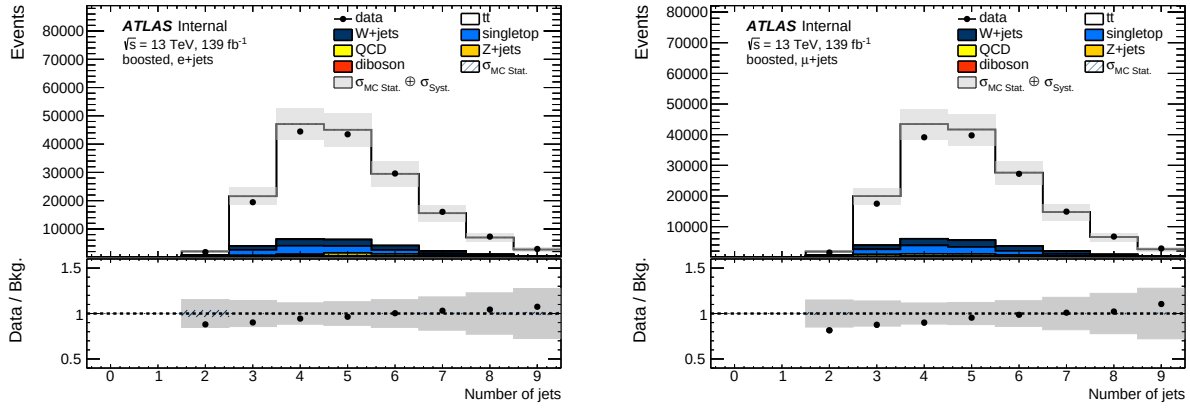

(a) (b)

Figure F.8: Number of jets distributions for the boosted e (left) and boosted μ (right) channels.

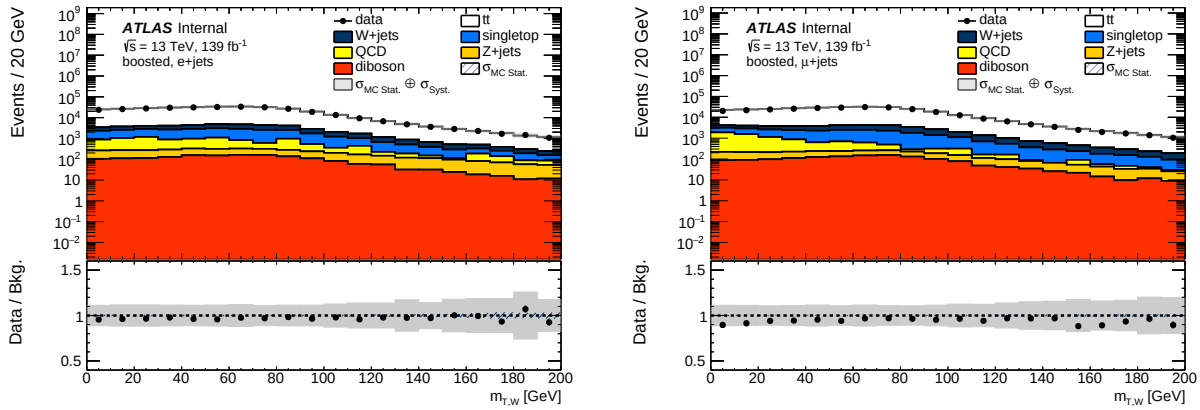

(a) (b)

Figure F.9: $m_{T,W}$ distributions for the boosted e (left) and boosted μ (right) channels.

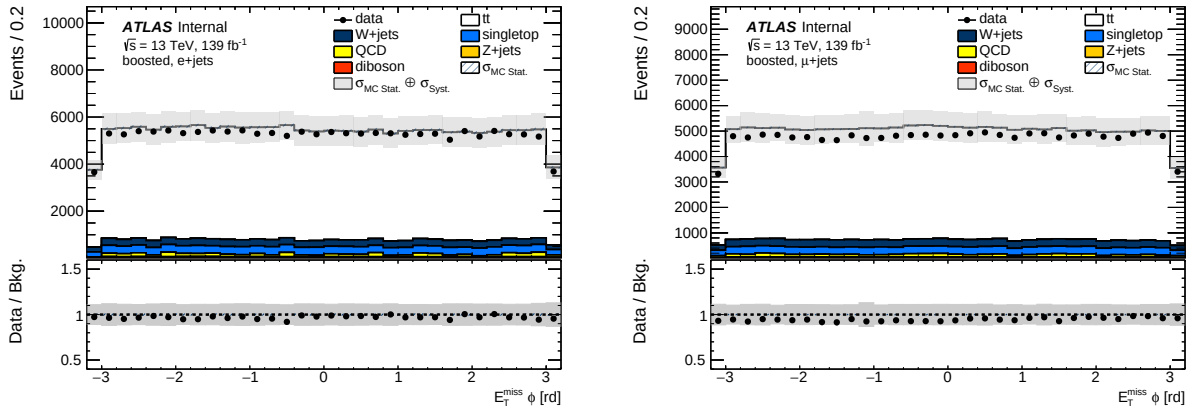

(a) (b)

Figure F.10: E_T^{miss} ϕ distributions for the boosted e (left) and boosted μ (right) channels.

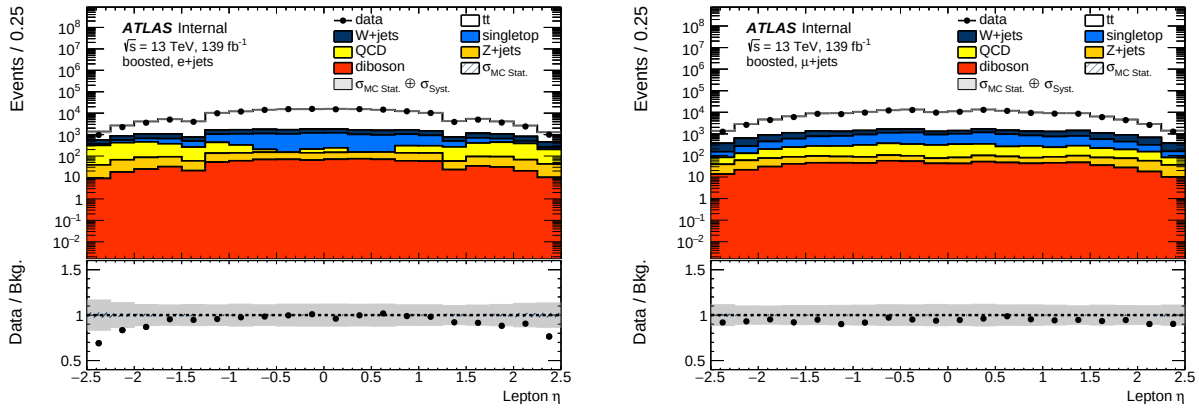

(a) (b)

Figure F.11: Lepton η distributions for the boosted e (left) and boosted μ (right) channels.

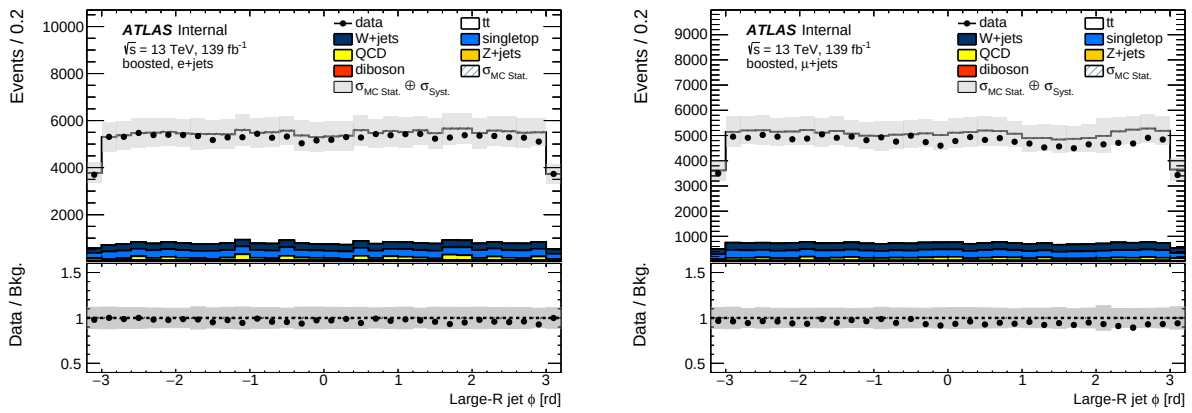

(a) (b)

Figure F.12: Large-R jet ϕ distributions for the boosted e (left) and boosted μ (right) channels.

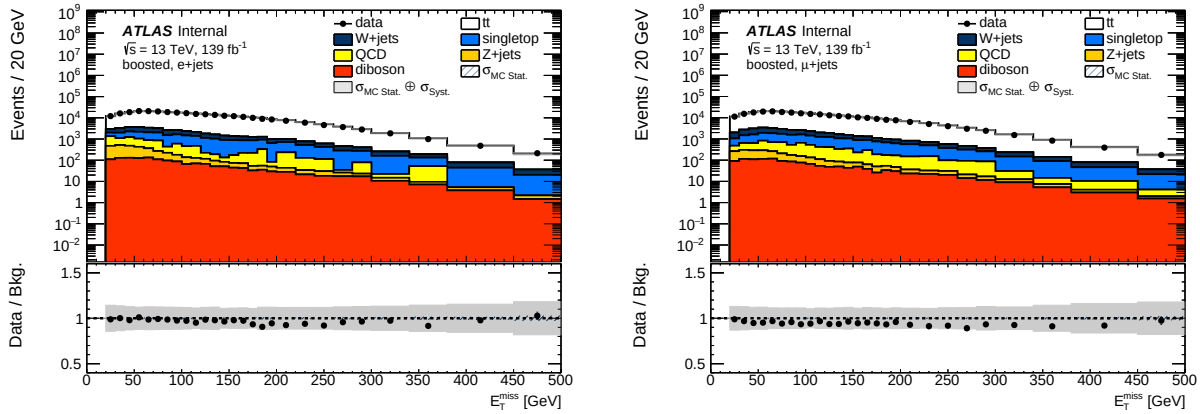

(a) (b)

Figure F.13: E_T^{miss} distributions for the boosted e (left) and boosted μ (right) channels.

REFERENCES

REFERENCES

[1] John Dalton. *A New System of Chemical Philosophy*, volume 1 of *Cambridge Library Collection - Physical Sciences*. Cambridge University Press, 2010.

[2] J. J. Thomson M.A. F.R.S. XL. Cathode Rays. *The London, Edinburgh, and Dublin Philosophical Magazine and Journal of Science*, 44(269):293–316, 1897.

[3] Professor E. Rutherford F.R.S. LXXIX. The scattering of α and β particles by matter and the structure of the atom. *The London, Edinburgh, and Dublin Philosophical Magazine and Journal of Science*, 21(125):669–688, 1911.

[4] J. Chadwick. Possible Existence of a Neutron. *Nature*, 129:312, 1932.

[5] J. D. Bjorken and Emmanuel A. Paschos. Inelastic Electron Proton and gamma Proton Scattering, and the Structure of the Nucleon. *Phys. Rev.*, 185:1975–1982, 1969.

[6] M. Tanabashi et al. Review of Particle Physics. *Phys. Rev. D*, 98(3):030001, 2018.

[7] Michal Czakon, Paul Fiedler, and Alexander Mitov. Total top-quark pair-production cross section at hadron colliders. *Physical Review Letters*, 110(25), jun 2013.

[8] John C. Baez and John Huerta. The algebra of grand unified theories. *Bulletin of the American Mathematical Society*, 47(3):483–552, 2010.

[9] Howard Georgi and S. L. Glashow. Unity of all elementary-particle forces. *Phys. Rev. Lett.*, 32:438–441, Feb 1974.

[10] Lisa Randall and Raman Sundrum. A Large mass hierarchy from a small extra dimension. *Phys. Rev. Lett.*, 83:3370–3373, 1999.

[11] Kaustubh Agashe, Hooman Davoudiasl, Gilad Perez, and Amarjit Soni. Warped Gravitons at the LHC and Beyond. *Phys. Rev. D*, 76:036006, 2007.

[12] Alexandra Oliveira. Gravity particles from Warped Extra Dimensions, predictions for LHC. 2014.

[13] Walter D. Goldberger and Mark B. Wise. Modulus stabilization with bulk fields. *Phys. Rev. Lett.*, 83:4922–4925, 1999.

[14] Walter D. Goldberger and Mark B. Wise. Phenomenology of a stabilized modulus. *Phys. Lett.*, B475:275–279, 2000.

[15] Edward Farhi and Leonard Susskind. Technicolour. *Physics Reports*, 74(3):277–321, 1981.

[16] Christopher T. Hill and Elizabeth H. Simmons. Strong dynamics and electroweak symmetry breaking. *Physics Reports*, 381(4-6):235–402, jul 2003.

[17] Robert M. Harris and Supriya Jain. Cross sections for leptophobic topcolor Z' decaying to top–antitop. *The European Physical Journal C*, 72(7), jul 2012.

[18] Duccio Pappadopulo, Andrea Thamm, Riccardo Torre, and Andrea Wulzer. Heavy vector triplets: bridging theory and data. *Journal of High Energy Physics*, 09:060, 2014.

[19] J. de Blas, J. M. Lizana, and M. Perez-Victoria. Combining searches of Z' and W' bosons. *Journal of High Energy Physics*, 01:166, 2013.

[20] Vernon D. Barger, Wai-Yee Keung, and Ernest Ma. Gauge model with light W and Z bosons. *Phys. Rev. D*, 22:727, 1980.

[21] Roberto Contino, David Marzocca, Duccio Pappadopulo, and Riccardo Rattazzi. On the effect of resonances in composite Higgs phenomenology. *Journal of High Energy Physics*, 10:081, 2011.

[22] Lyndon Evans and Philip Bryant. LHC machine. *Journal of Instrumentation*, 3(08):S08001–S08001, aug 2008.

[23] Oliver Sim Brüning, Paul Collier, P Lebrun, Stephen Myers, Ranko Ostojic, John Poole, and Paul Proudlock. *LHC Design Report Vol.1: The LHC main ring*. CERN Yellow Reports: Monographs. CERN, Geneva, 2004.

[24] Oliver Sim Brüning, Paul Collier, P Lebrun, Stephen Myers, Ranko Ostojic, John Poole, and Paul Proudlock. *LHC Design Report Vol 2. The LHC infrastructure and general services*. CERN Yellow Reports: Monographs. CERN, Geneva, 2004.

[25] Michael Benedikt, Paul Collier, V Mertens, John Poole, and Karlheinz Schindl. *LHC Design Report Vol 3. The LHC injector chain*. CERN Yellow Reports: Monographs. CERN, Geneva, 2004.

[26] The ATLAS Collaboration. The ATLAS experiment at the CERN large hadron collider. *Journal of Instrumentation*, 3(08):S08003–S08003, aug 2008.

[27] The CMS Collaboration. The CMS experiment at the CERN LHC. *Journal of Instrumentation*, 3(08):S08004–S08004, aug 2008.

[28] The ALICE Collaboration. The ALICE experiment at the CERN LHC. *Journal of Instrumentation*, 3(08):S08002–S08002, aug 2008.

[29] The LHCb Collaboration. The LHCb detector at the LHC. *Journal of Instrumentation*, 3(08):S08005–S08005, aug 2008.

[30] Mukund Gupta. Calculation of radiation length in materials. Technical report, CERN, Geneva, Jul 2010.

[31] The ATLAS collaboration. Operation of the ATLAS trigger system in run 2. *Journal of Instrumentation*, 15(10):P10004–P10004, oct 2020.

[32] Martijn Elsing, Luc Goossens, Armin Nairz, and Guido Negri. The ATLAS Tier-0: Overview and operational experience. *Journal of Physics: Conference Series*, 219:072011, 05 2010.

[33] *ATLAS Computing: technical design report*. Technical design report. ATLAS. CERN, Geneva, 2005.

[34] S. Agostinelli et al. GEANT4–a simulation toolkit. *Nucl. Instrum. Meth. A*, 506:250–303, 2003.

[35] Torbjörn Sjöstrand, Stefan Ask, Jesper R. Christiansen, Richard Corke, Nishita Desai, Philip Ilten, Stephen Mrenna, Stefan Prestel, Christine O. Rasmussen, and Peter Z. Skands. An introduction to PYTHIA 8.2. *Computer Physics Communications*, 191:159–177, jun 2015.

[36] Manuel Bähr, Stefan Gieseke, Martyn A. Gigg, David Grellscheid, Keith Hamilton, Oluseyi Latunde-Dada, Simon Plätzer, Peter Richardson, Michael H. Seymour, Alexander Sherstnev, and Bryan R. Webber. Herwig physics and manual. *The European Physical Journal C*, 58(4):639–707, nov 2008.

[37] T. Gleisberg, Stefan. Hoeche, F. Krauss, M. Schonherr, S. Schumann, F. Siegert, and J. Winter. Event generation with SHERPA 1.1. *JHEP*, 02:007, 2009.

[38] J. Alwall, R. Frederix, S. Frixione, V. Hirschi, F. Maltoni, O. Mattelaer, H.-S. Shao, T. Stelzer, P. Torrielli, and M. Zaro. The automated computation of tree-level and next-to-leading order differential cross sections, and their matching to parton shower simulations. *Journal of High Energy Physics*, 2014(7), jul 2014.

[39] Johan Alwall, Michel Herquet, Fabio Maltoni, Olivier Mattelaer, and Tim Stelzer. MadGraph 5: going beyond. *Journal of High Energy Physics*, 2011(6), jun 2011.

[40] Davison E. Soper. Parton distribution functions. *Nuclear Physics B - Proceedings Supplements*, 53(1-3):69–80, feb 1997.

[41] S. Agostinelli and et al. Geant4—a simulation toolkit. *Nuclear Instruments and Methods in Physics Research Section A: Accelerators, Spectrometers, Detectors and Associated Equipment*, 506(3):250–303, 2003.

[42] J. Allison and et al. Geant4 developments and applications. *IEEE Transactions on Nuclear Science*, 53(1):270–278, 2006.

[43] T Cornelissen, M Elsing, I Gavrilenko, W Liebig, E Moyse, and A Salzburger. The new atlas track reconstruction (newt). *Journal of Physics: Conference Series*, 119:032014, 07 2008.

[44] R. Frühwirth. Application of kalman filtering to track and vertex fitting. *Nuclear Instruments and Methods in Physics Research Section A: Accelerators, Spectrometers, Detectors and Associated Equipment*, 262(2):444–450, 1987.

[45] M. Aaboud and et al. Reconstruction of primary vertices at the ATLAS experiment in run 1 proton–proton collisions at the LHC. *The European Physical Journal C*, 77(5), may 2017.

[46] W Lampl, S Laplace, D Lelas, P Loch, H Ma, S Menke, S Rajagopalan, D Rousseau, S Snyder, and G Unal. Calorimeter Clustering Algorithms: Description and Performance. Technical report, CERN, Geneva, Apr 2008. All figures including auxiliary figures are available at https://atlas.web.cern.ch/Atlas/GROUPS/PHYSICS/PUBNOTES/ATL-LARG-PUB-2008-002.

[47] M. Aaboud and et al. Jet reconstruction and performance using particle flow with the ATLAS detector. *The European Physical Journal C*, 77(7), jul 2017.

[48] The ATLAS Collaboration. Electron and photon performance measurements with the ATLAS detector using the 2015–2017 LHC proton-proton collision data. *Journal of Instrumentation*, 14(12):P12006–P12006, dec 2019.

[49] M. Aaboud and et al. Electron reconstruction and identification in the ATLAS experiment using the 2015 and 2016 LHC proton–proton collision data at $\sqrt{s} = 13$ TeV. *The European Physical Journal C*, 79(8), aug 2019.

[50] Improved electron reconstruction in ATLAS using the Gaussian Sum Filter-based model for bremsstrahlung. Technical report, CERN, Geneva, May 2012. All figures including auxiliary figures are available at https://atlas.web.cern.ch/Atlas/GROUPS/PHYSICS/CONFNOTES/ATLAS-CONF-2012-047.

[51] The ATLAS Collaboration. Muon reconstruction performance of the ATLAS detector in proton–proton collision data at $\sqrt{s} = 13$ TeV. *The European Physical Journal C*, 76(5), may 2016.

[52] The ATLAS Collaboration. Muon reconstruction and identification efficiency in ATLAS using the full Run 2 *pp* collision data set at $\sqrt{s} = 13$ TeV. *Eur. Phys. J., C*, 81:578. 44 p, Dec 2020. 64 pages in total, author list starting page 42, auxiliary material starting at page 59, 34 figures, 3 tables. All figures including auxiliary figures are available at https://atlas.web.cern.ch/Atlas/GROUPS/PHYSICS/PAPERS/MUON-2018-03/.

[53] Matteo Cacciari, Gavin P Salam, and Gregory Soyez. The anti-k_t jet clustering algorithm. *Journal of High Energy Physics*, 2008(04):063–063, apr 2008.

[54] The ATLAS Collaboration. Performance of pile-up mitigation techniques for jets in *pp* collisions at $\sqrt{s}$=8 tev using the ATLAS detector. *The European Physical Journal C*, 76(11), oct 2016.

[55] M. Aaboud and et al. Jet energy scale measurements and their systematic uncertainties in proton-proton collisions at $\sqrt{s}$=13 tev with the ATLAS detector. *Physical Review D*, 96(7), oct 2017.

[56] David Krohn, Jesse Thaler, and Lian-Tao Wang. Jet trimming. *Journal of High Energy Physics*, 2010(2), feb 2010.

[57] The ATLAS Collaboration. Performance of jet substructure techniques for large-R jets in proton-proton collisions at $\sqrt{s} = 7$ tev using the ATLAS detector. *Journal of High Energy Physics*, 2013(9), sep 2013.

[58] Variable radius, exclusive-k$_T$, and center-of-mass subjet reconstruction for Higgs($\rightarrow b\bar{b}$) tagging in ATLAS. Technical report, CERN, Geneva, Jun 2017. All figures including auxiliary figures are available at https://atlas.web.cern.ch/Atlas/GROUPS/PHYSICS/PUBNOTES/ATL-PHYS-PUB-2017-010.

[59] M. Aaboud and et al. Performance of top-quark and W-boson tagging with atlas in run 2 of the LHC. *The European Physical Journal C*, 79(5), apr 2019.

[60] Optimisation and performance studies of the ATLAS b-tagging algorithms for the 2017-18 LHC run. Technical report, CERN, Geneva, Jul 2017. All figures including auxiliary figures are available at https://atlas.web.cern.ch/Atlas/GROUPS/PHYSICS/PUBNOTES/ATL-PHYS-PUB-2017-013.

[61] M. Aaboud and et al. Search for heavy particles decaying into top-quark pairs using lepton-plus-jets events in proton-proton collisions at $\sqrt{s} = 13$ tev with the atlas detector. *The European Physical Journal C*, 78(7), jul 2018.

[62] C. Oleari. The powheg box. *Nuclear Physics B - Proceedings Supplements*, 205-206:36–41, aug 2010.

[63] Stefano Frixione, Giovanni Ridolfi, and Paolo Nason. A positive-weight next-to-leading-order monte carlo for heavy flavour hadroproduction. *Journal of High Energy Physics*, 2007(09):126–126, sep 2007.

[64] Torbjörn Sjöstrand, Stephen Mrenna, and Peter Skands. A brief introduction to PYTHIA 8.1. *Computer Physics Communications*, 178(11):852–867, jun 2008.

[65] Richard D. Ball, , Valerio Bertone, Stefano Carrazza, Christopher S. Deans, Luigi Del Debbio, Stefano Forte, Alberto Guffanti, Nathan P. Hartland, José I. Latorre, Juan Rojo, and Maria Ubiali. Parton distributions for the LHC run II. *Journal of High Energy Physics*, 2015(4), apr 2015.

[66] Enrico Bothmann, Gurpreet Singh Chahal, Stefan Höche, Johannes Krause, Frank Krauss, Silvan Kuttimalai, Sebastian Liebschner, Davide Napoletano, Marek Schönherr, Holger Schulz, Steffen Schumann, and Frank Siegert. Event generation with sherpa 2.2. *SciPost Physics*, 7(3), sep 2019.

[67] Selection of jets produced in 13 TeV proton-proton collisions with the ATLAS detector. Technical report, CERN, Geneva, Jul 2015.

[68] The ATLAS Collaboration. Measurements of top-quark pair differential cross-sections in the lepton+jets channel in pp collisions at $\sqrt{s} = 8$ TeV using the ATLAS detector. *The European Physical Journal C*, 76(10), oct 2016.

[69] Michal Czakon, David Heymes, Alexander Mitov, Davide Pagani, Ioannis Tsinikos, and Marco Zaro. Top-pair production at the LHC through NNLO QCD and NLO EW. *Journal of High Energy Physics*, 2017(10), oct 2017.

[70] Massimiliano Grazzini, Stefan Kallweit, and Marius Wiesemann. Fully differential nnlo computations with matrix. *The European Physical Journal C*, 78, 11 2017.

[71] The ATLAS Collaboration. Measurement of the $t\bar{t}$ production cross-section in the lepton+jets channel at $\sqrt{s} = 13$ tev with the atlas experiment. *Physics Letters B*, 810:135797, nov 2020.

[72] CMS Collaboration. CMS Top Quark Physics Summary Figures (as of 7.2022).

[73] The ATLAS Collaboration. ATLAS b-jet identification performance and efficiency measurement with $t\bar{t}$ events in pp collisions at $\sqrt{s} = 13$ TeV. *The European Physical Journal C*, 79(11), nov 2019.

[74] G. Avoni. The new LUCID-2 detector for luminosity measurement and monitoring in ATLAS. *JINST*, 13:P07017, 2020.

[75] Georgios Choudalakis. On hypothesis testing, trials factor, hypertests and the bumphunter. 2011.

[76] Glen Cowan, Kyle Cranmer, Eilam Gross, and Ofer Vitells. Asymptotic formulae for likelihood-based tests of new physics. *The European Physical Journal C*, 71(2), feb 2011.

[77] ATLAS Collaboration. Combination of searches for heavy resonances decaying into bosonic and leptonic final states using $36\,\text{fb}^{-1}$ of proton–proton collision data at $\sqrt{s} = 13\,\text{TeV}$ with the ATLAS detector. *Phys. Rev. D*, 98:052008, 2018.

[78] CMS Collaboration. Combination of CMS searches for heavy resonances decaying to pairs of bosons or leptons. *Phys. Lett. B*, 798:134952, 2019.

[79] ATLAS Collaboration. Search for diboson resonances with boson-tagged jets in pp collisions at $\sqrt{s} = 13\,\text{TeV}$ with the ATLAS detector. *Phys. Lett. B*, 777:91, 2018.

[80] ATLAS Collaboration. Search for heavy diboson resonances in semileptonic final states in pp collisions at $\sqrt{s} = 13\,\text{TeV}$ with the ATLAS detector. *Eur. Phys. J. C*, 80:1165, 2020.

[81] ATLAS Collaboration. Search for resonant WZ production in the $WZ \to \ell\nu\ell'\ell'$ channel in $\sqrt{s} = 7\,\text{TeV}$ pp collisions with the ATLAS detector. *Phys. Rev. D*, 85:112012, 2012.

[82] ATLAS Collaboration. Search for resonances decaying into a weak vector boson and a Higgs boson in the fully hadronic final state produced in proton–proton collisions at $\sqrt{s} = 13\,\text{TeV}$ with the ATLAS detector. *Phys. Rev. D*, 102:112008, 2020.

[83] ATLAS Collaboration. Search for heavy resonances decaying into a W boson and a Higgs boson in final states with leptons and b-jets in $139\,\text{fb}^{-1}$ of pp collisions at $\sqrt{s} = 13\,\text{TeV}$ with the ATLAS detector. ATLAS-CONF-2021-026, 2021.

[84] ATLAS Collaboration. Search for heavy resonances decaying into a Z boson and a Higgs boson in final states with leptons and b-jets in $139\,\text{fb}^{-1}$ of pp collisions at $\sqrt{s} = 13\,\text{TeV}$ with the ATLAS detector. ATLAS-CONF-2020-043, 2020.

[85] ATLAS Collaboration. Search for high-mass dilepton resonances in pp collisions at $\sqrt{s} = 8\,\text{TeV}$ with the ATLAS detector. *Phys. Rev. D*, 90:052005, 2014.

[86] ATLAS Collaboration. Search for a heavy charged boson in events with a charged lepton and missing transverse momentum from pp collisions at $\sqrt{s} = 13\,\text{TeV}$ with the ATLAS detector. *Phys. Rev. D*, 100:052013, 2019.

[87] ATLAS Collaboration. Search for high-mass resonances in final states with a tau lepton and missing transverse momentum with the ATLAS detector. ATLAS-CONF-2021-025, 2021.

[88] ATLAS Collaboration. Search for new resonances in mass distributions of jet pairs using 139 fb^{-1} of pp collisions at $\sqrt{s} = 13$ TeV with the ATLAS detector. *Journal of High Energy Physics*, 2020(3), mar 2020.

[89] ATLAS Collaboration. Search for $t\bar{t}$ resonances in fully hadronic final states in pp collisions at $\sqrt{s} = 13$ TeV with the ATLAS detector. *Journal of High Energy Physics*, 10:061, 2020.

[90] Paolo Nason. A New method for combining NLO QCD with shower Monte Carlo algorithms. *Journal of High Energy Physics*, 11:040, 2004.

[91] Stefano Frixione, Paolo Nason, and Carlo Oleari. Matching NLO QCD computations with Parton Shower simulations: the POWHEG method. *Journal of High Energy Physics*, 11:070, 2007.

[92] Simone Alioli, Paolo Nason, Carlo Oleari, and Emanuele Re. A general framework for implementing NLO calculations in shower Monte Carlo programs: the POWHEG BOX. *Journal of High Energy Physics*, 06:043, 2010.

[93] Fabio Cascioli, Philipp Maierhofer, and Stefano Pozzorini. Scattering Amplitudes with Open Loops. *Phys. Rev. Lett.*, 108:111601, 2012.

[94] Tanju Gleisberg and Stefan Höche. Comix, a new matrix element generator. *Journal of High Energy Physics*, 12:039, 2008.

[95] ATLAS Collaboration. EGamma Recommendations. https://twiki.cern.ch/twiki/bin/view/AtlasProtected/EGammaRecommendationsR21.

[96] ATLAS Collaboration. MCP Recommendations. https://twiki.cern.ch/twiki/bin/view/AtlasProtected/MCPAnalysisConsolidationMC16.

[97] ATLAS Collaboration. Tau Recommendations. https://twiki.cern.ch/twiki/bin/view/AtlasProtected

[98] Peter Alfeld. A trivariate clough—tocher scheme for tetrahedral data. *Computer Aided Geometric Design*, 1(2):169–181, 1984.

[99] Wouter Verkerke and David Kirkby. The RooFit toolkit for data modeling, 2003.

[100] Lorenzo Moneta, Kevin Belasco, Kyle S. Cranmer, S. Kreiss, Alfio Lazzaro, Danilo Piparo, Gregory Schott, Wouter Verkerke, and Matthias Wolf. The RooStats Project, 2010.

[101] Kyle Cranmer, George Lewis, Lorenzo Moneta, Akira Shibata, and Wouter Verkerke. HistFactory: A tool for creating statistical models for use with RooFit and RooStats. CERN-OPEN-2012-016, New York, Jan 2012.

[102] H. Kroha, R. Fakhrutdinov, and A. Kozhin. New High-Precision Drift-Tube Detectors for the ATLAS Muon Spectrometer. New High-Precision Drift-Tube Detectors for the ATLAS Muon Spectrometer. *JINST*, 12:C06007. 12 p, Jun 2017. proceedings of INSTR17 conference, Novosibirsk, Russia, February 2017, extended version, to be publsihed in Journal of Instrumentation.

[103] R. Veenhof. GARFIELD Users Manual.

[104] Bernhard Bittner, Jörg Dubbert, Oliver Kortner, Hubert Kroha, Alessandro Manfredini, Sebastian Nowak, Sebastian Ott, Robert Richter, Philipp Schwegler, Daniele Zanzi, Otmar Biebel, Ralf Hertenberger, Alexander Ruschke, and Andre Zibell. Performance of drift-tube detectors at high counting rates for high-luminosity LHC upgrades. *Nuclear Instruments and Methods in Physics Research Section A: Accelerators, Spectrometers, Detectors and Associated Equipment*, 732:250–254, dec 2013.

[105] Oliver Kortner, Hubert Kroha, Felix Muller, Sebastian Nowak, and Robert Richter. Precision muon tracking at future hadron colliders with sMDT chambers. In *2015 IEEE Nuclear Science Symposium and Medical Imaging Conference (NSS/MIC)*. IEEE, oct 2015.